THE UNIVERSITY
of EDINBURGH

Investigating sources of uncertainty associated with the JULES land surface model

by

Darren Slevin

THE UNIVERSITY
of EDINBURGH

Thesis submitted in fulfilment of
the requirements for the degree of
Doctor of Philosophy
to the
University of Edinburgh
July 2015

Declaration

I confirm that the work submitted is my own, except where work which is part of a jointly-authored paper has been included. One of the results chapters is based on a paper published in a peer reviewed journal on which I am the lead author. Details of the publication is given below, including an outline of the contribution of each author. I confirm that appropriate credit has been given within the thesis where reference has been made to the work of others. No part of this work has been submitted for any other degree or professional qualification.

Chapter 4 is based on a paper published in Geoscientific Model Development: D. Slevin, S.F.B. Tett and M. Williams, 'Multi-site evaluation of the JULES land surface model using global and local data', Geoscientific Model Development, 8, 295-316, doi:10.5194/gmd-8-295-2015, 2015. I collated the various datasets required for the model simulations, performed the model simulations and data analysis and wrote the manuscript. My supervisors Simon Tett and Mat Williams provided scientific advice and edited the manuscript.

The other parts of the thesis were proofread by Simon Tett and feedback given.

Darren Slevin

July 2015

Acknowledgements

First and foremost I would like to thank my supervisors Simon Tett and Mat Williams without whom this work would not have been possible. Both taught me that good writing is as important as good science. They kept me going when times were tough, asked insightful questions, and offered invaluable advice. I want to thank Richard Essery and Eleanor Blyth for agreeing to be my examiners. I firmly believe the final thesis is better because of their critique and suggestions.

I would like to thank the members of the climate reading group, both past and present, from whom I have learned so much during our weekly discussions: Andrew Schurer, Debbie Polson, Oliver Browne, Tim Cowan, Simon Tett, Gabi Hegerl, Massimo Bollasina, Ioana Colfescu, Caroline Holmes, Emma Turner, Alessio Bozzo, Simone Morak, Oliver Krueger and Sabine Undorf. I would also like to thank members of Mat Williams' research group who have answered my questions during the past four years: Luke Smallman, Jeff Exbrayat, Andy Revill and Anthony Bloom. This work was made possible with the computing resources provided by the Edinburgh Compute and Data Facility (ECDF, http://www.ecdf.ed.ac.uk/). I would also like to thank the modelling officer Mike Mineter, who answered my questions regarding the use of the ECDF and running JULES on it. I want to thank Dean Thorpe, Carley Iles and Les Nagy for the much needed coffee and lunch breaks throughout the four years of my PhD.

The multi-site evaluation of the JULES model discussed in this dissertation was only possible with the help of many people. For the local parameter data at various flux tower sites, I would like to thank the following people: Danilo Dragoni (Morgan Monroe), Bill Munger (Harvard Forest), Thomas Grünwald (Tharandt), Pasi Kolari (Hyytiala), Eva Van

Gorsel (Tumbarumba) and Ray Leuning (Tumbarumba). Chris Jones and Andy Wiltshire at the UK Met Office kindly provided information on the global parameter data used by the global operational version of JULES. Differences between the local (standalone) and global operational versions of JULES were provided by Martin Best and Matt Pryor (both at the Met Office). Rutger Dankers explained how to compute the soil thermal and hydraulic parameters for the model. Graham Weedon (Met Office) provided advice on using the WFDEI dataset and further information on its creation. I also gratefully acknowledge advice from Tristan Quaife (Reading University) and Jose Gómez-Dans (University College London) on using the MODIS data and Doug Clark at the Centre for Ecology and Hydrology (CEH) on model spin-up and for answering questions on the JULES model. For the global scale simulations using JULES, I would like to thank Rich Ellis at CEH for providing the ancillary files and advice on modifying the namelist files in order to set up the model simulations on a 2d grid. Information on the snow schemes used by JULES and advice on which one to use at the point and global scale was provided by Richard Essery. I would like to gratefully acknowledge the School of Geosciences, University of Edinburgh, which provided me with a school scholarship that allowed me to pursue my PhD research.

I would also like to thank my mum Margaret, my sister Ruth, my brother David and my nephews and nieces, Sam, Issy, Caitlin, Alex and Mason, without whose support over the past 4 years, this thesis would not have been possible. Finally, I owe a debt of gratitude to Janlouise for her love and support throughout this PhD. She practically earned this PhD with me.

Darren Slevin
The University of Edinburgh
July 2015

Abstract

The land surface is a key component of the climate system and exchanges energy, water and carbon with the overlying atmosphere. It is the location of the terrestrial carbon sink and changes in the land surface can impact weather and climate at various time and spatial scales. It's ability to act as a source or a sink can influence atmospheric CO_2 concentrations. Both models and observations have shown the reduced ability of the land surface to absorb increased anthropogenic CO_2 emissions with results from the Coupled Climate–Carbon Cycle Model Intercomparison Project (C4MIP) and phase 5 of the Coupled Model Intercomparison Project (CMIP5) have shown that the terrestrial carbon cycle is a major source of model uncertainty. Land surface models (LSMs) represent the interaction between the biosphere and atmosphere in earth system models (ESMs) and are important for simulating the terrestrial carbon cycle. In the context of land surface modelling, uncertainty arises from an incomplete understanding of land surface processes and the inability to model these processes correctly. As LSMs become more advanced, there is a need to understand their accuracy. In this thesis, the ability of the Joint UK Land Environment Simulator (JULES), the land surface scheme of the UK Met Office Unified Model, to simulate Gross Primary Productivity (GPP) fluxes is evaluated at various spatial scales (point, regional and global) in order to identify and quantify sources of uncertainty in the model. This thesis has three main objectives. Firstly, JULES is evaluated at the point scale across a range of biomes and climatic conditions using local (site-specific), global and satellite datasets. It was found that JULES is biased with total annual GPP underestimated by 16 % and 30 % across all sites compared to observations when using local and global data, respectively. The model's phenology module was tested

by comparing results from simulations using the default phenology model to those forced with leaf area index (LAI) from the MODIS sensor. Model parameters were found to be a minor source of uncertainty compared to the meteorological driving data at the point scale as was the default phenology module in JULES. Secondly, in addition to evaluating simulated GPP fluxes at the point scale, the ability of JULES to simulate GPP at the global and regional scale for 2000–2010 was investigated with being able to simulate interannual variability and simulated global GPP estimates were found to be greater than the observation-based estimates, FLUXNET-MTE and MODIS, by 8 % and 25 %, respectively. At the regional scale, differences in GPP between JULES, FLUXNET-MTE and MODIS were observed mostly in the tropics and this was the reason for differences at the global scale. Simulating tropical GPP was found to be a major source of uncertainty in JULES. JULES was found to be insensitive to spatial resolution and when driven with the PRINCETON meteorological dataset, differences between model simulations driven using WFDEI-GPCC and PRINCETON occurred in the tropics (at 5°N–5°S) and extratropics (at 30°N–60°N). Finally, the response of JULES to changes in climate (surface air temperature, precipitation, atmospheric CO_2 concentrations) was explored at the global and regional scale. Simulated GPP was found to have greater sensitivity to changes in precipitation and CO_2 concentrations than air temperature at the global scale while LAI was sensitive only to changes in temperature and insensitive to changes in precipitation and CO_2 concentrations. It was found that model sensitivity to climate at the global scale was determined by its behaviour at the regional scale.

Contents

List of Figures

List of Tables

List of Equations

Chapter 1

Introduction

The overall objectives and scope of this research work involves exploring and identifying sources of uncertainty in the Joint UK Land Environment Simulator (JULES) land surface model when simulating gross primary production (GPP) at various scales (point, regional and global). In this dissertation, sources of uncertainty include the input data at the point scale, an evaluation of JULES' ability to simulate GPP at global and regional scales, the impact of spatial resolution and meteorological data on simulating GPP at global scales. A simple sensitivity study of the model to changes in climate at global scales was performed.

1.1 Motivation

Changes in atmospheric carbon dioxide and water vapour change the energy balance of the atmosphere and thus climate. One important influence on these greenhouse gases is the land surface. The land surface is an important component of the climate system, provides the lower boundary for the atmosphere and exchanges energy, water and carbon with the atmosphere (Pielke et al., 1998; Pitman, 2003; Seneviratne and Stöckli, 2008). The land surface controls the partitioning of available energy (into latent and sensible heat) and water (into evaporation and runoff) at the surface, is the location of the terrestrial carbon sink and influences weather and climate and vice versa (Bonan, 2008). Changes in the land surface can influence climate

at various time and spatial scales (Pielke et al., 1998) and since the land surface is the location of the terrestrial carbon cycle, it's ability to act as a carbon source or sink can influence atmospheric CO_2 concentrations.

Models and observations have shown the reduced ability of the land surface to absorb increased anthropogenic CO_2 emissions (Friedlingstein et al., 2006; Canadell et al., 2007; Friedlingstein et al., 2014; Sitch et al., 2015). Both the Coupled Climate–Carbon Cycle Model Intercomparison Project (Friedlingstein et al., 2006, C4MIP) and phase 5 of the Coupled Model Intercomparison Project (Arora et al., 2013; Friedlingstein et al., 2014, CMIP5) showed a large spread in the future projections of atmospheric CO_2 by coupled climate carbon-cycle models using the same emission scenario. The multi-model intercomparison project Trends in Net Land-Atmosphere Carbon Exchange (Sitch et al., 2015, TRENDY) found a modelled net carbon uptake in the tropics with no trend observed in the northern land area for the period 1990-2009. Using observations of atmospheric CO_2 concentrations since the 1960s, Canadell et al. (2007) showed a reduction in the efficiency of CO_2 sinks on land and oceans to store anthropogenic CO_2 emissions. Friedlingstein et al. (2006) and Friedlingstein et al. (2014) have suggested that a major source of model uncertainty is the land carbon cycle and this can affect the ability of earth system models (ESMs; also known as coupled carbon-cycle–climate models) to reliably simulate future atmospheric CO_2 concentrations and climate (Dalmonech et al., 2014).

Uncertainty is defined as a lack of certainty (where certainty is defined as a state of being reliably true), a state of having limited knowledge of a system and whether certain statements regarding the system cannot be answered as either true or false (Lindley, 2013). Uncertainty in climate (and land surface) modelling arises from an incomplete understanding of the climate (and land surface) system and the inability to model the climate (and land surface processes) correctly. Land Surface Models (LSMs) represent terrestrial ecosystem-atmosphere interactions at various spatial scales (point, regional and global) in ESMs and are used to simulate important land surface processes such as the terrestrial carbon and hydrological cycles (Pitman, 2003; Levis, 2010). Sources of uncertainty in LSMs include the input data (initial conditions and meteorological forcing data) and parameterisations (biophysical parameter values and process definitions) (Zaehle et al., 2005; Liu and Gupta, 2007; Williams et al., 2009). These sources of

uncertainty contribute towards uncertainty in carbon cycle simulations and thus uncertainty in future predictions of temperature and atmospheric CO_2 concentrations (Cox et al., 2000; Friedlingstein et al., 2006; Gregory et al., 2009; Brovkin et al., 2013).

LSMs have become considerably more complex since the simple "bucket model" of Manabe (1969). Deardorff (1978) developed a model which could simulate temperature and moisture for two soil layers and included a vegetation layer. Sellers et al. (1986) built on the work of Deardorff (1978) by developing a globally applicable LSM. Foley et al. (1996) incorporated vegetation dynamics into an LSM. These developments have led to LSMs which can realistically represent complex vegetation responses to meteorology, the climate effect of snow and biogeochemical processes (van den Hurk et al., 2011). Therefore, as LSMs become more complex, their accuracy must be evaluated.

In this dissertation, the ability of the Joint UK Land Environment Simulator (JULES) LSM (Clark et al., 2011; Best et al., 2011), the land surface scheme of the UK Met Office Unified Model (Walters et al., 2014, MetUM), to simulate fluxes of Gross Primary Productivity (GPP) is evaluated at various spatial scales (point, regional and global). Plants fix CO_2 as organic compounds through photosynthesis at the leaf scale and GPP is the total amount of carbon used in photosynthesis by plants at the ecosystem level (Beer et al., 2010; Chapin III et al., 2012). Photosynthesis at the leaf and canopy scale (GPP) vary in response to changes in climate (temperature, precipitation, humidity and downward radiation fluxes) and nutrient availability (Anav et al., 2015). Terrestrial GPP is an important (and the largest) carbon flux since it drives several ecosystem functions such as respiration and growth (Beer et al., 2010). GPP contributes to the production of food, fiber, and wood for humans and along with respiration, is one of the major processes controlling the exchange of CO_2 between the land and atmosphere (Beer et al., 2010). It also plays an important role in the global carbon cycle helping terrestrial ecosystems to partially offset anthropogenic CO_2 emissions (Janssens et al., 2003; Cox and Jones, 2008; Battin et al., 2009; Anav et al., 2015).

However, at the global scale there are no direct estimates of GPP (Anav et al., 2015). Global estimates of GPP do exist, but are not based only on measurements and, therefore, large uncertainties exist in these estimates

(Anav et al., 2015). In LSMs, the correct simulation of GPP is important since errors in its calculation can propagate through the model and affect biomass and other flux calculations, such as Net Ecosystem Exchange (Schaefer et al., 2012, NEE). In JULES, NEE is not a model output and is calculated as total ecosystem respiration minus GPP. The correct representation of leaf level stomatal conductance has an influence on GPP and transpiration and errors in GPP can also introduce errors into simulated latent and sensible heat fluxes.

Since the simulation of GPP can introduce errors into other ecosystem processes in JULES, examining sources of uncertainty, such as differences in quality of the input data, sensitivity to spatial resolution and the response of the model to changes in climate at various scales, have been explored in this thesis.

1.2 Dissertation outline

This dissertation is concerned with investigating sources of uncertainty, such as model parameters and meteorological driving data, associated with the JULES LSM by evaluating its ability to simulate GPP at a variety of scales (point, regional and global) using a wide range of input data (to the model) and observational datasets (local, global and satellite).

Chapter 2 describes the role of the land surface in the climate system, the importance of land surface models in Earth System Models (ESMs), when simulating land-atmosphere interactions, and how they have evolved from the simple "bucket model" of Manabe (1969) to complex models which can realistically simulate fluxes of carbon, water and energy across various temporal and spatial scales, sources of uncertainty in LSMs and a review of how LSMs (which includes JULES) are evaluated. Chapter 3 contains a description of JULES and the datasets used as input to the model (ancillary and meteorological data) and the observations against which model performance is compared. Two versions of JULES were used in this dissertation: JULES version 3.0 (point scale simulations; Chapter 4) and JULES version 3.4.1 (global scale simulations; Chapters 5 and 6).

1.2.1 Global versus local data

In Chapter 4, the ability of JULES to simulate GPP at 12 flux tower sites from the FLUXNET network across a range of ecosystem types (temperate, boreal, mediterranean and tropical) was examined in order to investigate differences between using local, global and satellite-derived datasets. The following research questions are asked:

- How well does JULES perform when using the best available local meteorological *and* parameter datasets? Can the model simulate interannual variability?
- How well does JULES perform when using global data?
- Of the global meteorological datasets used in this study which one compares best to FLUXNET data?
- Are improvements in simulated GPP observed when forcing JULES with daily satellite phenology compared to using the default phenology module?

Local datasets (model parameters and meteorological datasets) refer to those that are specific to a particular flux tower site, global datasets refer to those in which model parameters are taken from the datasets used by the global operational version of the model (used in the MetUM) and meteorological data from global gridded datasets. The satellite data used in this chapter refers to LAI data from the MODIS instrument (http://modis.gsfc.nasa.gov). In addition to evaluating JULES using local and global data, the model's phenology module was tested by comparing model simulations of GPP using its default phenology module to those forced with daily LAI data.

1.2.2 Global and regional evaluation

Following on from this evaluation of JULES at the point scale where differences in input to the model are quantified and the phenology module is tested, the ability of JULES to simulate GPP (and LAI) at the global and regional scale for the 2000–2010 period was explored in Chapter 5. The following research questions are asked:

- Can JULES capture interannual variability of GPP at the global scale? How do estimates of global GPP compare to those from observational datasets?

- How do fluxes of GPP simulated by JULES compare for various biomes at the global and regional scales?

- How sensitive are fluxes of GPP to the spatial resolution of the model?

- Is the meteorological dataset used to drive the model important at the global scale?

In Chapter 5, the ability of the model to simulate interannual variability (an important measure of its performance) for 2000–2010 was compared to that of global gridded estimates of GPP fluxes derived from upscaled FLUXNET observations (Jung et al., 2009, referred to as FLUXNET-MTE) and MODIS-based estimates of GPP and LAI (Zhao et al., 2005). These global gridded estimates of GPP (and LAI) allow JULES (and other LSMs) to be evaluated beyond the point scale to larger regional (continental) and global scales and means that land-atmosphere fluxes, such as CO_2 and latent and sensible heat, at the point scale (flux tower sites) can be studied to examine how they upscale to larger regions. Estimates of simulated global and regional GPP (integrated across all ecosystem types) and for various biomes (forests, grasslands and shrubs) were compared to the observation-based estimates. Two important sources of uncertainty in LSMs include the horizontal spatial resolution of the model and the meteorological data used to drive the model. Studies using atmospheric chemistry models have shown that the spatial resolution of the input meteorological data can affect model results (Ito et al., 2009; Pugh et al., 2013; Schaap et al., 2015). However, no studies exist on the effect of spatial resolution on simulations of land-atmosphere fluxes, such as GPP, by LSMs. The effect of spatial resolution on JULES output has been studied here with model simulations of GPP performed at $0.5^\circ \times 0.5^\circ$, $1^\circ \times 1^\circ$ and $2^\circ \times 2^\circ$. In addition to this, results from driving JULES with the WFDEI-GPCC meteorological dataset were compared to those driven with the PRINCETON and WFDEI-CRU dataset.

1.2.3 Sensitivity analysis

After JULES was evaluated at the global and regional scale, the sensitivity of the model to changes in climate when simulating GPP was examined for 2000–2010 in Chapter 6 as the model's ability to respond to changes in climate is important when predicting climate change at these scales. The research questions asked were:

- How sensitive is JULES to changes in temperature, precipitation and atmospheric CO_2 concentrations at the global scale?
- Which regions contribute most to the model's sensitivity at the global scale?
- Does the sensitivity of the model's biome types to changing climate explain the results at the global and regional scales?

Model simulations of GPP were performed in which the meteorological data (surface (2m) air temperature, precipitation and atmospheric CO_2 concentrations) were varied with the results compared to simulations with no changes to the meteorological data (referred to as the control simulation). Currently, studies of JULES' response to climate change have been performed at the point and regional scale (Galbraith et al., 2010; Rowland et al., 2015) with no sensitivity studies performed at the global scale.

Finally, in Chapter 7, the conclusions are drawn with a brief overview of the key results and areas for future work are suggested.

Bibliography

A. Anav, P. Friedlingstein, C. Beer, P. Ciais, A. Harper, C. Jones, G. Murray-Tortarolo, D. Papale, N. C. Parazoo, P. Peylin, S. Piao, S. Sitch, N. Viovy, A. Wiltshire, and M. Zhao. Spatio-temporal patterns of terrestrial gross primary production: A review. *Reviews of Geophysics*, 2015. doi:10.1002/2015RG000483.

V. K. Arora, G. J. Boer, P. Friedlingstein, M. Eby, C. D. Jones, J. R. Christian, G. Bonan, L. Bopp, V. Brovkin, P. Cadule, T. Hajima, T. Ilyina, K. Lindsay, J. F. Tjiputra, and T. Wu. Carbon–Concentration and Carbon–Climate Feedbacks in CMIP5 Earth System Models. *Journal of Climate*, 26:5289–5314, 2013. doi:10.1175/JCLI-D-12-00494.1.

T. J. Battin, S. Luyssaert, L. A. Kaplan, A. K. Aufdenkampe, A. Richter, and L. J. Tranvik. The boundless carbon cycle. *Nature Geoscience*, 2: 598–600, 2009. doi:10.1038/ngeo618.

C. Beer, M. Reichstein, E. Tomelleri, P. Ciais, M. Jung, N. Carvalhais, C. Rödenbeck, M. A. Arain, D. Baldocchi, G. B. Bonan, A. Bondeau, A. Cescatti, G. Lasslop, A. Lindroth, M. Lomas, S. Luyssaert, H. Margolis, K. W. Oleson, O. Roupsard, E. Veenendaal, N. Viovy, C. Williams, F. I. Woodward, and D. Papale. Terrestrial Gross Carbon Dioxide Uptake: Global Distribution and Covariation with Climate. *Science*, 329: 834–838, 2010. doi:10.1126/science.1184984.

M. J. Best, M. Pryor, D. B. Clark, G. G. Rooney, R .L. H. Essery, C. B. Ménard, J. M. Edwards, M. A. Hendry, A. Porson, N. Gedney, L. M.

Mercado, S. Sitch, E. Blyth, O. Boucher, P. M. Cox, C. S. B. Grimmond, and R. J. Harding. The Joint UK Land Environment Simulator (JULES), Model description–Part 1: Energy and water fluxes. *Geoscientific Model Development*, 4:677–699, 2011. doi:10.5194/gmd-4-677-2011.

G. B. Bonan. Forests and Climate Change: Forcings, Feedbacks, and the Climate Benefits of Forests. *Science*, 320:1444–1449, 2008. doi:10.1126/science.1155121.

V. Brovkin, L. Boysen, V. K. Arora, J. P. Boisier, P. Cadule, L. Chini, M. Claussen, P. Friedlingstein, V. Gayler, B. J. J. M. van den Hurk, G. C. Hurtt, C. D. Jones, E. Kato, N. de Noblet-Ducoudré, F. Pacifico, J. Pongratz, and M. Weiss. Effect of Anthropogenic Land-Use and Land-Cover Changes on Climate and Land Carbon Storage in CMIP5 Projections for the Twenty-First Century. *Journal of Climate*, 26:6859–6881, 2013. doi:10.1175/JCLI-D-12-00623.1.

J. G. Canadell, C. Le Quéré, M. R. Raupach, C. B. Field, E. T. Buitenhuis, P. Ciais, T. J. Conway, N. P. Gillett, R. A. Houghton, and G. Marland. Contributions to accelerating atmospheric CO_2 growth from economic activity, carbon intensity, and efficiency of natural sinks. *Proceedings of the National Academy of Sciences of the United States of America*, 104: 18866–18870, 2007. doi:10.1073/pnas.0702737104.

F. S. Chapin III, P. A. Matson, and P. Vitousek. *Principles of Terrestrial Ecosystem Ecology*. Springer-Verlag New York, 2012. doi:10.1007/978-1-4419-9504-9.

D. B. Clark, L. M. Mercado, S. Sitch, C. D. Jones, N. Gedney, M. J. Best, M. Pryor, G. G. Rooney, R. L. H. Essery, E. Blyth, O. Boucher, R. J. Harding, C. Huntingford, and P. M. Cox. The Joint UK Land Environment Simulator (JULES), model description–Part 2: Carbon fluxes and vegetation dynamics. *Geoscientific Model Development*, 4:701–722, 2011. doi:10.5194/gmd-4-701-2011.

P. Cox and C. Jones. Illuminating the Modern Dance of Climate and CO_2. *Science*, 321:1642–1644, 2008. doi:10.1126/science.1158907.

P. M. Cox, R. A. Betts, C. D. Jones, S. A. Spall, and I. J. Totterdell. Acceleration of global warming due to carbon–cycle feedbacks in a coupled climate model. *Nature*, 408:184–187, 2000. doi:10.1038/35041539.

D. Dalmonech, S. Zaehle, G. J. Schürmann, V. Brovkin, C. Reick, and R. Schnur. Separation of the Effects of Land and Climate Model Errors on Simulated Contemporary Land Carbon Cycle Trends in the MPI Earth System Model version 1. *Journal of Climate*, 28:272–291, 2014. doi:10.1175/JCLI-D-13-00593.1.

J. W. Deardorff. Efficient Prediction of Ground Surface Temperature and Moisture, With Inclusion of a Layer of Vegetation. *Journal of Geophysical Research*, 83:1889–1903, 1978. doi:10.1029/JC083iC04p01889.

J. A. Foley, I. C. Prentice, N. Ramankutty, S. Levis, D. Pollard, S. Sitch, and A. Haxeltine. An integrated biosphere model of land surface processes, terrestrial carbon balance, and vegetation dynamics. *Global Biogeochemical Cycles*, 10:603–628, 1996. doi:10.1029/96GB02692.

P. Friedlingstein, P. Cox, R. Betts, L. Bopp, W. Von Bloh, V. Brovkin, P. Cadule, S. Doney, M. Eby, I. Fung, et al. Climate-Carbon Cycle Feedback Analysis: Results from the C4MIP Model Intercomparison. *Journal of Climate*, 19:3337–3353, 2006. doi:10.1175/JCLI3800.1.

P. Friedlingstein, M. Meinshausen, V. K. Arora, C. D. Jones, A. Anav, S. K. Liddicoat, and R. Knutti. Uncertainties in CMIP5 climate projections due to carbon cycle feedbacks. *Journal of Climate*, 27:511–526, 2014. doi:10.1175/JCLI-D-12-00579.1.

D. Galbraith, P. E. Levy, S. Sitch, C. Huntingford, P. Cox, M. Williams, and P. Meir. Multiple mechanisms of Amazonian forest biomass losses in three dynamic global vegetation models under climate change. *New Phytologist*, 187:647–665, 2010. doi:10.1111/j.1469-8137.2010.03350.x.

J. M. Gregory, C. D. Jones, P. Cadule, and P. Friedlingstein. Quantifying Carbon Cycle Feedbacks. *Journal of Climate*, 22:5232–5250, 2009. doi:10.1175/2009JCLI2949.1.

A. Ito, S. Sillman, and J. E. Penner. Global chemical transport model study of ozone response to changes in chemical kinetics and biogenic

volatile organic compounds emissions due to increasing temperatures: Sensitivities to isoprene nitrate chemistry and grid resolution. *Journal of Geophysical Research: Atmospheres (1984–2012)*, 114:D09301, 2009. doi:10.1029/2008JD011254.

I. A. Janssens, A. Freibauer, P. Ciais, P. Smith, G.-J. Nabuurs, G. Folberth, B. Schlamadinger, R. W. A. Hutjes, R. Ceulemans, E.-D. Schulze, R. Valentini, and A. J. Dolman. Europe's Terrestrial Biosphere Absorbs 7 to 12% of European Anthropogenic CO_2 Emissions. *Science*, 300:1538–1542, 2003. doi:10.1126/science.1083592.

M. Jung, M. Reichstein, and A. Bondeau. Towards global empirical upscaling of FLUXNET eddy covariance observations: validation of a model tree ensemble approach using a biosphere model. *Biogeosciences*, 6:2001–2013, 2009. doi:10.5194/bg-6-2001-2009.

S. Levis. Modeling vegetation and land use in models of the Earth System. *Wiley Interdisciplinary Reviews: Climate Change*, 1:840–856, 2010. doi:10.1002/wcc.83.

D. V. Lindley. *Understanding uncertainty [electronic resource]*. Wiley, 2013. ISBN 1118650158. University of Edinburgh's Library Catalogue, EBSCOhost, viewed 1 May 2015.

Y. Liu and H. V. Gupta. Uncertainty in hydrologic modeling: Toward an integrated data assimilation framework. *Water Resources Research*, 43: W07401, 2007. doi:10.1029/2006WR005756.

S. Manabe. Climate and the ocean circulation: 1, the atmospheric circulation and the hydrology of the Earth's surface. *Monthly Weather Review*, 97:739–805, 1969. doi:10.1175/1520-0493(1969)097<0739:CATOC>2.3.CO;2.

R. A. Pielke, R. Avissar, M. Raupach, A. J. Dolman, X. Zeng, and A. S. Denning. Interactions between the atmosphere and terrestrial ecosystems: influence on weather and climate. *Global Change Biology*, 4:461–475, 1998. doi:10.1046/j.1365-2486.1998.t01-1-00176.x.

A. J. Pitman. The evolution of, and revolution in, land surface schemes designed for climate models. *International Journal of Climatology*, 23: 479–510, 2003. doi:10.1002/joc.893.

T. A. M. Pugh, K. Ashworth, O. Wild, and C. N. Hewitt. Effects of the spatial resolution of climate data on estimates of biogenic isoprene emissions. *Atmospheric Environment*, 70:1–6, 2013. doi:10.1016/j.atmosenv.2013.01.001.

L. Rowland, A. Harper, B. O. Christoffersen, D. R. Galbraith, H. M. A. Imbuzeiro, T. L. Powell, C. Doughty, N. M. Levine, Y. Malhi, S. R. Saleska, P. R. Moorcroft, P. Meir, and M. Williams. Modelling climate change responses in tropical forests: similar productivity estimates across five models, but different mechanisms and responses. *Geoscientific Model Development*, 8:1097–1110, 2015. doi:10.5194/gmd-8-1097-2015.

M. Schaap, C. Cuvelier, C. Hendriks, B. Bessagnet, J. M. Baldasano, A. Colette, P. Thunis, D. Karam, H. Fagerli, A. Graff, R. Kranenburg, A. Nyiri, M. T. Pay, L. RouÃ¯l, M. Schulz, D. Simpson, R. Stern, E. Terrenoire, and P. Wind. Performance of European chemistry transport models as function of horizontal resolution. *Atmospheric Environment*, 112:90–105, 2015. ISSN 1352-2310. doi:10.1016/j.atmosenv.2015.04.003.

K. Schaefer, C. R. Schwalm, C. Williams, M. A. Arain, A. Barr, J. M. Chen, K. J. Davis, D. Dimitrov, T. W. Hilton, D. Y. Hollinger, E. Humphreys, B. Poulter, B. M. Raczka, A. D. Richardson, A. Sahoo, P. Thornton, H. Vargas, R.and Verbeeck, R. Anderson, I. Baker, T. A. Black, P. Bolstad, J. Chen, P. S. Curtis, A. R. Desai, M. Dietze, D. Dragoni, C. Gough, R. F. Grant, L. Gu, A. Jain, C. Kucharik, B. Law, S. Liu, E. Lokipitiya, H. A. Margolis, R. Matamala, J. H. McCaughey, R. Monson, J. W. Munger, W. Oechel, C. Peng, D. T. Price, D. Ricciuto, W. J. Riley, N. Roulet, H. Tian, C. Tonitto, M. Torn, E. Weng, and X. Zhou. A model-data comparison of gross primary productivity: Results from the North American Carbon Program site synthesis. *Journal of Geophysical Research*, 117:G03010, 2012. doi:10.1029/2012JG001960.

P.J. Sellers, Y. Mintz, Y.C. Sud, and A. Dalcher. A Simple Biosphere Model (SiB) for Use within General Circulation Models. *Jour-*

nal of the Atmospheric Sciences, 43:505–531, 1986. doi:10.1175/1520-0469(1986)043<0505:ASBMFU>2.0.CO;2.

S. I. Seneviratne and R. Stöckli. *Climate Variability and Extremes during the Past 100 Years* , chapter The Role of Land-Atmosphere Interactions for Climate Variability in Europe, pages 179–193. Springer, 2008.

S. Sitch, P. Friedlingstein, N. Gruber, S. D. Jones, G. Murray-Tortarolo, A. Ahlström, S. C. Doney, H. Graven, C. Heinze, C. Huntingford, S. Levis, P. E. Levy, M. Lomas, B. Poulter, N. Viovy, S. Zaehle, N. Zeng, A. Arneth, G. Bonan, L. Bopp, J. G. Canadell, F. Chevallier, P. Ciais, R. Ellis, M. Gloor, P. Peylin, S. L. Piao, C. Le Quéré, B. Smith, Z. Zhu, and R. Myneni. Recent trends and drivers of regional sources and sinks of carbon dioxide. *Biogeosciences*, 12:653–679, 2015. doi:10.5194/bg-12-653-2015.

B. van den Hurk, M. Best, P. Dirmeyer, A. Pitman, J. Polcher, and J. Santanello. Acceleration of land surface model development over a decade of GLASS. *Bulletin of the American Meteorological Society*, 92:1593–1600, 2011. doi:10.1175/BAMS-D-11-00007.1.

D. N. Walters, K. D. Williams, I. A. Boutle, A. C. Bushell, J. M. Edwards, P. R. Field, A. P. Lock, C. J. Morcrette, R. A. Stratton, J. M. Wilkinson, M. R. Willett, N. Bellouin, A. Bodas-Salcedo, M. E. Brooks, D. Copsey, P. D. Earnshaw, S. C. Hardiman, C. M. Harris, R. C. Levine, C. MacLachlan, J. C. Manners, G. M. Martin, S. F. Milton, M. D. Palmer, M. J. Roberts, J. M. Rodríguez, W. J. Tennant, and P. L. Vidale. The Met Office Unified Model Global Atmosphere 4.0 and JULES Global Land 4.0 configurations. *Geoscientific Model Development*, 7:361–386, 2014. doi:10.5194/gmd-7-361-2014.

M. Williams, A. D. Richardson, M. Reichstein, P. C. Stoy, P. Peylin, H. Verbeeck, N. Carvalhais, M. Jung, D. Y. Hollinger, J. Kattge, R. Leuning, Y. Luo, E. Tomelleri, C. M. Trudinger, and Y.-P. Wang. Improving land surface models with FLUXNET data. *Biogeosciences*, 6:1341–1359, 2009. doi:10.5194/bg-6-1341-2009.

S. Zaehle, S. Sitch, B. Smith, and F. Hatterman. Effects of parameter uncertainties on the modeling of terrestrial biosphere dynamics. *Global Biogeochemical Cycles*, 19:GB3020, 2005. doi:10.1029/2004GB002395.

M. Zhao, F. A. Heinsch, R. R. Nemani, and S. W. Running. Improvements of the MODIS terrestrial gross and net primary production global data set. *Remote Sensing of Environment*, 95:164–176, 2005. doi:10.1016/j.rse.2004.12.011.

Chapter 2

Land Surface Models: Why They Matter, Evolution and Evaluation

This chapter describes the importance of the land surface in the climate system, how land surface models (LSMs) have evolved from the bucket model of Manabe (1969) to those which provide a realistic treatment of land-atmosphere interactions and how LSMs are evaluated. The 'land surface' relevant to the climate system is that which consists of the terrestrial biosphere, comprising vegetation and soil, and the processes which connect them and the carbon, water and energy they store. The land surface is the location of the terrestrial carbon cycle and atmospheric CO_2 concentrations are influenced by whether the land surface acts as a source or a sink for CO_2. One outcome of the Coupled Climate–Carbon Cycle Model Intercomparison Project (C4MIP), which examined the coupling between climate change and the carbon cycle, was that the terrestrial carbon cycle is a major source of uncertainty with increasing atmospheric CO_2 concentrations (Friedlingstein et al., 2006). As LSMs become more advanced and complex, there is a need to evaluate them offline (i.e. separately from its host climate model). This can provide insight into how the model behaves with changes in either parameters, meteorological conditions or modelled processes. Following a description of the importance of the land surface (Section 1) and the greenhouse effect (Section 2), the role of the land surface in the terrestrial carbon

cycle (Section 3) is described. The role of LSMs in Global Climate Models (GCMs), and their evolution from the simple "bucket models" of the 1960s to those which can realistically respond to changes in climate, is provided in Section 4. Sources of uncertainty within LSMs are discussed in Section 5. Finally, techniques for evaluating LSMs and how the JULES LSM has been evaluated are provided in Sections 6 and 7, respectively.

2.1 The Role of the Land Surface in the Climate System

The land surface is a key component of the climate system. Similar to the oceans, it provides the lower boundary for the atmosphere and exchanges energy, water, aerosols, CO_2 and other trace gases with the overlying atmosphere (Pielke et al., 1998; Seneviratne and Stöckli, 2008). The land surface is sensitive to climate and thus, future climate change, and vice versa. Key processes controlled by the land surface which affect the climate system include the surface energy balance (i.e. partitioning of available energy into sensible and latent heat), surface water balance (i.e. partitioning of available water into evaporation and surface runoff) and the climatic effect of snow (Pitman, 2003). Biogeochemical (carbon sequestration by the biosphere) and biogeophysical processes (land surface albedo and evapotranspiration) can also affect climate (Bonan, 2008). Human activity can affect the land surface through deforestation and agriculture and thus acts as a driver of climate change. Changes in the land surface can influence regional- to global-scale climate on timescales ranging from seconds to millions of years (Pielke et al., 1998).

The land surface is the location of the terrestrial carbon cycle and changes to the biosphere's ability to act as a carbon source or sink can influence atmospheric CO_2 concentrations (Pitman, 2003; Le Quéré et al., 2009; Pan et al., 2011; Le Quéré et al., 2013). The reduced ability of the land carbon sink to absorb increased anthropogenic CO_2 emissions has been shown by both models and observations (Friedlingstein et al., 2006; Canadell et al., 2007; Friedlingstein et al., 2014). This weakening of the land carbon sink can amplify global warming due to carbon loss. The first major study of the coupling between climate change and the carbon cycle was the Coupled

Climate–Carbon Cycle Model Intercomparison Project (Friedlingstein et al., 2006, C4MIP). Using a common protocol, 11 coupled climate–carbon cycle models of varying degrees of complexity showed a positive feedback with global warming i.e. climate-carbon cycle feedbacks increase atmospheric CO_2 concentrations with simulated atmospheric CO_2 ranging from 700 to 1000 ppm for the SRES A2 scenario (very similar to RCP8.5 described below) at the end of the 21st century (Friedlingstein et al., 2006). The largest uncertainty was associated with future anthropogenic CO_2 emissions with significant uncertainty associated with the response of the terrestrial carbon cycle to increased atmospheric CO_2 concentrations (Friedlingstein et al., 2006, Figure 2.1). It was found that both the land and ocean carbon sinks showed a reduced uptake of increased anthropogenic CO_2 emissions under a warming climate which contributed to the positive feedback (Friedlingstein and Prentice, 2010). The ability of the land carbon sink to absorb increased anthropogenic CO_2 emissions was reduced with the magnitude of the effect dependent on the model used.

Similar results were found in the context of phase 5 of the Coupled Model Intercomparison Project (Friedlingstein et al., 2014, CMIP5). Climate projections of 11 earth system models (ESMs) forced by RCP8.5 scenario CO_2 emissions show a large spread in atmospheric CO_2 concentrations at 2100 (ranging between 795 and 1145 ppm, which is slightly higher than the C4MIP results) (Friedlingstein et al., 2014). The RCPs (Representative Concentration Pathways) are a set of four new pathways (named RCP2.6, RCP4.5, RCP6, and RCP8.5 after the possible range of year 2100 radiative forcing values relative to the pre-industrial values: +2.6, +4.5, +6.0, and +8.5 $W\,m^{-2}$, respectively) developed for the climate modelling community which contain greenhouse gas concentrations and emissions and land-use trajectories for the 21st Century (Van Vuuren et al., 2011). RCP8.5 corresponds to a high greenhouse gas emissions scenario in the absence of climate change policies (Riahi et al., 2011). Differences in simulated atmospheric CO_2 concentrations from the CMIP5 project are due to differences in ocean or land carbon uptakes (Figure 2.2). Using observations of atmospheric CO_2 concentrations since the 1960s, Canadell et al. (2007) showed that there is a decline in the efficiency of CO_2 sinks on land and oceans to store anthropogenic CO_2. Results from the multi-model intercomparison project TRENDY (Trends in Net Land-Atmosphere Carbon Exchange;

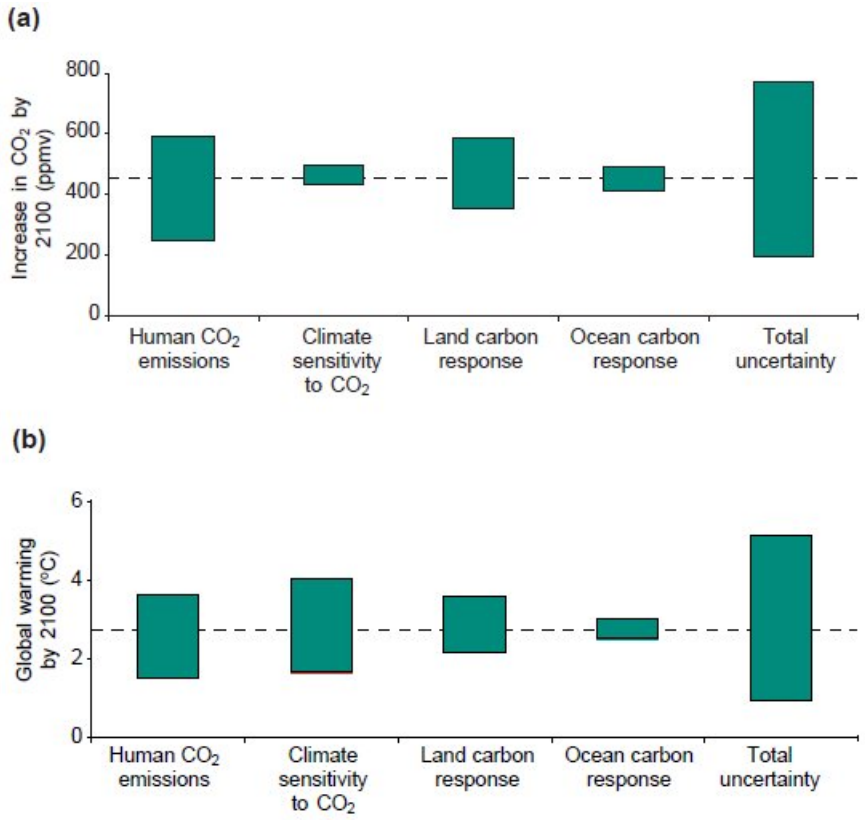

Figure 2.1: Atmospheric CO_2 concentrations and temperature uncertainties for the 21st century from the C4MIP project. **(a)** Contributions to uncertainties in increase in predicted atmospheric CO_2 concentrations by the end of the 21st century from anthropogenic and Earth system components. The "central estimate" based on the mean model sensitivity parameters and the SRES A2 emissions scenario is represented by the dotted line. **(b)** Contributions to uncertainties in increase in predicted global mean temperature by the end of the 21st century. Figure 1 of Meir et al. (2006).

http://dgvm.ceh.ac.uk/node/21), which used nine DGVMs (dynamic global vegetation models) and four OBGCMs (ocean biogeochemical general circulation models) to examine land and ocean CO_2 exchanges with the atmosphere over the period 1990-2009, show a mean global land carbon sink with most of the land-based trend due to a simulated net carbon uptake in the tropics, with no trend observed in the northern land area (Sitch et al., 2015). Friedlingstein et al. (2006) and Friedlingstein et al. (2014) suggest that the land carbon cycle is a major source of model uncertainty.

Ever since Charney first hypothesised that the land surface influenced climate (Charney et al., 1975), the land surface component of Global Climate Models (GCMs) has become increasingly complex in order to capture land-atmosphere interactions and feedbacks within the climate system (Pielke et al., 1998; Meir et al., 2006; Heimann and Reichstein, 2008). Predicting future changes in climate is influenced by our ability to represent ecological processes in land surface models (LSMs), how the land surface interacts with the atmosphere and how it changes due to human activity and natural processes (Pitman, 2003; Meir et al., 2006).

2.2 The Greenhouse Effect

Solar radiation powers Earth's climate system (Cubasch et al., 2013). The Earth absorbs incoming shortwave radiation (predominately in the visible or near-visible part of the spectrum) that is emitted by the Sun. Approximately half of the incoming shortwave radiation is absorbed by the Earth's surface with roughly 30% reflected back to space by gases and aerosols, clouds and by the Earth's surface (albedo) and the remaining 20% absorbed in the atmosphere (Cubasch et al., 2013). To balance the absorbed incoming shortwave radiation, the Earth re-radiates the same amount of energy back to space in the form of longwave radiation (also known as infrared radiation). Atmospheric constituents, such as carbon dioxide, water vapour, methane, nitrous oxide, ozone and several other greenhouse gases, absorb the outgoing longwave radiation and re-emit the longwave radiation in all directions with the downward directed component adding heat to the lower layers of the atmosphere and the Earth's surface (Cubasch et al., 2013). This is known as the greenhouse effect. Greenhouse gas concentrations,

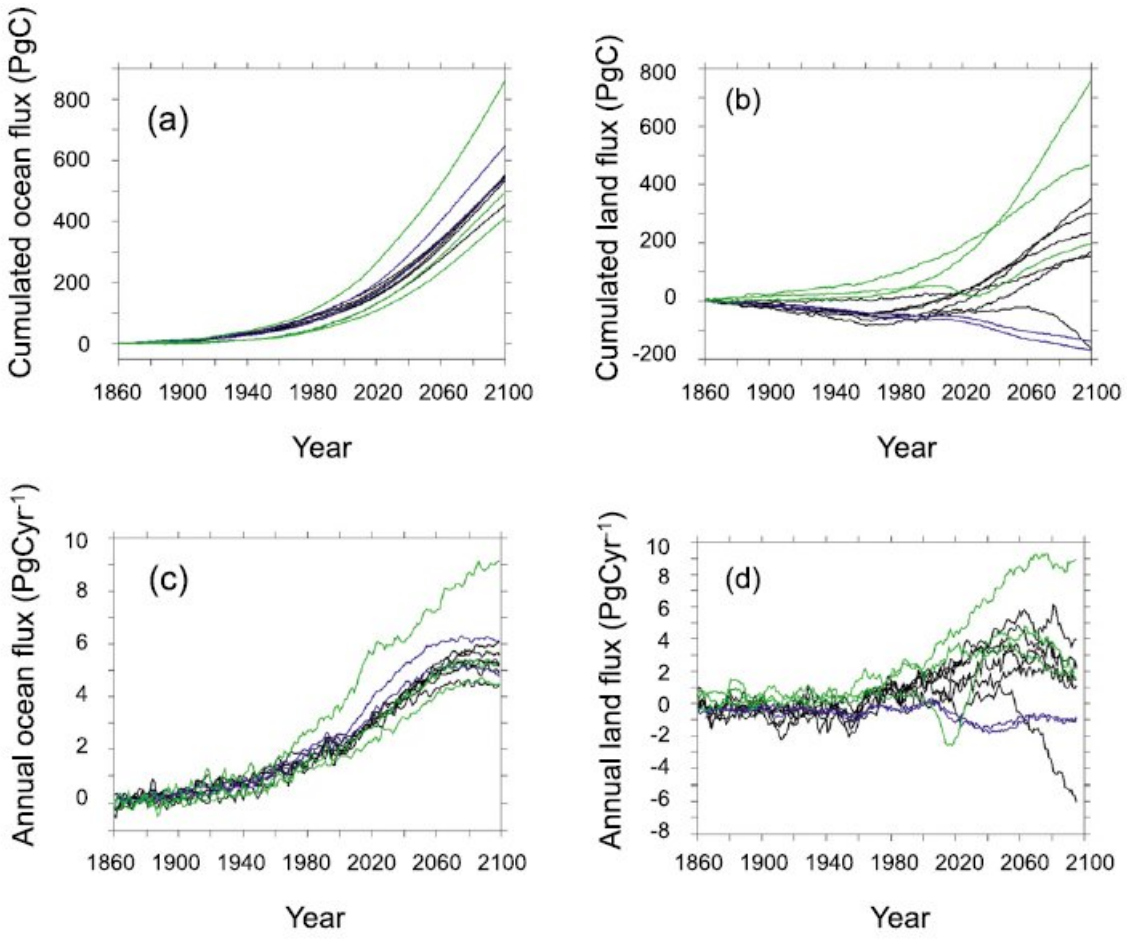

Figure 2.2: Cumulative global air to **(a)** ocean carbon flux (Pg C), **(b)** land carbon flux (Pg C) ranges and annual global air to **(c)** ocean carbon flux (Pg C yr^{-1}), **(d)** land carbon flux (Pg C $year^{-1}$) ranges from 11 earth system models (ESMs) emission-driven simulations. Green lines represent ESMs prescribing land use change emissions. Blue lines represent ESMs which include a terrestrial nitrogen cycle. Figure 4 of Friedlingstein et al. (2014).

therefore, have a direct effect on global mean surface temperatures. Over the past 420,000 years, atmospheric CO_2 concentrations have been between 180 and 280 ppmv (Falkowski et al., 2000). There has been a considerable increase in atmospheric CO_2 since the beginning of the industrial era (about 1750) and this had led to a rise in global surface temperatures (Falkowski et al., 2000). This anthropogenic warming far outweighs the contributions from natural processes, such as solar changes and volcanic eruptions, and will lead to significant changes in the Earth's future climate (Myhre et al., 2013).

2.3 Overview of the Carbon Cycle

The carbon cycle describes the flow of carbon from the atmosphere to the terrestrial biosphere, oceans and the Earth's interior, and vice versa (Figure 2.3; Ciais et al. (2013)). Atmospheric CO_2 represents only a small amount of carbon in the Earth System with the rest tied up in various reservoirs (Ciais et al., 2013) and carbon moves through these reservoirs by a variety of mechanisms. These reservoirs can be either sources (release more carbon than they absorb) or sinks (absorb more carbon than they release) (Ciais et al., 2013). Sources can be either man-made (combustion of fossil fuels, deforestation) or natural (plant and litter decomposition, soil respiration, ocean release) and sinks include land vegetation, soils, oceans and geological reservoirs, such as deep-sea carbonate sediments and the upper mantle (Ciais et al., 2013).

The burning of fossil fuels and change in land cover and use by humans has added a considerable quantity of carbon to the atmosphere (Pongratz et al., 2009). The additional injection of CO_2 into the atmosphere has led to the carbon cycle being perturbed and changes to natural sink strengths (Friedlingstein and Prentice, 2010). Of the CO_2 emitted into the atmosphere from the burning of fossil fuels, roughly half remains in the atmosphere and the rest is absorbed by carbon sinks on land and in the oceans (Canadell et al., 2007; Le Quéré et al., 2009; Sitch et al., 2015).

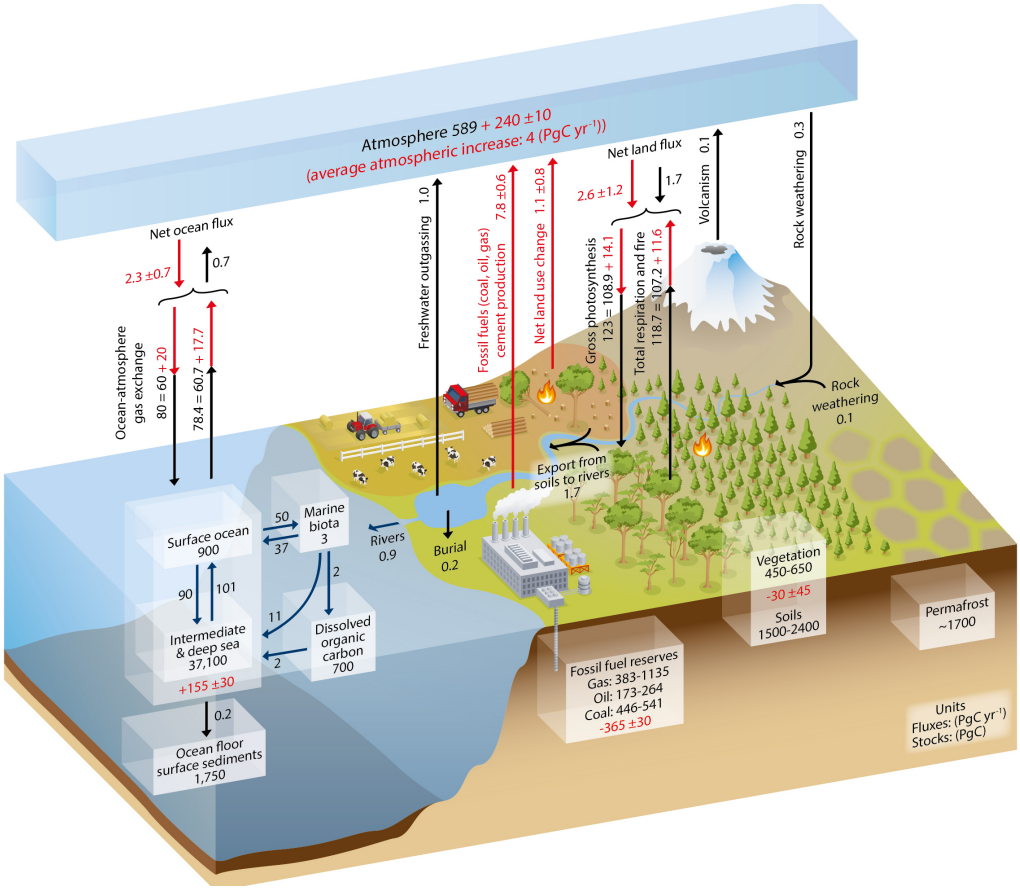

Figure 2.3: Brief overview of the global carbon cycle. Numbers represent reservoir mass, also called 'carbon stocks' in PgC (1 PgC = 10^{15} gC) and annual carbon exchange fluxes (in PgC yr^{-1}). Black numbers and arrows indicate carbon reservoir mass and exchange fluxes estimated for the pre-Industrial Era, about 1750. Red numbers and arrows the indicate annual anthropogenic carbon fluxes averaged over the 2000–2009 time period. Figure 6.1 of Ciais et al. (2013).

2.3.1 The Ocean Carbon Cycle

Atmospheric CO_2 is continually exchanged between the atmosphere and surface ocean via gas exchange and is controlled partly by the partial CO_2 pressure difference between the atmosphere and oceans (Friedlingstein and Prentice, 2010; Ciais et al., 2013). The ocean stores 50 times more carbon than the atmosphere and, on timescales of millennia, the oceans determine the atmospheric CO_2 concentration and not vice versa (Falkowski et al., 2000). The deep ocean and ocean sediments are an important long-term reservoir for carbon (Ciais et al., 2013). The carbon in the ocean is predominantly stored as Dissolved Inorganic Carbon (DIC), which occurs when CO_2 absorbed by the ocean reacts with seawater to form carbonic acid, which dissociates to form bicarbonate ions and hydrogen ions (which leads to acidification). In addition to DIC, Dissolved Organic Carbon (DOC; marine biota such as phytoplankton) represents a small carbon pool (Ciais et al., 2013).

The increasing acidification of the ocean surface will lead to dissolution of shallow-water carbonate sediments and this will affect marine calcifying organisms. When these organisms die, they sink to the ocean floor, become carbonate-rich deposits and over time, will become part of the lithosphere (outer solid part of the Earth and is about 100 km thick). Carbon can be stored in the lithosphere in two forms: inorganic and organic. Inorganic forms include fossil fuels, such as coal, oil and natural gas. Organic forms include leaf litter and organic matter in soils.

2.3.2 The Terrestrial Carbon Cycle

The terrestrial carbon cycle consists of five main processes; photosynthesis, plant respiration, soil respiration, litter fall and surface runoff. CO_2 is extracted from the atmosphere by plants, which are known as autotrophs (organisms that can produce their own food using light, water and carbon dioxide during photosynthesis), through pores in their leaves called stomata and then use it in a process called photosynthesis in order to create carbon-based sugar molecules, which in turn gets converted to plant biomass. The total amount of carbon uptake by plants (per unit area in unit time) and used in photosynthesis is known as Gross Primary Productivity (GPP).

Carbon enters the food chain when heterotrophs, organisms that do not fix carbon and must obtain carbon by feeding on organic material present in other organisms (e.g. humans), ingest plants.

In addition to affecting climate as a greenhouse gas, increasing atmospheric CO_2 concentrations have led to an increase in photosynthesis (Friedlingstein and Prentice, 2010; Beck et al., 2011; Fensholt et al., 2012; Sitch et al., 2015), which has increased both carbon uptake and storage by terrestrial ecosystems (Norby et al., 2005; Leakey et al., 2009). This is known as CO_2 fertilisation. This increase in atmospheric CO_2 has led to an increase in growing season Leaf Area Index (LAI) (Piao et al., 2006). It also reduces plant transpiration and increases plant water use efficiency through the partial closure of stomata (Warren et al., 2011).

CO_2 can be returned to the atmosphere in a number of ways, such as respiration, whereby autotrophs (plants) and heterotrophs (animals) release CO_2 and water due to the conversion of sugars (glucose) into energy. CO_2 is also released from the soil due to respiration from soil organisms. This includes respiration of plant roots and the decomposition of organic material by soil microbes. Litterfall can enhance the release of CO_2 into the atmosphere through its decomposition by soil microbes on the forest floor (Sayer et al., 2011). Even though most of the carbon lost from the soil reservoir is through respiration, carbon can be transported away via surface runoff through the transport of eroded rock and soil (Maynard et al., 2011). Carbon can also be returned to atmosphere when volcanoes erupt and CO_2 is released to the atmosphere.

Since the terrestrial carbon cycle is a major source of model uncertainty, the remainder of the chapter focuses on LSMs and their evaluation.

2.4 Land Surface Models

Land Surface Models (LSMs) are an important component of climate and weather models and simulate terrestrial ecosystem-atmosphere interactions at the point, regional and global scales. They represent the surface energy and water balance, climate effect of snow and carbon fluxes (Pitman, 2003) and are considered the lower boundary condition for Global Climate Models (GCMs) (Best et al., 2011). GCMs require the carbon, water and energy

fluxes between the land surface and atmosphere to be specified. Meteorological data (downward shortwave and longwave radiation fluxes, surface air temperature, precipitation and specific humidity), vegetation and soil characteristics are provided as inputs to LSMs, and using these, LSMs can predict land-atmosphere fluxes, such as latent and sensible heat, upward longwave radiation and net ecosystem exchange of CO_2 (NEE), which is used to determine global atmospheric CO_2 concentrations.

2.4.1 Evolution of LSMs

Various LSMs have been designed over the last 40 years to calculate energy, water and momentum fluxes (Dai et al., 2003). They range from the simple 'bucket model' of Manabe (1969) to LSMs which can realistically describe a comprehensive range of land-atmosphere interactions and can be used to understand the response of the biosphere to climate change (Table 2.1). The development of LSMs can be divided into three broad categories.

2.4.1.1 First generation

The first LSM to be implemented in a climate model included a simplified representation of the oceans and land surface, but did not model the seasonal or diurnal cycle (Manabe, 1969). Within this LSM, a globally constant soil depth (15 cm) and a parameterisation of hydrology now known as the 'Manabe bucket model' was implemented (Manabe, 1969). In this simple "bucket" model, the soil is assumed to have a fixed water capacity (like a bucket) and at each land grid square and each time step, the bucket is filled with precipitation and emptied by evaporation. The excess above its capacity is termed runoff. These first generation LSMs were used to study albedo, surface roughness and moisture availability in GCMs (Sellers et al., 1997). In these models, the vegetation is viewed as passive spongelike structures, which acts as a permeable sheet separating the soil from the atmosphere (Sellers et al., 1997). These first-generation models did not allow the modelling of CO_2 exchange or the ability to explore the impact of land cover change (Pitman, 2003). The 'bucket model' of Manabe (1969) was the first step in representing land surface processes in climate models (Pitman, 2003).

2.4.1.2 Second generation

The second generation of LSMs were developed to address the deficiencies of the 'Manabe bucket model' (Cox et al., 1999). These new models also attempted to explicitly represent the effects of vegetation in surface energy balance calculations (Sellers et al., 1997). In the second generation LSMs, the soil and vegetation layers interact with the atmosphere rather than being passive (as in the first-generation models) and more complex soil moisture parameterisations have been added to replace the simple "bucket" model of Manabe (1969) (Pitman, 2003). Second generation LSMs are also able to capture the effect of vegetation on momentum transfer which can enhance the exchange of latent and sensible heat fluxes. Deardorff (1978) developed a model which could simulate temperature and moisture for two soil layers and included one vegetation layer, which shielded a fraction of the land surface from solar radiation. This was a fundamental step forward from the 'Manabe bucket model' in LSM development.

Other second generation LSMs include the Biosphere-Atmosphere Transfer Scheme (BATS) (three soil layers and one vegetation layer) and the Simple Biosphere (SiB) Model (three soil layers and two vegetation layers) (Dickinson, 1986; Sellers et al., 1986) and built philosophically on the work of Deardorff (1978). Within these models, a snow sub-model was added. Snow was parameterised as part of the upper soil layer for thermal processes and a separate layer for hydrological processes (Pitman, 2003). More complicated schemes such as the UKMO scheme and its successor, MOSES, were included in the UK Met Office Unified Model (Cox et al., 1999). The second generation models led to improvements in forecasting precipitation events and made them more capable of calculating land-atmosphere fluxes than their first-generation counterparts (Sellers et al., 1997).

2.4.1.3 Third generation

By the end of the eighties, scientific interest had shifted its focus to the "greenhouse effect" and its ensuing impacts (Sellers et al., 1997). Models capable of providing a more complete picture of the climate system were required. A major improvement of second-generation over first generation LSMs was the addition of a model of canopy conductance. However, this sub-model only allowed a more realistic simulation of evapotranspiration

and not the uptake of carbon by plants (Pitman, 2003). Biochemical models of leaf photosynthesis were developed and linked to the biophysics of stomatal conductance (Farquhar et al., 1980; Bonan, 2008) and were then integrated into LSMs by Collatz et al. (1991), Sellers et al. (1992), Bonan (1995) and Cox et al. (1998). These new additions meant that the transpiration and photosynthesis parameterisations were closely coupled within LSMs and the biosphere could be modelled explicitly. The new models could compute more realistic fluxes of energy, water, and carbon, and required fewer parameters (Sellers et al., 1997; Bonan, 2008). They also responded to changes in atmospheric CO_2 in a more realistic way.

Model	Full name	Institution	Current version	Model features	References
CABLE	Community Atmosphere Biosphere Land Exchange	Commonwealth Scientific and Industrial Research Organisation (CSIRO)	2.0	13 surface types, 6 soil layers, 3 soil C pools, soil tiling, 3 snow layers, DGVM derived from LPJ	Kowalczyk et al. (2006)
CHTESSEL	Carbon-Hydrology-Tiled ECMWF Scheme for Surface Exchange over Land	European Centre for Medium-Range Weather Forecasts (ECMWF)	n/a	7 surface types, 4 soil layers, no soil C pools, 1 layer snow model, no DGVM	Boussetta et al. (2013)
CLM	Community Land Model	National Center for Atmospheric Research (NCAR) and the CESM Land Model Working Group	4.5	4 non-veg surface types, 15 PFTs (without DGVM), 12 PFTs (with DGVM), 10 soil layers (default), 4 soil C pools, multi-layer snow model (max. 5 layers), DGVM derived from LPJ	Oleson et al. (2013)
JSBACH	Jena Scheme of Biosphere Atmosphere Coupling in Hamburg	MPI-Jena/Hamburg	2.0	13 surface types, 5 soil layers, 2 soil C pools, multi-layer snow model (max. 5 layers), DGVM derived from Brovkin et al. (2009)	Raddatz et al. (2007) Brovkin et al. (2009)
JULES	Joint UK Land Environment Simulator	UK Met Office	4.1	9 surface types, 4 soil layers (default), 4 soil C pools, multi-layer snow model, TRIFFID DGVM	Best et al. (2011) Clark et al. (2011)
LPJmL	Lund-Potsdam-Jena managed Land	Potsdam Institute for Climate Impact Research (PIK)	3.2	23 surface types (10 PFTs + 13 CFTs), 2 soil C pools, 1 layer snow model, LPJ DGVM	Sitch et al. (2003) Bondeau et al. (2007)
ORCHIDEE	Organising Carbon and Hydrology in Dynamic Ecosystems	Institut Pierre Simon Laplace (IPSL)	1.9.5.2	13 surface types, 7 soil layers, 3 soil C pools, DGVM derived from LPJ	Krinner et al. (2005)

Table 2.1: Comparison of state-of-the-art land surface models (LSMs).

2.5 Sources of Uncertainty

LSM components are designed using results from research literature, idealised laboratory experiments and observations from limited field campaigns (Stöckli et al., 2008; Williams et al., 2009). This can lead to sources of uncertainty, which include the correct (mathematical) description of ecosystem processes, biophysical parameters, initial conditions and meteorological forcing data (Zaehle et al., 2005; Liu and Gupta, 2007). As LSMs become more advanced, there is a need to understand their complexity and accuracy and this is an important part of model development. LSMs can be evaluated in a variety of ways.

2.6 Evaluation of LSMs

LSMs are usually evaluated offline i.e. the model is run as a stand-alone model and is tested separately from its host GCM. In order to perform offline model simulations, the model must be provided with inputs such as vegetation and soil characteristics and driven with meteorological data. This can provide a number of advantages. Firstly, the sensitivity of the model to changes in parameters, meteorological forcing data or land-use, land-use change (LULUC) can be explored more effectively without the uncertainties associated with land-atmosphere feedbacks and large climate biases associated with GCM simulations. This can provide a better understanding of how a model behaves with changes in model parameters or under certain meteorological conditions, for example, with increasing temperatures. Secondly, it allows computationally inexpensive research to be conducted.

There are a number of ways to evaluate an LSM. These include directly comparing output from model simulations to observations, parameter perturbation experiments, multi-model intercomparison projects and benchmarking projects.

2.6.1 Model-observation comparisons

The first evaluation of an LSM was presented in 1978 by Deardorff using fluxes estimated from a few meteorological observations during two Summer days for a wheat crop in the UK (Deardorff, 1978). The Simple Biosphere

Model (SiB) was designed for use within GCMs to provide a realistic representation of the terrestrial biosphere (Sellers et al., 1986) and was tested offline by Sellers and Dorman (1987). While the initial data for these flux evaluations were obtained from micrometeorological towers, it was not until the advent of projects such as FLUXNET (Baldocchi et al., 2001) and PILPS (Henderson-Sellers et al., 1996), that enough high temporal resolution data was available to perform evaluations of land surface schemes across a range of biomes and climatic conditions. More recent evaluations include those by Morales et al. (2005), Friend et al. (2007), Stöckli et al. (2008) and Zaehle and Friend (2010).

2.6.2 Parameter perturbation experiments

Parameter perturbation experiments evaluate a single model and many simulations are performed where either one parameter is changed at a time within a given range (Knorr, 2000; Knorr and Heimann, 2001; El Maayar et al., 2002) or maximum and minimum values of parameters are used (Hallgren and Pitman, 2000).

2.6.3 Multi-model intercomparison projects

Multi-model intercomparison projects provide a measure of how various models behave under controlled conditions and can provide information on uncertainty surrounding future behaviour of the land surface (Huntzinger et al., 2013). Intercomparison projects can be used to identify weaker performing models and identify areas of uncertainty in multiple models (Levis, 2010). One of the first Model Intercomparison Projects (MIPs) was the Project for the Intercomparison of Land-Surface Parameterisation Schemes (Henderson-Sellers et al., 1993, PILPS). PILPS was an initiative of the Global Land/Atmosphere Systems Study (GLASS; http://www.gewex.org/glass.html), part of the Global Energy and Water Cycle Exchanges Project (GEWEX; http://www.gewex.org/), the core project of the World Climate Research Programme (WCRP; http://www.wcrp-climate.org/), which is an integrated program of research, observations and science activities focussed on modelling the global hydrological cycle and its impact on atmospheric and surface dynamics. Henderson-Sellers et al. (1993) launched PILPS in

order to evaluate multiple land surface models and to understand and improve parameterisations within models on regional to continental scales. This provided a within a *common framework* in which to test and compare LSMs against observational data at individual flux tower sites (van den Hurk et al., 2011). PILPS helped resolve many technical issues now commonly implemented in LSMs; running LSMs decoupled from the host GCM and the formal conservation of energy and water (van den Hurk et al., 2011).

Following on from PILPS, the Global Soil Wetness Project Phase 1 (GSWP-1; Dirmeyer et al. (1999)) used meteorological data from the International Satellite Land-Surface Climatology Project (ISLSCP; http://www.gewex.org/islscpdata.htm), to force LSMs *globally* in a framework similar to PILPS (Dirmeyer et al., 2006; Dirmeyer, 2011). In GSWP, LSMs were evaluated at the global scale compared to PILPS' point scale simulations. In addition to evaluating LSMs at the global scale, the primary purpose of GSWP was to produce products such as global estimates of soil moisture, temperature, snow-water equivalent and surface fluxes (Dirmeyer et al., 2006). GWSP was an important milestone in LSM development since it allowed for the first time a truly global evaluation of LSMs which encompassed all climate zones and interannual variability to some degree. Under the auspices of GLASS, GSWP-1 was further extended to a second phase (GSWP-2), which used a range of LSMs, multiple gridded forcing datasets, evaluation criteria and covered a longer time period (1986-1995) (Dirmeyer et al., 2006). Overall, GSWP-1/2 provided regional energy and water balances, uncertainties associated with the observational and reanalysis data and estimates of the various LSMs' ability to capture interannual variability in water and energy fluxes (van den Hurk et al., 2011).

Using a standard simulation protocol, the Carbon Cycle Model Linkage Project (CCMLP) studied the role of the land surface in the Earth system using four process-based terrestrial biosphere models to evaluate their response to CO_2, climate and land use for the terrestrial carbon cycle for the period 1920–1992 (McGuire et al., 2001). Results indicated that historical land-use change and CO_2 fertilisation were the dominant influences on the terrestrial carbon cycle and whether the terrestrial biosphere acted as a source or a sink for CO_2 depended on the model. The C4MIP project provided a conceptual framework, and was the first major study, to examine the coupling between climate change and the carbon cycle and diagnose the

causes of differences between models (Friedlingstein et al., 2006). Results from C4MIP showed a large spread in future projections of atmospheric CO_2 by coupled climate carbon-cycle models at the end of the 21^{st} century. Similar results were shown by CMIP5 (Friedlingstein et al., 2014). The C-LAMP (Carbon-LAnd Model Intercomparison Project) experimental protocol followed on from C4MIP and established a protocol and model performance metrics based upon comparison against best-available satellite- and ground-based measurements to evaluate two biogeochemistry models within the Community Climate System Model (CCSM) (Randerson et al., 2009). This model evaluation was used to guide development of CCSM.

As part of the North American Carbon Program (NACP) (http://nacarbon.org/nacp/) in 2008, a multi-model intercomparison project was carried out at the site (Schwalm et al., 2010; Schaefer et al., 2012) and regional scales (Hayes et al., 2012; Huntzinger et al., 2012). However, due to the short timescales of model runs (< 5 years), the non-representative sample of flux tower sites and complicated attribution of model performance, the NACP Multi-Scale Synthesis and Terrestrial Model Intercomparison Project (MsTMIP) was designed to create a consistent and unified model evaluation framework in order to better address differences among multiple models simulating carbon exchange at regional and global scales (Huntzinger et al., 2013; Wei et al., 2014, http://nacp.ornl.gov/MsTMIP.shtml). The goal of phase 1 of the project is to quantify how model structural differences affect carbon cycle simulations (Huntzinger et al., 2013). This project was created to complement other model comparison studies such as TRENDY (Sitch et al., 2015).

2.6.4 Benchmarking

Recently, in the LSM community, there has been effort to create a more standardised form of model evaluation known as benchmarking, whereby publicly available datasets, at various temporal and spatial resolutions, along with metrics and areas of model performance to be evaluated, are used by different modelling groups to test model performance (Abramowitz, 2012; Luo et al., 2012). This has previously been carried out by Abramowitz et al. (2008) and Blyth et al. (2011) to evaluate their institution's LSM. Modelling groups are now focussing their efforts on creating a comprehensive modelling

framework and a defined set of benchmarks against which land model performance can be evaluated. It means that areas for improvement in specific models and generic model problems among multiple models can be identified. Examples of such projects include ILAMB (http://ilamb.org/), PALS (Abramowitz, 2012) and PLUMBER, which is a land surface model (LSM) benchmarking intercomparison.

The International Land Model Benchmarking (ILAMB) project (http://ilamb.org/) is a model-data intercomparison project designed to create a framework to evaluate and improve land surface models (Luo et al., 2012). In addition to testing LSMs, ILAMB has the potential to stimulate new measurement campaigns in order to improve models and reduce uncertainties associated with important land surface processes and identify approaches to rectifying model deficiencies (Luo et al., 2012). PALS, Protocol for the Analysis of Land Surface models, a free online application for evaluating LSMs and the data used to test them, was created by the Climate Change Research Centre at the University of New South Wales (Abramowitz, 2012) (http://www.pals.unsw.edu.au). Once flux tower or model output data has been uploaded in a standardised format to the webpage, PALS will automatically run scripts (using the R language) to compare model output to observations and benchmark model time series and can produce a range of plots for various model output variables. The analysed model output include latent and sensible heat fluxes, net ecosystem exchange of CO_2 (NEE) and net radiation. PALS provides fast and efficient access to a large collection of model output data and flux tower observations and users are able to contribute to plot/analysis scripts. This method of evaluating LSMs means that differences in modelling strategies used by researchers in evaluating an LSM do not contribute towards differences between models and observations, but rather are due to uncertainty in model parameters or meteorological forcing (Knorr and Heimann, 2001).

The PALS Land sUrface Model Benchmarking Evaluation pRoject (PLUMBER) is an LSM benchmarking project using the PALS web based system (http://www.wenfo.org/ozewex/wgs/wg2-model-evaluation-and-benchmarking/91-the-pals-land-surface-model-benchmarking-evaluation-project-plumber). Unlike LSM evaluation or comparison, PLUMBER was designed to be an LSM benchmarking intercomparison in which it sets expectations of perfor-

mance using a range of metrics *a priori* i.e. before models simulations are performed. These metrics include older conceptual LSM implementations, such as a reference crop Penman-Monteith model and a Manabe bucket model, and three forms of statistical regression, as described in Abramowitz (2012). Multi-year model simulations were performed at 20 FLUXNET sites covering 10 IGBP vegetation types with 13 LSMs, including CABLE, CLM, JULES and ORCHIDEE (Table 2.1). The LSMs used in PLUMBER outperform the simple physically-based benchmarks when simulating latent heat fluxes, whereas for sensible heat fluxes, an out-of-sample linear regression against downward shortwave radiation performs better than the LSMs.

2.7 Evaluation of JULES

JULES (Joint UK Land Environment Simulator) is the land surface scheme of the UK Met Office Unified Model (MetUM), a single model family used to simulate weather and climate across a range of timescales (Walters et al., 2014). In the MetUM, different configurations of the same model are used for simulations across all time and spatial scales. A high resolution atmospheric model is more important than a high resolution ocean component for weather forecasting and a coupled ocean model is more beneficial for future climate predictions. JULES is a community model used for modelling all of the processes at the land surface, in the sub-surface soil and surface exchange processes (Best et al., 2011; Clark et al., 2011). JULES can be used *offline* (i.e. outside of its host GCM) and model simulations can be performed at the global, regional and point scale. A more detailed description of JULES is provided in Section 3.1.1.1.

JULES has been evaluated and used within GCM simulations a number of times. The land surface scheme MOSES 1 (Met Office Surface Exchange Scheme version 1), a precursor of JULES, improved the simulation of global surface climate when included in a GCM (Cox et al., 1999). Harding et al. (2000) validated MOSES against observed surface fluxes (latent and sensible heat) taken from a field site in the south of England. MOSES 1 was further improved by the addition of a tiled model of subgrid heterogeneity (MOSES 2), in which separate surface temperatures, shortwave and long-

wave radiative fluxes, latent and sensible heat fluxes and snow melt rates are computed for each surface type in a gridbox (Essery et al., 2001, 2003). Improved representation of snow processes in vegetation canopies and snow hydrology were included by Essery and Clark (2003) and was found to improve the simulation of runoff in two Swedish catchments used in the PILPS 2e intercomparison project. MOSES 2 was tested against observed fluxes of heat, water vapour and carbon dioxide at two primary rainforest sites in Brazil (Harris et al., 2004). Long-term water vapour fluxes were captured quite well by the model, but the modelled diurnal cycle of NEE was poor.

When MOSES 2 was included as the LSM of a GCM, the GCM was able to simulate the correlation in the interannual variability of atmospheric CO_2 concentration with ENSO (Jones et al., 2001) and the observed surface air temperature and atmospheric CO_2 response of the climate to volcanic eruptions (Jones and Cox, 2001). Betts et al. (2007) used the HadSM3 climate model, with MOSES 2 included as the land surface scheme, to investigate the effect of increased atmospheric CO_2 concentrations on continental surface water runoff. JULES differs from MOSES 2 in that it includes an explicit description of light interception for different canopy levels and provides a multilayer approach in scaling up leaf-level photosynthesis to canopy level (Mercado et al., 2007).

Alton et al. (2007) performed a sensitivity/uncertainty analysis of JULES for three forest sites focusing on the biophysical parameters, model processes and meteorological data which have the most effect on Gross Primary Productivity (GPP) and latent and sensible heat fluxes. Within this study, the most influential biophysical parameters were light-limited quantum efficiency and the Rubisco-limited rate of photosynthesis at the top of the canopy (V_{cmax}). The most important meteorological variables used to force the model were found to be the downward shortwave and longwave radiation fluxes (Alton et al., 2007). The performance of JULES in simulating changes in Amazonian vegetation carbon due to varying atmospheric CO_2, humidity, precipitation and temperature was compared with those from two dynamic global vegetation models (DGVMs), LPJ and Hyland (Galbraith et al., 2010). Galbraith et al. (2010) showed that JULES was insensitive to changes in precipitation. JULES has also been used to investigate tropical forest carbon stocks response to changes in climate (Huntingford et al., 2013), pan-arctic changes in near-surface permafrost (Burke et al., 2013),

hydrological fluxes in a humid tropical mountain basin in South America (Zulkafli et al., 2013), the inclusion and evaluation of a process-based isoprene emission scheme (Pacifico et al., 2011) and soil moisture estimates in southeast Australia compared to the CABLE LSM (Dumedah and Walker, 2014).

The first multi-site evaluation of JULES using sites representing a range of climatic conditions and biome types was performed by Blyth et al. (2010). The purpose of this study was to assess the ability of the model to partition incoming radiant energy into latent heat and how this partition varies with atmospheric evaporative demand and to identify weaknesses in model performance. Model output from these simulations were compared to observations from the FLUXNET network. Following on from this study, Blyth et al. (2011) performed a benchmarking study of JULES in which data used to force the model, a set of metrics used to quantify model performance and model simulations were defined in order to assess the ability of JULES to reproduce fluxes of water and carbon at the global and regional spatial scale.

2.8 Summary

In this chapter, the role of the land surface in the climate system, the evolution of LSMs, from the simple bucket models of the 1960s to the complex models which can now describe a comprehensive range of land-atmosphere interactions, and the methods used to evaluate them were discussed. Projects such as C4MIP and CMIP5 have shown a large range of simulated atmospheric CO_2 concentrations by 2100 using carbon cycle climate models for the SRES A2 and RCP8.5 scenarios, respectively. This large range is mainly due to the large uncertainty in the response of the terrestrial carbon cycle to increasing atmospheric CO_2 concentrations (carbon–concentration feedback) and climate change (carbon–climate feedback) (Friedlingstein et al., 2006, 2014). Evaluating LSMs offline can show how the model behaves with changes in either parameters, meteorological conditions or modelled processes and can help to reduce model uncertainty. JULES has been evaluated on a number of occasions (Alton et al., 2007; Galbraith et al., 2010; Blyth et al., 2011; Pacifico et al., 2011; Burke et al.,

2013) and the results from these studies have helped to inform on JULES behaviour across various biomes and climatic conditions. In the next chapter, the versions of JULES used to perform the model simulations for this dissertation and the datasets used as inputs to the model (soil, vegetation and meteorological data) and observations against which model performance is compared are described.

Bibliography

G. Abramowitz. Towards a public, standardized, diagnostic benchmarking system for land surface models. *Geoscientific Model Development*, 5:819–827, 2012. doi:10.5194/gmd-5-819-2012.

G. Abramowitz, R. Leuning, M. Clark, and A. Pitman. Evaluating the performance of land surface models. *Journal of Climate*, 21:5468–5481, 2008. doi:10.1175/2008JCLI2378.1.

P. Alton, L. Mercado, and P. North. A sensitivity analysis of the land-surface scheme JULES conducted for three forest biomes: Biophysical parameters, model processes, and meteorological driving data. *Global Biogeochemical Cycles*, 20:GB1008, 2007. doi:10.1029/2005GB002653.

D. Baldocchi, E. Falge, L. H. Gu, R. Olson, and D. Hollinger. FLUXNET: A New Tool to Study the Temporal and Spatial Variability of Ecosystem-Scale Carbon Dioxide, Water Vapor, and Energy Flux Densities. *Bulletin of the American Meteorological Society*, 82:2415–2434, 2001. doi:10.1175/1520-0477(2001)082<2415:FANTTS>2.3.CO;2.

H. E. Beck, T. R. McVicar, A. I. J. M. van Dijk, J. Schellekens, R. A. M. de Jeu, and L. A. Bruijnzeel. Global evaluation of four AVHRR–NDVI data sets: Intercomparison and assessment against Landsat imagery. *Remote Sensing of Environment*, 115:2547–2563, 2011. doi:10.1016/j.rse.2011.05.012.

R. A. Betts, O. Boucher, M. Collins, P. M. Cox, P. D. Falloon, N. Gedney, D. L. Hemming, C. Huntingford, C. D. Jones, D. M. H. Sexton, and M. J. Webb. Projected increase in continental runoff due to plant responses to increasing carbon dioxide. *Nature*, 448:1037–1041, 2007. doi:10.1038/nature06045.

E. Blyth, J. Gash, A. Lloyd, M. Pryor, G. P. Weedon, and J. Shuttleworth. Evaluating the JULES Land Surface Model Energy Fluxes Using FLUXNET Data. *Journal of Hydrometeorology*, 11:509–519, 2010. doi:10.1175/2009JHM1183.1.

E. Blyth, D. B. Clark, R. Ellis, C. Huntingford, S. Los, M. Pryor, M. Best, and S. Sitch. A comprehensive set of benchmark tests for a land surface model of simultaneous fluxes of water and carbon at both the global and seasonal scale. *Geoscientific Model Development*, 4:255–269, 2011. doi:10.5194/gmd-4-255-2011.

G. B. Bonan. Land-atmosphere CO_2 exchange simulated by a land surface process model coupled to an atmospheric general circulation model. *Journal of Geophysical Research: Atmospheres (1984–2012)*, 100:2817–2831, 1995. doi:10.1029/94JD02961.

G. B. Bonan. Forests and Climate Change: Forcings, Feedbacks, and the Climate Benefits of Forests. *Science*, 320:1444–1449, 2008. doi:10.1126/science.1155121.

A. Bondeau, P. C. Smith, S. Zaehle, S. Schaphoff, W. Lucht, W. Cramer, D. Gerten, H. Lotze-Campen, C. Müller, M. Reichstein, and B. Smith. Modelling the role of agriculture for the 20th century global terrestrial carbon balance. *Global Change Biology*, 13:679–706, 2007. doi:10.1111/j.1365-2486.2006.01305.x.

S. Boussetta, G. Balsamo, A. Beljaars, A.-A. Panareda, J.-C. Calvet, C. Jacobs, B. Hurk, P. Viterbo, S. Lafont, E. Dutra, L. Jarlan, M. Balzarolo, D. Papale, and G. van der Werf. Natural land carbon dioxide exchanges in the ECMWF Integrated Forecasting System: Implementation and offline validation. *Journal of Geophysical Research: Atmospheres*, 118:5923–5946, 2013. doi:10.1002/jgrd.50488.

V. Brovkin, T. Raddatz, C. H. Reick, M. Claussen, and V. Gayler. Global biogeophysical interactions between forest and climate. *Geophysical Research Letters*, 36:L07405, 2009. doi:10.1029/2009GL037543.

E. J. Burke, R. Dankers, C. D. Jones, and A. J. Wiltshire. A retrospective analysis of pan Arctic permafrost using the JULES land surface model. *Climate Dynamics*, 41:1025–1038, 2013. doi:10.1007/s00382-012-1648-x.

J. G. Canadell, C. Le Quéré, M. R. Raupach, C. B. Field, E. T. Buitenhuis, P. Ciais, T. J. Conway, N. P. Gillett, R. A. Houghton, and G. Marland. Contributions to accelerating atmospheric CO_2 growth from economic activity, carbon intensity, and efficiency of natural sinks. *Proceedings of the National Academy of Sciences of the United States of America*, 104: 18866–18870, 2007. doi:10.1073/pnas.0702737104.

J. G. Charney, P. H. Stone, and W. J. Quirk. Drought in the Sahara: A Biogeophysical Feedback Mechanism. *Science*, 187:434–435, 1975. doi:10.1126/science.187.4175.434.

P. Ciais, C. Sabine, G. Bala, L. Bopp, V. Brovkin, J. Canadell, A. Chhabra, R. DeFries, J. Galloway, M. Heimann, C. Jones, C. Le Quéré, R. B. Myneni, S. Piao, and P. Thornton. Carbon and Other Biogeochemical Cycles. In *Climate Change 2013: The Physical Science Basis. Contribution of Working Group I to the Fifth Assessment Report of the Intergovernmental Panel on Climate Change [T. F. Stocker, D. Qin, G.-K. Plattner, M. Tignor, S. K. Allen, J. Boschung, A. Nauels, Y. Xia, V. Bex and P. M. Midgley (eds)]*, pages 465–570. Cambridge University Press, Cambridge, UK and New York, NY, USA, 2013.

G. J. Collatz, J. T. Ball, C. Grivet, and J. A. Berry. Physiological and environmental regulation of stomatal conductance, photosynthesis and transpiration: a model that includes a laminar boundary layer. *Agricultural and Forest Meteorology*, 54:107–136, 1991. doi:10.1016/0168-1923(91)90002-8.

P. M. Cox, C. Huntingford, and R. J. Harding. A canopy conductance and photosynthesis model for use in a gcm land surface scheme. *Journal of Hydrology*, 212:79–94, 1998. doi:10.1016/S0022-1694(98)00203-0.

P. M. Cox, R. A. Betts, C. B. Bunton, R. L. H. Essery, P. R. Rowntree, and J. Smith. The impact of new land surface physics on the GCM simulation of climate and climate sensitivity. *Climate Dynamics*, 15:183–203, 1999. doi:10.1007/s003820050276.

U. Cubasch, D. Wuebbles, D. Chen, M. C. Facchini, D. Frame, N. Mahowald, and J.-G. Winther. Introduction. In *Climate Change 2013: The Physical Science Basis. Contribution of Working Group I to the Fifth Assessment Report of the Intergovernmental Panel on Climate Change [T. F. Stocker, D. Qin, G.-K. Plattner, M. Tignor, S. K. Allen, J. Boschung, A. Nauels, Y. Xia, V. Bex and P. M. Midgley (eds)]*, pages 119–158. Cambridge University Press, Cambridge, United Kingdom and New York, NY, USA, 2013.

Y. Dai, X. Zeng, R. E. Dickinson, I. Baker, G. B. Bonan, M. G. Bosilovich, A. S. Denning, P. A. Dirmeyer, P. R. Houser, G. Niu, K. W. Oleson, C. A. Schlosser, and Z.-L. Yang. The Common Land Model. *Bulletin of the American Meteorological Society*, 84:1013–1023, 2003. doi:10.1175/BAMS-84-8-1013.

J. W. Deardorff. Efficient Prediction of Ground Surface Temperature and Moisture, With Inclusion of a Layer of Vegetation. *Journal of Geophysical Research*, 83:1889–1903, 1978. doi:10.1029/JC083iC04p01889.

R. E. Dickinson. Biosphere/Atmosphere Transfer Scheme (BATS) for the NCAR Community Climate Model. *Technical report*, 1986.

P. A. Dirmeyer. A History and Review of the Global Soil Wetness Project (GSWP). *Journal of Hydrometeorology*, 12:729–749, 2011. doi:10.1175/JHM-D-10-05010.1.

P. A. Dirmeyer, A. J. Dolman, and N. Sato. The Pilot Phase of the Global Soil Wetness Project. *Bulletin of the American Meteorological Society*, 80:851–878, 1999. doi:10.1175/1520-0477(1999)080<0851:TPPOTG>2.0.CO;2.

P. A. Dirmeyer, G. Xiang, M. Zhao, G. Zhichang, T. Oki, and N. Hanasaki. GSWP-2: Multimodel Analysis and Implications for Our Perception of

the Land Surface. *Bulletin of the American Meteorological Society*, 87: 1381–1397, 2006. doi:10.1175/BAMS-87-10-1381.

G. Dumedah and J. P. Walker. Intercomparison of the JULES and CABLE land surface models through assimilation of remotely sensed soil moisture in southeast Australia. *Advances in Water Resources*, 74:231 – 244, 2014. doi:10.1016/j.advwatres.2014.09.011.

M. El Maayar, D. T. Price, T. A. Black, E. R. Humphreys, and E.-M. Jork. Sensitivity tests of the integrated biosphere simulator to soil and vegetation characteristics in a Pacific coastal coniferous forest. *Atmosphere-Ocean*, 40:313–332, 2002. doi:10.3137/ao.400303.

R. Essery and D. B. Clark. Developments in the MOSES 2 land-surface model for PILPS 2e. *Global and Planetary Change*, 38:161–164, 2003. doi:10.1016/S0921-8181(03)00026-2.

R. Essery, M. Best, and P. Cox. Moses 2.2 technical documentation. Technical report, Hadley Centre technical note 30, 2001.

R. L. H. Essery, M. J. Best, R. A. Betts, P. M. Cox, and C. M. Taylor. Explicit representation of subgrid heterogeneity in a GCM land surface scheme. *Journal of Hydrometeorology*, 4:530–543, 2003. doi:10.1175/1525-7541(2003)004<0530:EROSHI>2.0.CO;2.

P. Falkowski, R. J. Scholes, E. Boyle, J. Canadell, D. Canfield, J. Elser, N. Gruber, K. Hibbard, P. Högberg, S. Linder, F. T. Mackenzie, B. Moore III, T. Pedersen, Y. Rosenthal, S. Seitzinger, V. Smetacek, and W. Steffen. The Global Carbon Cycle: A Test of Our Knowledge of Earth as a System. *Science*, 290:291–296, 2000. doi:10.1126/science.290.5490.291.

G. D. Farquhar, S. Caemmerer, and J. A. Berry. A Biochemical Model of Photosynthetic CO_2 Assimilation in Leaves of C_3 Species. *Planta*, 149: 78–90, 1980. doi:10.1007/BF00386231.

R. Fensholt, T. Langanke, K. Rasmussen, A. Reenberg, S. D. Prince, C. Tucker, R. J. Scholes, Q. B. Le, A. Bondeau, R. Eastman, H. Epstein, A. E. Gaughan, U. Hellden, C. Mbow, L. Olsson, J. Paruelo,

C. Schweitzer, J. Seaquist, and K. Wessels. Greenness in semi-arid areas across the globe 1981–2007 - An Earth Observing Satellite based analysis of trends and drivers. *Remote Sensing of Environment*, 121:144–158, 2012. doi:10.1016/j.rse.2012.01.017.

P. Friedlingstein and I. C. Prentice. Carbon–climate feedbacks: a review of model and observation based estimates. *Current Opinion in Environmental Sustainability*, 2:251–257, 2010. doi:10.1016/j.cosust.2010.06.002.

A. D. Friend, A. Arneth, N. Y. Kiang, M. Lomas, J. Ogee, C. Rödenbeck, S. W. Running, J.-D. Santaren, S. Sitch, N. Viovy, F. I. Woodward, and S. Zaehle. FLUXNET and modelling the global carbon cycle. *Global Change Biology*, 13:610–633, 2007. doi:10.1111/j.1365-2486.2006.01223.x.

D. Galbraith, P. E. Levy, S. Sitch, C. Huntingford, P. Cox, M. Williams, and P. Meir. Multiple mechanisms of Amazonian forest biomass losses in three dynamic global vegetation models under climate change. *New Phytologist*, 187:647–665, 2010. doi:10.1111/j.1469-8137.2010.03350.x.

W. S. Hallgren and A. J. Pitman. The uncertainty in simulations by a Global Biome Model (BIOME3) to alternative parameter values. *Global Change Biology*, 6:483–495, 2000. doi:10.1046/j.1365-2486.2000.00325.x.

R. J. Harding, C. Huntingford, and P. M. Cox. Modelling long-term transpiration measurments from grassland in southern England. *Agricultural and Forest Meteorology*, 100:309–322, 2000. doi:10.1016/S0168-1923(99)00152-5.

P. P. Harris, C. Huntingford, J. H. C. Gash, M. G. Hodnett, P. M. Cox, Y. Malhi, and A. C. Araujo. Calibration of a land-surface model using data from primary forest sites in Amazonia. *Theoretical and Applied Climatology*, 78:27–45, 2004. doi:10.1007/s00704-004-0042-y.

D. J. Hayes, D. P. Turner, G. Stinson, A. D. McGuire, Y. Wei, T. O. West, L. S. Heath, B. de Jong, B. G. McConkey, R. A. Birdsey, W. A. Kurz, A. R. Jacobson, D. N. Huntzinger, Y. Pan, W. M. Post, and R. B. Cook. Reconciling estimates of the contemporary North American carbon balance among terrestrial biosphere models, atmospheric inversions, and a new approach for estimating net ecosystem exchange

from inventory-based data. *Global Change Biology*, 18:1282–1299, 2012. doi:10.1111/j.1365-2486.2011.02627.x.

M. Heimann and M. Reichstein. Terrestrial ecosystem carbon dynamics and climate feedbacks. *Nature*, 451:289–292, 2008. doi:10.1038/nature06591.

A. Henderson-Sellers, Z. L. Yang, and R. E. Dickinson. The Project for Intercomparison of Land-surface Parameterization Schemes. *Bulletin of the American Meteorological Society*, 74:1335–1349, 1993. doi:10.1175/1520-0477(1993)074<1335:TPFIOL>2.0.CO;2.

A. Henderson-Sellers, K. McGuffie, and A. J. Pitman. The Project for Intercomparison of Land-Surface Parametrization Schemes (PILPS): 1992 to 1995. *Climate Dynamics*, 12:849–859, 1996. doi:10.1007/s003820050147.

C. Huntingford, P. Zelazowski, D. Galbraith, L. M. Mercado, S. Sitch, R. Fisher, M. Lomas, A. P. Walker, C. D. Jones, B. B. B. Booth, Y. Malhi, D. Hemming, G. Kay, P. Good, S. L. Lewis, O. L. Phillips, O. K. Atkin, J. Lloyd, E. Gloor, J. Zaragoza-Castells, P. Meir, R. Betts, P. P. Harris, C. Nobre, J. Marengo, and P. M. Cox. Simulated resilience of tropical rainforests to CO_2-induced climate change. *Nature Geosciences*, 6:268–273, 2013. doi:10.1038/ngeo1741.

D. N. Huntzinger, W. M. Post, Y. Wei, A. M. Michalak, T. O. West, A. R. Jacobson, I. T. Baker, J. M. Chen, K. J. Davis, D. J. Hayes, F. M. Hoffman, A. K. Jain, S. Liu, A. D. McGuire, R. P. Neilson, C. Potter, B. Poulter, D. Price, B. M. Raczka, H. Q. Tian, P. Thornton, E. Tomelleri, N. Viovy, J. Xiao, W. Yuan, N. Zeng, M. Zhao, and R. Cook. North American Carbon Program (NACP) regional interim synthesis: Terrestrial biospheric model intercomparison. *Ecological Modelling*, 232:144 – 157, 2012. doi:10.1016/j.ecolmodel.2012.02.004.

D. N. Huntzinger, C. Schwalm, A. M. Michalak, K. Schaefer, A. W. King, Y. Wei, A. Jacobson, S. Liu, R. B. Cook, W. M. Post, G. Berthier, D. Hayes, M. Huang, A. Ito, H. Lei, C. Lu, J. Mao, C. H. Peng, S. Peng, B. Poulter, D. Riccuito, X. Shi, H. Tian, W. Wang, N. Zeng, F. Zhao, and Q. Zhu. The North American Carbon Program Multi-Scale Synthesis and Terrestrial Model Intercomparison Project - Part 1: Overview

and experimental design. *Geoscientific Model Development*, 6:2121–2133, 2013. doi:10.5194/gmd-6-2121-2013.

C. D. Jones and P. M. Cox. Modeling the volcanic signal in the atmospheric CO_2 record. *Global Biogeochemical Cycles*, 15:453–465, 2001. doi:10.1029/2000GB001281.

C. D. Jones, M. Collins, P. M. Cox, and S. A. Spall. The Carbon Cycle Response to ENSO: A Coupled Climate–Carbon Cycle Model Study. *Journal of Climate*, 14:4113–4129, 2001. doi:10.1175/1520-0442(2001)014<4113:TCCRTE>2.0.CO;2.

W. Knorr. Annual and interannual CO_2 exchanges of the terrestrial biosphere: process-based simulations and uncertainties. *Global Ecology and Biogeography*, 9:225–252, 2000. doi:10.1046/j.1365-2699.2000.00159.x.

W. Knorr and M. Heimann. Uncertainties in global terrestrial biosphere modeling: 1. A comprehensive sensitivity analysis with a new photosynthesis and energy balance scheme. *Global Biogeochemical Cycles*, 15: 207–225, 2001. doi:10.1029/1998GB001059.

E. A. Kowalczyk, Y. P. Wang, R. M. Law, H. L. Davies, J. L. McGregor, and G. Abramowitz. The CSIRO Atmosphere Biosphere Land Exchange (CABLE) model for use in climate models and as an offline model . Technical report, CSIRO Marine and Atmospheric Research, November 2006.

G. Krinner, N. Viovy, N. de Noblet-Ducoudré, J. Ogée, J. Polcher, P. Friedlingstein, P. Ciais, S. Sitch, and I. C. Prentice. A dynamic global vegetation model for studies of the coupled atmosphere-biosphere system. *Global Biogeochemical Cycles*, 19:33, 2005. doi:10.1029/2003GB002199.

C. Le Quéré, M. R. Raupach, J. G. Canadell, and G. Marland. Trends in the sources and sinks of carbon dioxide. *Nature Geoscience*, 2:831–836, 2009. doi:10.1038/ngeo689.

C. Le Quéré, R. J. Andres, T. Boden, T. Conway, R. A. Houghton, J. I. House, G. Marland, G. P. Peters, G. R. van der Werf, A. Ahlström, R. M. Andrew, L. Bopp, J. G. Canadell, P. Ciais, S. C. Doney, C. Enright, P. Friedlingstein, C. Huntingford, A. K. Jain, C. Jourdain, E. Kato, R. F.

Keeling, K. Klein Goldewijk, S. Levis, P. Levy, M. Lomas, B. Poulter, M. R. Raupach, J. Schwinger, S. Sitch, B. D. Stocker, N. Viovy, S. Zaehle, and N. Zeng. The global carbon budget 1959–2011. *Earth System Science Data*, 5:165–185, 2013. doi:10.5194/essd-5-165-2013.

A. D. B. Leakey, E. A. Ainsworth, C. J. Bernacchi, A. Rogers, S. P. Long, and D. R. Ort. Elevated CO_2 effects on plant carbon, nitrogen, and water relations: six important lessons from FACE. *Journal of Experimental Botany*, 60:2859–2876, 2009. doi:10.1093/jxb/erp096.

S. Levis. Modeling vegetation and land use in models of the Earth System. *Wiley Interdisciplinary Reviews: Climate Change*, 1:840–856, 2010. doi:10.1002/wcc.83.

Y. Q. Luo, J. T. Randerson, G. Abramowitz, C. Bacour, E. Blyth, N. Carvalhais, P. Ciais, D. Dalmonech, J. B. Fisher, R. Fisher, P. Friedlingstein, K. Hibbard, F. Hoffman, D. Huntzinger, C. D. Jones, C. Koven, D. Lawrence, D. J. Li, M. Mahecha, S. L. Niu, R. Norby, S. L. Piao, X. Qi, P. Peylin, I. C. Prentice, W. Riley, M. Reichstein, C. Schwalm, Y. P. Wang, J. Y. Xia, S. Zaehle, and X. H. Zhou. A framework for benchmarking land models. *Biogeosciences*, 9:3857–3874, 2012. doi:10.5194/bg-9-3857-2012.

J. J. Maynard, R. A. Dahlgren, and A. T. O'Geen. Soil carbon cycling and sequestration in a seasonally saturated wetland receiving agricultural runoff. *Biogeosciences*, 8:3391–3406, 2011. doi:10.5194/bg-8-3391-2011.

A. D. McGuire, S. Sitch, J. S. Clein, R. Dargaville, G. Esser, J. Foley, M. Heimann, F. Joos, J. Kaplan, and D. W. and Kicklighter. Carbon balance of the terrestrial biosphere in the Twentieth Century: Analyses of CO_2, climate and land use effects with four process-based ecosystem models. *Global Biogeochemical Cycles*, 15:183–206, 2001. doi:10.1029/2000GB001298.

P. Meir, P. Cox, and J. Grace. The influence of terrestrial ecosystems on climate. *Trends in Ecology & Evolution*, 21:254–260, 2006. doi:10.1016/j.tree.2006.03.005.

L. M. Mercado, C. Huntingford, J. H. C. Gash, P. M. Cox, and V. Jogireddy. Improving the representation of radiation interception and photosynthesis for climate model applications. *Tellus B*, 59:553–565, 2007. doi:10.1111/j.1600-0889.2007.00256.x.

P. Morales, M. T. Sykes, I. C. Prentice, P. Smith, B. Smith, H. Bugmann, B. Zierl, P. Friedlingstein, N. Viovy, S. Sabaté, A. Sánchez, E. Pla, C. A. Gracia, S. Sitch, A. Arneth, and J. Ogee. Comparing and evaluating process-based ecosystem model predictions of carbon and water fluxes in major European forest biomes. *Global Change Biology*, 11:2211–2233, 2005. doi:10.1111/j.1365-2486.2005.01036.x.

G. Myhre, D. Shindell, F.-M. Bréon, W. Collins, J. Fuglestvedt, J. Huang, D. Koch, J.-F. Lamarque, D. Lee, B. Mendoza, T. Nakajima, A. Robock, G. Stephens, T. Takemura, and H. Zhang. Anthropogenic and Natural Radiative Forcing. In *Climate Change 2013: The Physical Science Basis. Contribution of Working Group I to the Fifth Assessment Report of the Intergovernmental Panel on Climate Change [T. F. Stocker, D. Qin, G.-K. Plattner, M. Tignor, S. K. Allen, J. Boschung, A. Nauels, Y. Xia, V. Bex and P. M. Midgley (eds)]*, pages 659–740. Cambridge University Press, Cambridge, United Kingdom and New York, NY, USA, 2013.

R. J. Norby, E. H. DeLucia, B. Gielen, C. Calfapietra, C. P. Giardina, J. S. King, J. Ledford, H. R. McCarthy, D. J. P. Moore, R. Ceulemans, P. De Angelis, A. C. Finzi, D. F. Karnosky, M. E. Kubiske, M. Lukac, K. S. Pregitzer, G. E. Scarascia-Mugnozza, W. H. Schlesinger, and R. Oren. Forest response to elevated CO_2 is conserved across a broad range of productivity. *Proceedings of the National Academy of Sciences of the United States of America*, 102:18052–18056, 2005. doi:10.1073/pnas.0509478102.

K. Oleson, D. M. Lawrence, G. B. Bonan, B. Drewniak, M. Huang, C. D. Koven, S. Levis, F. Li, W. J. Riley, Z. M. Subin, S. Swenson, P. E. Thornton, A. Bozbiyik, R. Fisher, C. L. Heald, E. Kluzek, J.-F. Lamarque, P. J. Lawrence, L. R. Leung, W. Lipscomb, S. P. Muszala, D.M. Ricciuto, W. J. Sacks, Y. Sun, J. Tang, and Z.-L. Yang. Technical Description of version 4.5 of the Community Land Model (CLM). Technical report, National Center for Atmospheric Research, 2013. NCAR/TN-503+STR.

F. Pacifico, S. P. Harrison, C. D. Jones, A. Arneth, S. Sitch, G. P. Weedon, M. P. Barkley, P. I. Palmer, D. Serça, M. Potosnak, T.-M. Fu, A. Goldstein, J. Bai, and G. Schurgers. Evaluation of a photosynthesis-based biogenic isoprene emission scheme in JULES and simulation of isoprene emissions under present-day climate conditions. *Atmospheric Chemistry and Physics*, 11:4371–4389, 2011. doi:10.5194/acp-11-4371-2011.

Y. Pan, R. A. Birdsey, J. Fang, R. Houghton, P. E. Kauppi, W. A. Kurz, O. L. Phillips, A. Shvidenko, S. L. Lewis, J. G. Canadell, P. Ciais, R. B. Jackson, S. W. Pacala, A. D. McGuire, S. Piao, A. Rautiainen, S. Sitch, and D. Hayes. A Large and Persistent Carbon Sink in the World's Forests. *Science*, 333:988–993, 2011. doi:10.1126/science.1201609.

S. Piao, P. Friedlingstein, P. Ciais, L. Zhou, and A. Chen. Effect of climate and CO_2 changes on the greening of the Northern Hemisphere over the past two decades. *Geophysical Research Letters*, 33:L23402, 2006. doi:10.1029/2006GL028205.

R. A. Pielke, R. Avissar, M. Raupach, A. J. Dolman, X. Zeng, and A. S. Denning. Interactions between the atmosphere and terrestrial ecosystems: influence on weather and climate. *Global Change Biology*, 4:461–475, 1998. doi:10.1046/j.1365-2486.1998.t01-1-00176.x.

A. J. Pitman. The evolution of, and revolution in, land surface schemes designed for climate models. *International Journal of Climatology*, 23: 479–510, 2003. doi:10.1002/joc.893.

J. Pongratz, C. H. Reick, T. Raddatz, and M. Claussen. Effects of anthropogenic land cover change on the carbon cycle of the last millennium. *Global Biogeochemical Cycles*, 23:GB4001, 2009. doi:10.1029/2009GB003488.

T. J. Raddatz, C. H. Reick, W. Knorr, J. Kattge, E. Roeckner, R. Schnur, K.-G. Schnitzler, P. Wetzel, and J. Jungclaus. Will the tropical land biosphere dominate the climate–carbon cycle feedback during the twenty-first century? *Climate Dynamics*, 29:565–574, 2007. doi:10.1007/s00382-007-0247-8.

J. T. Randerson, F. M. Hoffman, P. E. Thornton, N. M. Mahowald, K. Lindsay, Y.-H. Lee, C. D Nevison, S. C. Doney, G. Bonan, R. Stöckli, C. Covey, S. W. Running, and I. Y. Fung. Systematic assessment of terrestrial biogeochemistry in coupled climate–carbon models. *Global Change Biology*, 15:2462–2484, 2009. doi:10.1111/j.1365-2486.2009.01912.x.

K. Riahi, S. Rao, V. Krey, C. Cho, V. Chirkov, G. Fischer, G. Kindermann, N. Nakicenovic, and P. Rafaj. RCP 8.5–A scenario of comparatively high greenhouse gas emissions. *Climatic Change*, 109:33–57, 2011. doi:10.1007/s10584-011-0149-y.

E. J. Sayer, M. S. Heard, H. K. Grant, T. R. Marthews, and E. V. J. Tanner. Soil carbon release enhanced by increased tropical forest litterfall. *Nature Climate Change*, 1:304–307, 2011. doi:10.1038/nclimate1190.

K. Schaefer, C. R. Schwalm, C. Williams, M. A. Arain, A. Barr, J. M. Chen, K. J. Davis, D. Dimitrov, T. W. Hilton, D. Y. Hollinger, E. Humphreys, B. Poulter, B. M. Raczka, A. D. Richardson, A. Sahoo, P. Thornton, H. Vargas, R.and Verbeeck, R. Anderson, I. Baker, T. A. Black, P. Bolstad, J. Chen, P. S. Curtis, A. R. Desai, M. Dietze, D. Dragoni, C. Gough, R. F. Grant, L. Gu, A. Jain, C. Kucharik, B. Law, S. Liu, E. Lokipitiya, H. A. Margolis, R. Matamala, J. H. McCaughey, R. Monson, J. W. Munger, W. Oechel, C. Peng, D. T. Price, D. Ricciuto, W. J. Riley, N. Roulet, H. Tian, C. Tonitto, M. Torn, E. Weng, and X. Zhou. A model-data comparison of gross primary productivity: Results from the North American Carbon Program site synthesis. *Journal of Geophysical Research*, 117:G03010, 2012. doi:10.1029/2012JG001960.

C. R. Schwalm, C. A. Williams, K. Schaefer, R. Anderson, M. A. Arain, I. Baker, A. Barr, T. A. Black, G. Chen, J. M. Chen, P. Ciais, K. J. Davis, A. Desai, M. Dietze, D. Dragoni, M. L. Fischer, L. B. Flanagan, R. Grant, L. Gu, D. Hollinger, R. C. Izaurralde, C. Kucharik, P. Lafleur, B. E. Law, L. Li, Z. Li, S. Liu, E. Lokupitiya, Y. Luo, S. Ma, H. Margolis, R. Matamala, H. McCaughey, R. K. Monson, W. C. Oechel, C. Peng, B. Poulter, D. T. Price, D. M. Riciutto, W. Riley, A. K. Sahoo, M. Sprintsin, J. Sun, H. Tian, C. Tonitto, H. Verbeeck, and S. B. Verma. A model-data intercomparison of CO_2 exchange across North America: Results from the

North American Carbon Program site synthesis. *Journal of Geophysical Research: Biogeosciences*, 115:G00H05, 2010. doi:10.1029/2009JG001229.

P. J. Sellers and J. L. Dorman. Testing the Simple Biosphere model (SiB) using Point Micrometeorological and Biophysical Data. *Journal of Applied Meteorology*, 26:622–651, 1987. doi:10.1175/1520-0450(1987)026<0622:TTSBMU>2.0.CO;2.

P. J. Sellers, J. A. Berry, G. J. Collatz, C. B. Field, and F. G. Hall. Canopy reflectance, photosynthesis, and transpiration. III. A reanalysis using improved leaf models and a new canopy integration scheme. *Remote Sensing of Environment*, 42:187–216, 1992. doi:10.1016/0034-4257(92)90102-P.

P. J. Sellers, R. E. Dickinson, D. A. Randall, A. K. Betts, F. G. Hall, J. A. Berry, G. J. Collatz, A. S. Denning, H. A. Mooney, C. A. Nobre, N. Sato, C. B. Field, and A. Henderson-Sellers. Modeling the Exchanges of Energy, Water, and Carbon Between Continents and the Atmosphere. *Science*, 275:502, 1997. doi:10.1126/science.275.5299.502.

P.J. Sellers, Y. Mintz, Y.C. Sud, and A. Dalcher. A Simple Biosphere Model (SiB) for Use within General Circulation Models. *Journal of the Atmospheric Sciences*, 43:505–531, 1986. doi:10.1175/1520-0469(1986)043<0505:ASBMFU>2.0.CO;2.

S. Sitch, B. Smith, I. C. Prentice, A. Arneth, A. Bondeau, W. Cramer, J. O. Kaplan, S. Levis, W. Lucht, M. T. Sykes, K. Thonicke, and S. Venevsky. Evaluation of ecosystem dynamics, plant geography and terrestrial carbon cycling in the LPJ dynamic global vegetation model. *Global Change Biology*, 9:161–185, 2003. doi:10.1046/j.1365-2486.2003.00569.x.

S. Sitch, P. Friedlingstein, N. Gruber, S. D. Jones, G. Murray-Tortarolo, A. Ahlström, S. C. Doney, H. Graven, C. Heinze, C. Huntingford, S. Levis, P. E. Levy, M. Lomas, B. Poulter, N. Viovy, S. Zaehle, N. Zeng, A. Arneth, G. Bonan, L. Bopp, J. G. Canadell, F. Chevallier, P. Ciais, R. Ellis, M. Gloor, P. Peylin, S. L. Piao, C. Le Quéré, B. Smith, Z. Zhu, and R. Myneni. Recent trends and drivers of regional sources and sinks of carbon dioxide. *Biogeosciences*, 12:653–679, 2015. doi:10.5194/bg-12-653-2015.

R. Stöckli, D. M. Lawrence, G. Y. Niu, K .W. Oleson, P. E. Thornton, Z. L. Yang, G. B. Bonan, A. S. Denning, and S. W. Running. Use of FLUXNET in the Community Land Model development. *Journal of Geophysical Research*, 113:G01025, 2008. doi:10.1029/2007JG000562.

B. van den Hurk, M. Best, P. Dirmeyer, A. Pitman, J. Polcher, and J. Santanello. Acceleration of land surface model development over a decade of GLASS. *Bulletin of the American Meteorological Society*, 92:1593–1600, 2011. doi:10.1175/BAMS-D-11-00007.1.

D. P. Van Vuuren, J. Edmonds, M. Kainuma, K. Riahi, A. Thomson, K. Hibbard, G. C. Hurtt, T. Kram, V. Krey, J.-F. Lamarque, T. Masui, M. Meinshausen, N. Nakicenovic, S. J. Smith, and S. K. Rose. The representative concentration pathways: an overview. *Climatic Change*, 109:5–31, 2011. doi:10.1007/s10584-011-0148-z.

J. M. Warren, E. Pötzelsberger, S. D. Wullschleger, P. E. Thornton, H. Hasenauer, and R. J. Norby. Ecohydrologic impact of reduced stomatal conductance in forests exposed to elevated CO_2. *Ecohydrology*, 4:196–210, 2011. doi:10.1002/eco.173.

Y. Wei, S. Liu, D. N. Huntzinger, A. M. Michalak, N. Viovy, W. M. Post, C. R. Schwalm, K. Schaefer, A. R. Jacobson, C. Lu, H. Tian, D. M. Ricciuto, R. B. Cook, J. Mao, and X. Shi. The North American Carbon Program Multi-scale Synthesis and Terrestrial Model Intercomparison Project - Part 2: Environmental driver data. *Geoscientific Model Development*, 7:2875–2893, 2014. doi:10.5194/gmd-7-2875-2014.

M. Williams, A. D. Richardson, M. Reichstein, P. C. Stoy, P. Peylin, H. Verbeeck, N. Carvalhais, M. Jung, D. Y. Hollinger, J. Kattge, R. Leuning, Y. Luo, E. Tomelleri, C. M. Trudinger, and Y.-P. Wang. Improving land surface models with FLUXNET data. *Biogeosciences*, 6:1341–1359, 2009. doi:10.5194/bg-6-1341-2009.

S. Zaehle and A. D. Friend. Carbon and nitrogen cycle dynamics in the O-CN land surface model: 1. Model description, site-scale evaluation, and sensitivity to parameter estimates. *Global Biogeochemical Cycles*, 24: GB1005, 2010. doi:10.1029/2009GB003521.

Z. Zulkafli, W. Buytaert, C. Onof, W. Lavado, and J. L. Guyot. A critical assessment of the JULES land surface model hydrology for humid tropical environments. *Hydrology and Earth System Sciences*, 17:1113–1132, 2013. doi:10.5194/hess-17-1113-2013.

Chapter 3

Models and Data

In this chapter, descriptions of the JULES LSM, the datasets containing the soil and vegetation properties used by the model, the various meteorological datasets used to drive the model, at both the local and global scale, and the datasets used to compare model performance against are provided. Two versions of the JULES LSM have been used within this thesis: JULES version 3.0 (single point simulations) and JULES version 3.4.1 (global scale simulations) are both described in Section 3.1. A description of the soil and vegetation datasets used by the model at both the point and global scale is provided in Section 3.2.1. The meteorological and satellite datasets used to drive the model are discussed in Section 3.2.2. Finally, the observational datasets against which model performance is compared are described in Section 3.2.3.

3.1 Models

Two versions of the JULES LSM have been used for the various model simulations performed as part of this thesis. JULES version 3.0 (Section 3.1.1) was used for the model simulations at the point scale in Chapter 4 and JULES version 3.4.1 (Section 3.1.2) was used for the model simulations at the global scale in Chapters 5 and 6.

3.1.1 JULES version 3.0

3.1.1.1 Model overview

The Joint UK Land Environment Simulator (JULES) is the land surface scheme of the UK Met Office Unified Model (Walters et al., 2014, MetUM, current version 10.2), a family of models which includes the Hadley Centre Global Environmental Model (HadGEM) climate model (http://www.metoffice.gov.uk/research/modelling-systems/unified-model). It has evolved from the Met Office Surface Exchange Scheme (Cox et al., 1999, MOSES). JULES is a mechanistic model and is able to model such processes as photosynthesis, evapotranspiration, soil and snow physics, and soil microbial activity (Blyth et al., 2011). Each model gridbox is composed of 9 different surface types, five of which are vegetation, referred to as Plant Functional Types (PFTs) (broadleaf trees, needleleaf trees, C3 (temperate) grass, C4 (tropical) grass and shrubs), and four non-vegetation types (urban, inland water, bare soil and land-ice). Each gridbox can be made up of the first 8 surface types or is land-ice. The standalone (i.e. run separately from its host GCM) and global operational versions of the JULES model are quite similar. Since UM version 8.1 (using JULES version 3.0), the JULES code for both have been the same with some exceptions, such as the UM/standalone initialisation code. The science code (e.g. photosynthesis, hydrology and soil processes) remains the same between the two. JULES was compared to other LSMs in Table 2.1. A more detailed description of JULES can be found in Clark et al. (2011) and Best et al. (2011).

3.1.1.2 Computing surface fluxes of CO_2

The surface fluxes of CO_2 associated with photosynthesis (described in more detail in Section 3.1.1.3) are computed on each timestep (typically 30 to 60 minutes) for each PFT using a coupled photosynthesis-stomatal conductance model (Cox et al., 1998). These accumulated carbon fluxes are passed to TRIFFID (Top-down Representation of Interactive Foliage and Flora Including Dynamics), JULES' dynamic global vegetation model and also its terrestrial carbon cycle component (Cox, 2001) TRIFFID updates the areal coverage, LAI and canopy height for each PFT on a longer timestep (usually every 10 days), based on the net carbon available to it and competition

with other vegetation types (Cox, 2001). In JULES, phenology (bud burst and leaf drop) is, typically, updated once per day by multiplying the annual maximum LAI by a scaling factor, which is calculated by using temperature-dependent leaf turnover rates (Clark et al., 2011). When calculating GPP, a multi-layer canopy was used for the scaling up of leaf-level photosynthesis to canopy level. The option used takes into account the vertical gradient of canopy photosynthetic capacity (decreasing leaf nitrogen from top to bottom of canopy) and includes light inhibition of leaf respiration. LAI is calculated for each canopy level (default number is 10), with a maximum LAI prescribed for each PFT.

3.1.1.3 Photosynthesis

The following description of the equations used to calculate photosynthesis and the scaling up of leaf-level CO_2 fluxes to canopy-level was taken from Clark et al. (2011). The photosynthesis model in JULES is based upon observations at the leaf scale scaled up to the canopy scale. In JULES, potential (without water and ozone stress) leaf-level photosynthesis (A_p) is calculated using the C_3 and C_4 photosynthesis models of Collatz et al. (1991) and Collatz et al. (1992), respectively. This is calculated as the minimum of three limiting rates:

1. Rubisco-limited rate (W_c)

$$W_c = \begin{cases} V_{cmax}\left(\frac{c_i-\Gamma}{c_i+K_c(1+O_a/K_o)}\right) & \text{for } C_3 \text{ plants} \\ V_{cmax} & \text{for } C_4 \text{ plants} \end{cases} \tag{3.1}$$

where V_{cmax} is the maximum rate of carboxylation of Rubisco (mol CO_2 $m^{-2}s^{-1}$), c_i is the internal leaf CO_2 partial pressure (Pa), Γ is the CO_2 compensation point in the absence of mitochondrial respiration, O_a is the atmospheric oxygen partial pressure (Pa) and K_c and K_o are the Michaelis-Menten parameters for CO_2 and O_2, respectively. Rubisco, short for ribulose-1,5-bisphosphate carboxylase/oxygenase, is an enzyme that catalyses the primary chemical reactions that govern carbon fixation in plants (Jensen, 2000). 30% of the total protein found in plants is attributed to Rubisco and it is a major sink for plant nitrogen (Jensen, 2000). Rubisco is considered the main limit-

ing rate of photosynthetic carbon fixation under saturated irradiance and limiting atmospheric CO_2 concentrations (Marcus et al., 2008).

2. Light-limited rate (W_l)

$$W_l = \begin{cases} \alpha(1-\omega)I_{par}\left(\frac{c_i-\Gamma}{c_i+2\Gamma}\right) & \text{for } C_3 \text{ plants} \\ \alpha(1-\omega)I_{par} & \text{for } C_4 \text{ plants} \end{cases} \tag{3.2}$$

where α is the quantum efficiency of photosynthesis ($\mathrm{mol\,CO_2\,mol^{-1}\,PAR}$), ω is the leaf scattering coefficient for PAR and I_{par} is the incident photosynthetically active radiation (PAR in $\mathrm{mol\,m^{-2}s^{-1}}$).

3. Rate of transport of photosynthetic products (C_3 plants) and PEP-Carboxylase limitation (C_4 plants) (W_e)

$$W_e = \begin{cases} 0.5V_{cmax} & \text{for } C_3 \text{ plants} \\ 2\times 10^4 V_{cmax}\frac{c_i}{P_*} & \text{for } C_4 \text{ plants} \end{cases} \tag{3.3}$$

where P_* is the surface air pressure.

V_{cmax}, K_o, K_c and Γ are all temperature dependent. V_{cmax} is calculated at any desired temperature from the maximum rate of carboxylation of the Rubisco enzyme at 25°C (V_{cmax25}):

$$V_{cmax} = \frac{V_{cmax25} f_T(T_c)}{[1+e^{0.3(T_c-T_{upp})}][1+e^{0.3(T_{low}-T_c)}]} \tag{3.4}$$

where T_c is the canopy (leaf) temperature (°C), T_{low} and T_{upp} are the lower and upper temperature limits for photosynthesis (°C), respectively, and f_T is the standard Q_{10} temperature dependence:

$$f_T(T_c) = Q_{10_{leaf}}^{0.1(T_c-25)} \tag{3.5}$$

where $Q_{10_{leaf}}$ has a default value of 2. V_{cmax25} is linearly related to leaf

nitrogen concentration, n_l, by

$$V_{cmax25} = n_e n_l \tag{3.6}$$

where n_e has values of 0.0008 and 0.0004 mol CO_2 m^{-2} s^{-1} kg C (kg N)$^{-1}$ for C_3 and C_4 plants, respectively, and n_l is the leaf N concentration at the top of the canopy.

The gross photosynthesis rate (W) is calculated as the smoothed minimum of the three potentially-limiting rates, W_c, W_l and W_e (Equations 3.1, 3.2 and 3.3, respectively):

$$\beta_1 W_p{}^2 - W_p(W_c+W_l) + W_c W_l = 0 \tag{3.7}$$

$$\beta_2 W^2 - W(W_p+W_e) + W_p W_e = 0 \tag{3.8}$$

where W_p is the smoothed minimum of W_c and W_l, W is the smoothed minimum of W_p and W_e and $\beta_1 = 0.83$ and $\beta_2 = 0.93$ are "co-limitation" coefficents. Since Equations 3.7 and 3.8 are quadratic equations, which take the form $ax^2 + bx + c = 0$, they can be solved using the quadratic formula,

$$x = \frac{-b \pm \sqrt{b^2 - 4ac}}{2a} \tag{3.9}$$

Therefore, since a = β_1, b = -(W_c+W_l) and c = $W_c W_l$, then

$$W_p = \frac{W_c + W_l}{2\beta_1} - \sqrt{\frac{(W_c + W_l)^2}{4\beta_1^2} - \frac{W_c W_l}{\beta_1}} \tag{3.10}$$

To calculate W, let a = β_2, b = -(W_p+W_e) and c = $W_p W_e$. Therefore

$$W = \frac{W_p + W_e}{2\beta_2} - \sqrt{\frac{(W_p + W_e)^2}{4\beta_2^2} - \frac{W_p W_e}{\beta_2}} \tag{3.11}$$

Note that the smaller root of each quadratic is selected. The leaf dark

respiration (R_d) is calculated as follows:

$$R_d = f_{dr} V_{cmax} \tag{3.12}$$

where f_{dr} is the dark respiration coefficient . The net potential (i.e. unstressed) leaf-level photosynthesis (A_p) is calculated as

$$A_p = W - R_d \tag{3.13}$$

where $W = \min(W_c, W_l, W_e)$ and R_d is leaf dark respiration. Leaf photosynthesis is linked to stomatal conductance via the CO_2 diffusion equation using the Jacobs (1994) formulation. By taking soil moisture stress into account, leaf-level photosynthesis (A_l) is calculated by multiplying the potential leaf-level photosynthesis by a soil moisture factor (β):

$$A_l = A_p \beta \tag{3.14}$$

where β is a dimensionless soil moisture stress factor (also known as the beta factor), with values ranging from 0–1 (Cox et al., 1998). The soil moisture stress factor is calculated by

$$\beta = \begin{cases} 0 & \text{for } \theta < \theta_w \\ \dfrac{\theta - \theta_w}{\theta_c - \theta_w} & \text{for } \theta_w < \theta < \theta_c \\ 1 & \text{for } \theta > \theta_c \end{cases} \tag{3.15}$$

where θ is the volumetric soil moisture concentration, θ_w is the volumetric soil moisture concentration at the 'wilting point' (point below which transpiration ceases) and θ_c is the volumetric soil moisture concentration at the 'critical point' (point above which plants are not water limited). Note that the effect of O_3 on leaf photosynthesis can also be included on the right-hand side of Equation 3.14, but it is not shown here.

There are two options available in JULES for radiation interception and the scaling of photosynthesis from leaf-level to canopy-level: (i) big leaf

Option	Leaf to canopy scaling	Radiation	N profile	Inhibition of leaf respiration in light
1	Big leaf	Beer's Law	Beer's Law	no
2	Multi-layer	Two stream	Constant through canopy	no
3	Multi-layer with two classes for photosynthesis (sunlit and shaded)	Two stream	Constant through canopy	no
4	Multi-layer	Two stream	Decreases through canopy	yes
5	Multi-layer including sunlit and shaded leaves in each layer	Two stream with sunfleck penetration	Decreases through canopy	yes

Table 3.1: Available options for the calculation of canopy photosynthesis. Table 3 of Clark et al. (2011).

approach and (ii) multi-layer approach (Table 3.1). In the big leaf approach, irradiance beneath the canopy is expressed as a function of irradiance at the top of the canopy using Beer's Law (Option 1 in Table 3.1). Since leaf-level photosynthesis (A_l; Equation 3.16) is assumed to vary proportionally with the vertical distribution of irradiance, it can also be expressed as a function of top of the canopy leaf photosynthesis

$$A_l = A_o e^{-kL} \tag{3.16}$$

where A_o is top of the canopy leaf photosynthesis, k is the light extinction coefficient and L is leaf area index. Canopy photosynthesis (A_l; Equation 3.17) is then calculated as the integral of the leaf-level photosynthesis over the entire canopy LAI.

$$A_c = \int_0^{L_c} A_l dL = A_o \frac{[1 - e^{-kL_c}]}{k} \tag{3.17}$$

For all model simulations in this dissertation, the multi-layer approach was used. In the multi-layer approach, the amount of radiation absorbed and photosynthesis are estimated for a number of user defined canopy layers ($dL_c = L_c/n$, where L_c is the canopy leaf area and dL_c is the canopy layer leaf area). The two-stream approximation of radiation interception of (Sellers et al., 1992) is used by JULES to calculate surface spectral albedos and the incoming radiation absorbed by each canopy layer (Clark et al., 2011). The absorption and scattering of both direct and diffuse radiation fluxes in each canopy layer is explicitly described by JULES, which means that

the upward and downward diffuse fluxes of scattered direct beam radiation and scattered diffuse radiation for each canopy layer can be calculated. These fluxes are then normalised by the incident direct and diffuse fluxes respectively to compute the direct and diffuse fractions of absorbed incident PAR at each canopy layer (Clark et al., 2011). The two-stream approach provides a vertical profile of radiation interception throughout the canopy which means that photosynthesis and leaf respiration can be calculated for each canopy layer (Clark et al., 2011).

With the multi-layer approach, there are four variations (Options 2-5 in Table 3.1) that consider the vertical profile of canopy photosynthetic capacity, light inhibition of leaf respiration, the inclusion of sunfleck penetration and the division of canopy layers into sunlit and shaded leaves. Option 4 was used for the point scale model simulations in Chapter 4 and the regional and global scale simulations in Chapters 5 and 6. This option includes the decrease in photosynthetic capacity from top to bottom of the canopy and the inhibition of leaf respiration in light.

For all of the multi-layer options, canopy-scale fluxes (A_c) are estimated to be the sum of the leaf-level fluxes in each canopy layer, scaled by leaf area:

$$A_i = A_{li} dL_c \tag{3.18}$$

$$A_c = \sum_{i=1}^{n} A_i \tag{3.19}$$

where A_i is the photosynthesis for each canopy layer.

3.1.2 JULES version 3.4.1

In order to perform model simulations at the global scale using JULES, version 3.4.1 of the model was built and run in parallel mode using the Flexible Configuration Management (FCM) build system, which is a set of open-source tools for managing and building source code (mainly Fortran applications). FCM was developed by the UK Met Office and is freely available for general use. It can be downloaded from the Met Office (http://www.metoffice.gov.uk/research/collaboration/fcm) or from

github (https://github.com/metomi/fcm). From JULES version 3.3 onwards, JULES can run at multiple points in parallel. This is done using Messaging Passing Interface (MPI), which is a specification for the message passing parallel programming model (i.e. data is moved from the address space of one process to that of another through cooperation of processes), and provides a standard which allows for running multiple processes in parallel to communicate with each other when required. Several implementations of MPI are available with the most common being MPICH2 and openMPI. The sharing of results from parallel processes is important for JULES and means that multiple MPI processes can read and write to the same netCDF file using the parallel I/O features of HDF5/netCDF4. This parallel processing means that JULES can use multiple cores on the same machine or a cluster of machines or both and leads to increased speed up of global scale model simulations. Using JULES version 3.4.1, it was found that for a 2 year global model simulation forced with the meteorological dataset WFDEI (Section 3.2.2.2), the increase in model runtime was observed to be the same as the number of processes used up to 24 processes (i.e. using 12 and 24 processes resulted in 12 times and 24 times speedup, respectively) and after 24 processes speedup slowed (Figure 3.1). For global model simulations on the Edinburgh University cluster (Edinburgh Compute and Data Facilities), 24 processes were used.

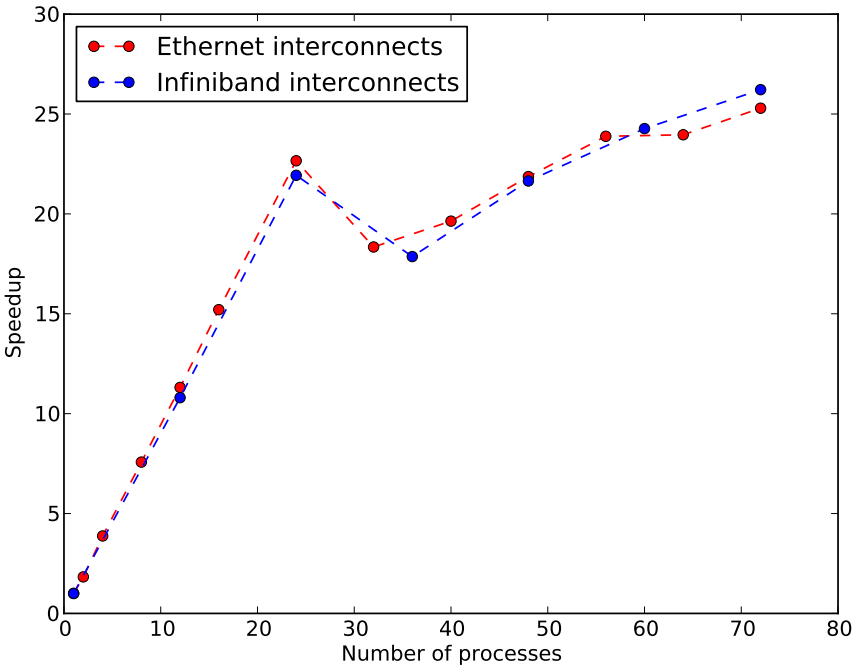

Figure 3.1: Speedup observed when using a different number of processes by JULES version 3.4.1 for 2 year global scale simulations forced with the WFDEI meteorological dataset. The Ethernet and Infiniband interconnects refer to the type of network communication links used in the Edinburgh University cluster (Edinburgh Compute and Data Facilities).

3.1.3 Differences between JULES versions 3.0 and 3.4.1

Differences in the model code between version 3.0 and 3.4.1 are related to the user interface (the monolithic run control file has been replaced by several smaller files containing Fortran namelists which are used to specify input and various options), the implementation of Biogenic Volatile Organic Compound (BVOC) emissions (Pacifico et al., 2011), the introduction of an alternative build system (FCM make; Section 3.1.2), the ability to run JULES in parallel (Section 3.1.2), a more streamlined process for adding new variables for input and/or output and a variety of bug fixes between different intermediate versions. More detailed information on changes to the code between model versions can be found at http://www.jchmr.org/jules/documentation/user_guide/vn3.4/release_notes/contents.html. With the exception of the addition of BVOC emissions to the model code, which may affect carbon cycle simulations at the global scale when implemented in the UM due to interactive BVOC emissions (i.e. with feedbacks), there have been no other changes to the code for the terrestrial carbon cycle between model versions 3.0 and 3.4.1.

3.2 Data

The datasets used in Chapters 4, 5 and 6 to assess the ability of the JULES LSM to reproduce fluxes of GPP at various temporal and spatial scales include the vegetation and soil datasets for the various model simulations (Section 3.2.1), the data (meteorological and satellite) used to drive the model (Section 3.2.2) and the observational datasets used to compare model performance against (Section 3.2.3).

3.2.1 Vegetation and soil data

The land cover classification scheme (specifying PFT fractions) used for model simulations at the point scale using global data (Chapter 4) and simulations at the global scale (Chapters 5 and 6) was the Global Land Cover Characterization database. The soil dataset (specifying soil texture fractions) used for these simulations was the Harmonized World Soil Database.

3.2.1.1 Global Land Cover Characterization database

The Global Land Cover Characterization database version 2.0 (GLCC2.0; http://edc2.usgs.gov/glcc/glcc.php), generated by the US Geological Survey, the University of Nebraska-Lincoln, and the European Commission's Joint Research Centre, is a 1 km resolution global land cover dataset for use in environmental and modelling research and was created as part of the International Geosphere-Biosphere Programme, Data and Information Systems (IGBP-DIS) initiative (Loveland et al., 2000). The dataset is derived from 1 km Advanced Very High Resolution Radiometer (AVHRR) data for a 12-month time period (April 1992-March 1993). The global database of land cover characteristics was developed on a continent-by-continent basis and used 1 km AVHRR 10-day composites, followed by extensive post-processing using additional ancillary data (Loveland et al., 2000). A number of derived datasets, using different classification schemes (Global Ecosystems, IGBP Land Cover Classification, Simple Biosphere Model), are included in the global land cover database (Loveland et al., 2000). For model simulations at the point scale using global data, the International Geosphere-Biosphere Programme (IGBP) scheme is used. The IGBP scheme was a new land cover classification scheme and was created specifically for the purpose of the IGBP programme. In the IGBP land cover classification scheme, land cover is classified into 17 categories (Table A.1). The GLCC2.0 dataset (using the IGBP land classification scheme) was downloaded from the GLCC website (http://edc2.usgs.gov/glcc/tabgeo_globe.php).

3.2.1.2 Harmonized World Soil Database

The Harmonized World Soil Database version 1.2 (HWSD) is a global database of soil resources created by the International Institute for Applied Systems Analysis (IIASA) and Food and Agriculture Organisation of the United Nations (FAO) in association with ISRIC-World Soil Information, the European Soil Bureau Network and the Institute of Soil Science (Chinese Academy of Sciences) (http://webarchive.iiasa.ac.at/Research/LUC/External-World-soil-database/HTML/). It is a 30 arc-second (~1 km) raster database consisting of 21600 rows and 43200 columns with each grid cell in the database linked to soil property data such as soil texture fractions, water storage capacity, soil depth and pH (Nachtergaele et al., 2012). The HWSD

database was downloaded from http://webarchive.iiasa.ac.at/Research/LUC/External-World-soil-database/HTML/HWSD_Data.html?sb=4.

3.2.2 Forcing data

The datasets used to drive JULES include the meteorological datasets at the point scale, FLUXNET (Section 3.2.2.1), and global scale, WFDEI (Section 3.2.2.2) and PRINCETON (Section 3.2.2.3), and the MODerate resolution Imaging Spectroradiometer (MODIS) leaf area index (LAI) satellite dataset (Section 3.2.2.4) used to force the model at the point scale.

3.2.2.1 FLUXNET

FLUXNET, a "network of regional networks", is a global network of micrometeorological tower sites that use eddy covariance methods to measure the exchange of carbon dioxide, water vapour and energy between the biosphere and atmosphere across a range of biomes and timescales (Baldocchi et al., 2001). Data and site information are available at http://www.fluxnet.ornl.gov/. Over 650 tower sites are located worldwide from all continents except Antarctica (Figure 3.2) and are used to study a range of vegetation types such as temperate conifer and broadleaved (deciduous and evergreen) forests, tropical and boreal forests, crops, grasslands, wetlands, and tundra on a long-term and continuous basis (Baldocchi et al., 2001). However, the majority of sites are situated within the Northern Hemisphere extratropics with crop sites underrepresented outside North America and Europe (Williams et al., 2009).

As well as high temporal resolution meteorological data, both at the local and global scales, FLUXNET sites have observations of latent and sensible heat, gross primary productivity, ecosystem respiration and net ecosystem exchange. The FLUXNET database also contains information about tower location, site characteristics, such as soil and plant data, and the availability of data (http://fluxnet.ornl.gov/fluxnetdb). This network therefore provides an important platform for the collection, archival and dissemination of meteorological, ecological and flux data.

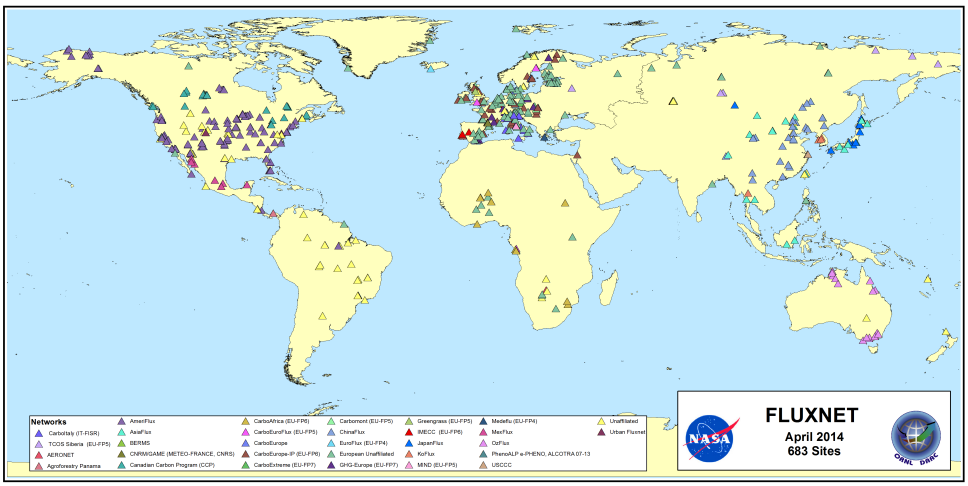

Figure 3.2: Location map showing distribution of flux tower sites within the FLUXNET network. Figure taken from the Oak Ridge National Laboratory Distributed Active Archive Center (ORNL DAAC) FLUXNET Maps & Graphics Web Page (http://fluxnet.ornl.gov/maps-graphics).

3.2.2.2 WFDEI

The WATCH Forcing Data (WFD) (1901-2001) was created in the framework of the EU Water and Global Change (WATCH) project (Harding et al., 2011, http://www.eu-watch.org/), which sought to assess the terrestrial water cycle using LSMs and general hydrological models. WFD was derived using the European Centre for Medium-range Weather Forecasts (ECMWF) ERA-40 reanalysis for 1958–2001 and data for 1901–1957 was obtained using random years extracted from the ERA-40 data (Weedon et al., 2010, 2011). The ERA-40 data was interpolated to $0.5^\circ \times 0.5^\circ$ resolution and monthly bias corrections from gridded observations and sequential elevation corrections were applied to the meteorological data (Weedon et al., 2014). As part of the EMBRACE EU FP7 programme (http://www.embrace-project.eu/), the WFD methodology was applied to the ERA-Interim reanalysis data for the 1979–2010 period to generate the WFDEI meteorological forcing data (Weedon et al., 2014). The WFDEI dataset can be used for forcing global hydrological and LSMs for the late twentieth and early twenty-first centuries (Weedon et al., 2014) and also provides opportunities for comparing relevant hydrological and ecological model outputs from 2001 onwards to data from satellite sensors such as ASCAT (wind speed, soil moisture), GRACE

(ice mass loss), SEVIRI (evapotranspiration), SMOS (soil moisture) and MODIS (LAI, NPP).

WFDEI is only available for land points including Antarctica, and consists of 3 hourly, regularly (latitude-longitude) gridded data at half-degree ($0.5^\circ \times 0.5^\circ$) resolution. This resolution produces a global grid of 360 × 720 grid cells and is equivalent to a surface resolution of about 56 km × 56 km at the equator and 56 km × 32 km at 55 degrees north (temperate regions). The meteorological variables within the dataset include downward shortwave and longwave radiation fluxes ($\mathrm{W\,m^{-2}}$), rainfall rate ($\mathrm{kg\,m^{-2}\,s^{-1}}$), snowfall rate ($\mathrm{kg\,m^{-2}\,s^{-1}}$), 2 m temperature (K), 10 m wind speed ($\mathrm{m\,s^{-1}}$), surface pressure (Pa) and 2 m specific humidity ($\mathrm{kg\,kg^{-1}}$). Within WFDEI, there are two precipitation products, the first corrected using the Climate Research Unit (CRU) at the University of East Anglia (CRU TS3.101/TS3.21) precipitation totals and the second using the Global Precipitation Climatology Centre (GPCC version 5/version 6) precipitation totals (Weedon et al., 2014). The WFDEI datasets incorporating the GPCC- and CRU-corrected precipitation products are referred to as WFDEI-GPCC and WFDEI-CRU, respectively. The GPCC data product is a gridded gauged precipitation dataset and provides a higher resolution dataset (i.e. better station coverage, particularly at high latitudes, and especially for the end of the 20^{th} century) than the CRU precipitation totals (Weedon et al., 2014).

Weedon et al. (2014) compared three hourly WFDEI values to data from Tharandt, Germany (Grünwald and Bernhofer, 2007, temperate) and Manaus, Brazil (Araújo et al., 2002, tropical) for the 2000-2001 time period. The daily surface air temperature, downward shortwave radiation and precipitation rates were in good agreement with the daily average fluxes at Tharandt. However, at the tropical site, Manaus, there is far less agreement between WFDEI and the flux tower values. Iizumi et al. (2014) showed that WFDEI was similar to other near-global daily observational datasets for wind speed, surface air temperature, humidity, downward shortwave radiation and precipitation. Meteorological forcing data are a major source of uncertainty in global-scale land surface modelling as a result of measurement errors in the original input data and interpolation errors due to low spatial and temporal monitoring network density and (temporal) data gapfilling (Müller Schmied et al., 2014). The WFDEI dataset was downloaded from the WATCH ftp site hosted by the International Institute for Applied Systems Analysis

(IIASA), Vienna (ftp://rfdata:forceDATA@ftp.iiasa.ac.at/WFDEI).

3.2.2.3 PRINCETON

The Sheffield et al. (2006) dataset (referred to as PRINCETON) is a global 60 year meteorological dataset for driving land surface models developed by the Terrestrial Hydrology Research Group at Princeton University (http://hydrology.princeton.edu/home.php). PRINCETON is only available for land points (excluding Antarctica), and consists of 3 hourly, 1° resolution, meteorological data for the 1948-2008 period. This dataset has a resolution half that of WFDEI (Section 3.2.2.2) with a global grid of 180 × 360 grid cells and is equivalent to a surface resolution of about 111 km × 111 km at the equator and 111 km × 64 km at 55 degrees north. The meteorological variables within the dataset include downward shortwave and longwave radiation fluxes ($W\,m^{-2}$), precipitation ($kg\,m^{-2}\,s^{-1}$), air temperature (K), 10 m wind speed ($m\,s^{-1}$), surface pressure (Pa) and specific humidity ($kg\,kg^{-1}$).

The dataset was constructed by combining a number of global observation-based datasets of precipitation, surface air temperature and radiation, such as CRU TS2.0 and the Global Precipitation Climatology Project (GPCP) daily precipitation product, with the National Centers for Environmental Prediction-National Center for Atmospheric Research (NCEP-NCAR) reanalysis, which includes near-surface meteorological variables from 1948-present (Sheffield et al., 2006). These global observation-based datasets are used to correct for known biases in the reanalysis precipitation and near-surface meteorology which can have an effect on modelled land surface water and energy budgets (Sheffield et al., 2006). The long time-period of the renanalyses data means that the variability of the land surface can be studied at multidecadel time scales.

Sheffield et al. (2006) evaluated the dataset against the bias-corrected meteorological forcing dataset of the second Global Soil Wetness Project (GSWP2). The GSWP2 forcing dataset has the same temporal (3 hourly) and spatial (1°) resolution as PRINCETON but for a shorter time period (1986–1995) and is derived from a different reanalysis dataset (NCEP–DOE). Monthly mean values of precipitation, surface air temperature and downward radiation fluxes (shortwave and longwave) were compared between the two datasets (Sheffield et al., 2006). It was found that differences in the monthly temperatures and downward shortwave and longwave radiation fluxes were due to differences in the observations used to create them and widespread differences existed in the monthly precipitation mainly due to the observation data used by each dataset being from independent sources. The PRINCETON dataset was downloaded from the Terrestrial Hydrology Research Group webpage hosted by Princeton University (http://hydrology.princeton.edu/data.pgf.php).

3.2.2.4 MODIS Land Product Subsets

The MODIS Land Product Subsets, created by the Oak Ridge National Laboratory Distributed Active Archive Center (ORNL DAAC), provide summaries of selected MODIS Land Products for use in model validation and field site characterisation and include data for more than 1000 field sites and flux towers (http://daac.ornl.gov/MODIS/modis.shtml). MODIS Subsets (Collection 5) are available for a number of MODIS products (Leaf area index, Land Surface Temperature, GPP). Leaf area index (LAI) is a key component of land surface models and is defined as the total one-sided green leaf area per ground surface area (Kala et al., 2014). LAI affects the surface albedo which influences the amount of net radiation available for partitioning into latent and sensible heat fluxes, the transfer of water from within vegetation to the atmosphere and the terrestrial carbon cycle (photosynthesis and net primary productivity of plant canopies) (Kala et al., 2014). The MODIS Leaf area index (LAI) Land Product (ASCII format) contains LAI data for a 7 km × 7 km grid of 49 pixels containing the flux tower or field site (pixel 25; Figure 3.3), with each pixel representing the 1 km × 1 km scale, at 8 day composite intervals. The average of the 3 x 3 gridbox (pixels 17, 18, 19, 24, 25, 26, 31,

32 and 33; red) centred on the flux tower is taken to be that day's LAI value. More information on MODIS LAI can be found in Section 3.2.3.3. The MODIS Land Product Subsets for each flux tower site was downloaded from http://daac.ornl.gov/cgi-bin/MODIS/GR_col5_1/mod_viz.html.

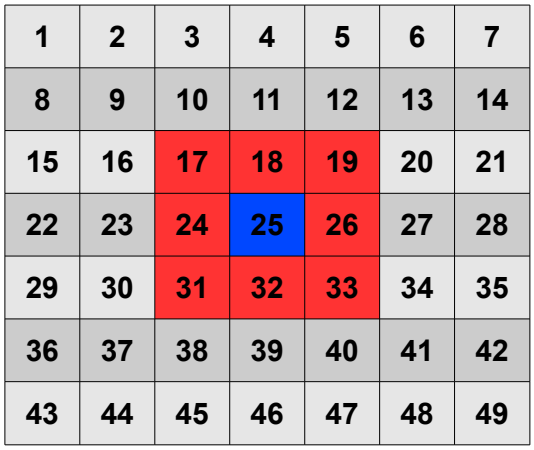

Figure 3.3: The MODIS Land Product Subset contains leaf area index (LAI) data for a 7 km × 7 km grid of 49 pixels centred on the flux tower or field site (pixel 25; blue) with each pixel representing the 1 km × 1 km scale. The average of the 3 x 3 gridbox (pixels 17, 18, 19, 24, 25, 26, 31, 32 and 33; red) centred on the flux tower is taken to be that day's LAI value.

3.2.3 Observations

The observational datasets used to compare model performance against include flux tower observations of GPP from the FLUXNET network (Section 3.2.3.1), global estimates of GPP from the upscaling of observations from the FLUXNET network using a machine learning approach (Section 3.2.3.2) and satellite observations of GPP (Section 3.2.3.4) and LAI (Section 3.2.3.3) from the MODIS instrument. These datasets, used to evaluate model performance, are not pure observations, but are derived from models. The algorithms used to generate the datasets and their limitations are discussed in the following sections.

3.2.3.1 FLUXNET GPP

Local observations of GPP were obtained from the FLUXNET network. Flux tower sites use the eddy covariance method to measure net ecosystem exchange (NEE), which is defined as the net flux of CO_2, and is separated into GPP and terrestrial ecosystem respiration (TER) with a 'flux-partitioning algorithm' (Reichstein et al., 2005). There are a number of approaches used to separate NEE into its two component fluxes, which include extrapolating night-time respiration measurements to the daytime (Reichstein et al., 2005) and fitting light-response curves to daytime NEE measurements (Lasslop et al., 2010). Lasslop et al. (2010) partitioned NEE using a hyperbolic light response curve fit to daytime NEE, which took the temperature sensitivity of respiration and the VPD limitation of photosynthesis into account, and compared it to the method by Reichstein et al. (2005), which extrapolated respiration measurements made at night to the daytime. A strong correlation and no significant biases between the GPP and TER estimates from the two methods were found by Lasslop et al. (2010).

Errors in flux measurements can be both random and systematic with sources of error due to limitations from the measurement technique, the stochastic nature of turbulence and differences in data processing protocols used by individual sites (Moncrieff et al., 1996; Papale et al., 2006; Richardson et al., 2006). In addition to flux-partitioning, the data must also be gap-filled due to unfavourable meteorological conditions and instrument failure (Reichstein et al., 2005). These processes carry with it some uncertainty which must be quantified. Hagen et al. (2006) found that the uncertainty at the half-hourly timescale was of the order of the observations themselves (i.e. ~100%), but only ~10% at annual timescales for a temperate deciduous forest.

3.2.3.2 Upscaled FLUXNET GPP

Global gridded ($0.5^\circ \times 0.5^\circ$ spatial and monthly temporal resolution) estimates of GPP derived from the upscaling of observations from the FLUXNET network of tower sites (Sections 3.2.2.1 and 3.2.3.1) using a model tree ensemble (MTE) approach, a type of machine learning technique that can be trained to predict fluxes (Jung et al., 2009) and provides

a means to evaluate land surface models (LSMs) at large scales (Jung et al., 2009, 2010; Beer et al., 2010; Jung et al., 2011; Bonan et al., 2011). Machine learning algorithms provide a means to construct a model based on data. These models are typically data limited due to the quantity, quality and representativeness of the training data set (Jung et al., 2009). MTEs are an ensemble approach in which the base learning algorithm is perturbed to produce different model trees (tree shape structures that partition the data space into units where a specific regression model is valid) which evolve over time (Jung et al., 2009). The upscaling procedure uses MTEs to predict estimates of carbon fluxes at FLUXNET sites using available quality-filtered flux data and the trained model is then applied spatially using grids of the input data (Jung et al., 2009, 2011). Upscaling usually involves both interpolation (fluxes are predicted at locations where the training data set captures its environmental characteristics) and extrapolation (fluxes are predicted at locations where the training data set does not capture its environmental characteristics).

There are a number of limitations to the upscaled FLUXNET observations. Since the machine learning algorithm is a data-based model, the results of the algorithm can be affected by the availability of data at the site scale and the corresponding global data sets, which are required for predicting carbon fluxes. These include information on land use history, disturbance history, soil moisture, and fertility (Jung et al., 2011). Therefore, all the relevant data required to train the model may not be available. The inputs to the training algorithm include the land cover type for a particular gridcell, the meteorological and climate data and the fraction of absorbed photosynthetic active radiation (fAPAR) (Jung et al., 2009). In addition to there existing uncertainties in the input data, there is also uncertainty in the mismatch between the flux tower and satellites for the fAPAR data (Jung et al., 2009).

Jung et al. (2011) evaluated the ability of the upscaling method to estimate GPP against the Lund-Potsdam-Jena managed Land model (Sitch et al., 2003; Bondeau et al., 2007, LPJmL) for the 1982–2008 time period and found the upscaling method was able to reproduce predicted GPP as well as the model. The use of the LPJmL model to evaluate the upscaled FLUXNET product is also a source of uncertainty since it is assumed that this model is "truth". Two different methods can be used to partition

NEE into GPP and TER (Reichstein et al., 2005; Lasslop et al., 2010). Reichstein et al. (2005) estimated TER by extrapolating nighttime values of TER into the daytime using a temperature response function and Lasslop et al. (2010) estimated GPP using a hyperbolic light response curve fit to daytime NEE modified to account for the temperature sensitivity of respiration and the vapor pressure deficit (VPD) limitation of photosynthesis. There is global monthly upscaled GPP derived from GPP based on the work by Lasslop et al. (2010) and Reichstein et al. (2005) at half-degree ($0.5^\circ \times 0.5^\circ$) resolution for the period 1982-2011. These datasets were downloaded from the Max Planck Institute for Biogeochemistry Data Portal (https://www.bgc-jena.mpg.de/bgi/index.php/Services/Overview).

3.2.3.3 MODIS LAI

The Moderate Resolution Imaging Spectroradiometer (MODIS) is a key instrument aboard the U.S. National Aeronautics and Space Administration (NASA) Earth Observation System (EOS) satellites, Terra and Aqua (Yang et al., 2006). The satellites carrying the instrument, Terra (launched December 1999, observations started February 2000) and Aqua (launched May 2002, observations started July 2002), have orbits which are timed to pass from north to south across the equator in the morning and from south to north over the equator in the afternoon, respectively, and together the satellites are viewing the entire Earth's surface every 1 to 2 days collecting information for environmental research (http://modis.gsfc.nasa.gov). MODIS land products, such LAI and Fraction of Photosynthetically Active Radiation (FPAR), are important inputs to land surface models and can be used to evaluate them.

The MOD15 MODIS LAI/FPAR product, computed from MODIS spectral reflectances, provides continuous and consistent LAI/FPAR coverage for the entire global land surface at 1 km resolution and 8 day frequency (Yang et al., 2006). MODIS products versions are referred to as Collections. Collections 3 and 4 LAI/FPAR products have product accuracy (evaluation against field measurements at selected locations) estimated and the MODIS data of Collection 5 products have been reprocessed using revised algorithms. The MODIS Land Product Subsets described in Section 3.2.2.4 are a Collection 5 product. Gaps and noise in the data, due to the presence of

cloudiness, seasonal snow cover and instrument problems, can limit the usefulness of the product (Lawrence and Chase, 2007; Gao et al., 2008; Yuan et al., 2011). Yang et al. (2006) recommended that MODIS data not be compared with field measurements because of scale-mismatch, geolocation errors and vegetation heterogeneity at the MODIS data resolution. Instead an intermediate step involving the generation of a fine resolution map of the variable of interest, using field data and other high resolution satellite data (10–30 m), is used and the resulting dataset is then aggregated to the resolution of the MODIS data (Tian et al., 2002a,b). Wang et al. (2004) evaluated the MODIS LAI product against field measurements at a needle-leaf forest site in Finland and found that the MODIS LAI values were within 0.5 LAI of the aggregated LAI values. Tan et al. (2005) showed that at a cropland site in France, the MODIS LAI values were within 0.3 LAI of the aggregated values. The global monthly MODIS LAI product at half-degree ($0.5^\circ \times 0.5^\circ$) resolution for the 2000-2011 time period was downloaded from the NASA Earth Observations (NEO) website (http://neo.sci.gsfc.nasa.gov/).

3.2.3.4 MODIS GPP

The MOD17 MODIS Gross/Net Primary Productivity (GPP/NPP) product provides continuous estimates of GPP/NPP for the Earth's entire land surface and is produced as part of the NASA's EOS program. The MOD17 algorithm produces two subproducts, MOD17A2 (which stores 8-day composite GPP, net photosynthesis and QC flags) and MOD17A3 (annual NPP and QC flags) (Zhao et al., 2005). The resulting datasets contain regular gridded global estimates of GPP and NPP for the terrestrial land surface at the 1 km spatial resolution (Running et al., 2000).

The MOD17 algorithm is the first algorithm to provide calculation of global GPP and NPP products from the MODIS sensor (Zhao et al., 2005). The output of the algorithm consists of two subproducts: (i) MOD17A2, which contains 8-day composite GPP, net photosynthesis (PsnNet) and the corresponding quality control flags, and (ii) MOD17A3, which contains annual NPP and corresponding quality control flags. It should be noted that the MOD17A2 subproduct is an 8-day summation of GPP and PsnNet and the annual NPP from the MOD17A3 subproduct is an annual summation (Zhao et al., 2005). The MOD17 algorithm is based on the work of Monteith

(1972); Monteith and Moss (1977), which suggests that the productivity of annual crops under well-watered and fertilised (non-stressed) conditions is linearly related to the amount of absorbed solar energy (i.e. absorbed Photosynthetically Active Radiation (APAR)). In order to convert APAR to productivity estimates, a conversion efficiency parameter, ε, which varies by vegetation type and climate conditions must be used. The MOD17 algorithm also includes differences in maximum ε for various vegetation types and the effects of water-stressed (Water_Stress_Scalar) and cold temperature (Temperature_Scalar) conditions on ε. Using the MOD17 algorithm, 8-day GPP (Equation 3.20) is output as follows

$$\text{GPP} = \varepsilon_{\max} \times \text{Temperature\_Scalar} \times \text{Water\_Stress\_Scalar} \times \text{APAR} \quad (3.20)$$

There are three sources of inputs to the MOD17 algorithm: (i) biome type information for each MODIS pixel derived from MODIS land cover products (MOD12Q1), (ii) daily meteorological data derived from the Data Assimilation Office (DAO) data set and (iii) FPAR and LAI data provided by the MOD15A2 product. Limitations in the MOD17 algorithm are due to uncertainties in the MOD12Q1, DAO and MOD15A2 data sets, and the algorithm itself, and this can influence the output of the algorithm (Zhao et al., 2005).

In the MOD12Q1 data set, a MODIS pixel with misclassified land cover can result in incorrect parameters from the MOD17 Biome Parameter Look-Up Table (BPLUT) and this can introduce error into the MOD17 results (Zhao et al., 2005). The same set of parameters are applied to all croplands, which can introduce uncertainties for crops in some regions. The second input to the MOD17 algorithm, the DAO data set, is an assimilated meteorological data set (it is not observed data) and may contain systematic errors from its data assimilation system (Zhao et al., 2005). Thirdly, there is poor correlation between ground-based and MOD15A2 LAI measurements with a pixel-by-pixel comparison and the MOD15A2 LAI tends to be overestimated under most conditions (Wang et al., 2004). Finally, weaknesses in the algorithm itself can lead to uncertainties in GPP. There is little known about the correct values of some of the parameters in the BPLUT, such as fine root maintenance respiration base and biomass ratio

of fine root to leaf (Zhao et al., 2005).

The current version of the MOD17 MODIS Gross/Net Primary Productivity (GPP/NPP) product is Collection 4 primary production (denoted as C4 MOD17) and sources of error in the product include mismatching spatial resolution between the gridded meteorological data ($1^\circ \times 1.25^\circ$) and MODIS pixels (1 km), contaminated or missing 8-day LAI/FPAR (MOD15A2 MODIS product) due to cloud cover or sensor malfunction and misclassified land cover from the MODIS land cover product (MOD12Q1) which can result in incorrect parameters from the MOD17 Biome Property Look-Up Table (BPLUT) and therefore leads to incorrect GPP estimates (Zhao et al., 2005).

The Numerical Terradynamic Simulation Group (NTSG) (http://www.ntsg.umt.edu/project/mod17) at the University of Montana rectified these problems by spatial interpolation of the coarse resolution meteorological data, temporal infilling of cloud-contaminated MOD15A2 data and modification of BPLUT parameters based on observed GPP from flux tower measurements in order to create an improved MOD17 GPP product (hereafter known as MODIS NTSG) (Zhao et al., 2005). Zhao et al. (2005) evaluated the MODIS NTSG GPP against observations from the FLUXNET network and found a high correlation (r^2=0.7) when comparing MODIS annual GPP with tower-based observations for 37 site-years. Heinsch et al. (2006) found that MODIS and tower-based estimates of annual GPP compared favourably for most biomes with MODIS GPP overestimated by 20%–30%. The global monthly MODIS NTSG (version 55) data set at $0.05^\circ \times 0.05^\circ$ resolution for the 2000-2013 time period was downloaded from the NTSG ftp server (ftp://ftp.ntsg.umt.edu/pub/MODIS/NTSG_Products/)

3.3 Summary

A description of the JULES LSM (Section 3.1), the datasets (vegetation, soil and meteorological) used to drive the model and the observational datasets used to compare model performance against has been provided in this chapter (Section 3.2). Two versions of the JULES model have been used within this project. JULES version 3.0 was used to evaluate the model at the point scale using local, global and satellite data in Chapter 4 and version 3.4.1

was used in Chapters 5 and 6 to evaluate the model at the global scales. Differences between the model versions are small with regards to the carbon cycle with the main difference being the implementation of Biogenic Volatile Organic Compound (BVOC) emissions in the more recent version (version 3.4.1). The soil and vegetation data used for model simulations using global data (at both the local and global scale) were obtained from the HWSD and GLCC datasets, respectively (Section 3.2.1). A number of meteorological datasets and a satellite derived dataset were used to drive the model (Section 3.2.2). These include meteorological data from the FLUXNET network (point scale), WFDEI (point and global scale), and PRINCETON (point and global scale), and the MODIS LAI data (point scale). The datasets used to compare model performance against include estimates of GPP from the FLUXNET network (point scale), the upscaling of observations from the FLUXNET network (global scale), the MODIS instrument (global scale) and MODIS LAI data (global scale) (Section 3.2.3). In the next chapter, JULES is evaluated at the point scale across a range of biomes and climatic conditions using local (site-specific), global and satellite datasets.

Bibliography

A. C. Araújo, A. D. Nobre, B. Kruijt, J. A. Elbers, R. Dallarosa, P. Stefani, C. von Randow, A. O. Manzi, A. D. Culf, J. H. C. Gash, R. Valentini, and P. Kabat. Comparative measurements of carbon dioxide fluxes from two nearby towers in a central Amazonian rainforest: The Manaus LBA site. *Journal of Geophysical Research*, 107:LBA 58–1–LBA 58–20, 2002. doi:10.1029/2001JD000676.

D. Baldocchi, E. Falge, L. H. Gu, R. Olson, and D. Hollinger. FLUXNET: A New Tool to Study the Temporal and Spatial Variability of Ecosystem-Scale Carbon Dioxide, Water Vapor, and Energy Flux Densities. *Bulletin of the American Meteorological Society*, 82:2415–2434, 2001.

C. Beer, M. Reichstein, E. Tomelleri, P. Ciais, M. Jung, N. Carvalhais, C. Rödenbeck, M. A. Arain, D. Baldocchi, G. B. Bonan, A. Bondeau, A. Cescatti, G. Lasslop, A. Lindroth, M. Lomas, S. Luyssaert, H. Margolis, K. W. Oleson, O. Roupsard, E. Veenendaal, N. Viovy, C. Williams, F. I. Woodward, and D. Papale. Terrestrial Gross Carbon Dioxide Uptake: Global Distribution and Covariation with Climate. *Science*, 329: 834–838, 2010. doi:10.1126/science.1184984.

G. B. Bonan, P. J. Lawrence, K. W. Oleson, S. Levis, M. Jung, M. Reichstein, D. M. Lawrence, and S. C. Swenson. Improving canopy processes in the Community Land Model version 4 (CLM4) using global flux fields empirically inferred from FLUXNET data. *Journal of Geophysical Research: Biogeosciences*, 116:G02014, 2011. doi:10.1029/2010JG001593.

A. Bondeau, P. C. Smith, S. Zaehle, S. Schaphoff, W. Lucht, W. Cramer, D. Gerten, H. Lotze-Campen, C. Müller, M. Reichstein, and B. Smith. Modelling the role of agriculture for the 20th century global terrestrial carbon balance. *Global Change Biology*, 13:679–706, 2007. doi:10.1111/j.1365-2486.2006.01305.x.

D. B. Clark, L. M. Mercado, S. Sitch, C. D. Jones, N. Gedney, M. J. Best, M. Pryor, G. G. Rooney, R. L. H. Essery, E. Blyth, O. Boucher, R. J. Harding, C. Huntingford, and P. M. Cox. The Joint UK Land Environment Simulator (JULES), model description–Part 2: Carbon fluxes and vegetation dynamics. *Geoscientific Model Development*, 4:701–722, 2011. doi:10.5194/gmd-4-701-2011.

G. J. Collatz, M. Ribas-Carbo, and J. A. Berry. Coupled photosynthesis-stomatal conductance model for leaves of C_4 plants. *Functional Plant Biology*, 19:519–538, 1992. doi:10.1071/PP9920519.

P. M. Cox. Description of the "TRIFFID" Dynamic Global Vegetation Model. Technical Report 24, Hadley Centre, Met Office, London Road, Bracknell, Berks, RG122SY, UK, 2001.

P. M. Cox, C. Huntingford, and R. J. Harding. A canopy conductance and photosynthesis model for use in a GCM land surface scheme. *Journal of Hydrology*, 212–213:79–94, 1998. doi:10.1016/S0022-1694(98)00203-0.

F. Gao, J. T. Morisette, R. E. Wolfe, G. Ederer, J. Pedelty, E. Masuoka, R. Myneni, B. Tan, and J. Nightingale. An algorithm to produce temporally and spatially continuous MODIS-LAI time series. *Geoscience and Remote Sensing Letters, IEEE*, 5:60–64, 2008. doi:10.1109/LGRS.2007.907971.

T. Grünwald and C. Bernhofer. A decade of carbon, water and energy flux measurements of an old spruce forest at the Anchor Station Tharandt. *Tellus B*, 59:387–396, 2007. doi:10.1111/j.1600-0889.2007.00259.x.

S. C. Hagen, B. H. Braswell, E. Linder, S. Frolking, A. D. Richardson, and D. Y. Hollinger. Statistical uncertainty of eddy flux–based estimates of gross ecosystem carbon exchange at Howland Forest, Maine. *Journal*

of Geophysical Research: Atmospheres (1984–2012), 111:D08S03, 2006. doi:10.1029/2005JD006154.

R. Harding, M. Best, E. Blyth, S. Hagemann, P. Kabat, L. M. Tallaksen, T. Warnaars, D. Wiberg, G. P. Weedon, H. van Lanen, F. Ludwig, and I. Haddeland. WATCH: Current Knowledge of the Terrestrial Global Water Cycle. *Journal of Hydrometeorology*, 12:1149–1156, 2011. doi:10.1175/JHM-D-11-024.1.

F. A. Heinsch, Maosheng Z., S. W. Running, J. S. Kimball, R. R. Nemani, K. J. Davis, P. V. Bolstad, B. D. Cook, A. R. Desai, D. M. Ricciuto, B. E. Law, W. C. Oechel, Hyojung K., Hongyan L., S. C. Wofsy, A. L. Dunn, J. W. Munger, D. D. Baldocchi, Liukang X., D. Y. Hollinger, A. D. Richardson, P. C. Stoy, M. B. S. Siqueira, R. K. Monson, S. P. Burns, and L. B. Flanagan. Evaluation of remote sensing based terrestrial productivity from MODIS using regional tower eddy flux network observations. *Geoscience and Remote Sensing, IEEE Transactions on*, 44:1908–1925, 2006. doi:10.1109/TGRS.2005.853936.

T. Iizumi, M. Okada, and M. Yokozawza. A meteorological forcing data set for global crop modeling: Development, evaluation, and intercomparison. *Journal of Geophysical Research: Atmospheres*, 119:363–384, 2014. doi:10.1002/2013JD020130.

C. M. J. Jacobs. *Direct impact of atmospheric CO_2 enrichment on regional transpiration*. PhD thesis, Wageningen Agricultural University, 1994.

R. G. Jensen. Activation of Rubisco regulates photosynthesis at high temperature and CO_2. *Proceedings of the National Academy of Sciences of the United States of America*, 97:12937–12938, 2000. doi:10.1073/pnas.97.24.12937.

M. Jung, M. Reichstein, and A. Bondeau. Towards global empirical upscaling of FLUXNET eddy covariance observations: validation of a model tree ensemble approach using a biosphere model. *Biogeosciences*, 6:2001–2013, 2009. doi:10.5194/bg-6-2001-2009.

M. Jung, M. Reichstein, P. Ciais, S. I. Seneviratne, J. Sheffield, M. L. Goulden, G. Bonan, A. Cescatti, J. Chen, R. de Jeu, A. J. Dolman,

W. Eugster, D. Gerten, D. Gianelle, N. Gobron, J. Heinke, J. Kimball, B. E. Law, L. Montagnani, Q. Mu, B. Mueller, K. Oleson, D. Papale, A. D. Richardson, O. Roupsard, S. Running, E. Tomelleri, N. Viovy, U. Weber, C. Williams, E. Wood, S. Zaehle, and K. Zhang. Recent decline in the global land evapotranspiration trend due to limited moisture supply. *Nature*, 467:951–954, 2010. doi:10.1038/nature09396.

M. Jung, M. Reichstein, H. A. Margolis, A. Cescatti, A. D. Richardson, M. A. Arain, A. Arneth, C. Bernhofer, D. Bonal, J. Chen, D. Gianelle, N. Gobron, G. Kiely, W. Kutsch, G. Lasslop, B. E. Law, A. Lindroth, L. Merbold, L. Montagnani, E. J. Moors, D. Papale, M. Sottocornola, F. Vaccari, and C. Williams. Global patterns of land-atmosphere fluxes of carbon dioxide, latent heat, and sensible heat derived from eddy covariance, satellite, and meteorological observations. *Journal of Geophysical Research*, 116:G00J07, 2011. doi:10.1029/2010JG001566.

J. Kala, M. Decker, J.-F. Exbrayat, A. J. Pitman, C. Carouge, J. P. Evans, G. Abramowitz, and D. Mocko. Influence of Leaf Area Index Prescriptions on Simulations of Heat, Moisture, and Carbon Fluxes. *Journal of Hydrometeorology*, 15:489–503, 2014. doi:10.1175/JHM-D-13-063.1.

G. Lasslop, M. Reichstein, D. Papale, A. D. Richardson, A. Arneth, A. Barr, P. Stoy, and G. Wohlfahrt. Separation of net ecosystem exchange into assimilation and respiration using a light response curve approach: critical issues and global evaluation. *Global Change Biology*, 16:187–208, 2010. doi:10.1111/j.1365-2486.2009.02041.x.

P. J. Lawrence and T. N. Chase. Representing a new MODIS consistent land surface in the Community Land Model (CLM 3.0). *Journal of Geophysical Research: Biogeosciences (2005–2012)*, 112:G01023, 2007. doi:10.1029/2006JG000168.

T. R. Loveland, B. C. Reed, J. F. Brown, D. O. Ohlen, Z. Zhu, L. Yang, and J. W. Merchant. Development of a global land cover characteristics database and IGBP DISCover from 1 km AVHRR data. *International Journal of Remote Sensing*, 21:1303–1330, 2000. doi:10.1080/014311600210191.

Y. Marcus, H. Altman-Gueta, A. Snir, Y. Wolff, and M. Gurevitz. *Photosynthesis. Energy from the Sun: 14th International Congress on Photosynthesis*, chapter Does Rubisco Limit the Rate of Photosynthesis?, pages 863–866. Springer Netherlands, 2008. doi:10.1007/978-1-4020-6709-9_191.

J. B. Moncrieff, Y. Malhi, and R. Leuning. The propagation of errors in long-term measurements of land-atmosphere fluxes of carbon and water. *Global Change Biology*, 2:231–240, 1996. doi:10.1111/j.1365-2486.1996.tb00075.x.

J. L. Monteith. Solar radiation and productivity in tropical ecosystems. *Journal of Applied Ecology*, 9:747–766, 1972. doi:10.2307/2401901.

J. L. Monteith and C. J. Moss. Climate and the efficiency of crop production in Britain. *Philosophical Transactions of the Royal Society B: Biological Sciences*, 281:277–294, 1977. doi:10.1098/rstb.1977.0140.

H. Müller Schmied, S. Eisner, D. Franz, M. Wattenbach, F. T. Portmann, M. Flörke, and P. Döll. Sensitivity of simulated global-scale freshwater fluxes and storages to input data, hydrological model structure, human water use and calibration. *Hydrology and Earth System Sciences*, 18: 3511–3538, 2014. doi:10.5194/hess-18-3511-2014.

F. Nachtergaele, H. van Velthuizen, L. Verelst, D. Wiberg, N. Batjes, K. Dijkshoorn, V. van Engelen, G. Fischer, A. Jones, L. Montanarella, M. Petri, S. Prieler, E. Teixeira, and X. Shi. Harmonized World Soil Database v1.2. Technical report, International Institute for Applied Systems Analysis (IIASA), Food and Agriculture Organization of the United Nations (FAO), February 2012.

D. Papale, M. Reichstein, M. Aubinet, E. Canfora, C. Bernhofer, W. Kutsch, B. Longdoz, S. Rambal, R. Valentini, T. Vesala, and D. Yakir. Towards a standardized processing of Net Ecosystem Exchange measured with eddy covariance technique: algorithms and uncertainty estimation. *Biogeosciences*, 3:571–583, 2006. doi:10.5194/bg-3-571-2006.

M. Reichstein, E. Falge, D. Baldocchi, D. Papale, M. Aubinet, P. Berbigier, C. Bernhofer, N. Buchmann, T. Gilmanov, A. Granier, T. Grünwald, K. Havránková, D. Ilvesniemi, H abd Janous, A. Knohl, T. Laurila,

A. Lohila, D. Loustau, G. Matteucci, T. Meyers, F. Miglietta, J.-M. Ourcival, J. Pumpanen, S. Rambal, E. Rotenberg, M. Sanz, J. Tenhunen, G. Seufert, F. Vaccari, T. Vesala, D. Yakir, and R. Valentini. On the separation of net ecosystem exchange into assimilation and ecosystem respiration: review and improved algorithm. *Global Change Biology*, 11: 1424–1439, 2005. doi:10.1111/j.1365-2486.2005.001002.x.

A. D. Richardson, D. Y. Hollinger, G. G. Burba, K. J. Davis, L. B. Flanagan, G. G. Katul, J. W. Munger, D. M. Ricciuto, P. C. Stoy, A. E. Suyker, S. B. Verma, and S. C. Wofsy. A multi-site analysis of random error in tower-based measurements of carbon and energy fluxes. *Agricultural and Forest Meteorology*, 136:1–18, 2006. doi:10.1016/j.agrformet.2006.01.007.

S. W. Running, P. E. Thornton, R. Nemani, and J. M. Glassy. Global terrestrial gross and net primary productivity from the earth observing system. In *Methods in Ecosystem Science*, pages 44–57. Springer, 2000.

J. Sheffield, G. Goteti, and E. F. Wood. Development of a 50-year high-resolution global dataset of meteorological forcings for land surface modeling. *Journal of Climate*, 19:3088–3111, 2006. doi:10.1175/JCLI3790.1.

S. Sitch, B. Smith, I. C. Prentice, A. Arneth, A. Bondeau, W. Cramer, J. O. Kaplan, S. Levis, W. Lucht, M. T. Sykes, and S. Venevsky. Evaluation of ecosystem dynamics, plant geography and terrestrial carbon cycling in the LPJ dynamic global vegetation model. *Global Change Biology*, 9: 161–185, 2003. doi:10.1046/j.1365-2486.2003.00569.x.

B. Tan, J. Hu, P. Zhang, D. Huang, N. Shabanov, M. Weiss, Y. Knyazikhin, and R. B. Myneni. Validation of Moderate Resolution Imaging Spectroradiometer leaf area index product in croplands of Alpilles, France. *Journal of Geophysical Research*, 110, 2005. doi:10.1029/2004JD004860.

Y. Tian, C. E. Woodcock, Y. Wang, J. L. Privette, N. V. Shabanov, L. Zhou, Y. Zhang, W. Buermann, J. Dong, B. Veikkanen, T. Häme, K. Andersson, M. Ozdogan, Y. Knyazikhin, and R. B. Myneni. Multiscale analysis and validation of the MODIS LAI product: I. Uncertainty assessment. *Remote Sensing of Environment*, 83:414–430, 2002a. doi:10.1016/S0034-4257(02)00047-0.

Y. Tian, C. E. Woodcock, Y. Wang, J. L. Privette, N. V. Shabanov, L. Zhou, Y. Zhang, W. Buermann, J. Dong, B. Veikkanen, T. Häme, K. Andersson, M. Ozdogan, Y. Knyazikhin, and R. B. Myneni. Multiscale analysis and validation of the MODIS LAI product: II. Sampling strategy. *Remote Sensing of Environment*, 83:431–441, 2002b. doi:10.1016/S0034-4257(02)00058-5.

Y. Wang, C. E. Woodcock, W. Buermann, P. Stenberg, P. Voipio, H. Smolander, T. Häme, Y. Tian, J. Hu, Y. Knyazikhin, and R. B. Myneni. Evaluation of the MODIS LAI algorithm at a coniferous forest site in Finland. *Remote Sensing of Environment*, 91:114–127, 2004. doi:10.1016/j.rse.2004.02.007.

G. P. Weedon, S. Gomes, P. Viterbo, H. Österle, J. C. Adam, N. Bellouin, O. Boucher, and M. Best. The WATCH Forcing Data 1958–2001: A meteorological forcing dataset for land surface- and hydrological-models. Technical Report 22, WATCH Technical Report, 41 pp [Available at http://www.eu-watch.org.], 2010.

G. P. Weedon, S. Gomes, P. Viterbo, W. J. Shuttleworth, E. Blyth, H. Österle, J. C. Adam, N. Bellouin, O. Boucher, and M. Best. Creation of the WATCH forcing data and its use to assess global and regional reference crop evaporation over land during the twentieth century. *Journal of Hydrometeorology*, 12:823–848, 2011. doi:10.1175/2011JHM1369.1.

G. P. Weedon, G. Balsamo, N. Bellouin, S. Gomes, M. J. Best, and P. Viterbo. The WFDEI meteorological forcing data set: WATCH Forcing Data methodology applied to ERA-Interim reanalysis data. *Water Resources Research*, 50:7505–7514, 2014. doi:10.1002/2014WR015638.

W. Yang, B. Tan, D. Huang, M. Rautiainen, N. V. Shabanov, Y. Wang, J. L. Privette, K. F. Huemmrich, R. Fensholt, I. Sandholt, et al. MODIS leaf area index products: From validation to algorithm improvement. *Geoscience and Remote Sensing, IEEE Transactions on*, 44:1885–1898, 2006. doi:10.1109/TGRS.2006.871215.

H. Yuan, Y. Dai, Z. Xiao, D. Ji, and W. Shangguan. Reprocessing the MODIS Leaf Area Index products for land surface and cli-

mate modelling. *Remote Sensing of Environment*, 115:1171–1187, 2011. doi:10.1016/j.rse.2011.01.001.

M. Zhao, F. A. Heinsch, R. R. Nemani, and S. W. Running. Improvements of the MODIS terrestrial gross and net primary production global data set. *Remote Sensing of Environment*, 95:164–176, 2005. doi:10.1016/j.rse.2004.12.011.

M. Zhao, S. W. Running, and R. R. Nemani. Sensitivity of Moderate Resolution Imaging Spectroradiometer (MODIS) terrestrial primary production to the accuracy of meteorological reanalyses. *Journal of Geophysical Research*, 111:G01002, 2006. doi:10.1029/2004JG000004.

Chapter 4

Multi-site evaluation of JULES using global and local data

Declaration

This chapter is adapted from the following published paper on which I am the first author and Simon Tett and Mat Williams (both School of Geosciences, University of Edinburgh) are co-authors: D. Slevin, S.F.B. Tett and M. Williams, 'Multi-site evaluation of the JULES land surface model using global and local data', Geoscientific Model Development, 8, 295-316, doi:10.5194/gmd-8-295-2015, 2015. I collated the various datasets required for the model simulations, performed the model simulations and data analysis and wrote the manuscript. My supervisors Simon Tett and Mat Williams provided scientific advice and edited the manuscript. The paper's introduction and methods and model sections have been significantly shortened to avoid repetition, and the deleted material moved to Chapters 2 and 3, respectively.

The ability of the JULES land surface model (LSM) to simulate photosynthesis is evaluated at 12 flux tower sites from the FLUXNET network across a range of biomes and climatic conditions using local, global and satellite datasets. Local datasets are those relevant to a particular flux tower site (i.e. are site-specific), global datasets refer to those used by the global operational version of the model and satellite data refers to leaf area index

(LAI) data from NASA's MODerate resolution Imaging Spectroradiometer (MODIS) instrument. Firstly, Gross Primary Productivity (GPP) estimates from driving JULES with data derived from local site measurements were compared to observations from the FLUXNET network. Secondly, GPP estimates from driving JULES with data derived from global parameter and atmospheric reanalysis (on scales of 100 km or so) were compared to FLUXNET observations. JULES was also driven using local parameters and global meteorological data. Thirdly, the global meteorological datasets, WFDEI and PRINCETON, were compared to local data to find that the WFDEI dataset more closely matches the local meteorological measurements (FLUXNET). Finally, the JULES phenology model was tested by comparing results from simulations using the default phenology model to those forced with the remote sensing product MODIS leaf area index (LAI). The layout of the chapter is as follows. A brief introduction and the questions asked are provided in Section 4.1. In Section 4.2, information is provided on JULES version 3.0, the types of model simulations performed, the input data to the model, the observations used to compare model output against and how model performance is quantified. In Sections 4.3 and 4.4, the results from the various model simulations are provided and are followed by a discussion of the results. Finally, the conclusions of the multi-site evaluation are provided in Section 4.5.

4.1 Introduction

The land surface is an important component of the climate system and the location of the terrestrial carbon cycle (Section 2.3). Atmospheric CO_2 concentrations are influenced by the ability of the land surface to act as a carbon source or sink. It has been shown by both models and observations that with increasing anthropogenic CO_2 emissions the land carbon sink's ability to absorb CO_2 will decrease (Friedlingstein et al., 2006; Canadell et al., 2007; Friedlingstein et al., 2014). One of the main conclusions from the Coupled Climate–Carbon Cycle Model Intercomparison Project (C4MIP; Section 2.1) was that the terrestrial carbon cycle is a major source of model uncertainty. LSM evaluation is an important part of model development and can be carried out in a number of ways (section 2.6). These include com-

paring model output to observations, parameter perturbation experiments, multi-model intercomparison projects and benchmarking projects. JULES has been evaluated at the point, regional and global scale (Section 2.7). Blyth et al. (2011) evaluated JULES at 10 FLUXNET sites, representing a range of biomes and climatic conditions, where model parameter values were taken as if the model was embedded in a GCM, in order to assess the model's ability to predict observed water and carbon fluxes. This work is extended by performing model simulations whereby model parameters (Table 4.1) are set to observed local site conditions and compared to those using global and satellite data. Local site conditions are those relevant to a particular flux tower site and were obtained from the research literature, communications with site Primary Investigator and the Ameriflux data archive. Global data refers to model parameters taken from datasets used by the global operational version of JULES and meteorological data from global gridded datasets extracted for each flux tower gridbox. The satellite data refers to LAI data from the MODerate resolution Imaging Spectroradiometer (MODIS) instrument, aboard NASA's Earth Observing System (EOS) satellites, Terra and Aqua (http://modis.gsfc.nasa.gov).

In this study, we use 12 FLUXNET sites that cover a range of ecosystem types; temperate (6), boreal (2), mediterranean (2) and tropical (2) (Figure 4.1, Table 4.2), to investigate differences between using local, global and satellite-derived datasets when performing model simulations with JULES version 3.0 (Clark et al., 2011; Best et al., 2011, Section 3.1.1). In particular, we address the following research questions:

- How well does JULES perform when using the best available local meteorological *and* parameter datasets? Can the model simulate interannual variability?
- How well does JULES perform when using global data?
- Of the global meteorological datasets used in this study which one compares best to FLUXNET data?
- Are improvements in simulated GPP observed when forcing JULES with daily satellite phenology compared to using the default phenology module?

4.2 Methods and model

A brief description of the JULES LSM used to perform the point scale model simulations, a general overview of the model simulations performed, the datasets used as input to the model, the observational data which acts as the baseline case against which model performance is compared, an outline of the experiments performed and how model-observation differences were quantified are provided in this section.

4.2.1 Model description

JULES version 3.0 was used to perform the point scale model simulations described in Section 4.2.2. Two versions of JULES were used in this multi-site evaluation. JULES3.0 is the original and publicly available release code of JULES version 3.0. The source code was downloaded from https://jules.jchmr.org/. In addition, JULES3.0 was modified in order to force it with daily MODIS LAI (JULESmod). The local (standalone) and global operational versions of JULES are quite similar. Since Unified Model (UM) v8.1 (using JULES v3.0), the JULES code for both have been the same with some exceptions, such as the UM/standalone initialisation code. The science code (e.g. photosynthesis, hydrology and soil processes) remains the same between the two. A more detailed description of JULES version 3.0 can be found in Section 3.1.1.

Dataset	Variable name	Units
Model parameters	PFT fractions	Dimensionless
	Annual Maximum LAI	$m^2\,m^{-2}$
	Canopy Height	metres
	V_{cmax} (maximum rate of Rubisco carboxylase activity)	$\mu mol\,CO_2\,m^{-2}\,s^{-1}$
	Rooting depth	metres
	Soil texture fractions[a]	% of sand, silt and clay
Meteorological data	Downward shortwave radiation	$W\,m^{-2}$
	Downward longwave radiation	$W\,m^{-2}$
	Precipitation rate[b]	$kg\,m^{-2}\,s^{-1}$
	Surface air temperature	K
	Wind speed	$m\,s^{-1}$
	Surface air pressure	Pa
	Specific humidity	$kg\,kg^{-1}$

[a] The soil texture fractions (%) are used to compute the soil hydraulic and thermal characteristics.
[b] At some of the flux tower sites, the precipitation variable was separated into a rainfall rate ($kg\,m^{-2}\,s^{-1}$) and snowfall rate ($kg\,m^{-2}\,s^{-1}$).

Table 4.1: Model parameters and meteorological variables which are altered between global and local model simulations.

Figure 4.1: Map showing location of flux tower sites.

Number	Site	Location		Altitude (m)	Biome Type	Year	Climate Zone
		Lat [°N]	Lon [°E]				
1	Harvard Forest	42.54	−72.17	303	DBF	2008	Temperate
2	Tharandt	50.96	13.57	380	ENF	2003	Temperate
3	Bondville	40.01	−88.29	219	CRO	2000	Temperate
4	Fort Peck	48.31	−105.10	634	GRA	2004	Temperate
5	Morgan Monroe	39.32	−86.41	275	DBF	2007	Temperate
6	Tumbarumba	−35.66	148.15	1200	EBF	2008	Temperate
7	Kaamanen	69.14	27.29	155	TUN	2002	Boreal
8	Hyytiala	61.85	24.29	181	ENF	2003	Boreal
9	Santarem KM67	−2.86	−54.96	130	EBF	2003	Tropical
10	Santarem KM83	−3.02	−54.98	130	EBF	2001	Tropical
11	El Saler	39.35	−0.32	10	ENF	2003	Mediterranean
12	Vaira Ranch	38.41	−120.95	129	GRA	2005	Mediterranean

Table 4.2: Flux towers used in this study. The following biome types were used: Deciduous Broadleaf Forest (DBF), Evergreen Needleleaf Forest (ENF), Cropland (CRO), Grassland (GRA), Tundra (TUN), Evergreen Broadleaf Forest (EBF).

4.2.2 Experimental design

Offline single point simulations of GPP were performed at each of the 12 flux tower sites using various global and local datasets (Table 4.3). These study sites (Blyth et al., 2011; Abramowitz et al., 2008, Table 4.4) were chosen to validate model performance in carbon flux simulation since gap-filled meteorological data, local observations of vegetation and soil characteristics and observed GPP fluxes were available. One year model simulations were performed and span a range of years due to limited availability of local gap-filled meteorological data, observations of GPP fluxes and vegetation characteristics (Table 4.2). Prior to performing the model simulations, the soil carbon pools at each site were brought to equilibrium using a 10 year spin-up by cycling 5 year averaged meteorological data (in equilibrium mode), followed by a 1000 year spin-up by cycling observed meteorological data (in dynamical mode). At Tumbarumba, Santarem Km67 and Santarem Km83, 3 year averaged meteorological data was used in the first part of the spin-up process due to limited data availability. More information on model spin-up can be found in Clark et al. (2011).

4.2.3 Data

JULES requires meteorological data at 6 hourly intervals or less in order to drive the model offline. In this study, half-hourly/hourly meteorological data was used for model

	Model simulations[a]	Parameter sets	Meteorological forcing	LAI[b]	Phenology[c]
local vs. global data	local-F	local	FLUXNET	local	Default
	local-WEIG	local	WFDEI-GPCC	local	Default
	global-WEIG	global	WFDEI-GPCC	global	Default
	global-WEIC	global	WFDEI-CRU	global	Default
	global-P	global	PRINCETON	global	Default
Satellite phenology	local-FNM	local	FLUXNET	Site max. MODIS LAI	Default
	local-FM	local	FLUXNET	Site max. MODIS LAI	Daily forcing

[a] For model simulation names, local and global refer to the parameter set and F, WEIG, WEIC and P refer to the meteorological forcing dataset used.
[b] For LAI, local refers to the observed annual maximum LAI at each site and global refers to that obtained from the look-up tables used by the global operational version of the model.
[c] Default refers to the default phenology model used by JULES and daily forcing means that the default phenology has been switched off and the model forced with daily MODIS LAI.

Table 4.3: Types of model simulations performed in this study.

runs using local data and 3 hourly data for simulations using global data. For offline simulations, the model requires downward shortwave and longwave radiation ($W\,m^{-2}$), rainfall and snowfall rate ($kg\,m^{-2}\,s^{-1}$), air temperature (K), wind speed ($m\,s^{-1}$), surface pressure (Pa) and specific humidity ($kg\,kg^{-1}$) (Table 4.1). Gap-filled meteorological forcing data at the local scale was obtained from the FLUXNET network and data at the global scale was obtained from two gridded datasets; WFDEI (Weedon et al., 2014, 2011) and that developed by Sheffield et al. (2006) (referred to as PRINCETON). Vegetation and soil parameters (Table 4.1) were adjusted to local or global values depending on the model simulations (Table 4.3) performed at the 12 flux tower sites. Local vegetation (Table 4.4, Table 4.5) and soil parameters (Appendix B) were obtained from the research literature, communications with site Primary Investigator and the Ameriflux data archive. Global vegetation (Table 4.4, Table 4.5) and soil parameters (Appendix B) were taken from datasets used in the global operational version of JULES as used in the Hadley Centre Global Environmental Model (HadGEM) climate model. These datasets include the Global Land Cover Characterization database version 2 (GLCC2.0; http://edc2.usgs.gov/glcc/glcc.php) (PFT fractions), and the Harmonized World Soil Database version 1.2 (Nachtergaele et al., 2012) (soil texture fractions).

There are several global LAI datasets available, such as ECOCLIMAP (1992) (Masson et al., 2003), CYCLOPES (1997-2007) (Baret et al., 2007), GLOBCARBON (1998-2003) (Deng et al., 2006), MOD15 (2000-present) (Yang et al., 2006) and MISR LAI (2000-present) (Diner et al., 2008; Hu et al., 2007). For the majority of sites used in

this study, gap-filled meteorological data and GPP flux observations are only available for the 2000s and therefore, a global dataset of satellite LAI was required that covered this period. The MODIS LAI product was used because it is a high spatial and temporal resolution dataset with global coverage.

4.2.3.1 Forcing data

The local meteorological data used to drive the model at the 12 flux tower sites was derived from FLUXNET, a global network of micrometeorological tower sites (Section 3.2.2.1, Table 4.1). Global meteorological data for each of the 12 FLUXNET sites was extracted from two global gridded meteorological datasets; WFDEI (Section 3.2.2.2) and PRINCETON (Section 3.2.2.3).

4.2.3.2 Observational data

The observational data which acts as the baseline case against which model performance is compared was derived from flux tower estimates of GPP from the FLUXNET network (Section 3.2.3.1).

4.2.3.3 Ecological and soil data

Vegetation and soil datasets are also required as input to the model. These include the land cover classification scheme which specifies the fraction of each grid box covered by each PFT and soil texture fraction (% of sand, silt and clay) data. Information on local observations of PFT fractions and soil texture data can be found in Section 4.2.3. The land cover category for each of the flux tower sites (as used in the global operational version of JULES) was extracted from the Global Land Cover Characteristics database version 2.0 (Section 3.2.1.1). These IGBP codes were then used to derive the annual maximum LAI and canopy height for each PFT from the look-up tables used in the global operational version of JULES. Further information on how these variables are derived can be found in Appendix A. The global soil texture fractions (% of sand, silt and clay) for each of the 12 FLUXNET sites (Table B.1) were extracted from the Harmonized World Soil Database version 1.2 (HWSD) (Section 3.2.1.2). The equations used to compute soil hydraulic and thermal characteristics were taken from the Unified Model Documentation Paper No 70 (Jones, 2007). Note that the equations in Jones (2007) apply only to mineral soils, as organic soils behave differently (Gornall et al., 2007). In this multi-site evaluation, the soils are classified as mineral at all 12 sites.

Since the HWSD dataset contains soil textures for two soil depths (0-30 and 30-100 cm) and JULES contains four soil layers (thicknesses of 0.1, 0.25, 0.65 and 2.0), the 0-30 cm soil textures were assigned to the top two model soil layers (thicknesses 0.1 and 0.25 m, respectively), and the 30-100 cm textures were assigned to the bottom two layers (thicknesses 0.65 and 2.0 m, respectively). The local soil textures are provided as site averages and therefore, each model soil layer (4 in total) is assigned the same set of soil textures (Table B.1).

4.2.3.4 MODIS LAI products

The MODIS LAI data from the Land Product Subset (Section 3.2.2.4) was used to drive JULES at the point scale. The MODIS LAI Land Product contains LAI data for each flux tower on a 7 km $\times$ 7 km grid of 49 pixels (Figure 3.3). The average of the 3 x 3 gridbox (pixels 17, 18, 19, 24, 25, 26, 31, 32 and 33; red) centred on the flux tower (pixel 25; blue), is taken to be the LAI value for that day. Only pixel values with an even quality control (QC) flag were used for the averaging and this produced a time-series of 8 day observations at each of the sites. Missing data were dealt with by using the previous good value in the time-series. The exception to this was Bondville, where missing data occurred in January 2000, since MODIS only started recording data in February 2000 (this year was used due to limited data availability at the site). To gap-fill the missing data, an 11 year average was computed and the missing data replaced with the average for January 2000. Finally, each time-series of 8 day composite values was linearly interpolated to obtain a daily LAI time-series. The MODIS LAI time-series for the 12 flux tower sites can be found in Appendix C (Figure C.1).

Site	IGBP code	IGBP class	Plant Functional Types BL	NL	C3g	C4g	sh	bs	References
Harvard Forest	4	DB forest	0.60		0.05	0.10	0.05	0.20	
		DB forest	0.95					0.05	Urbanski et al. (2007)
Vaira Ranch	8	Woody savannah	0.50		0.15		0.25	0.10	
		Grassland			0.95			0.05	Ryu et al. (2008)
Morgan Monroe	4	DB forest	0.60		0.05	0.10	0.05	0.20	
		DB forest	0.90					0.10	Schmid et al. (2000)
Hyytiala	1	EN forest		0.70	0.20			0.10	
		EN forest		0.95				0.05	Suni et al. (2003)
Tharandt	5	Mixed forest	0.35	0.35	0.20			0.10	
		EN forest		0.95				0.05	Grünwald and Bernhofer (2007)
Tumbarumba	2	EB forest	0.85			0.10		0.05	
		EN forest		0.90				0.10	Leuning et al. (2005)
El Saler	7	Open shrub			0.05	0.10	0.35	0.50	
		EN forest		0.90				0.10	Stöckli et al. (2008)
Fort Peck	10	Grassland			0.70	0.15	0.05	0.10	
		Grassland			0.90			0.10	Gilmanov et al. (2005)
Kaamanen	1	EN forest		0.70	0.20			0.10	
		Grassland			0.90			0.10	Laurila et al. (2001)
Santarem KM67	2	EB forest	0.85			0.10		0.05	
		EB forest	0.98					0.02	Hutyra et al. (2007)
Santarem KM83	2	EB forest	0.85			0.10		0.05	
		EB forest	0.98					0.02	Goulden et al. (2004)
Bondville	12	Cropland			0.75	0.05		0.20	
		Grassland			0.90			0.10	Meyers and Hollinger (2004)

Table 4.4: Vegetation (PFT) and non-vegetation land cover type (BL: broadleaf tree, NL: needleleaf tree, C3g: C3 grass, C4g: C4 grass, sh: shrubs, bs: bare soil) fractions at the 12 FLUXNET sites. For each site, the first row refers to global data and the second refers to local.

Site	LAI ($m^2\,m^{-2}$)	Canopy height (m)	V_{cmax} ($\mu mol\,CO_2\,m^{-2}\,s^{-1}$)	References
Harvard Forest	5.00 5.00[a] 6.03	19.01 24.00[a] –	32.00 35.20[a] –	[a]Harvard Forest Data Archive/Exchange
Vaira Ranch	4.00 2.74[b] 3.46	1.26 0.67[b] –	48.00 42.25[c] –	[b]Ameriflux Biological Data [c]Beerling and Quick (1995)
Morgan Monroe	5.00 5.23[b] 6.81	19.01 27.00[b] –	32.00 34.80[c] –	
Hyytiala	6.00 3.00[d] 4.56	21.46 14.00[e] –	24.00 60.00[d] –	[d]P. Kolari, personal communication, 2013 [e]Suni et al. (2003)
Tharandt	6.00 7.10[f] 3.82	21.46 26.50[g] –	24.00 62.50[h] –	[f]T. Grünwald, personal communication, 2013 [g]Grünwald and Bernhofer (2007) [h]Kattge et al. (2009)
Tumbarumba	4.00 2.50[i] 6.08	16.38 40.00[j] –	24.00 74.33[k] –	[i]E. van Gorsel, personal communication, 2013 [j]Cleugh et al. (2007) [k]Haverd et al. (2009)
El Saler	4.00 4.00[l] 1.04	16.38 12.00[m] –	24.00 62.5[h] –	[l]Blyth et al. (2010) [m]Obtained from http://www.bgc-jena.mpg.de
Fort Peck	3.00 2.00[l] 1.41	1.04 0.40[n] –	48.00 42.25[s] –	[n]Obtained from http://ameriflux.ornl.gov/
Kaamanen	2.00 0.70[o] 1.33	0.79 1.00[p] –	48.00 42.25[c] –	[o]Laurila et al. (2001) [p]Aurela et al. (1998)
Santarem Km67	9.00 5.25[q] 6.73	28.12 45.00[r] –	32.00 81.00[s] –	[q]Oak Ridge National Laboratory DAAC [r]Hutyra et al. (2007) [s]Domingues et al. (2007)
Santarem Km83	9.00 6.00[t] 6.63	28.12 40.00[u] –	32.00 81.00[v] –	[t]Doughty and Goulden (2008) [u]Bruno et al. (2006) [v]Domingues et al. (2007)
Bondville	5.00 6.74[b] 3.37	1.46 0.90[w] –	48.00 117.35[c] –	[w]Meyers and Hollinger (2004)

Table 4.5: Local and global biophysical parameters (site annual maximum LAI, canopy height and V_{cmax}) at the 12 FLUXNET sites. For each site, the first row refers to global data, the second refers to local and the third refers to satellite. Online data was accessed in April 2013.

4.2.4 Outline of experiments

This section describes the model simulations performed in the study. In the model simulation names, local and global refer to the parameter set and F, WEIG, WEIC and P refer to the meteorological forcing dataset used (Table 4.3). Vegetation competition has been disabled for all model simulations, which means that the PFT fractions for each site are prescribed and do not vary with time. If vegetation competition had been switched on during the spin-up process, this would have introduced error into the model simulations due to unrealistic vegetation fractions.

4.2.4.1 Effect of local data on simulated GPP

Using JULES3.0, model simulations using local parameter and meteorological datasets (local-F; Table 4.3) were compared to observations of GPP from the FLUXNET network. For this set of model simulations, the default phenology model (used to update LAI) and TRIFFID were used. The ability of the model to simulate interannual variability was also examined. Multi-year model simulations were performed for 6 of the sites using local data; one from each of the various climate zones (Harvard Forest, Vaira Ranch, Hyytiala, Santarem Km67), the Southern Hemisphere site (Tumbarumba) and the temperate site, Morgan Monroe. Since meteorological data were available for multiple years at these sites, but not model parameter data, the same parameter datasets used for the single-year runs (Table 4.2) would be used for the multi-year runs at specific sites.

4.2.4.2 Effect of global data on simulated GPP

Using JULES3.0, model simulations using parameter sets from the HadGEM model and global meteorological data (global-WEIG, global-WEIC and global-P; Table 4.3) were compared to observations of GPP from the FLUXNET network. In addition to this, the error introduced into model simulations (using local model parameters) when using global (WFDEI-GPCC) instead of local meteorological data (local-WEIG and local-F in Table 4.3) is quantified. In these model simulations, the default phenology model and TRIFFID were used.

4.2.4.3 Comparison of global to local meteorological data

The WFDEI-GPCC, WFDEI-CRU and PRINCETON datasets are compared to FLUXNET to find out which one more closely captures the local meteorological conditions.

4.2.4.4 Daily satellite phenology

Using JULES3.0 and JULESmod, the ability of the JULES phenology model to simulate the seasonal cycle of GPP is tested by comparing model simulations where JULES uses MODIS LAI data (local-FM and local-FNM; Table 4.3) to those using the default phenology model (local-F; Table 4.3). When using the default phenology module, LAI is computed internally by scaling the annual maximum LAI, which is then used to calculate GPP. When forcing JULES with daily MODIS data (local-FM), the phenology module is switched off and the MODIS LAI is used to compute GPP. For model simulations using MODIS data and the default phenology module (local-FNM), the annual maximum MODIS LAI is set to be the annual maximum LAI. Vegetation competition has been switched off and local parameters are used for both sets of model simulations (local-FM, local-FNM)

4.2.5 Model analyses

To quantify differences between output from the various model simulations and observations, the following metrics were used. Root Mean Squared Error (RMSE; Equation 4.1), which is a measure of the average error of the simulations, bias (Equation 4.2), which is the average difference between model and observations (a measure of under- or overprediction), and the absolute (Equation 4.3) and percentage differences (Equation 4.4).

$$\mathrm{RMSE} = \sqrt{\frac{\sum_{t=1}^{t=n}(x_t - x_{\mathrm{o},t})^2}{n}} \tag{4.1}$$

$$\mathrm{Bias} = \frac{\sum_{t=1}^{t=n} x_t - \sum_{t=1}^{t=n} x_{\mathrm{o},t}}{n} \tag{4.2}$$

x_t and $x_{\mathrm{o},t}$ are model and observed daily GPP fluxes, respectively, which have been smoothed using a 7 day moving average since we are interested in the long-term average and not daily variability. n is the number of paired values (number of days in year). The absolute difference (ΔGPP) between the model and observations is the absolute value of the difference in total annual GPP for each and the percentage difference ($\Delta\%$) is the absolute difference divided by the observed total annual GPP.

$$\Delta\mathrm{GPP} = |\sum GPP_{\mathrm{obs}} - \sum GPP_{\mathrm{model}}| \tag{4.3}$$

$$\Delta\% = \frac{\Delta\mathrm{GPP}}{\sum GPP_{\mathrm{obs}}} \times 100 \tag{4.4}$$

In order to describe JULES' ability to reproduce simulated GPP, a simple, but subjective, ranking system using qualitative terms (*Very well*, *Good* and *Poorly*) was devised based on RMSE and bias (Table 4.6, Figure 4.3a). These ranges were used as interannual variability was about $+/-1\,\mathrm{g\,C\,m^{-2}\,day^{-1}}$ in both RMSE and bias (Section 4.3.1).

Qualitative term	RMSE ($= x$)	Bias ($= y$)
Very well	$0 < x < +2$	$\lvert y\rvert \leq +1$
Good	$0 < x < +3$	$\lvert y\rvert \leq +2$
Poorly	$0 < x + 5$	$\lvert y\rvert \geq +2$

Table 4.6: Definition of qualitative terms used to describe JULES' ability to simulate GPP when compared to observed FLUXNET GPP. Both RMSE and Bias have units of $\mathrm{g\,C\,m^{-2}\,day^{-1}}$. Starting at *Very well*, the term associated with the first condition satisfied is used to describe model performance.

4.3 Results

Results from model simulations using local and global data (model parameters and meteorological), a comparison of global to local meteorological data and an evaluation of the JULES phenology model are presented here.

4.3.1 Effect of local data on simulated GPP

When driven with local meteorological and parameter datasets (local-F; Figure 4.2), JULES has a negative bias with total annual GPP underestimated by 16 % ($3049\,\mathrm{g\,C\,m^{-2}\,year^{-1}}$; Table 4.7) across all sites compared to observations. By using local data, JULES performs *very well* (see Figure 4.3a and Table 4.6 for definition of qualitative terms used to describe model performance) at the temperate forest sites, Harvard Forest, Morgan Monroe, Hyytiala and Tharandt, where RMSEs range from 1.1–$1.4\,\mathrm{g\,C\ m^{-2}\,day^{-1}}$, biases from -0.2 to $+0.3\,\mathrm{g\,C\,m^{-2}\,day^{-1}}$ (Figure 4.3a) and absolute differences from 40–$211\,\mathrm{g\,C\,m^{-2}\,year^{-1}}$ (Table 4.7) and *good* at Vaira Ranch with an RMSE of $2.78\,\mathrm{g\,C\,m^{-2}\,day^{-1}}$, bias of $-0.19\,\mathrm{g\,C\,m^{-2}\,day^{-1}}$ and absolute difference of $71\,\mathrm{g\,C\,m^{-2}\,year^{-1}}$. The model performs *poorly* at Tumbarumba, El Saler, Bondville and the tropical sites, Santarem Km67 and Santarem Km83, with RMSEs ranging from 1.8–$4.1\,\mathrm{g\,C\,m^{-2}\,day^{-1}}$, biases from -3.7 to
$-0.2\,\mathrm{g\,C\,m^{-2}\,day^{-1}}$ and absolute differences from 71–$1340\,\mathrm{g\,C\,m^{-2}\,year^{-1}}$.

At the temperate forest sites, JULES simulates the summer carbon uptake and leaf onset and senescence *very well*. For example, at the needleleaf forests, Hyytiala and Tharandt, the model correctly captures the timing and magnitude of the seasonal cycle of GPP (Figure 4.2). JULES is able to capture the beginning and ending of the growing season, but underestimates the summer carbon uptake at Tumbarumba, a temperate sclerophyll forest (forests dominated by plants that have hard leaves and are adapted to drought) (Figure 4.2). At the tropical sites, Santarem Km67 and Santarem Km83, the seasonal cycle has been modelled *poorly* with the total annual GPP being underestimated by 42 % ($1340\,\mathrm{g\,C\,m^{-2}\,year^{-1}}$) and 21 % ($583\,\mathrm{g\,C\,m^{-2}\,year^{-1}}$), respectively (Table 4.7).

JULES can simulate interannual variability when using local data with average RMSEs across all 6 sites for all years being within $0.7\,\mathrm{g\,C\,m^{-2}\,day^{-1}}$

and average biases within 1.2 g C m^{-2} day^{-1} of model results from the corresponding single-site runs (Figure 4.4). Interannual variability is captured *very well* at the temperate sites (Harvard Forest, Hyytiala and Morgan Monroe) and Vaira Ranch with RMSEs ranging from +1 to +3 g C m^{-2} day^{-1} and biases from +1 to -1 g C m^{-2} day^{-1}. As observed with the single-site model simulations, the model fails to capture interannual variability at Santarem Km67 and Tumbarumba (Figure 4.4).

Overall, JULES performs *very well* with the use of local data (meteorological and parameter datasets) with negative biases observed at the tropical sites and the Southern Hemisphere site, Tumbarumba, with the same trend also observed when the model simulates interannual variability.

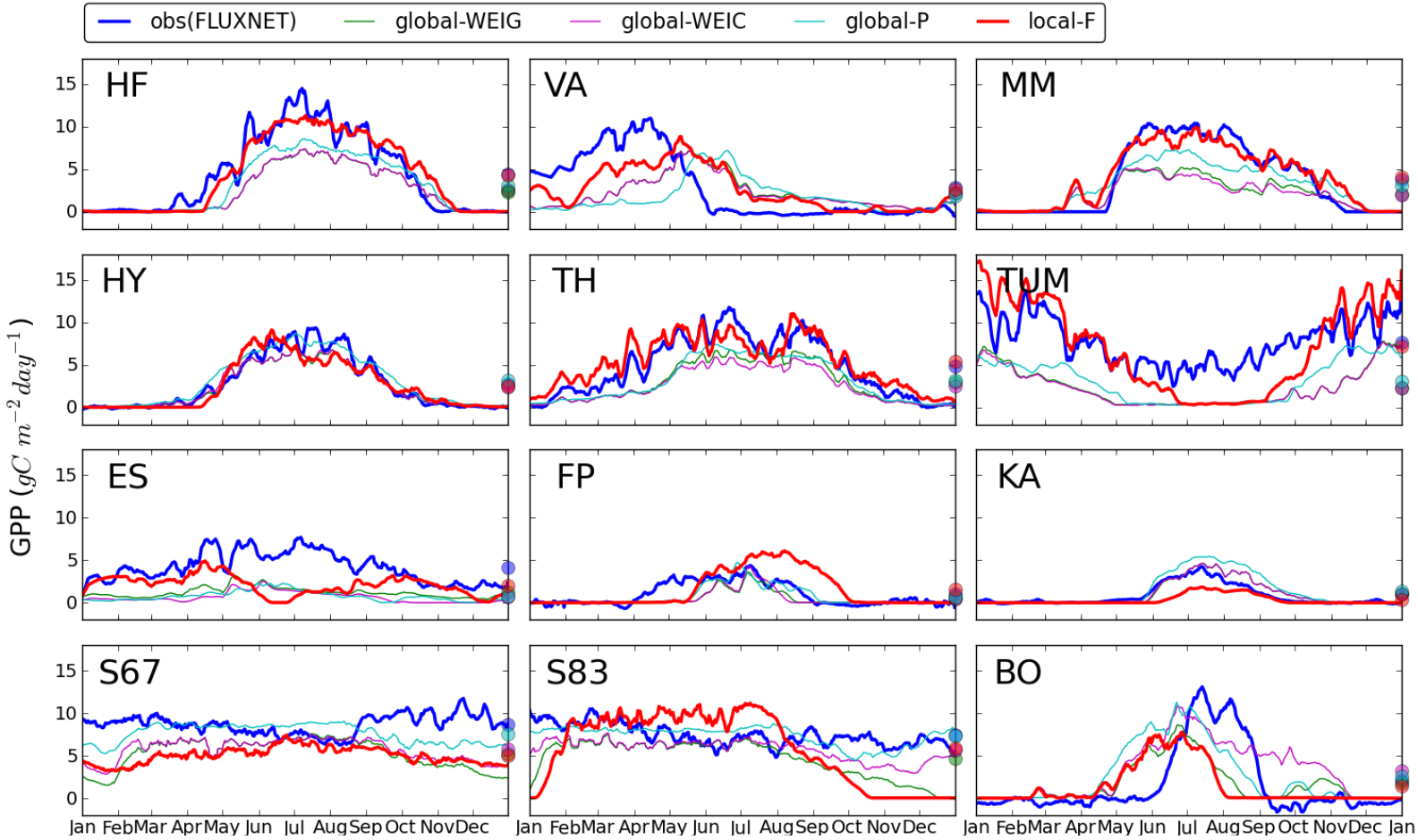

Figure 4.2: Seasonal cycle of model-predicted (local-F, global-WEIG, global-WEIC and global-P in Table 4.3) and observed GPP fluxes, smoothed with a 7 day moving average window, at the 12 FLUXNET sites (HF: Harvard Forest, VA: Vaira Ranch, MM: Morgan Monroe, HY: Hyytiala, TH: Tharandt, TUM: Tumbarumba, ES: El Saler, FP: Fort Peck, KA: Kaamanen, S67: Santarem Km67, S83: Santarem Km83, BO: Bondville). Model simulation years are given in Table 4.2. The thick lines refer to FLUXNET observations (blue) and simulated GPP from local-F model simulations (red). Annual averages for model simulations and observations are plotted as thick dots on right of each plot in the same colours.

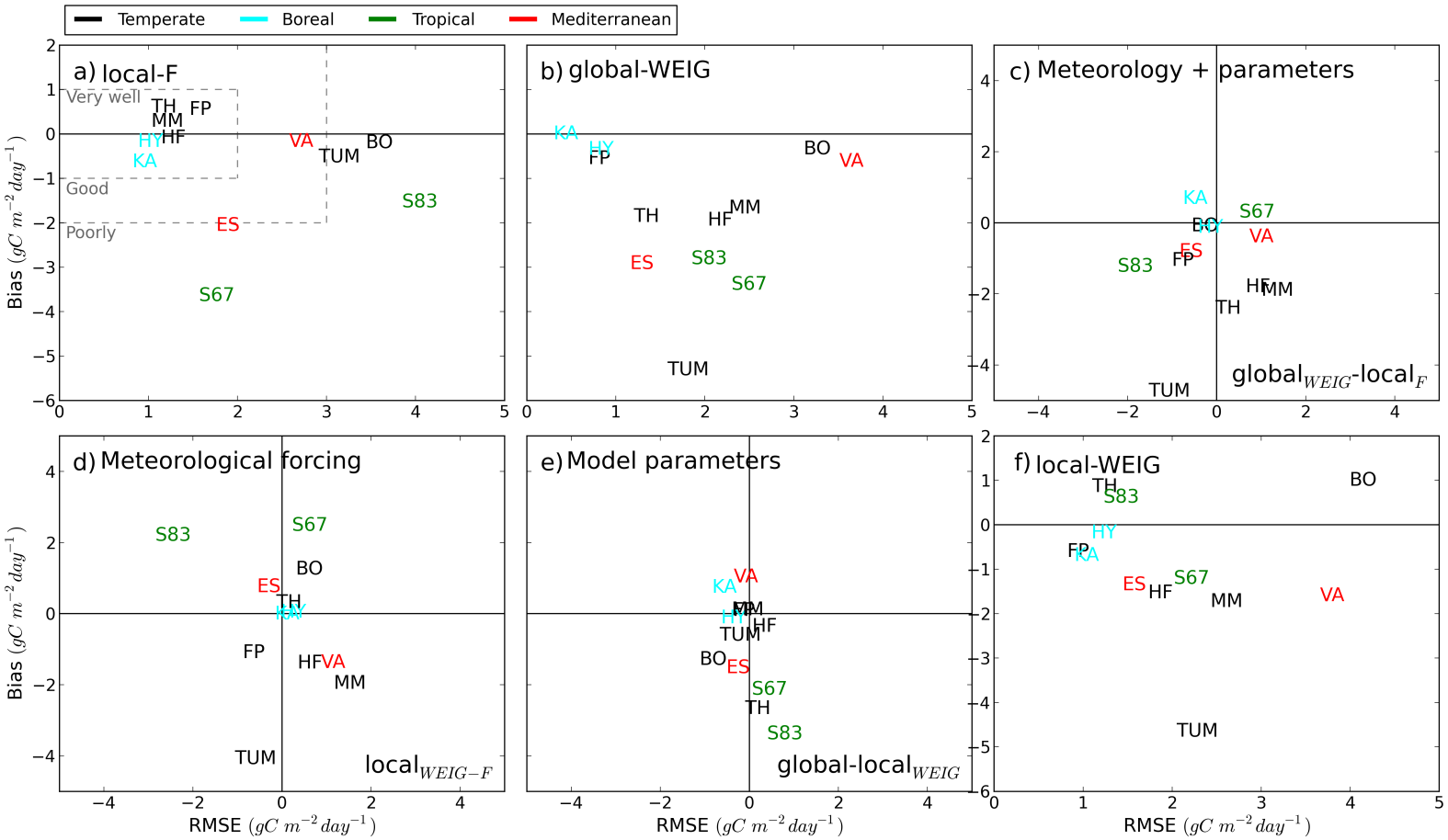

Figure 4.3: Comparison of modelled and observed GPP using bias and RMSE at the 12 FLUXNET sites (HF: Harvard Forest, VA: Vaira Ranch, MM: Morgan Monroe, HY: Hyytiala, TH: Tharandt, TUM: Tumbarumba, ES: El Saler, FP: Fort Peck, KA: Kaamanen, S67: Santarem Km67, S83: Santarem Km83, BO: Bondville) for three sets of model simulations; **(a)** local-F, **(b)**global-WEIG and **(f)** local-WEIG (Table 4.3). **(c)** displays the differences between bias and RMSE for global-WEIG and local-F model simulations, **(d)** differences between local-WEIG and local-F model simulations and **(e)** differences between global-WEIG and local-WEIG model simulations. Marked on **(c)**, **(d)** and **(e)** next to the figure letter are how the sets of model simulations differ. The site labels are coloured according to their climate zone (Table 4.2). The dashed lines on **(a)** show the regions defined by the qualitative terms (Table 4.6) used to describe model performance.

Site	FLUXNET	local-F		local-WEIG		global-WEIG		global-WEIC		global-P	
	$\sum$GPP$_{obs}$	ΔGPP	Δ%	ΔGPP	Δ%	ΔGPP	Δ%	ΔGPP	Δ%	ΔGPP	Δ%
Harvard Forest	1621	40	2	567	35	716	44	711	44	486	30
Vaira Ranch	1047	71	7	592	57	235	22	259	25	369	35
Morgan Monroe	1385	94	7	639	46	616	44	661	48	256	18
Hyytiala	997	68	7	73	7	135	14	120	12	144	14
Tharandt	1754	211	12	306	17	687	39	819	47	590	34
Tumbarumba	2806	197	7	1710	61	1951	70	1984	71	1690	60
El Saler	1512	760	50	499	33	1073	71	1276	84	1234	82
Fort Peck	367	194	53	229	62	213	58	200	54	105	29
Kaamanen	368	249	68	273	74	8	2	5	1	124	34
Santarem Km67	3171	1340	42	451	14	1245	39	1075	34	392	12
Santarem Km83	2724	583	21	202	7	1033	38	644	24	40	1
Bondville	766	240	31	200	26	131	17	406	53	177	23
Total	18,518	3049		4325		8043		7348		4717	

Table 4.7: Absolute and percentage differences between model simulated and observed (FLUXNET) total annual GPP ($gC\,m^{-2}\,year^{-1}$) at the 12 flux tower sites. $\sum$GPP$_{obs}$ is the observed total annual GPP, ΔGPP is the absolute difference (Eq. 4.3) between the model and observed total annual GPP, and Δ% is the percentage difference (Eq. 4.4) between the model and observed total annual GPP. Values highlighted in red mean that the difference is negative (i.e. $\sum GPP_{obs} < \sum GPP_{model}$). The total value for each of the model simulations was computed using the differences and not the absolute differences.

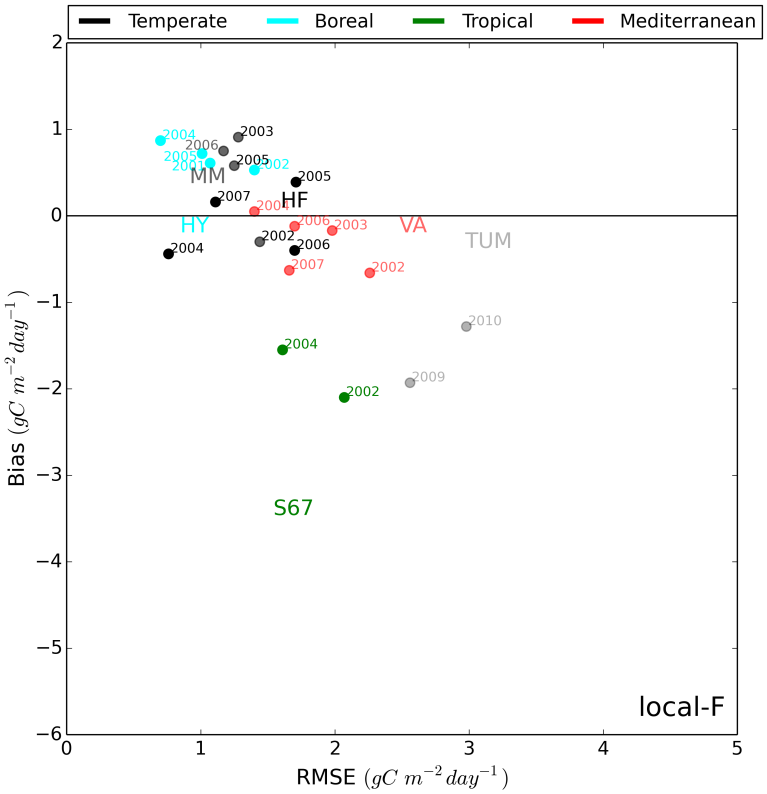

Figure 4.4: Multi-year comparison of modelled and observed GPP using bias and RMSE at 6 FLUXNET sites (HF: Harvard Forest, VA: Vaira Ranch, MM: Morgan Monroe, HY: Hyytiala, TUM: Tumbarumba, S67: Santarem Km67) for model simulations using local parameter and meteorological data (local-F). The site labels are coloured according to their climate zone (Table 4.2) and represent data from model simulations performed for the year specified in Table 4.2, with results from other years plotted using the model simulation year and labels coloured the same as the original site label.

4.3.2 Effect of global data on simulated GPP

By replacing the local data with global parameter and meteorological data, JULES had a much greater negative bias with total annual GPP underestimated by 30 % (6703 g C m^{-2} $year^{-1}$; Table 4.7) on average across all sites compared to observations (global-WEIG, global-WEIC and global-P; Figure 4.2). This is also shown in the annual average GPP which has been plotted for each of the model simulations and observations at the 12 sites (Figure 4.2) and the percentage differences (Table 4.7), which are, in general, larger for simulations using global data than for those using local. This trend occurs at all sites, with the exception of the wetland site, Kaamanen, and Santarem Km83, where modelled total annual GPP (2684 g C m^{-2} $year^{-1}$ and 492 g C m^{-2} $year^{-1}$, respectively) is overestimated (global-P; Table 4.7) compared to model runs using only local data (2141 g C m^{-2} $year^{-1}$ and 119 g C m^{-2} $year^{-1}$, respectively; Table 4.7).

As well as quantifying differences in model simulations using either local or global data, it is useful to know how global meteorological data affects local model runs. Global meteorological data can be used in place of FLUXNET data in order to drive JULES (local-WEIG; Table 4.3). This is important for ecological research sites where there is limited or no local meteorological data available. Using the WFDEI-GPCC meteorological dataset (local-WEIG; Table 4.3) to force the model increases the negative bias of model simulations using only local data (Figure 4.3f), with a 7 % reduction in simulated total annual GPP (15 469 g C m^{-2} $year^{-1}$ for local-F reduced to 14 193 g C m^{-2} $year^{-1}$ for local-WEIG; Table 4.7).

Forcing the model with WFDEI-GPCC (local-WEIG) results in decreases in model performance (increases in bias and RMSE) at the majority of sites. The tropical sites, Santarem Km67 and Santarem Km83, are two exceptions and show a noticeable improvement in modelled yearly GPP (66 % and 61 % reduction of bias, respectively) and changes to modelled seasonal cycle (25 % increase and 65 % reduction of RMSE, respectively). However, at some sites, such as Tharandt, Kaamanen and Hyytiala, forcing JULES with global meteorological data has not introduced large negative biases into GPP predictions (Table 4.7), with RMSEs ranging from 1.1–1.3 g C m^{-2} $year^{-1}$ (Figure 4.3f).

In general, it was found that the meteorological data had a greater im-

pact on modelled GPP fluxes than model parameters. Larger differences exist between local-WEIG and local-F ($\text{local}_{\text{WEIG}-\text{F}}$; Figure 4.3d), which differ only in the atmospheric forcings dataset used, compared to between global-WEIG and local-WEIG ($\text{global} - \text{local}_{\text{WEIG}}$; Figure 4.3e), which differ only in the model parameter sets used.

The ability of JULES to capture yearly GPP (bias) and the seasonal cycle (RMSE) is affected at the majority of sites when using global meteorological data (Figure 4.3d), with improvements observed at Santarem Km67 and Santarem Km83. However, model parameters were found to affect bias at all 12 sites (Figure 4.3e) with the tropical sites being the most influenced. With the exception of Tumbarumba, biases associated with meteorological data compensate for those associated with model parameters at the tropical sites ($\text{global}_{\text{WEIG}} - \text{local}_{\text{F}}$; Figure 4.3c).

Overall, it was found that with the use of global data (model parameter and meteorological data), model performance decreased from *very well* to *good* or *poorly* at most sites, with the exception of the tropical sites. Driving JULES with global meteorological data introduces biases into single site simulations. At the majority of sites, these biases are negative, but at tropical sites, the global meteorological data improves model performance. The meteorological data had a greater impact on GPP fluxes than model parameters.

4.3.3 Global versus local meteorological data

As well as quantifying the error introduced into model simulations by using global meteorological data instead of local, the global meteorological data were compared to local. Only the downward shortwave and longwave radiation fluxes, precipitation and surface air temperature variables have been compared to FLUXNET values, since these variables play the most influential role of the meteorological forcings in canopy photosynthesis and light propagation in JULES (Alton et al., 2007). In order to compare the meteorological datasets, the data was normalised against the annual mean for each site before computing the RMSE and bias.

Of the two global meteorological datasets used in this study, the WFDEI dataset compares best to FLUXNET (lower RMSEs and biases than PRINCETON) at the majority of sites (Figure 4.5). Surface air tem-

peratures compare best to local meteorological measurements with average RMSEs of 0.4 % and 0.7 % (7 day filtered RMSE expressed as percentages of the annual mean value) (1.5 K and 2.4 K) across all sites for the WFDEI and PRINCETON datasets, respectively (Figure 4.5d), followed by the downward shortwave radiation fluxes with average RMSEs of 13 % and 17 % (27.0 $W m^{-2}$ and 33.2 $W m^{-2}$) for WFDEI and PRINCETON, respectively (Figure 4.5a), and downward longwave radiation fluxes with average RMSEs of 4 % and 5 % (18.9 $W m^{-2}$ and 25.0 $W m^{-2}$) for WFDEI and PRINCETON, respectively (Figure 4.5b). Precipitation data from global datasets differ most from local values with RMSEs of 112–178 % (2.7–4.4 $mm day^{-1}$) for WFDEI-GPCC, WFDEI-CRU and PRINCETON, respectively, which may be due to how the precipitation products of each global dataset are corrected (Sheffield et al., 2006; Weedon et al., 2011, 2014).

In addition to comparing the global meteorological variables to their local values, the two precipitation products, WFDEI-GPCC (GPCC-corrected) and WFDEI-CRU (CRU-corrected), within the WFDEI dataset were examined. It was found that WFDEI-GPCC and WFDEI-CRU compare equally well at the 12 FLUXNET sites (Figure 4.5c) with average RMSEs of 2.7 and 2.8 $mm day^{-1}$, respectively. Differences between GPCC- and CRU-corrected precipitation RMSEs are small (0.0–1.4 $g C m^{-2} day^{-1}$) at individual flux tower sites. When forcing JULES with WFDEI, there is little difference when either WFDEI-GPCC or WFDEI-CRU is used as the precipitation product, with average RMSEs of 2.9 and 2.8 $g C m^{-2} day^{-1}$, respectively, across all sites, although differences in the datasets may be more important when JULES is run globally.

Even though WFDEI compares better to the local meteorological data than PRINCETON, it was found that when JULES is forced with the PRINCETON dataset, improvements in GPP predictions were observed at Santarem Km67 and Santarem Km83 (Figure 4.2). It was observed that at the tropical sites, the meteorological forcings were the primary driver of productivity for model simulations using global data and that biases associated with the global meteorological data compensated for incorrect parameter values.

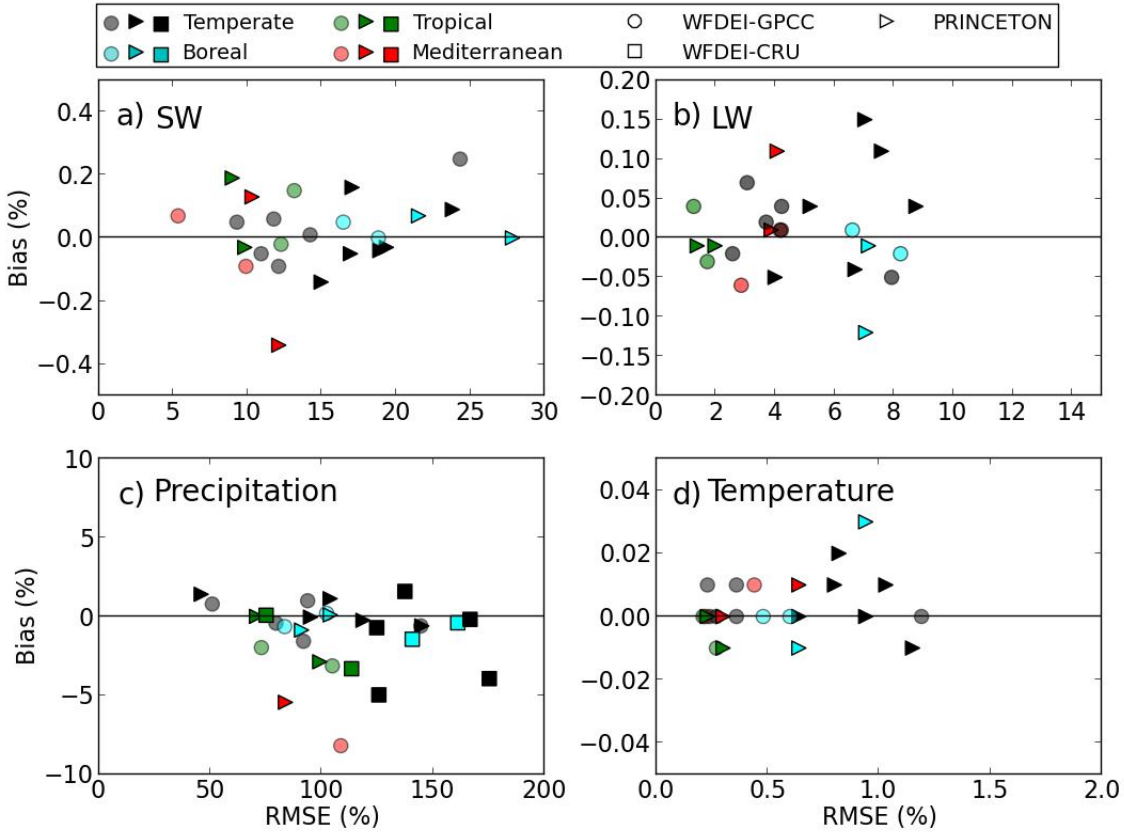

Figure 4.5: Bias and RMSE, expressed as percentages of daily average, when comparing global (WFDEI-GPCC (circles), WFDEI-CRU (squares) and PRINCETON (triangles)) to local meteorological data for four meteorological variables; **(a)** downward shortwave radiation (SW), **(b)** downward longwave radiation (LW), **(c)** precipitation and **(d)** surface air temperature, at the 12 FLUXNET sites (HF: Harvard Forest, VA: Vaira Ranch, MM: Morgan Monroe, HY: Hyytiala, TH: Tharandt, TUM: Tumbarumba, ES: El Saler, FP: Fort Peck, KA: Kaamanen, S67: Santarem Km67, S83: Santarem Km83, BO: Bondville). The site labels are coloured according to their climate zone (Table 4.2). Note that before computing bias and RMSE, the meteorological data was normalised against the annual mean for each site.

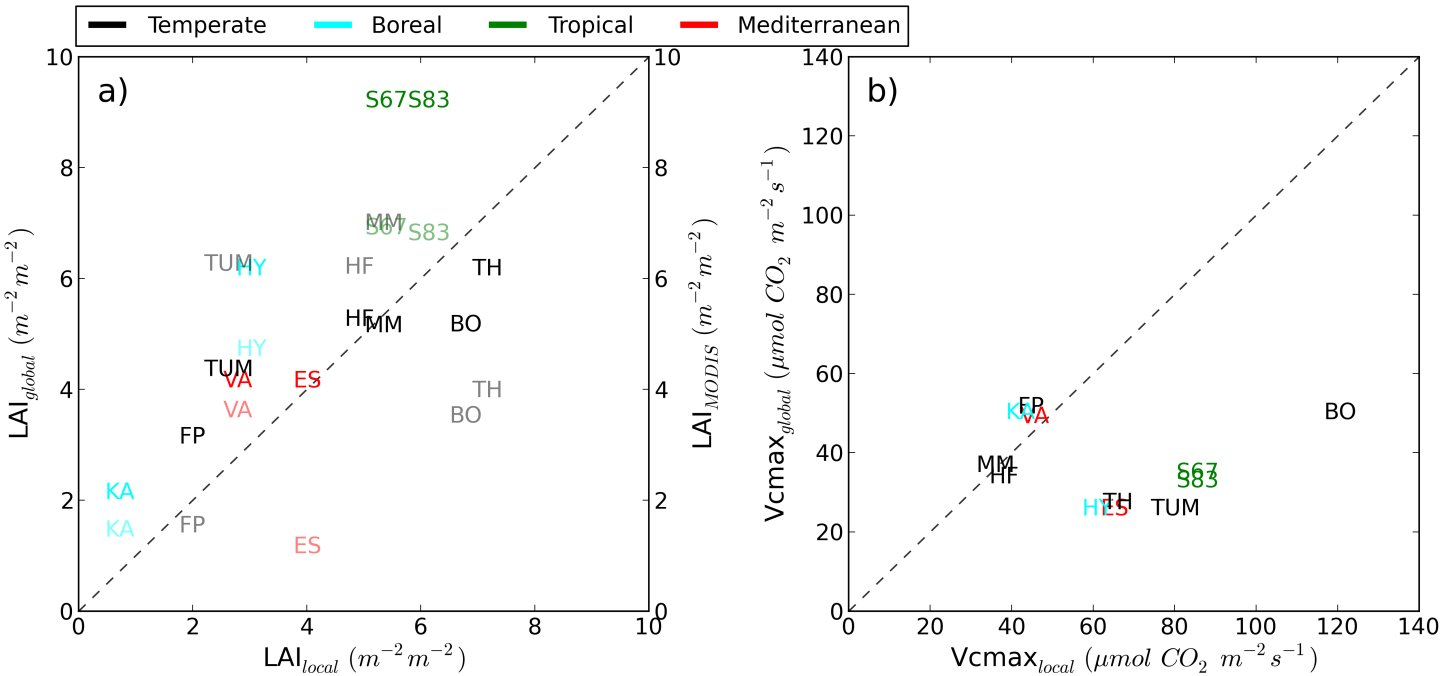

Figure 4.6: Comparison of **(a)** global, MODIS (site annual maximum) and local Leaf Area Index (LAI) and **(b)** global and local maximum rate of Rubisco carboxylase activity (V_{cmax}) at the 12 FLUXNET sites (HF: Harvard Forest, VA: Vaira Ranch, MM: Morgan Monroe, HY: Hyytiala, TH: Tharandt, TUM: Tumbarumba, ES: El Saler, FP: Fort Peck, KA: Kaamanen, S67: Santarem Km67, S83: Santarem Km83, BO: Bondville). The LAI data displayed for each study site refer to the annual maximum LAI of the dominant PFT. The site labels are coloured according to their climate zone (Table 4.2) and in **(a)**, the lighter shades are the MODIS data. The dashed grey lines represent LAI and V_{cmax}, where global, MODIS and local values match, with overestimated global and MODIS values above the dashed line and underestimated values below it.

By swapping local meteorological data with global meteorological data (PRINCETON) for model simulations using local data (local-F), it was found that the positive bias associated with global surface air temperature (PRINCETON) at Santarem Km83 is the primary cause of improved model performance (39 % reduction in RMSE) when using global data and by forcing JULES with the PRINCETON dataset and using the lower global V_{cmax} value (Table 4.5), the model was able to reproduce the seasonal cycle very well (RMSE of $1.26\,\mathrm{g\,C\,m^{-2}\,day^{-1}}$). At Santarem Km67, the downward longwave radiation was the main reason for the improved seasonal cycle (35 % reduction in RMSE) and by using the PRINCETON dataset and global V_{cmax} value (Table 4.5), model performance was improved (RMSE of $2.12\,\mathrm{g\,C\,m^{-2}\,day^{-1}}$).

Compensation between meteorological data and model parameters also occurs at Hyytiala, where the model performs *very well* with global meteorological and parameter datasets (Figure 4.2). The global downward shortwave radiation is larger than its locally measured value and this offsets the low global V_{cmax} value at this site (Table 4.5, Figure 4.6b).

Overall, the WFDEI dataset compares better than PRINCETON to FLUXNET and of the four meteorological variables examined, the radiation fluxes (downward shortwave and longwave) and surface air temperatures compare *very well* to local values. Within the WFDEI dataset, the two precipitation products (WFDEI-GPCC and WFDEI-CRU) compare equally well to FLUXNET precipitation. Improvements were observed at the tropical sites when JULES is forced with PRINCETON and this is due to biases associated with the meteorological data.

4.3.4 Forcing JULES with daily satellite phenology

The performance of LSMs depend on how well the seasonal variation of LAI is represented since GPP is strongly influenced by the timing of budburst and leaf senescence (Liu et al., 2008). In JULES, LAI is essential for the calculation of plant canopy photosynthesis and is updated daily in response to temperature. The JULES phenology model was evaluated by comparing model predictions of GPP when JULES uses its default phenology model with those in which JULES uses local data with the annual maximum LAI set to be the MODIS annual maximum LAI (local-FNM) and with those

in which the model uses local data and is forced with daily MODIS LAI (local-FM).

Forcing JULES with daily satellite LAI (local-FM) results in either small improvements (average reduction in RMSE by $0.2\,\mathrm{g\,C\,m^{-2}\,day^{-1}}$) or none at all at the 12 flux tower sites (Figure 4.7c). An average RMSE of $2.2\,\mathrm{g\,C\,m^{-2}\,day^{-1}}$ across all sites is observed when the model is forced with daily MODIS LAI (local-FM), which is less than that for model simulations using no MODIS information (local-F; average RMSE of $2.4\,\mathrm{g\,C\,m^{-2}\,day^{-1}}$) and those which use the annual maximum MODIS LAI as the annual maximum LAI at each site (local-FNM; average RMSE of $2.39\,\mathrm{g\,C\,m^{-2}\,day^{-1}}$).

By using MODIS data, there is only a small reduction (8 % and 0.04 % for local-FM and local-FNM, respectively) in average RMSE when simulating GPP compared to model runs which do not use it. Of the 12 sites, only seven (Harvard Forest, Vaira Ranch, Hyytiala, Tharandt, Tumbarumba, Kaamanen and Santarem Km67) show improved model performance when either being forced with daily MODIS LAI (Figure 4.7c) or using the annual maximum MODIS LAI as the model annual maximum LAI (Figure 4.7b). At these 7 sites, simulated yearly GPP increases in total by 21 %. At the remaining sites, JULES performs better using the default phenology module (Fig. 4.7a).

Of the 7 sites where JULES' performance improved using MODIS data, forcing JULES with daily satellite phenology (local-FM) only resulted in improved model performance at Santarem Km67 (Figure 4.7c) and at the remaining six sites, using the default phenology with the annual maximum MODIS LAI set to be the annual maximum LAI (Figure 4.7b), JULES' performance improved. Even with the addition of MODIS data, the model still performed *poorly* at Bondville, with only a slight improvement in predicted GPP (1% and 15% reduction of RMSE for local-FM and local-FNM, respectively) compared to using only local data (RMSE of $3.66\,\mathrm{g\,C\,m^{-2}\,day^{-1}}$).

The sites which display the largest improvements in simulated GPP, when forced with MODIS LAI, are those which have low LAI values (54 % and 24 % reduction in RMSE at Vaira Ranch and Fort Peck, respectively) (Figure 4.7c). Small improvements were also observed at the tropical sites (13 % and 14 % reduction in RMSE at Santarem Km67 and Santarem Km83, respectively). At some sites, using MODIS data had no effect on model results (El Saler) and in some cases, the model performed worse (Tum-

barumba).

The total annual simulated GPP for model runs using MODIS data (15 334 and 15 227 $g\,C\,m^{-2}\,year^{-1}$, for local-MF and local-NMF, respectively) is slightly lower than when using only local data (15 469 $g\,C\,m^{-2}\,year^{-1}$), but better than when using global data (global-WEIG; 14 193 $g\,C\,m^{-2}\,year^{-1}$). This is a result of the annual maximum MODIS LAI being closer to local values than global (Figure 4.7a). The increased LAI of the global data does not result in increased GPP predictions since the meteorological data and vegetation parameters, such as V_{cmax}, may have a greater impact on predicted GPP than LAI.

Overall, when JULES is forced with daily MODIS LAI small improvements (8 % reduction in average RMSE; local-FM) in predicted GPP are observed at a number of sites, though there exists a negative bias associated with using MODIS data. By setting the annual maximum MODIS LAI to be the annual maximum LAI at each site, the model performs equally well (0.04 % reduction in average RMSE; local-FNM) to local model simulations. Improvements in simulated GPP were observed at sites with low LAI values, such as grasslands, when JULES is forced with daily LAI.

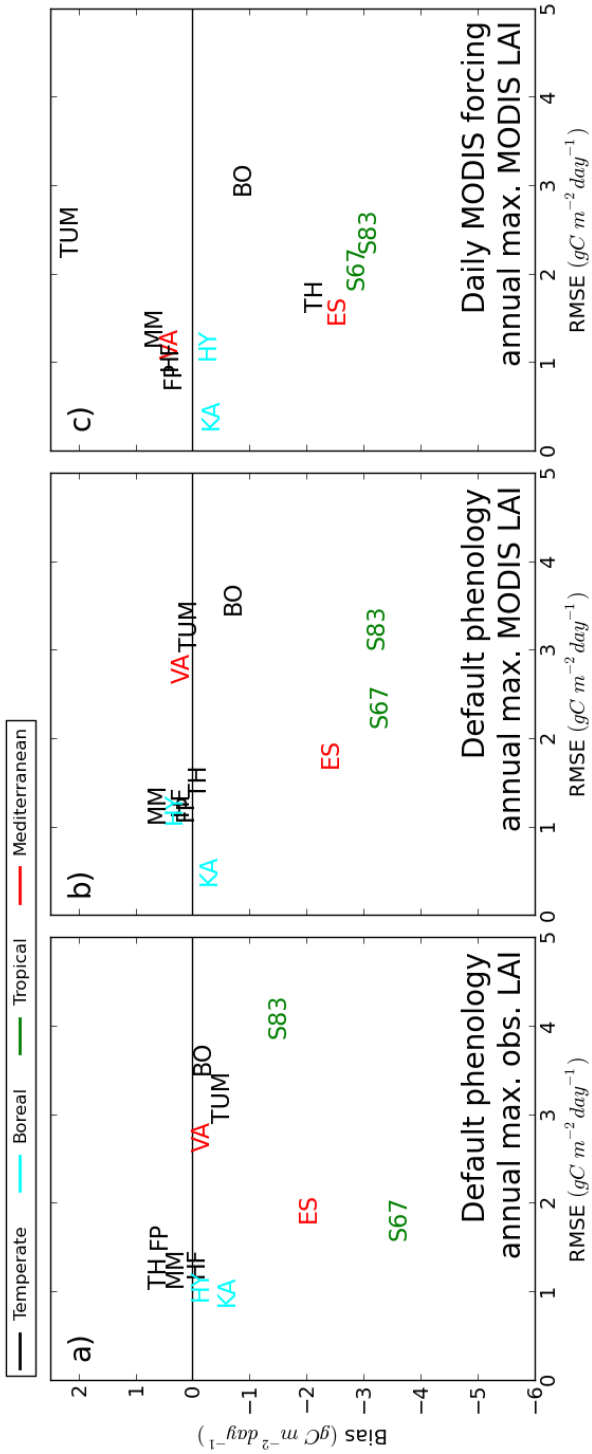

Figure 4.7: Comparison of modelled and observed GPP using bias and RMSE (computed using anomalies) at the 12 FLUXNET sites (HF: Harvard Forest, VA: Vaira Ranch, MM: Morgan Monroe, HY: Hyytiala, TH: Tharandt, TUM: Tumbarumba, ES: El Saler, FP: Fort Peck, KA: Kaamanen, S67: Santarem Km67, S83: Santarem Km83, BO: Bondville) for three sets of model simulations; **(a)** default phenology model with locally observed annual maximum LAI (data values used same as in Figure 4.3a (local-F)), **(b)** default phenology model with annual maximum MODIS LAI (model simulations local-FNM) and **(c)** daily MODIS forced model simulations with annual maximum MODIS LAI (model simulations local-FM). The site labels are coloured according to their climate zone (Table 4.2).

4.4 Discussion

A discussion of the results presented in Section 4.3 is provided here.

4.4.1 How well does JULES perform when using the best available local meteorological and parameter datasets compared to those using global data?

At more than half of the sites, JULES performs *very well* when using local meteorological and parameter datasets with a negative bias observed for the remaining sites (Figure 4.3a). At the 6 sites where multi-year model simulations were performed, interannual variability is captured by the model using local data with the exception of Santarem Km67 and Tumbarumba. This trend is also observed with the single-year runs.

The use of global parameter and meteorological datasets introduces a negative bias into GPP simulations at all sites with the exception of the mediterranean site, El Saler, and the tropical sites (Figure 4.3b). This decrease in model performance when using global data (model parameter and meteorological data) at Morgan Monroe, Tharandt, Tumbarumba and Fort Peck is due to soil moisture stress which reduces vegetation productivity (Figures 4.2 and 4.8). In JULES, soil moisture stress is taken into account by multiplying the potential (nonstressed) leaf photosynthesis by the beta factor (Equation 3.15), which ranges in value between 0 (stressed) and 1 (nonstressed).

At the tropical sites, Santarem Km67 and Santarem Km83, model performance decreases when using local data (local-F) due to increased soil moisture stress (Figures 4.8 and 4.9). At Santarem Km67, the beta factor ranges from 0.4–0.8 (local-F) throughout the year and when using global data (global-WEIG, global-WEIC and global-P), the beta factor ranges from 0.7–1.0. This means that simulated canopy photosynthesis when using local data will be less than that simulated using global data. At Santarem Km83, the increase in soil moisture stress at the beginning and end of the year results in a corresponding decrease of simulated GPP. The high correlation between simulated GPP and soil moisture stress can be found when using

global meteorological data as well (Figures 4.10 and 4.11).

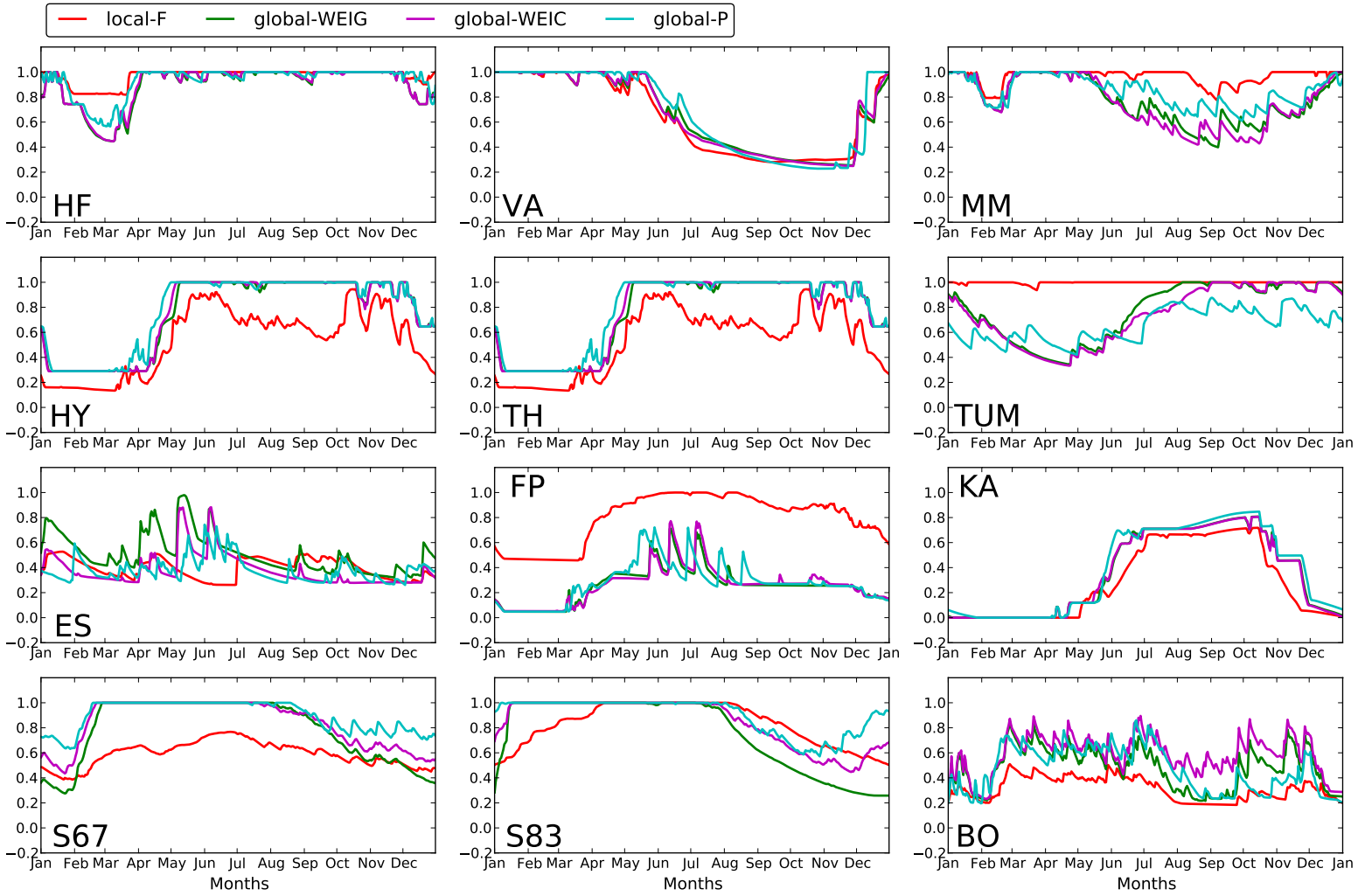

Figure 4.8: Model simulations of the soil moisture stress factor (beta factor; Equation 3.15) when using local (local-F) and global data (global-WEIG, global-WEIC and global-P) at the 12 FLUXNET sites (HF: Harvard Forest, VA: Vaira Ranch, MM: Morgan Monroe, HY: Hyytiala, TH: Tharandt, TUM: Tumbarumba, ES: El Saler, FP: Fort Peck, KA: Kaamanen, S67: Santarem Km67, S83: Santarem Km83, BO: Bondville). The soil moisture stress factor is a dimensionless quantity with values ranging from 0 (stressed) to 1 (nonstressed).

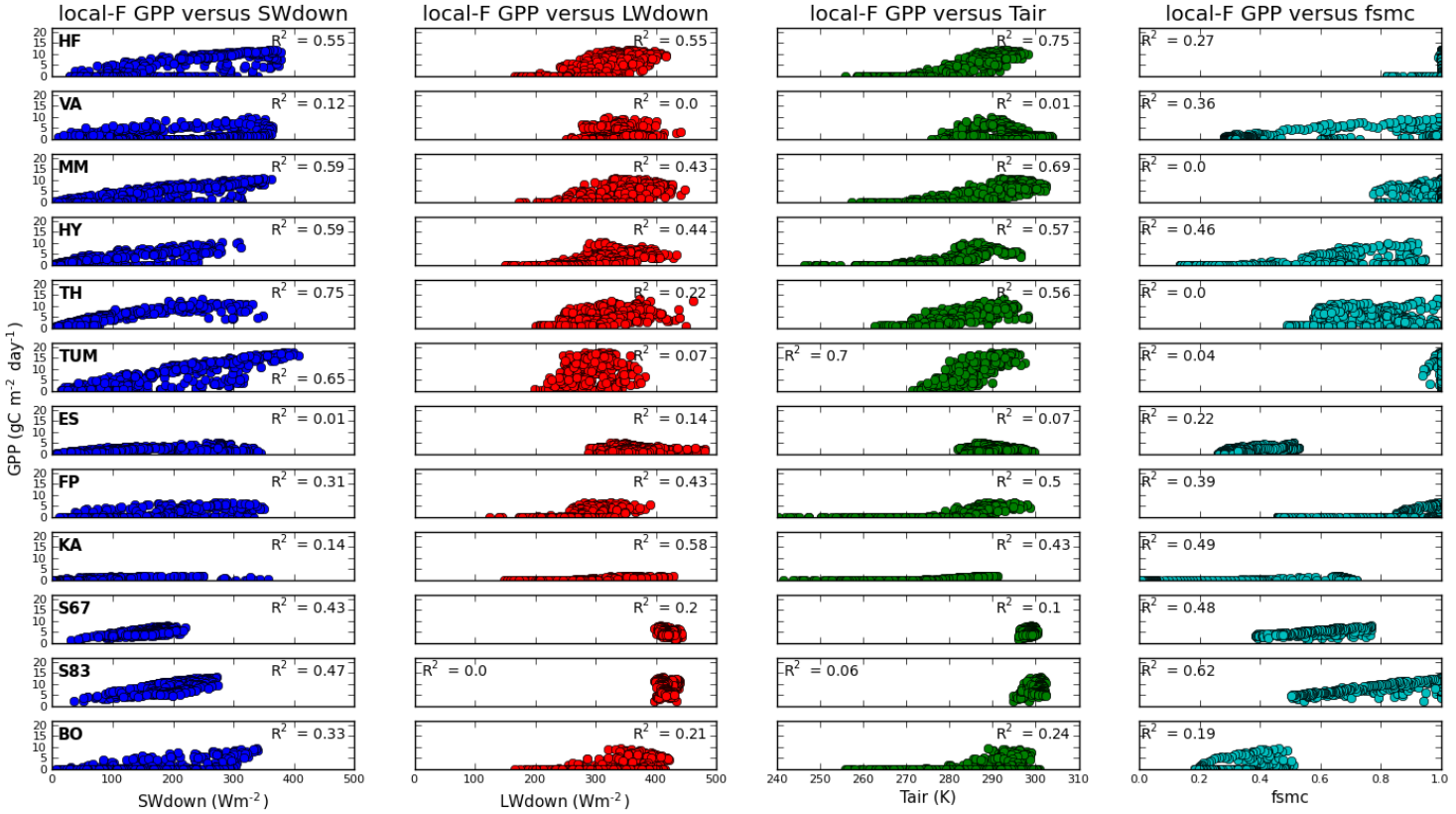

Figure 4.9: Daily average simulated GPP ($gC\,m^{-2}\,day^{-1}$) from the local-F model simulations (Table 4.3) plotted against daily average SWdown (downward shortwave radiation; blue filled circles), LWdown (downward longwave radiation; red filled circles) and surface air temperature (Tair; green filled circles) from the FLUXNET network and the simulated soil moisture stress factor (fsmc; cyan filled circles) at the 12 FLUXNET sites (HF: Harvard Forest, VA: Vaira Ranch, MM: Morgan Monroe, HY: Hyytiala, TH: Tharandt, TUM: Tumbarumba, ES: El Saler, FP: Fort Peck, KA: Kaamanen, S67: Santarem Km67, S83: Santarem Km83, BO: Bondville). The coefficient of determination (R^2) is included on each subfigure.

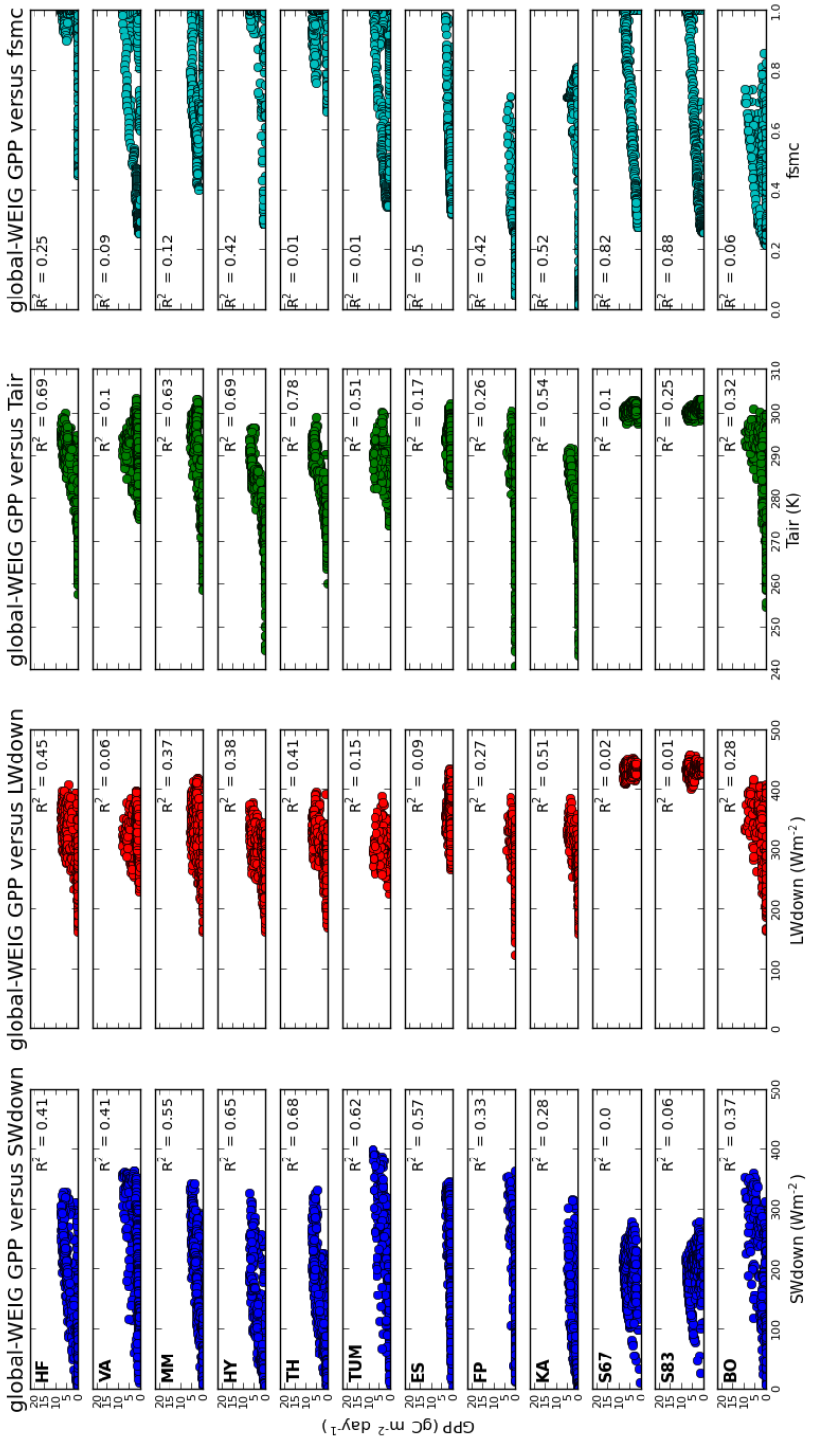

Figure 4.10: Daily average simulated GPP (gC m^{-2} day^{-1}) from the global-WEIG model simulations (Table 4.3) plotted against daily average SWdown (downward shortwave radiation; blue filled circles), LWdown (downward longwave radiation; red filled circles) and surface air temperature (Tair; green filled circles) from the WFDEI-GPCC dataset and the simulated soil moisture stress factor (fsmc; cyan filled circles) at the 12 FLUXNET sites (HF: Harvard Forest, VA: Vaira Ranch, MM: Morgan Monroe, HY: Hyytiala, TH: Tharandt, TUM: Tumbarumba, ES: El Saler, FP: Fort Peck, KA: Kaamanen, S67: Santarem Km67, S83: Santarem Km83, BO: Bondville). The coefficient of determination (R^2) is included on each subfigure.

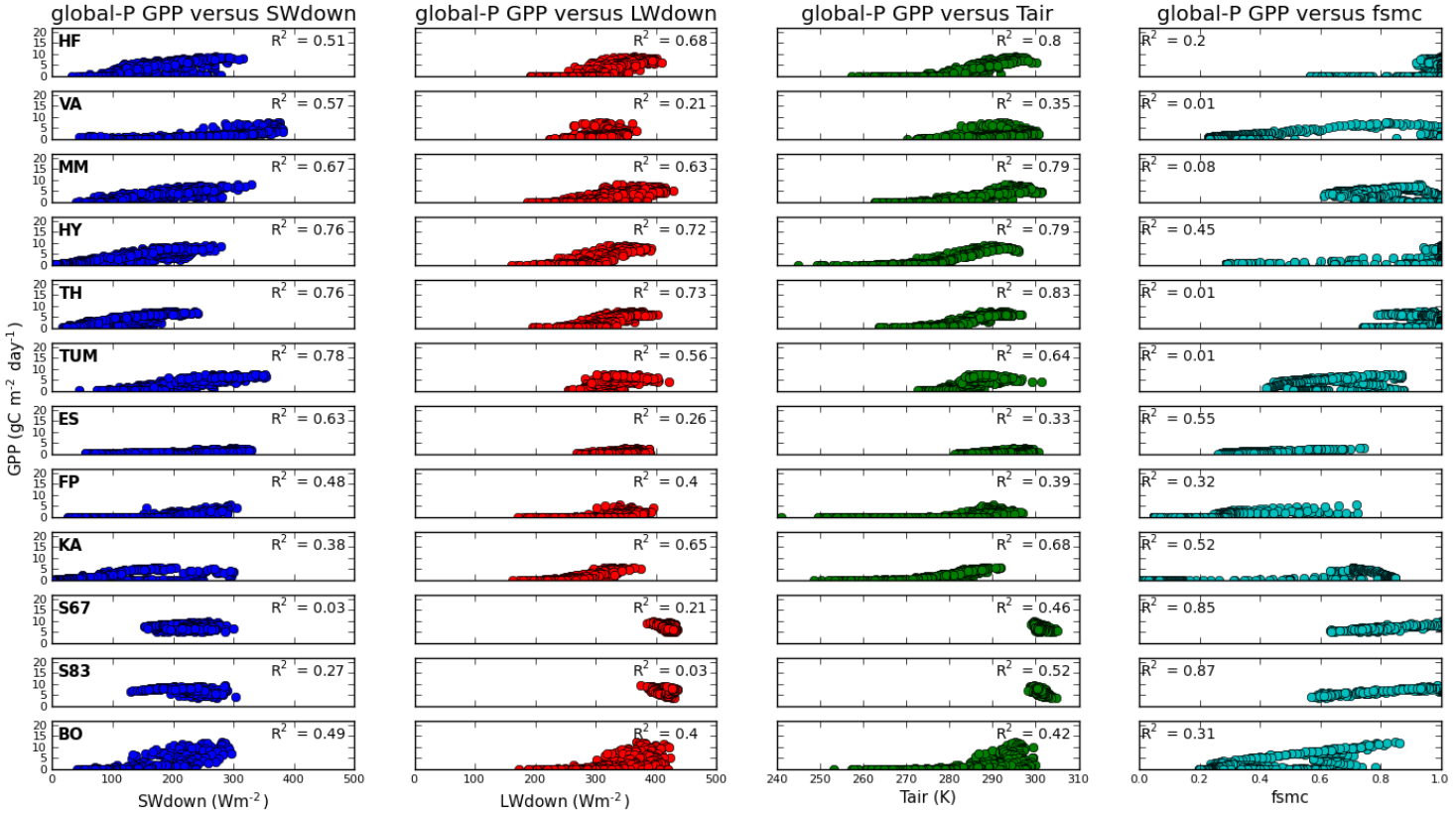

Figure 4.11: Daily average simulated GPP ($gC\,m^{-2}\,day^{-1}$) from the global-P model simulations (Table 4.3) plotted against daily average SWdown (downward shortwave radiation; blue filled circles), LWdown (downward longwave radiation; red filled circles) and surface air temperature (Tair; green filled circles) from the PRINCETON dataset and the simulated soil moisture stress factor (fsmc; cyan filled circles) at the 12 FLUXNET sites (HF: Harvard Forest, VA: Vaira Ranch, MM: Morgan Monroe, HY: Hyytiala, TH: Tharandt, TUM: Tumbarumba, ES: El Saler, FP: Fort Peck, KA: Kaamanen, S67: Santarem Km67, S83: Santarem Km83, BO: Bondville). The coefficient of determination (R^2) is included on each subfigure.

For the temperate sites, such as Harvard Forest, Morgan Monroe and Tharandt, simulated GPP is determined by the downward radiation fluxes and surface air temperature and occurs when using both local and global meteorological data to drive JULES (Figures 4.9, 4.10 and 4.11). At sites with a mediterranean-type climate, such as El Saler and Vaira Ranch, the global downward shortwave radiation was important (R^2 ranges from 0.41–0.63) when simulating GPP (Figures 4.10 and 4.11).

Using local parameter and global meteorological data to drive JULES (local-WEIG) increases the negative bias of local model simulations (local-F) (Figure 4.3f). Decreases in model performance were observed at the majority of sites, with the exceptions being the tropical sites (Santarem Km67/Km83). At some sites, such as Hyytiala and Kaamanen, using global meteorological data produced similar results (Figure 4.3a, f) to using FLUXNET data.

Our results compare well with the evaluation of JULES by Blyth et al. (2011), where parameters were obtained as though the model was embedded in a GCM. Differences between the two studies include different model versions and global meteorological datasets used. Comparing our results with Figure 3 of Blyth et al. (2011), it was found that simulated photosynthesis was underestimated for the temperate forests (Harvard Forest, Tharandt and Morgan Monroe), grasslands (Fort Peck), mediterranean sites (El Saler) and the tropical forests (Santarem Km67), and overestimated for the wetlands (Kaamanen). The use of local observations of site characteristics, such as PFT fractions and vegetation properties, lead to improvements in model performance at more than half of the sites (Figure 4.3a), though errors still exist with percentage differences ranging from 2 - 12%.

Differences between global and local data include PFT fractions (Table 4.4), soil texture fractions, vegetation parameters (Table 4.5) and meteorological data. At some sites, such as Bondville and Santarem Km67/Km83, the global and local values for LAI and V_{cmax} were markedly different (Figure 4.6), though for the majority of sites, global and local LAI values are quite close (Figure 4.6a), whereas global V_{cmax} values were underestimated compared to local values (below dashed line in Fig. 4.6b). Overall, the MODIS LAI values were closer to the local values and in general, lower than global values (Figure 4.6a).

In general, it was observed that the meteorological data played a more

important role than model parameters in determining GPP fluxes at sites, such as Santarem Km67 and Santarem Km83. At these sites, the meteorological forcing data was the primary driver of productivity and biases associated with the global meteorological data compensated for incorrect parameter values. However, at Tumbarumba, incorrectly predicted GPP was due to model error rather than meteorological data or model parameters. A temperature sensitivity study was performed at Tumbarumba using local meteorological and parameter datasets (local-F; Table 4.3). The winter and spring surface air temperatures (May-October) of the FLUXNET data were increased by increments of 1°C and the model was re-ran each time. Improvements in simulated seasonal cycle were observed, but only at high surface air temperatures (an increase in 7 degree Celsius). Since the model performed *poorly* when using both global and local data meteorological data, it was assumed that this is due to the model itself rather than the forcing data. Tumbarumba is classified as a sclerophyll forest (these are a typically Australian vegetation type which are generally dominated by plants with hard leaves adapted to drought) and JULES does not have this land cover type. The Needleleaf (NL) PFT was assigned to JULES at this site. The introduction of the correct PFT and associated parameters may improve the results at this site.

4.4.2 Of the global meteorological datasets used in this study which one compares best to FLUXNET data?

At the majority of sites, the WFDEI dataset compares better to local meteorological measurements (FLUXNET) than the PRINCETON dataset does (Figure 4.5). This is likely due to the WFDEI dataset being derived from the ECMWF Re-analysis (ERA-Interim) dataset (Dee et al., 2011). The ERA-Interim re-analysis is a higher resolution dataset ($0.75^\circ \times 0.75^\circ$; equivalent to a surface resolution of about 83 km x 83 km at the equator and 83 km x 48 km at 55 degrees north) than the NCEP-NCAR re-analsysis ($2.0^\circ \times 2.0^\circ$; equivalent to a surface resolution of about 222 km x 222 km at the equator and 222 km x 128 km at 55 degrees north), from which the PRINCETON dataset is derived (Kistler et al., 2001). The ERA-Interim re-analysis also uses a more advanced data assimilation system than the

NCEP-NCAR re-analysis (Kistler et al., 2001; Weedon et al., 2014).

At the sites considered, differences between global and local values for downward shortwave and longwave radiation fluxes and surface air temperatures are quite small (Figure 4.5a, b and d), with average percentage RMSEs ranging from 0.4–17 % (expressed as percentages of the annual mean value), while larger differences are observed for precipitation (Figure 4.5c), with average percentage RMSEs ranging from 112–178 %. At the majority of sites, there is a negative bias associated with precipitation (Figure 4.5c), but this will have little effect on GPP fluxes since JULES is relatively insensitive to precipitation (Galbraith et al., 2010). For the remaining meteorological variables, there is a positive surface air temperature bias, but no dominant bias associated with the radiation fluxes. However, at individual sites, such as the tropical sites, Santarem Km67 and Santarem Km83, biases in the meteorological data can affect model results.

4.4.3 Are improvements in simulated GPP observed when forcing JULES with daily satellite phenology compared to using the default phenology module?

In general, it was found that using MODIS data resulted in only small decreases in RMSE at a limited number of sites compared to using locally observed LAI. At sites where model performance improved, improvements were a result of setting the annual maximum LAI to be the annual maximum MODIS LAI rather than forcing the model with daily MODIS LAI. The largest improvements in simulated GPP occur at sites with low annual LAI, such as the grassland (Vaira Ranch, Fort Peck, Kaamanen) and cropland (Bondville) sites and the tropical sites (Santarem Km67 and Santarem Km83). At the boreal sites, Tharandt and Hyytiala, the MODIS LAI tended to be quite noisy and this led to underestimated GPP (Figure 4.7c).

At sites where the MODIS LAI timeseries was noisy (large day-to-day variations), this resulted in decreased model performance. At some of the flux tower sites, the MODIS data failed to capture aspects of the seasonal cycle of leaf phenology, such as the magnitude of the seasonal cycle (Tharandt, El Saler) and the beginning and end of the growing season (Bondville).

For example, at Tumbarumba, the MODIS instrument estimated the annual maximum LAI to be $6.08\,m^2\,m^{-2}$ and the daily LAI to be quite noisy whereas the ground level observations show it to be $2.5\,m^2\,m^{-2}$ (Table 4.5) and LAI to be constant for much of the year.

The MODIS instrument provides a valuable source of information that can be used by land surface models. However, in this study, the quality of the LAI data can affect model performance. At the tropical sites, MODIS was unable to capture the magnitude of seasonal variation in LAI with MODIS overestimating the locally observed annual maximum LAI at Santarem Km67 and Santarem Km83 by 28 % and 10 %, respectively (Table 4.5). It was also unable to correctly capture LAI during the Amazonian rainy season, which runs from December to June, as a result of increased cloud cover. The MODIS LAI is very noisy in these regions, but should be constant throughout the year.

Overall, the JULES' phenology module performed *very well* at the temperate sites and *poorly* at the tropical and cropland sites. The ability of the phenology model to simulate GPP fluxes reasonably well at temperate sites, with slight underestimation of the summer carbon uptake and phase shift (leaf onset and senescence), is due to its design; temperature-dependent for the BL/NL PFT classes, with model parameters tuned for temperate regions. Forcing the model with MODIS LAI only slightly improved model performance. However, setting the annual maximum LAI for each PFT to be the annual maximum MODIS LAI resulted in improved model performance, without the computational overhead of forcing JULES with daily satellite data. More accurate GPP predictions could be possible with the inclusion of tropical PFTs, such as tropical evergreen broadleaf and tropical deciduous broadleaf, with associated model parameters and a phenology model modified to take these tropical PFTs into account.

4.5 Conclusions

A multi-site evaluation of the JULES LSM was performed using local, global and satellite data. In general, it was found that when using local meteorological and parameter datasets, JULES performed *very well* at temperate sites with a negative bias observed at the tropical and cropland sites. At

a limited number of sites, the model was able to simulate interannual variability correctly using local data, with the exception of the tropical site, Santarem Km67, and Tumbarumba.

The use of global data worsens model performance by introducing negative biases into model simulations of GPP at the majority of sites with the exception of the tropical sites. When using global data, increased soil moisture stress results in reduced simulated GPP at temperate sites, such as Morgan Monroe, Fort Peck and Tumbarumba and decreased soil moisture stress at the tropical sites, Santarem Km7 and Santarem Km83, results in simulated GPP which are closer to the observations. The downward radiation fluxes and surface air temperature play an important role when simulating GPP at temperate sites (Harvard Forest, Morgan Monroe and Tharandt).

The improvement in model simulated GPP when using local values of vegetation properties implies that global values may be incorrect. At sites where model performance improved using global data, this was due to biases associated with the meteorological data (i.e. higher precipitation amounts in the global meteorological data than the local). It was observed that the meteorological data had a greater impact on modelled GPP fluxes than model parameters.

The use of meteorological data extracted from global meteorological datasets was used to drive JULES. The global meteorological data increased the negative biases of local model simulations at all sites with the exception of the tropical sites, where GPP predictions were improved. Of the two global meteorological datasets used in this study, the WFDEI dataset more closely captures the local meteorological conditions, though the PRINCETON dataset results in improved performance at some of the sites due to positive biases associated with the downward radiation fluxes and surface air temperature. This implies that there are compensating errors within the model which need to be identified and addressed.

LAI is an important parameter used in the calculation of canopy photosynthesis. Model simulations using local and MODIS data displayed improvements in modelled GPP compared to using only local data. Improvements in modelled GPP were observed at the beginning and ending of the growing season. Using MODIS data for the annual maximum LAI allows for improved model performance without the complication of assimilating

daily satellite data into the model. It was found the default phenology module allowed JULES to perform *very well* at temperate sites, but not at the tropical sites. More realistic simulation of the seasonal cycle of GPP was observed at sites with low LAI values, such as grasslands. Even though the MODIS data is described as being noisy at a number of sites, it provides a valuable source of information as it is a high spatial and temporal resolution dataset. It allows a better understanding of plant response to climate and is a useful aid to modellers.

Although only a limited number of model parameters were modified at the 12 flux tower sites, due to limited data availability at FLUXNET sites, it was shown that with more accurate information regarding flux tower sites, improved predictions of GPP are possible. However, negative biases still exist in this situation due to model error and incorrect modelling of tropical processes. It is suggested that improved model performance with regards to the terrestrial carbon cycle could be achieved with the introduction of more PFT classes, such as tropical evergreen broadleaf and tropical deciduous broadleaf, and their associated model parameters and a phenology model which can properly simulate carbon fluxes in both temperate and tropical regions.

4.6 Summary

This study evaluated the ability of the JULES LSM to simulate photosynthesis using local, global and satellite datasets at 12 FLUXNET sites. Firstly, when using local data (model parameter and meteorological datasets) to simulate GPP, JULES is biased with total annual GPP underestimated by 16 % across all sites compared to observations. Secondly, it was found that when using global data (model parameter and meteorological datasets), model performance decreased further with total annual GPP underestimated by 30 % across all sites compared to observations. When JULES was driven using local parameters and global meteorological data, it was shown that global data could be used in place of FLUXNET data with a 7 % reduction in total annual simulated GPP. Thirdly, when the global meteorological datasets, WFDEI and PRINCETON, were compared to FLUXNET data, it was found that the WFDEI dataset compared best

to FLUXNET. Finally, it was found that forcing the model with daily satellite LAI results in only small improvements in predicted GPP at a small number of sites compared to using the default phenology model. In the next chapter, JULES is evaluated at the global and regional scales using upscaled FLUXNET and satellite datasets.

Bibliography

P. Alton, L. Mercado, and P. North. A sensitivity analysis of the land-surface scheme jules conducted for three forest biomes: Biophysical parameters, model processes, and meteorological driving data. *Global biogeochemical cycles*, 20:GB1008, 2007. doi:10.1029/2005GB002653.

M. Aurela, J.-P. Tuovinen, and T. Laurila. Carbon dioxide exchange in a subarctic peatland ecosystem in northern europe measured by the eddy covariance technique. *Journal of Geophysical Research: Atmospheres (1984–2012)*, 103:11289–11301, 1998. doi:10.1029/98JD00481.

F. Baret, O. Hagolle, B. Geiger, P. Bicheron, B. Miras, M. Huc, B. Berthelot, F. Niño, M. Weiss, O. Samain, J. L. Roujean, and M. Leroy. LAI, fAPAR and fCover CYCLOPES global products derived from VEGETATION, Part 1: Principles of the algorithm. *Remote Sensing of Environment*, 110:275–286, 2007. doi:10.1016/j.rse.2007.02.018.

D. J. Beerling and W. P. Quick. A new technique for estimating rates of carboxylation and electron transport in leaves of c3 plants for use in dynamic global vegetation models. *Global Change Biology*, 1:289–294, 1995. doi:10.1111/j.1365-2486.1995.tb00027.x.

E. Blyth, J. Gash, A. Lloyd, M. Pryor, G. P. Weedon, and J. Shuttleworth. Evaluating the JULES Land Surface Model Energy Fluxes Using FLUXNET Data. *Journal of Hydrometeorology*, 11:509–519, 2010. doi:10.1175/2009JHM1183.1.

R. D. Bruno, H. R. Da Rocha, H. C. De Freitas, M. L. Goulden, and S. D. Miller. Soil moisture dynamics in an eastern Amazonian tropical forest. *Hydrological Processes*, 20:2477–2489, 2006. doi:10.1002/hyp.6211.

H. A. Cleugh, R. Leuning, Q. Mu, and S. W. Running. Regional evaporation estimates from flux tower and MODIS satellite data. *Remote Sensing of Environment*, 106:285–304, 2007. doi:10.1016/j.rse.2006.07.007.

D. P. Dee, S. M. Uppala, A. J. Simmons, P. Berrisford, P. Poli, S. Kobayashi, U. Andrae, M. A. Balmaseda, G. Balsamo, P. Bauer, P. Bechtold, A. C. M. Beljaars, L. van de Berg, J. Bidlot, N. Bormann, C. Delsol, R. Dragani, M. Fuentes, A. J. Geer, L. Haimberger, S. B. Healy, H. Hersbach, E. V. Hólm, L. Isaksen, P. Kållberg, M. Köhler, M. Matricardi, A. P. McNally, B. M. Monge-Sanz, J.-J. Morcrette, B.-K. Park, C. Peubey, P. de Rosnay, C. Tavolato, J.-N. Thópaut, and F. Vitart. The ERA-Interim reanalysis: configuration and performance of the data assimilation system. *Quarterly Journal of the Royal Meteorological Society*, 137:553–597, 2011. doi:10.1002/qj.828.

F. Deng, M. Chen, S. Plummer, , and J. Pisek. Algorithm for Global Leaf Area Index Retrieval Using Satellite Imagery. *IEEE Transactions on Geoscience and Remote Sensing*, 44:2219–2229, 2006. doi:10.1109/TGRS.2006.872100.

D. J. Diner, J. V. Martonchik, C. Borel, S. A. W. Gerstl, H. R. Gordon, R. Myneni, B. Pinty, and M. M. Verstraete. MISR Level 2 Surface Retrieval Algorithm Theoretical Basis. Technical report, Jet Propulsion Laboratory, California Institute of Technology, Pasadena., pp 1–81, 2008.

T. F. Domingues, L. A. Martinelli, and J. R. Ehleringer. Ecophysiological traits of plant functional groups in forest and pasture ecosystems from eastern Amazonia, Brazil. *Plant Ecology*, 193:101–112, 2007. doi:10.1007/s11258-006-9251-z.

C. E. Doughty and M. L. Goulden. Seasonal patterns of tropical forest leaf area index and CO_2 exchange. *Journal of Geophysical Research*, 113: G00B06, 2008. doi:10.1029/2007JG000590.

T. G. Gilmanov, L. L. Tieszen, B. K. Wylie, L. B. Flanagan, A. B. Frank, M. R. Haferkamp, T. P. Meyers, and J. A. Morgan. Integration of CO_2 flux and remotely-sensed data for primary production and ecosystem respiration analyses in the Northern Great Plains: Potential for quantitative spatial extrapolation. *Global Ecology and Biogeography*, 14:271–292, 2005. doi:10.1111/j.1466-822X.2005.00151.x.

J. L. Gornall, I. S. Jónsdóttir, S. J. Woodin, and R. Van der Wal. Arctic mosses govern below-ground environment and ecosystem processes. *Oecologia*, 153:931–941, 2007. doi:10.1007/s00442-007-0785-0.

M. L. Goulden, S. D. Miller, H. R. Da Rocha, M. C. Menton, H. C. de Freitas, A. M. e Silva Figueira, and C. A. D. de Sousa. Diel and seasonal patterns of tropical forest CO_2 exchange. *Ecological Applications*, 14: 42–54, 2004. doi:10.1890/02-6008.

T. Grünwald and C. Bernhofer. A decade of carbon, water and energy flux measurements of an old spruce forest at the Anchor Station Tharandt. *Tellus B*, 59:387–396, 2007. doi:10.1111/j.1600-0889.2007.00259.x.

V. Haverd, R. Leuning, D. Griffith, E. van Gorsel, and M. Cuntz. The turbulent Lagrangian time scale in forest canopies constrained by fluxes, concentrations and source distributions. *Boundary-Layer Meteorology*, 130:209–228, 2009. doi:10.1007/s10546-008-9344-4.

J. Hu, Y. Su, B. Tan, D. Huang, W. Yang, M. Schull, M. A. Bull, J. V. Martonchik, D. J. Diner, Y. Knyazikhin, and R. B. Myneni. Analysis of the MISR LAI/FPAR product for spatial and temporal coverage, accuracy and consistency. *Remote Sensing of Environment*, 107:334–347, 2007. doi:10.1016/j.rse.2006.06.020.

L. R. Hutyra, J. W. Munger, S. R. Saleska, E. Gottlieb, B. C. Daube, A. L. Dunn, D. F. Amaral, P. B. De Camargo, and S. C. Wofsy. Seasonal controls on the exchange of carbon and water in an Amazonian rain forest. *Journal of Geophysical Research*, 112:G03008, 2007. doi:10.1029/2006JG000365.

C. P. Jones. Unified Model Documentation Paper No 70: Ancillary File Data Sources. Technical report, UK Met Office, 2007.

J. Kattge, W. Knorr, T. Raddatz, and C. Wirth. Quantifying photosynthetic capacity and its relationship to leaf nitrogen content for global-scale terrestrial biosphere models. *Global Change Biology*, 15:976–991, 2009. doi:10.1111/j.1365-2486.2008.01744.x.

R. Kistler, E. Kalnay, W. Collins, S. Saha, G. White, J. Woollen, M. Chelliah, W. Ebisuzaki, M. Kanamitsu, V. Kousky, H. van den Dool, R. Jeanne, and M. Fiorino. The NCEP-NCAR 50-year reanalysis: Monthly means CD-ROM and documentation. *Bulletin of the American Meteorological society*, 82:247–267, 2001. doi:10.1175/1520-0477(2001)082<0247:TNNYRM>2.3.CO;2.

T. Laurila, H. Soegaard, C. R. Lloyd, M. Aurela, J.-P. Tuovinen, and C. Nordstroem. Seasonal variations of net CO_2 exchange in European Arctic ecosystems. *Theoretical and Applied Climatology*, 70:183–201, 2001. doi:10.1007/s007040170014.

R. Leuning, H. A. Cleugh, S. J. Zegelin, and D. Hughes. Carbon and water fluxes over a temperate Eucalyptus forest and a tropical wet/dry savanna in Australia: measurements and comparison with MODIS remote sensing estimates. *Agricultural and Forest Meteorology*, 129:151–173, 2005. doi:10.1016/j.agrformet.2004.12.004.

Q. Liu, L. Gu, R. E. Dickinson, Y. Tian, L. Zhou, and W. M. Post. Assimilation of satellite reflectance data into a dynamical leaf model to infer seasonally varying leaf areas for climate and carbon models. *Journal of Geophysical Research*, 113:D19113, 2008. doi:10.1029/2007JD009645.

V. Masson, J.-L. Champeaux, F. Chauvin, C. Meriguet, and R. Lacaze. Global Database of Land Surface Parameters at 1-km Resolution in Meteorological and Climate Models. *Journal of Climate*, 16:1261–1282, 2003. doi:10.1175/1520-0442-16.9.1261.

T. P. Meyers and S. E. Hollinger. An assessment of storage terms in the surface energy balance of maize and soybean. *Agricultural and Forest Meteorology*, 125:105–115, 2004. doi:10.1016/j.agrformet.2004.03.001.

F. Nachtergaele, H. van Velthuizen, L. Verelst, D. Wiberg, N. Batjes, K. Dijkshoorn, V. van Engelen, G. Fischer, A. Jones, L. Montanarella, M. Petri,

S. Prieler, E. Teixeira, and X. Shi. Harmonized World Soil Database v1.2. Technical report, International Institute for Applied Systems Analysis (IIASA), Food and Agriculture Organization of the United Nations (FAO), February 2012.

Y. Ryu, D. D. Baldocchi, S. Ma, and T. Hehn. Interannual variability of evapotranspiration and energy exchange over an annual grassland in California. *Journal of Geophysical Research*, 113:D09104, 2008. doi:10.1029/2007JD009263.

H. P. Schmid, C. S. B. Grimmond, F. Cropley, B. Offerle, and H.-B. Su. Measurements of CO_2 and energy fluxes over a mixed hardwood forest in the mid-western United States. *Agricultural and Forest Meteorology*, 103: 357–374, 2000. doi:10.1016/S0168-1923(00)00140-4.

R. Stöckli, D. M. Lawrence, G. Y. Niu, K. W. Oleson, P. E. Thornton, Z. L. Yang, G. B. Bonan, A. S. Denning, and S. W. Running. Use of FLUXNET in the Community Land Model development. *Journal of Geophysical Research*, 113:G01025, 2008. doi:10.1029/2007JG000562.

T. Suni, J. Rinne, A. Reissell, N. Altimir, P. Keronen, U. Rannik, M. Kulmala, and T. Vesala. Long-term measurements of surface fluxes above a scots pine forest in hyytiala, southern finland, 1996-2001. *Boreal Environment Research*, 8:287–302, 2003.

S. Urbanski, C. Barford, S. Wofsy, C. Kucharik, E. Pyle, J. Budney, K. McKain, D. Fitzjarrald, M. Czikowsky, and J. W. Munger. Factors controlling CO_2 exchange on timescales from hourly to decadal at Harvard Forest. *Journal of Geophysical Research*, 112:G02020, 2007. doi:10.1029/2006JG000293.

G. P. Weedon, G. Balsamo, N. Bellouin, S. Gomes, M. J. Best, and P. Viterbo. The WFDEI meteorological forcing data set: WATCH Forcing Data methodology applied to ERA-Interim reanalysis data. *Water Resources Research*, 50:7505–7514, 2014. doi:10.1002/2014WR015638.

W. Yang, B. Tan, D. Huang, M. Rautiainen, N. V. Shabanov, Y. Wang, J. L. Privette, K. F. Huemmrich, R. Fensholt, I. Sandholt, M. Weiss, D. E. Ahl, S. T. Gower, R. R. Nemani, Y. Knyazikhin, and R. B. Myneni. MODIS

Leaf Area Index Products: From Validation to Algorithm Improvement. *Geoscience and Remote Sensing, IEEE Transactions on*, 44:1885–1898, 2006.

Chapter 5

Global evaluation of JULES against upscaled FLUXNET and satellite data

In this chapter, the ability of JULES to simulate GPP at the global scale for the 2000–2010 period is examined. A number of model simulations, performed at various spatial resolutions and driven with a variety of meteorological datasets (WFDEI-GPCC, WFDEI-CRU and PRINCETON), are compared to global spatially gridded estimates of Gross Primary Productivity (GPP) derived from the upscaling of observations from the FLUXNET network (FLUXNET-MTE) and satellite observations (MODIS). Firstly, the ability of JULES to simulate interannual variability at the global scale and global GPP (integrated across all ecosystem types) was examined. The minimum limiting rates used to calculate simulated photosynthesis (from JULES driven with the WFDEI-GPCC and PRINCETON datasets) at global scales was examined. Secondly, GPP fluxes simulated by JULES for various biomes (forests, grasslands and shrubs) at global and regional scales were compared to the observation-based estimates. Thirdly, the sensitivity of the model to simulations of GPP at various spatial resolutions ($0.5^\circ \times 0.5^\circ$, $1^\circ \times 1^\circ$ and $2^\circ \times 2^\circ$) was investigated (the results from these model simulations were used to design the simulations performed in Chapter 6). Finally, the meteorological data used to drive LSMs is a major source of uncertainty and therefore, the sensitivity of JULES to the meteorological

dataset used to drive the model was examined.

5.1 Introduction

JULES' ability to reproduce fluxes of GPP has been examined at the point scale in the previous chapter and by Blyth et al. (2011) and Rowland et al. (2015), but not at the global scale. Previous studies using JULES have usually involved adjusting model parameters and then evaluation at one or more flux tower sites (Galbraith et al., 2010; Marthews et al., 2012; Chadburn et al., 2015; Slevin et al., 2015). In Chapter 4, JULES was evaluated at 12 FLUXNET sites that covered a range of ecosystem types (temperate, boreal, mediterranean and tropical) in order to investigate differences between model simulations of GPP when using local, global and satellite-derived datasets. This work is extended by performing global model simulations of GPP and comparing the results to global gridded estimates of GPP derived from the upscaling of observations from the current global network of FLUXNET sites (FLUXNET-MTE; Section 3.2.3.2) and MODIS GPP product (MODIS; Section 3.2.3.4). These datasets provide a means to evaluate LSMs at global and regional scales in spite of potential errors in the datasets (Bonan et al., 2011). FLUXNET-MTE and MODIS can be used to evaluate models at large scales and identify areas for model improvement (Bonan et al., 2011). Sitch et al. (2015) used JULES as part of a multi-model project to identify regional sources and sinks of CO_2.

In this chapter, the ability of JULES version 3.4.1 (Section 3.1.2) to simulate global and regional fluxes of GPP for various biomes, spatial resolutions and using different meteorological datasets is evaluated. In particular, the following research questions are addressed:

- Can JULES capture interannual variability of GPP at the global scale? How do estimates of global GPP compare to those from observational datasets?

- How do fluxes of GPP simulated by JULES compare for various biomes at the global and regional scales?

- How sensitive are fluxes of GPP to the spatial resolution of the model?

- Is the meteorological dataset used to drive the model important at the global scale?

5.2 Methods

A brief description of the JULES LSM used to perform the global scale model simulations is provided, followed by an overview of the simulations performed. Then the global datasets used as ancillary data for the model and the observational datasets against which model performance is compared are described. Finally, the quantification of model-observation differences is provided.

5.2.1 Model description

JULES version 3.4.1 was used to perform the global scale model simulations described in Section 5.2.2 and a more detailed description of this version of JULES can be found in Section 3.1.2. Differences between JULES version 3.0 (used in Chapter 4) and version 3.4.1 are discussed in Section 3.1.3 with the main reason for using version 3.4.1 being the ability to run JULES in parallel which leads to increased speed up of global scale model simulations (Section 3.1.2).

5.2.2 Experimental design

Offline simulations of GPP at the global scale for the 2000–2010 period were carried out using various meteorological datasets and spatial resolutions (Table 5.1). The land cover was kept constant at values for the year 2000 (Section 3.2.1.1) and annual atmospheric CO_2 concentrations were varied as in the historical record. The simulation of GPP is important since errors in its calculation can affect other land-atmosphere flux calculations (Section 1.1). Global gridded estimates of GPP derived from the upscaling of observations from the FLUXNET network (Section 3.2.3.2) and satellite estimates of LAI and GPP from the MODIS instrument (Sections 3.2.3.3 and 3.2.3.4, respectively) provide a means to evaluate LSMs at large scales (Jung et al., 2009, 2010; Beer et al., 2010; Bonan et al., 2011; Lei et al., 2014). Prior to performing the global scale model simulations, the soil

moisture was brought to equilibrium using a 40 year global spin-up by cycling 10 years of meteorological data (1979–1989) twice and 10 years of meteorological data (1989–1999) twice (in equilibrium mode), followed by a 10 year spin-up by cycling 10 years of meteorological data (1999–2010) once (in dynamical mode). Finally, the actual model simulation was performed for 2000–2010 due to the availability of observation-based estimates of GPP (upscaled FLUXNET and MODIS) for this period.

Model simulations	Meteorological forcing[a]	Spatial resolution	Grid dimensions[b]
JULES-WFDEI-GPCC	WFDEI-GPCC	$0.5^\circ \times 0.5^\circ$	720×360
JULES-WFDEI-CRU	WFDEI-CRU	$0.5^\circ \times 0.5^\circ$	720×360
JULES-WFDEI-GPCC-1degree	WFDEI-GPCC	$1^\circ \times 1^\circ$	360×180
JULES-PRINCETON	PRINCETON	$1^\circ \times 1^\circ$	360×180
JULES-WFDEI-GPCC-2degree	WFDEI-GPCC	$2^\circ \times 2^\circ$	180×90

[a] More detailed information on the global meteorological datasets used to drive JULES can be found in Section 3.2.2.
[b] Grid dimensions are given as the number of grid boxes in the west-east direction by the number of grid boxes in the north-south direction.

Table 5.1: Types of global scale model simulations performed.

5.2.3 Data

The datasets used as input to JULES include the vegetation and soil datasets, the meteorological data required to drive the model and the observations against which model performance was compared. The vegetation data used is the Global Land Cover Characterization database (Section 3.2.1.1) which is the land cover classification scheme used for the global scale model simulations (and by the global operational version of JULES). This dataset specifies the PFT fractions for each model gridbox at half-degree ($0.5^\circ \times 0.5^\circ$) resolution (Figure 5.2). The soil dataset used was the Harmonized World Soil Database (Section 3.2.1.2). Since JULES requires meteorological data at 6 hourly intervals or less in order to drive the model offline, a number of datasets were used; WFDEI (Weedon et al., 2014), which is a 3 hourly land-only (including Antarctica) dataset used to drive global hydrological and LSMs at half-degree ($0.5^\circ \times 0.5^\circ$) spatial resolution

for the 1979–2012 period; and PRINCETON (Sheffield et al., 2006), which is a 3 hourly land-only (excluding Antarctica), 1-degree ($1^\circ \times 1^\circ$) resolution, meteorological dataset for the 1948–2008 period.

For model simulations performed at $1^\circ \times 1^\circ$ and $2^\circ \times 2^\circ$ spatial resolution, the $0.5^\circ \times 0.5^\circ$ spatial and monthly temporal resolution observational data were regridded to these lower resolutions (Appendix D). It was previously explained in Section 3.2.2 that a $0.5^\circ \times 0.5^\circ$ spatial resolution grid produced a global grid of 360×720 grid cells, which is equivalent to a surface resolution of about 56 km $\times$ 56 km at the equator and 56 km $\times$ 32 km at 55 degrees north (temperate regions), and a $1^\circ \times 1^\circ$ spatial resolution grid produced a global grid of 180×360 grid cells, which is equivalent to a surface resolution of about 111 km $\times$ 111 km at the equator and 111 km $\times$ 64 km at 55 degrees north. The lowest spatial resolution of $2^\circ \times 2^\circ$ (JULES-WFDEI-GPCC-2degree; Table 5.1) produces a global grid of 90×180 grid cells and is equivalent to a surface resolution of about 222 km $\times$ 222 km at the equator and 222 km $\times$ 128 km at 55 degrees north.

5.2.3.1 Observations

The data against which the model's performance is compared includes global gridded ($0.5^\circ \times 0.5^\circ$ spatial and monthly temporal resolution) estimates of GPP derived from the upscaling of observations from the FLUXNET network using the Model Tree Ensemble (MTE) approach which is a machine learning approach where a set of multiple linear regressions are used to predict GPP (Section 3.2.3.1), satellite observations of GPP (Section 3.2.3.4) and LAI (Section 3.2.3.3), also at $0.5^\circ \times 0.5^\circ$ resolution, from NASA's MODerate resolution Imaging Spectroradiometer (MODIS) instrument. For the lower spatial resolutions at $1^\circ \times 1^\circ$ and $2^\circ \times 2^\circ$, the $0.5^\circ \times 0.5^\circ$ spatial and monthly temporal resolution observational data were regridded like the meteorological data (Appendix D).

There are two upscaled FLUXNET GPP datasets available depending on the flux partitioning method used to separate net ecosystem exchange of CO_2 (NEE) into GPP and terrestrial ecosystem respiration (TER) (Reichstein et al., 2005; Lasslop et al., 2010). I chose GPP based on the work by Reichstein et al. (2005) (referred to as FLUXNET-MTE). However, differences between the two upscaled FLUXNET GPP are small with differences

in total annual GPP for 2000–2010 ranging between +7 and -7 $\mathrm{kg\,C\,m^{-2}}$ (Figure G.1). The FLUXNET-MTE and MODIS datasets are not true observations of GPP, but are derived from flux tower observations, and in this chapter, for the sake of brevity, they are referred to as observations.

5.2.4 Outline of experiments

This section describes the global scale model simulations performed. The first part of the model simulation name refers to JULES version 3.4.1 and the second part refers to the global meteorological dataset used to drive the model (Table 5.1). The phenology model was switched on for all model simulations, but vegetation competition and TRIFFID were switched off. In Chapter 4, vegetation competition was disabled in order to prevent unrealistic vegetation fractions at each of the flux tower sites developing during the spin-up process (Section 4.2.4). This same reason was used to disable vegetation competition for global scale simulations of GPP.

Results from JULES-WFDEI-CRU have not been included since differences between JULES-WFDEI-GPCC and JULES-WFDEI-CRU are small with differences in simulated total annual GPP for 2000–2010 ranging between -21 and +27 $\mathrm{kg\,C\,m^{-2}}$ (Figure G.2) and differences in estimates of annual average global GPP being 2 $\mathrm{Pg\,C\,year^{-1}}$ (Figures 5.5c and G.3c). There is little difference in total annual GPP (integrated across all ecosystem types) when either precipitation product is used at the global and regional scale (Figure G.4).

5.2.4.1 Interannual variability of GPP

The ability of JULES to simulate the interannual variability of GPP at the global scale was examined. Model simulations were performed for 2000–2010 using global parameter and meteorological datasets (JULES-WFDEI-GPCC and JULES-WFDEI-CRU; Table 5.1) with the results compared to the observation-based estimates (FLUXNET-MTE and MODIS GPP).

5.2.4.2 Total annual GPP

Model estimates of total annual GPP (JULES-WFDEI-GPCC) integrated across the globe were compared to the FLUXNET-MTE (Section 3.2.3.2)

and MODIS datasets (Section 3.2.3.4). FLUXNET-MTE (global flux datasets derived from individual flux tower sites) and MODIS (satellite datasets) provide a means to evaluate JULES (and other LSMs) at global and regional scales (Bonan et al., 2011). The minimum limiting rates used to calculate photosynthesis (Section 3.1.1.3) with JULES driven with the WFDEI-GPCC dataset (at $1^\circ \times 1^\circ$ spatial resolution) was examined. In JULES, the minimum limiting rate used to calculate leaf photosynthesis is not a model output, so the JULES code (and its io) were modified in order to calculate which limiting rate was the minimum for each model gridbox. Two methods were used to create maps of global minimum limiting rates (Appendix F).

5.2.4.3 Global and regional comparison for various biomes

In addition to deriving estimates of globally integrated GPP fluxes, the modelled (JULES-WFDEI-GPCC) and observed GPP were compared by biome type (Forest, Grassland and Shrub) at the global and regional scales (Global, Tropics and Extratropics). The global GPP was further analysed by biome type at the regional scale by dividing the global land area into seven regions (Table 5.2; Figure 5.1).

Name	Latitude (°)	Longitude (°)
Europe	30N–90N	15W–45E
Northern Asia	30N–90N	45E–180E
South & South-East Asia	30S–30N	60E–150E
Extratropical Southern Hemisphere	60S–30S	120W–180E
Africa	30S–30N	30W–60E
Central & Southern America	30S–30N	120W–30W
North America & Greenland	30N–90N	180W–15W

Table 5.2: List of regions used. Only land grid points are used in the analysis.

5.2.4.4 Sensitivity to the spatial resolution of the input data

No research has been performed on the effects of varying spatial resolution on simulations of GPP by JULES. A number of studies exploring differing horizontal spatial resolution in atmospheric chemistry models have

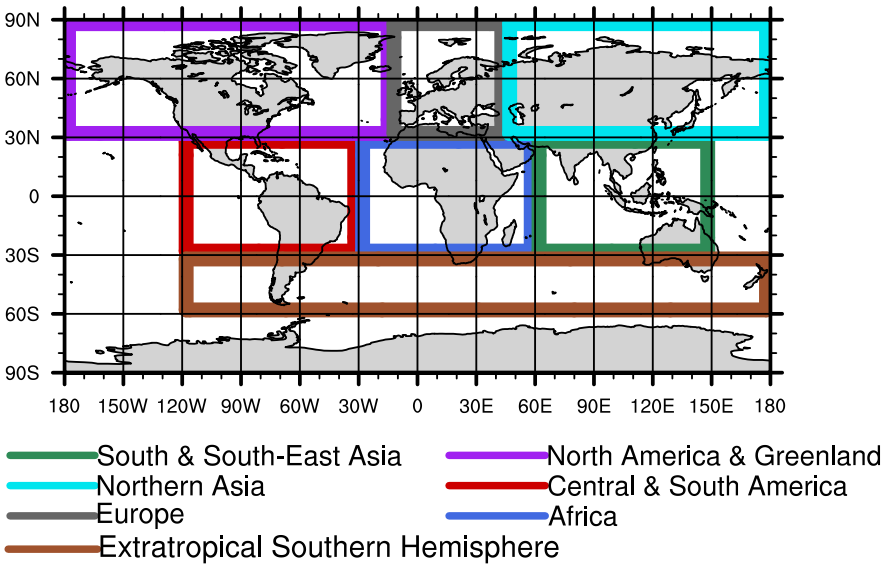

Figure 5.1: Map showing the regions specified in Table 5.2.

been performed in order to ascertain if increases in model resolution can provide more accurate and detailed information on atmospheric processes (Ito et al., 2009; Pugh et al., 2013; Schaap et al., 2015). The sensitivity of the model to the spatial resolution of the input data was evaluated by varying the resolution of the ancillary data (soil and vegetation) and meteorological data (WFDEI-GPCC) and re-running the model simulations for 2000–2010. The input data was regridded from $0.5^\circ \times 0.5^\circ$ to $1^\circ \times 1^\circ$ spatial resolution (JULES-WFDEI-GPCC-1degree; Table 5.1) and from $0.5^\circ \times 0.5^\circ$ to $2^\circ \times 2^\circ$ spatial resolution (JULES-WFDEI-GPCC-2degree) using the first order conservative remapping function (remapcon) of the Climate Data Operators (CDO) software package (https://code.zmaw.de/projects/cdo). The observation-based (FLUXNET-MTE and MODIS) datasets were regridded using this method. The output from these simulations were compared to those at $0.5^\circ \times 0.5^\circ$ spatial resolution (JULES-WFDEI-GPCC). A more detailed description of the regridding process ($0.5^\circ \times 0.5^\circ$ to $1^\circ \times 1^\circ$) can be found in Appendix D. The same method was used to regrid the ancillary and meteorological data from $0.5^\circ \times 0.5^\circ$ spatial resolution to $2^\circ \times 2^\circ$.

5.2.4.5 Sensitivity to the meteorological dataset used to drive JULES

The sensitivity of JULES to the meteorological driving data was evaluated by comparing model simulations driven using the WFDEI-GPCC (JULES-WFDEI-GPCC-1degree) and PRINCETON datasets (JULES-PRINCETON; Table 5.1) at $1^\circ \times 1^\circ$ spatial resolution. In these model simulations, the same ancillary datasets are used by both with the only difference in the model runs being the meteorological data used to drive the model. The model gridbox limiting rates were examined using JULES driven with the PRINCETON dataset. This was done in order to compare limiting rate information when the model was driven with two different meteorological datasets.

5.2.5 Model Analyses

In order to quantify how the model performs at the global scale, the following metrics were used: global area-weighted mean ($\bar{x}$; Equation 5.1), coefficient Of variation (CV; Equation 5.2) and monthly anomalies (Equation 5.3).

$$\bar{x} = \frac{\sum_{i,j=1}^{i=m,\,j=n} a_{i,j}\, x_{i,j}}{\sum_{i,j=1}^{i=m,\,j=n} a_{i,j}} \tag{5.1}$$

$$\mathrm{CV} = \frac{\sigma}{\mu} \times 100 \tag{5.2}$$

$$\text{Monthly anomaly} = x - \bar{x}_{clim} \tag{5.3}$$

The global area-weighted mean is calculated by multiplying the monthly GPP flux for each grid box ($x_{i,j}$) by the area of its grid box ($a_{i,j}$) and dividing the sum of these values by the total land surface area. m and n are the total number of grid boxes in the x- and y-direction, respectively. For example, when running a global scale model simulation at half-degree ($0.5^\circ \times 0.5^\circ$) spatial resolution, $m = 720$ (number of grid boxes in the west-east direction)

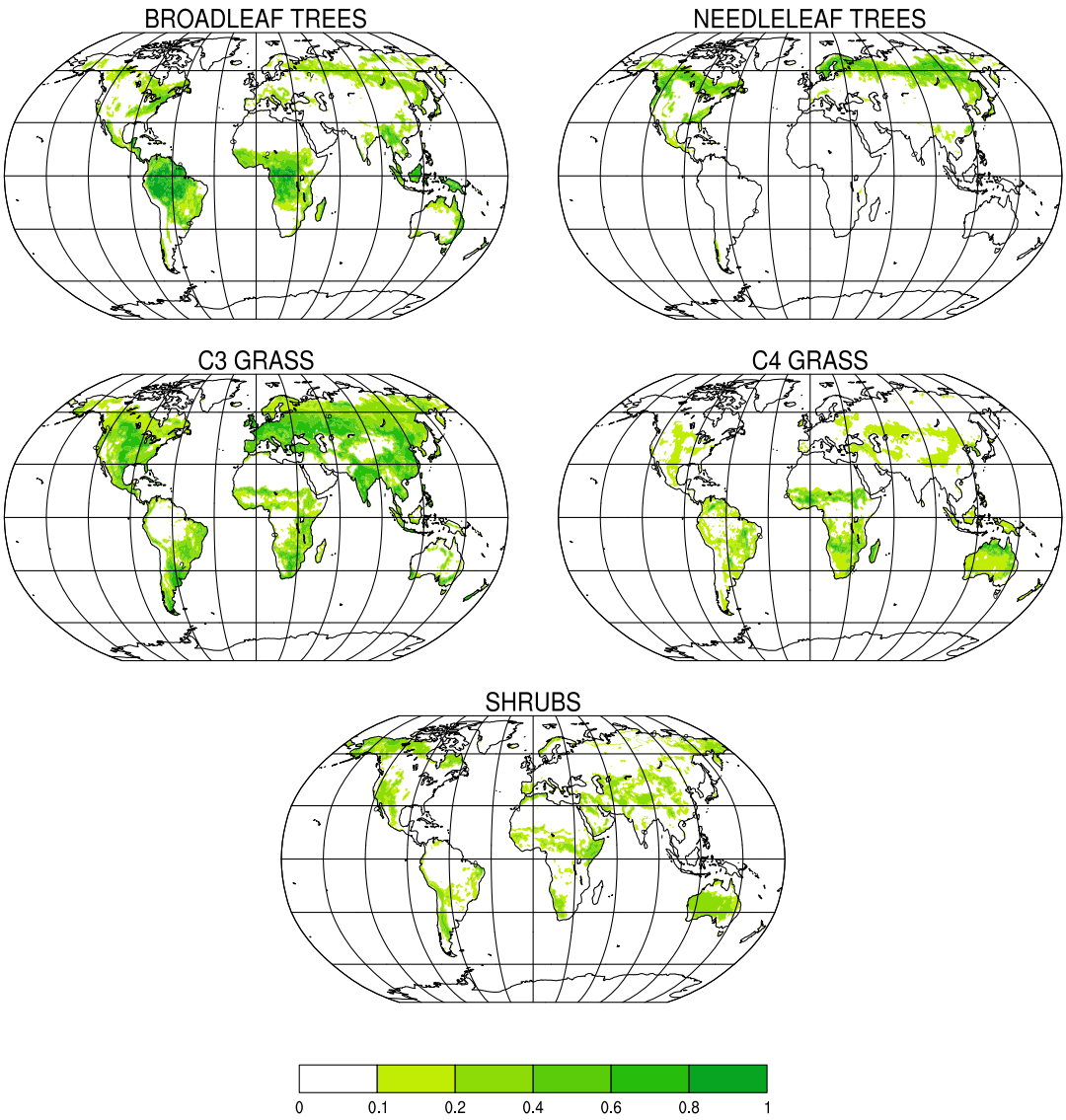

Figure 5.2: Maps of the fractions of grid cell covered by each PFT used by JULES at half-degree ($0.5^\circ \times 0.5^\circ$) resolution. Only vegetation land cover types are shown here.

and $n = 360$ (number of grid boxes in the north-south direction). CV (also known as relative variability) is a measure of the relative magnitude of the standard deviation (σ) and is calculated by dividing the standard deviation by the mean (μ). It is expressed as a percentage and is always positive. CV is a useful statistic since it allows the degree of variation of various datasets to be compared even if the means are quite different from each other. It is also dimensionless which means that CVs can be used to compare the dispersion (variability) of the data when other measures like standard deviation or root mean squared error cannot. To quantify model performance at the global scale, CV was calculated by first computing the standard deviation and means of the global area-weighted means for each month and then dividing the average of the standard deviations by the average of the means for each month. The monthly anomaly is defined as the departure of the observed monthly values (x) from the long-term (climatological) average for that month ($\bar{x}_{clim}$).

5.3 Results

Results from model simulations examining interannual variability, estimates of global GPP, comparisons of estimated GPP for various biomes at global and regional scales, evaluating the effect of varying the spatial resolution of the input data and evaluating the impact of using different meteorological driving data are presented here.

5.3.1 Interannual variability of GPP

JULES simulates well the seasonal cycle of GPP (JULES-WFDEI-GPCC; Table 5.1) at the global scale (Figure 5.3a) with the global area-weighted average of its monthly GPP for 2000–2010 falling within range of the FLUXNET-MTE and MODIS GPP values for much of the year (between 64 and 107 $\mathrm{g\,C\,m^{-2}\,month^{-1}}$). The exception to this are the winter months (January, February, March and December) with JULES overestimating the global mean by 2 $\mathrm{g\,C\,m^{-2}\,month^{-1}}$ on average compared to FLUXNET-MTE. The MODIS GPP means are lower than FLUXNET-MTE for each of the monthly climatologies by 10 $\mathrm{g\,C\,m^{-2}\,month^{-1}}$ on average (Figure 5.3a).

The standard deviation of the monthly GPP fluxes is used to measure

the interannual variability and this is expressed as a percentage of the mean monthly GPP fluxes (monthly climatologies) using coefficient of variation (CV). The CV of the model simulated and observed GPP fluxes range between 1–4 % for the monthly climatologies with the highest differences between the monthly values being for winter and spring (February, March, April, November and December) (Figure 5.3b). This pattern is similar to the global area-weighted average of the monthly climatologies (Figure 5.3a). Low values of CV mean that differences between the monthly GPP fluxes and the monthly climatology are small and larger CV values mean the opposite.

The monthly anomalies (computed using the global area-weighted mean values) expressed as percentages of the global area-weighted mean of the monthly climatologies for model simulated GPP (JULES-WFDEI-GPCC) compare equally well to both FLUXNET-MTE and MODIS GPP for 2000–2010 with both having RMSEs of 2.4 % (Figure 5.3c). However, the high variation in simulated GPP at the beginning and end of the year is observed in the monthly anomalies from 2000 to 2010 which in some years, such as 2000 and 2002, the model is unable to capture monthly GPP (Figure 5.3c).

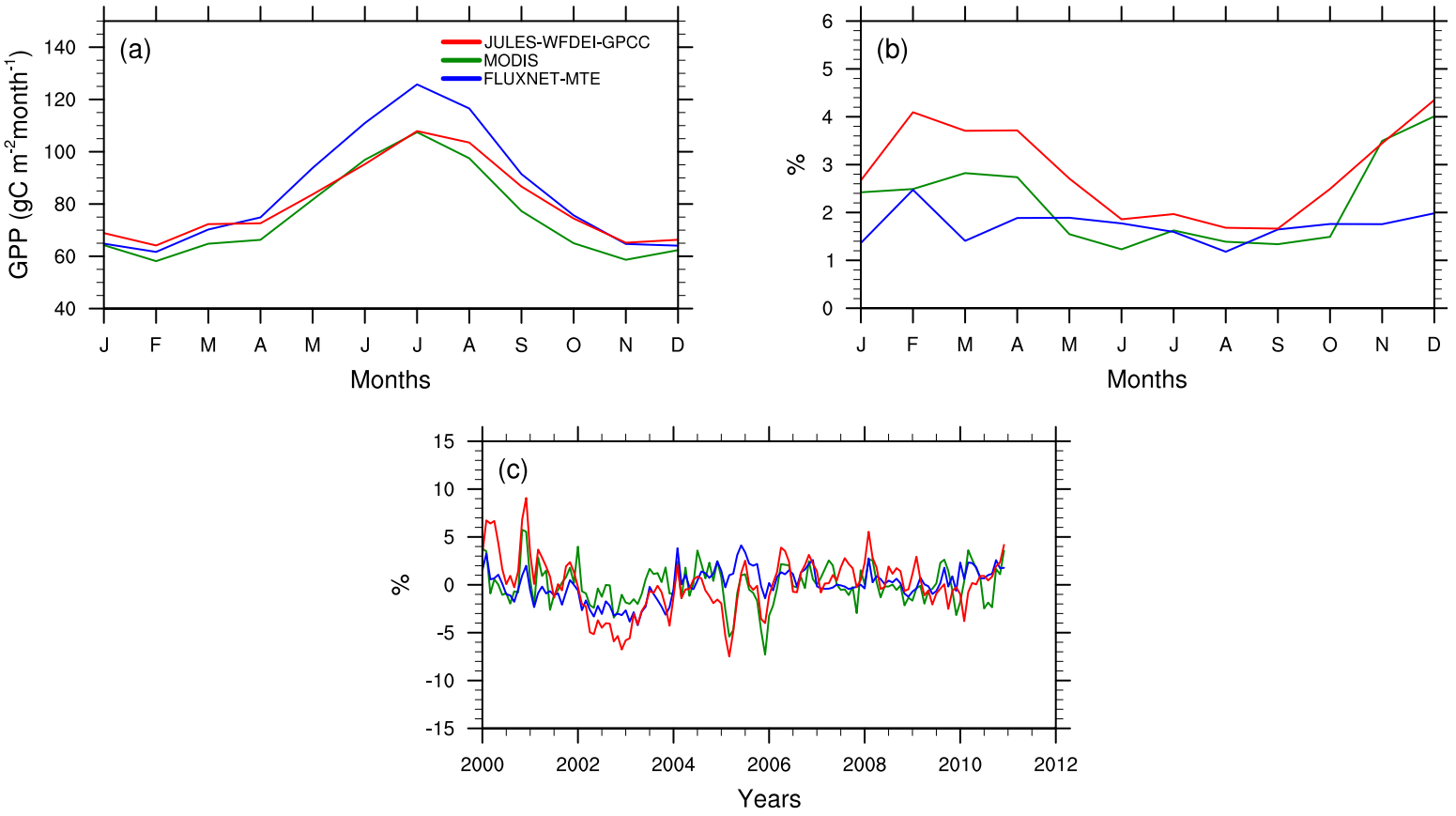

Figure 5.3: Comparison of model simulated (JULES-WFDEI-GPCC; Table 5.1) and observed (FLUXNET-MTE and MODIS) GPP fluxes for the 2000–2010 period at the global scale. **(a)** displays the global area-weighted average of the monthly climatologies, **(b)** displays the coefficient of variation (CV) expressed as percentages of the monthly climatologies and **(c)** displays the monthly anomalies (global area-weighted mean) expressed as percentages of the monthly climatologies (global area-weighted mean) for each month.

5.3.2 Global GPP

When driven with the WFDEI-GPCC dataset (JULES-WFDEI-GPCC; Table 5.1), JULES simulates global GPP with an annual average of 140 $\mathrm{Pg\,C\,year^{-1}}$ (the combined GPP of all terrestrial ecosystems) over the period 2000–2010 (Figure 5.4; Figures 5.5c). This value is greater than that estimated by FLUXNET-MTE and MODIS GPP with annual average global GPP estimated to be 130 and 112 $\mathrm{Pg\,C\,year^{-1}}$, respectively, for the same period (Figure 5.5a and 5.5b). The higher global GPP simulated by the JULES-WFDEI-GPCC driven simulations is greater than the FLUXNET-MTE and MODIS estimates by 8 % and 25 % on average, respectively.

The difference in average annual global GPP between JULES-WFDEI-GPCC and MODIS (both at $0.5^\circ \times 0.5^\circ$ spatial resolution) is three times greater (28 $\mathrm{Pg\,C\,year^{-1}}$) than that between JULES-WFDEI-GPCC and FLUXNET-MTE (10 $\mathrm{Pg\,C\,year^{-1}}$; Figure 5.4a). This difference between the model simulated and observed GPP is also shown in the zonal mean of the total annual JULES-WFDEI-GPCC, FLUXNET-MTE and MODIS GPP (Figure 5.5d). The largest differences between datasets in the zonal mean are in the tropics (10°S-10°N and 15°N-30°N) with this trend also being observed in the monthly zonal mean GPP at 5°N and 5°S for 2000–2010 in the tropical regions (Figure 5.11a) and at 55°N in the temperate regions (Figure 5.11b).

The differences between JULES (JULES-WFDEI-GPCC) and MODIS GPP can be partly explained by differences in LAI (Figure 5.10). In JULES, LAI is computed internally using the default phenology module by scaling the annual maximum LAI, which is then used to calculate GPP. Like the model simulations performed in the multi-site evaluation of JULES in the previous chapter (Chapter 4), a multi-layer canopy was used for the global scale model simulations for the scaling up of leaf-level photosynthesis to canopy level. Canopy-scale fluxes are estimated as the sum of leaf-level fluxes in each layer scaled by leaf area (Clark et al., 2011). LAI from the MODIS MOD15 LAI/FPAR product (Section 3.2.3.3) was used as input for the generation of the MODIS GPP product (Section 3.2.3.4). As with GPP, MODIS LAI is very similar to JULES LAI except in the tropics (30°S-30°N) where JULES LAI is underestimated compared to MODIS (Figure 5.10c).

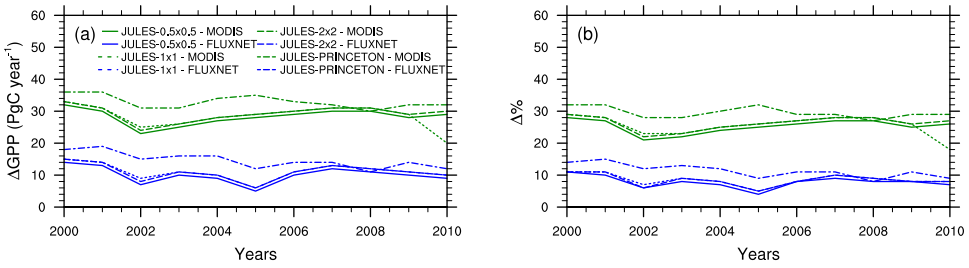

Figure 5.4: Absolute and percentage differences between model simulated (JULES-WFDEI-GPCC) and observation-based estimates (FLUXNET-MTE and MODIS) of annual average global GPP for each year for 2000–2010. FLUXNET-MTE and MODIS GPP have a spatial resolution of 0.5° × 0.5°. JULES-0.5×0.5, JULES-1×1 and JULES-2×2 refer to JULES driven with WFDEI-GPCC at 0.5° × 0.5°, 1° × 1° and 2° × 2° spatial resolution, respectively. **(a)** displays the absolute difference in annual GPP between simulations at various resolutions and observation-based estimates and **(b)** displays the percentage differences for the same simulations.

The same trend is observed in the monthly zonal mean LAI at 5°N and 5°S in the tropical regions (Figure 5.12a) and at 55°N in the temperate regions (Figure 5.12b).

In JULES, the potential (nonstressed by water and ozone) leaf photosynthesis is calculated as the minimum of three limiting rates: (1) Rubisco-limited, (2) Light-limited and (3) Transport-limited (Equations 3.1, 3.2 and 3.3, respectively.). In the multi-layer approach for radiation interception and scaling from leaf-level to canopy-level photosynthesis (Option 4 in Table 3.1 was used for all model simulations in this thesis), the model simulates competition between Rubisco-limited and light-limited photosynthesis for each canopy layer (Clark et al., 2011). This means that lower in the canopy, there is increased light limitation and in the upper layers of the canopy, there is increased Rubisco limitation (Clark et al., 2011).

In general, when JULES was driven with the WFDEI-GPCC dataset at global scales (JULES-WFDEI-GPCC-1degree), it was found that simulated photosynthesis was Rubisco-limited (Equation 3.1; Figures 5.6 and 5.7). Under saturated irradiance and limited CO_2 concentrations, the Rubisco limiting rate is considered the main limiting factor (Marcus et al., 2008). In regions dominated by grasses and shrubs, photosynthesis was found to be transport-limited (Equation 3.3; Figure 5.6). Transport limitation refers to

the rate of transport of photosynthetic products (for C_3 plants) and PEP-Carboxylase limitation (for C_4 plants). Transport limitation occurs mostly in Northern Eurasia and North America during the Spring and Summer months (March–September) and during the Autumn and Winter months (October–February) in Central Asia (Figures 5.6 and 5.9). The percentage of model gridboxes that were found to be Rubisco-limited was high (40-100%), whereas the percentage of model gridboxes that were found to be light-limited were small (0-20%) (Figures 5.7 and 5.8, respectively).

In general, JULES simulates higher annual average global GPP than FLUXNET-MTE and MODIS with model GPP closer to estimates of FLUXNET-MTE GPP. It was found that the potential leaf photosynthesis was mostly Rubisco-limited.

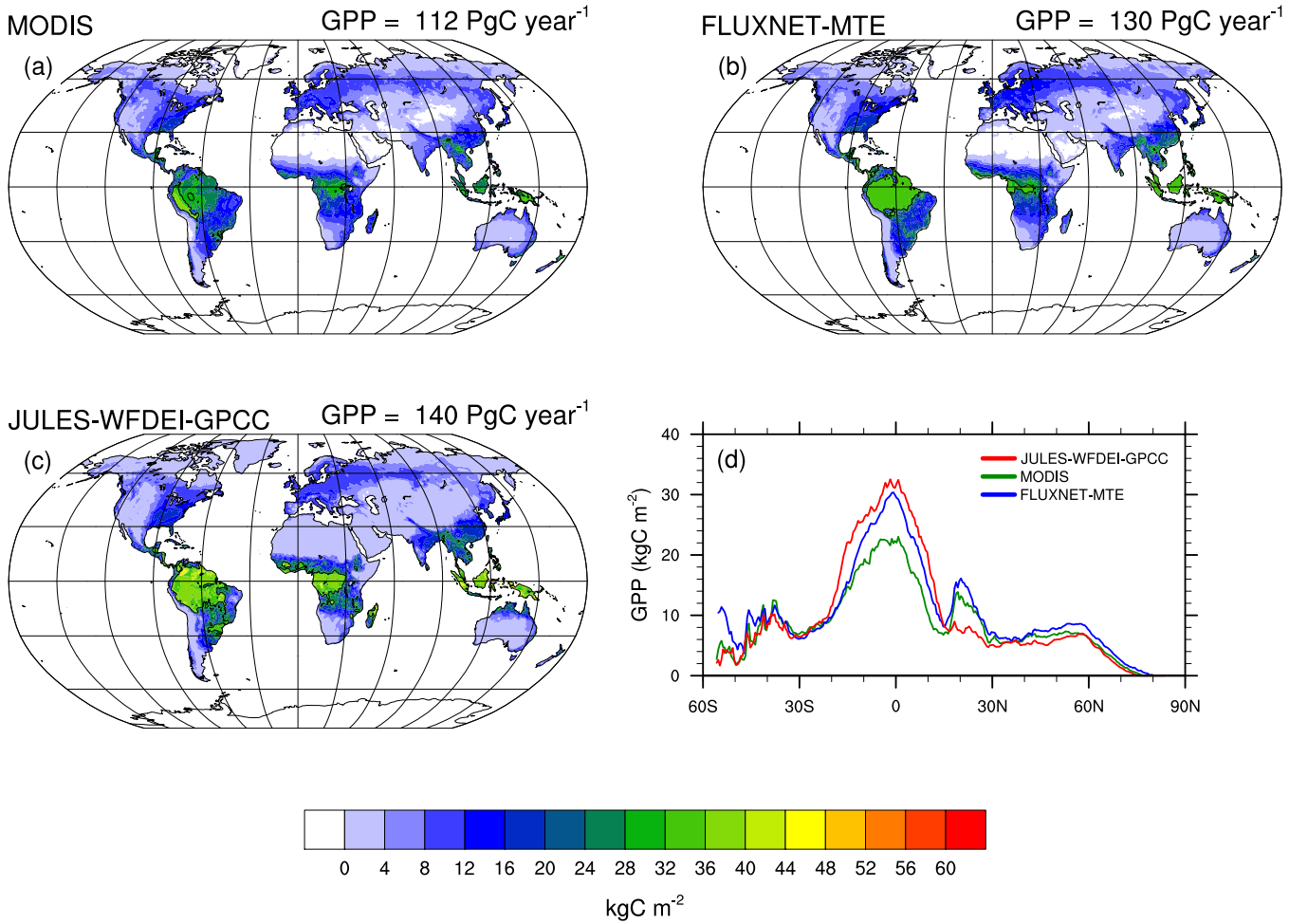

Figure 5.5: Total annual and zonal mean model simulated (JULES-WFDEI-GPCC) and observed (FLUXNET-MTE and MODIS) GPP fluxes for the 2000–2010 period at the global scale ($0.5° \times 0.5°$ spatial resolution). **(a)**, **(b)** and **(c)** show the total annual GPP of JULES-WFDEI-GPCC, FLUXNET-MTE and MODIS GPP, respectively. At the top right of each subplot, the average global annual GPP for 2000–2010 is displayed. **(d)** shows the zonal mean of the total annual JULES-WFDEI-GPCC, FLUXNET-MTE and MODIS GPP, respectively.

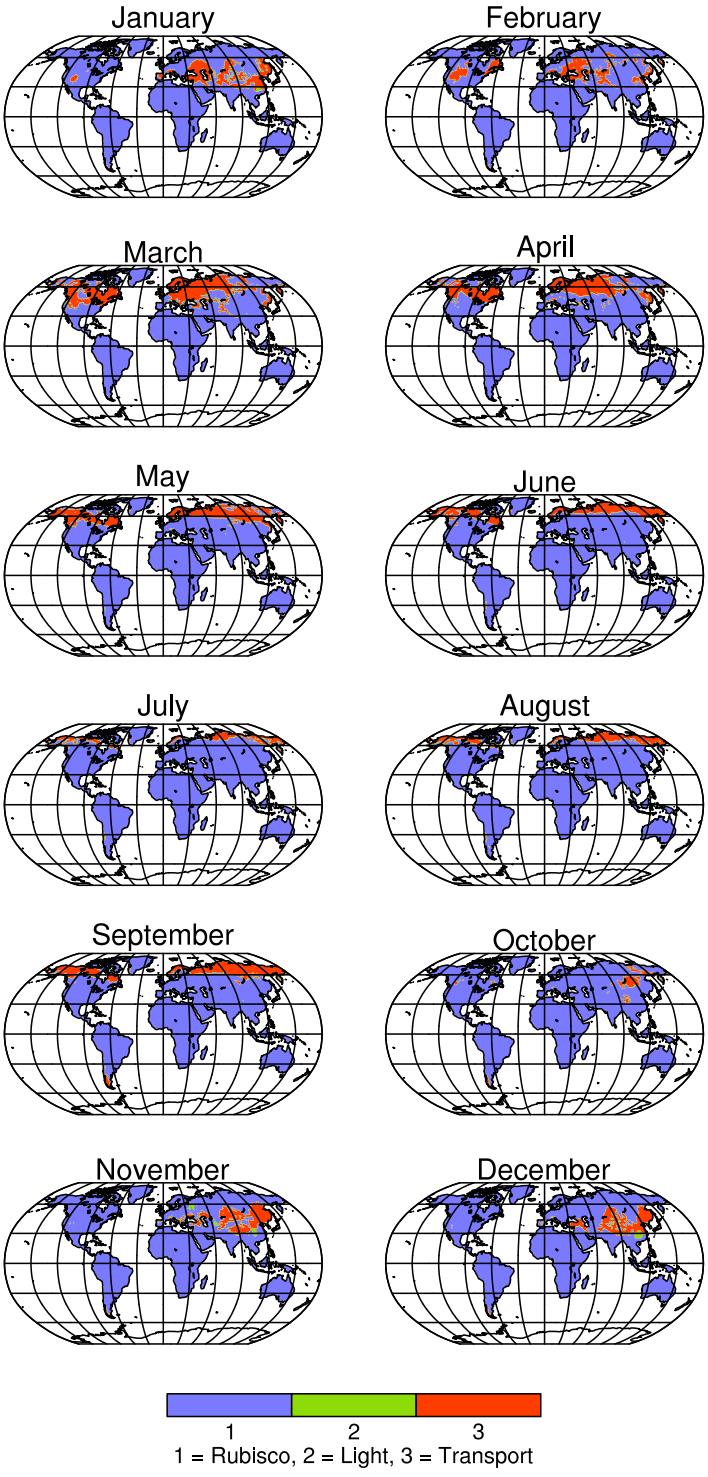

Figure 5.6: Monthly climatologies of potential (nonstressed by water and ozone) leaf photosynthesis minimum limiting rates (1 = Rubisco-limited, 2 = Light-limited and 3 = Transport-limited) which dominate model gridboxes from the JULES-WFDEI-GPCC-1degree model simulation at global scales (calculated using Method 1 in Appendix F). The Rubisco-limited, Light-limited and Transport-limited photosynthetic rates are determined by Equations 3.1, 3.2 and 3.3, respectively.

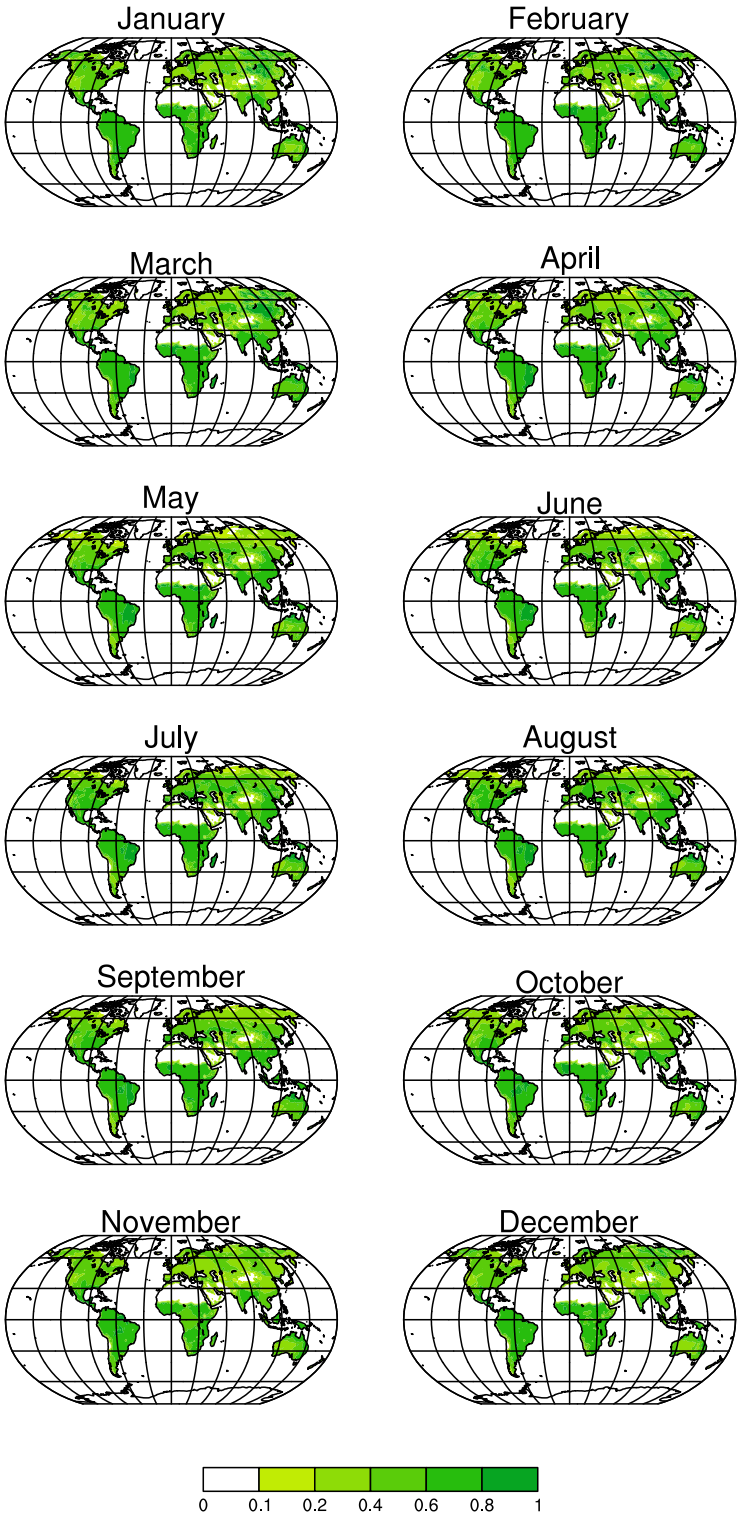

Figure 5.7: Monthly climatologies of Rubisco-limited model gridbox fractions (0–1) from the JULES-WFDEI-GPCC-1degree model simulation at global scales (calculated using Method 2 in Appendix F).

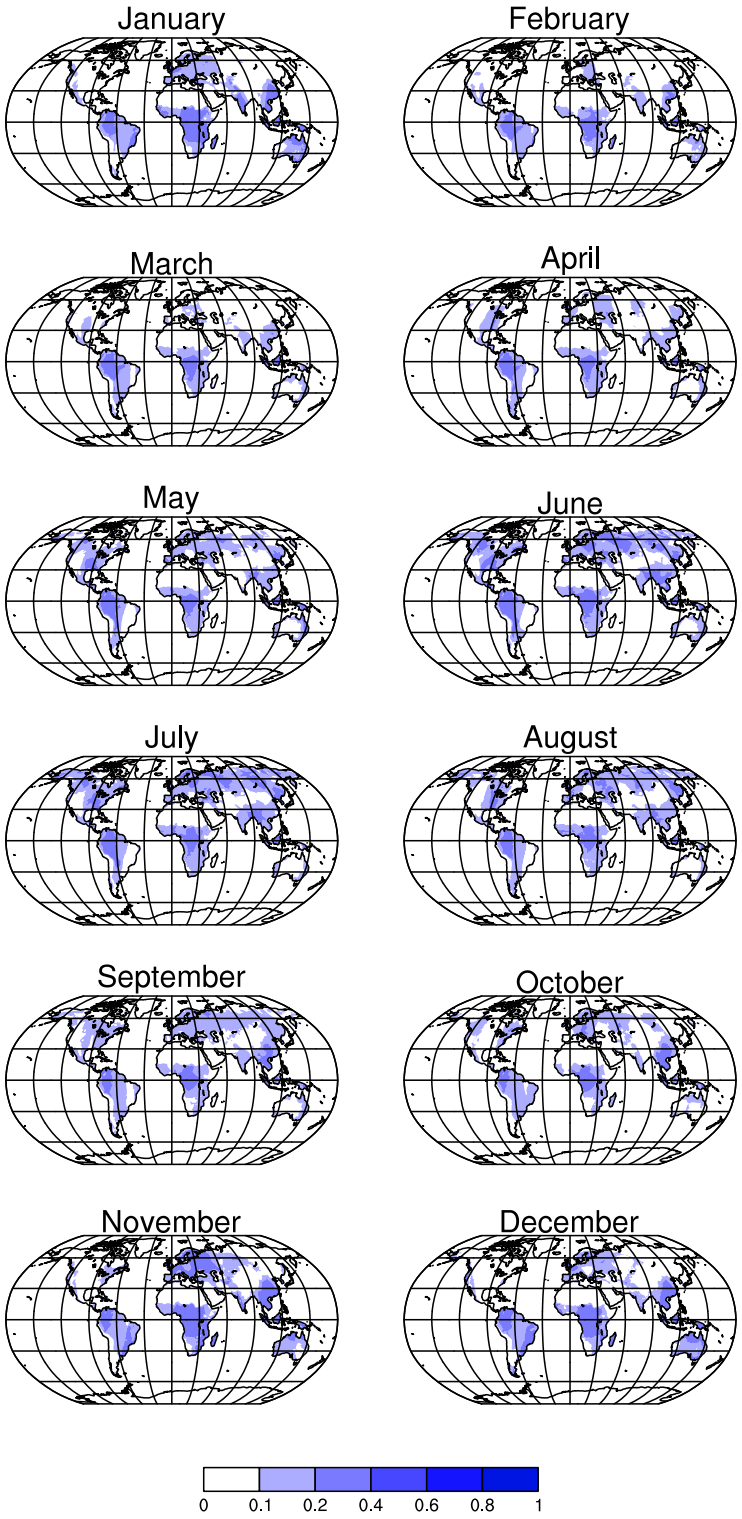

Figure 5.8: Monthly climatologies of Light-limited model gridbox fractions (0–1) from the JULES-WFDEI-GPCC-1degree model simulation at global scales (calculated using Method 2 in Appendix F).

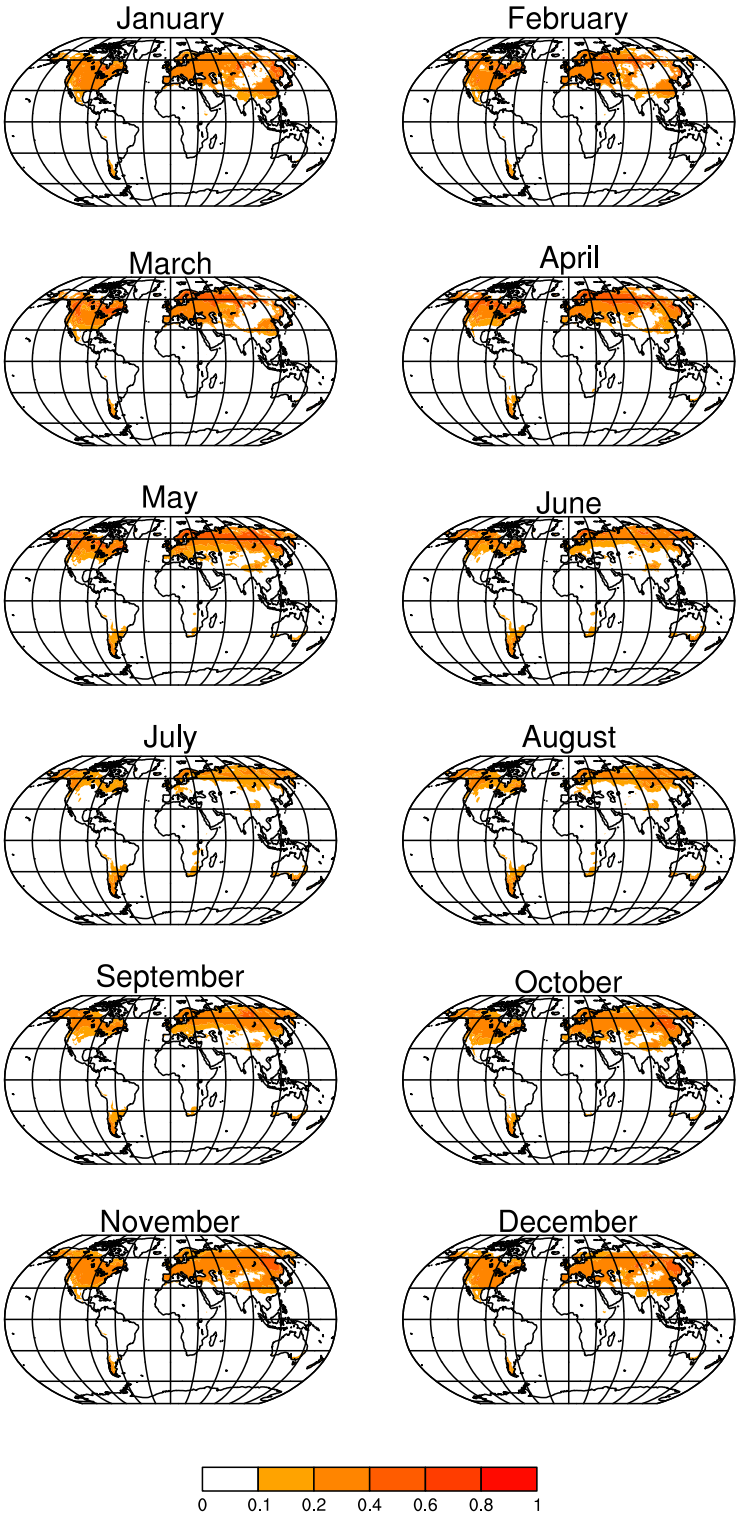

Figure 5.9: Monthly climatologies of Transport-limited model gridbox fractions (0–1) from the JULES-WFDEI-GPCC-1degree model simulation at global scales (calculated using Method 2 in Appendix F).

5.3.3 Global and regional comparison for various biomes

In addition to examining the ability of JULES to simulate global GPP (integrated across all ecosystem types), the total annual GPP for 2000–2010 was compared for various biomes (forests, grasslands and shrubs) at global and regional scales (Figures 5.13, 5.14 and 5.15). This means that areas for model improvement can be identified at scales smaller than the global. When JULES was driven with WFDEI-GPCC (JULES-WFDEI-GPCC; Table 5.1), JULES simulates total annual GPP to be 675 Pg C, 592 Pg C and 81 Pg C for forests, grasslands and shrubs, respectively (Figure 5.13a) with annual average GPP for forests, grasslands and shrubs being 61 Pg C year^{-1}, 54 Pg C year^{-1} and 7 Pg C year^{-1}, respectively. With the exception of shrubs, JULES overestimates total annual GPP by 13 % and 32 % compared to FLUXNET-MTE and MODIS GPP, respectively, for forests and by 10 % and 28 % compared to FLUXNET-MTE and MODIS GPP, respectively, for grasslands (Figure 5.13a). Differences between JULES, FLUXNET-MTE and MODIS GPP for shrubs are small with total annual GPP ranging within 77–86 Pg C.

The differences in total annual GPP at the global scale is mainly due to differences between model simulated and observed GPP in the tropics (30°S–30°N) (Figure 5.13b). In the tropics, JULES simulates total annual GPP to be 553 Pg C, 429 Pg C and 58 Pg C for forests, grasslands and shrubs, respectively, for 2000–2010. JULES overestimates total annual GPP by 20 % and 41 % compared to FLUXNET-MTE and MODIS GPP, respectively, for forests and by 25 % and 48 % compared to FLUXNET-MTE and MODIS GPP, respectively, for grasslands. Differences between model simulated and observed GPP are small with total annual GPP for shrubs ranging from 48–58 Pg C. In the extratropics (30°N–90°N and 30°S–90°S), differences between model and observed GPP are small with total annual GPP for forests, grasslands and shrubs to be 122–136 Pg C, 163–196 Pg C and 23–31 Pg C, respectively (Figure 5.13c). These values show that tropical forests play a very important role in assimilating global terrestrial GPP.

Total annual GPP at the regional scale was examined by dividing the land area into seven regions (Table 5.2; Figure 5.1). The tropical regions (30°S–30°N) have been further divided up into three regions; Central and

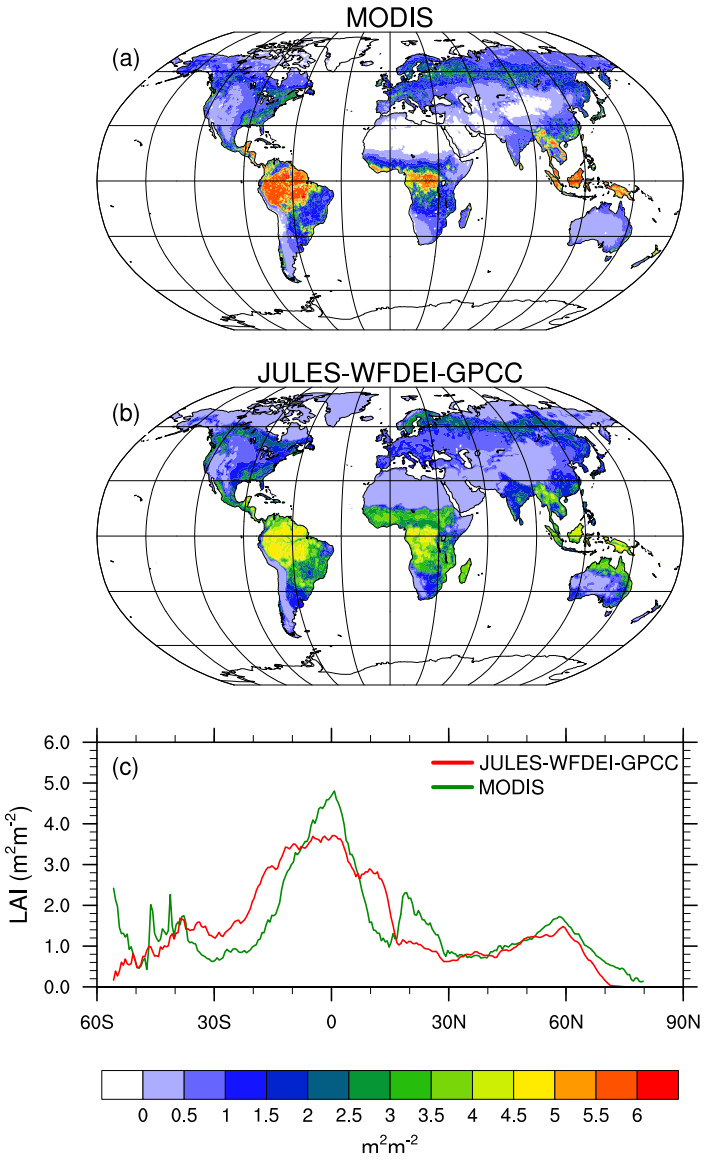

Figure 5.10: Monthly climatological and zonal mean of model simulated (JULES-WFDEI-GPCC) and observed (MODIS) LAI for the 2000–2010 period at the global scale. **(a)** and **(b)** display the monthly climatological mean LAI and **(c)** displays the monthly zonal mean.

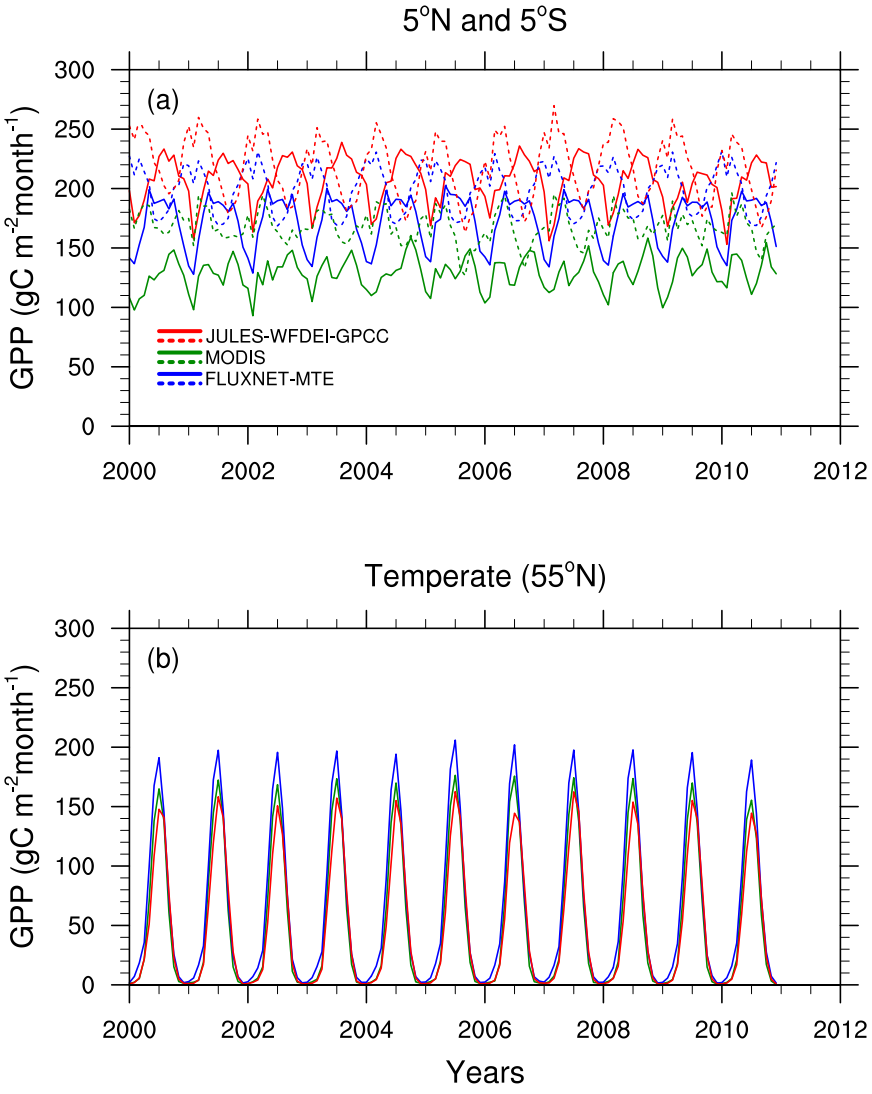

Figure 5.11: Monthly zonal mean model simulated (JULES-WFDEI-GPCC) and observed (FLUXNET-MTE and MODIS) GPP fluxes for the 2000–2010 period for tropical and temperate regions. **(a)** displays monthly zonal mean GPP at 5°N (solid lines) and 5°S (dotted lines) in the tropical regions and **(b)** at 55°N (solid lines) in the temperate regions.

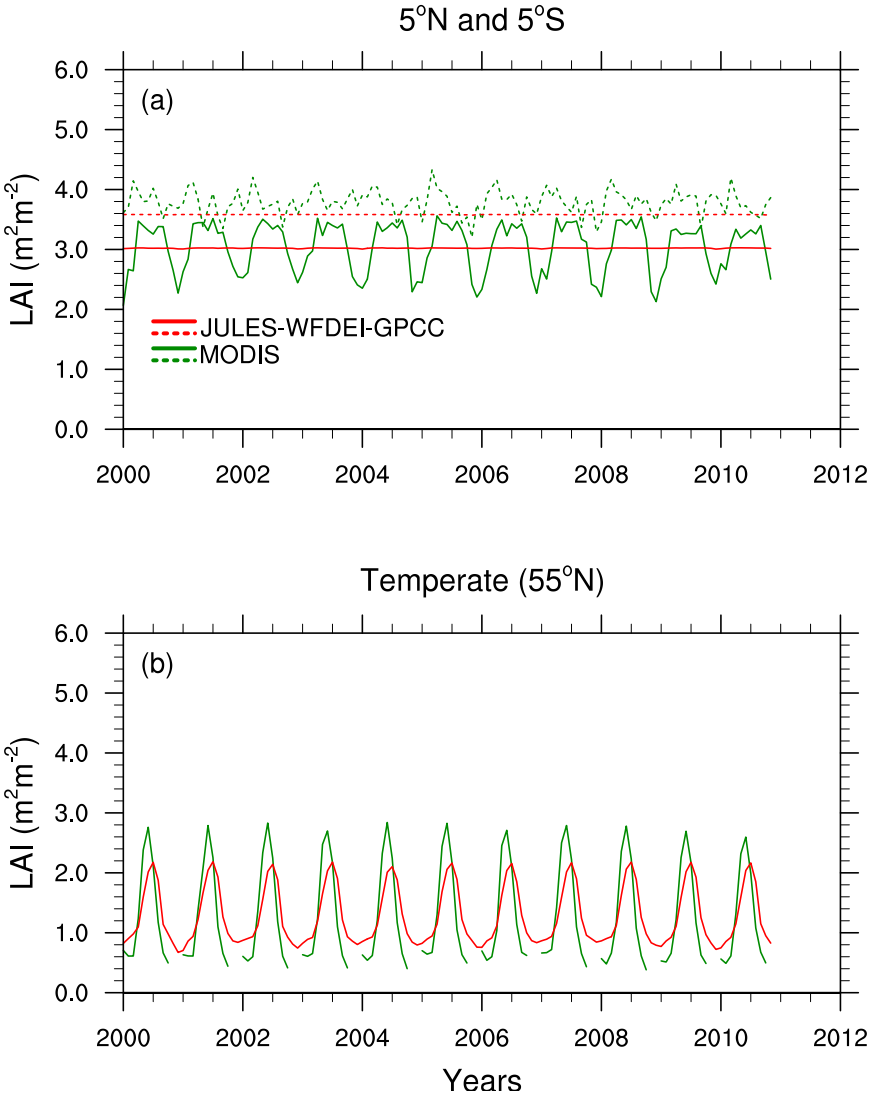

Figure 5.12: Monthly zonal mean model simulated (JULES-WFDEI-GPCC) and observed (MODIS) LAI for the 2000–2010 period for tropical and temperate regions. **(a)** displays monthly zonal mean LAI at at 5°N (solid lines) and 5°S (dotted lines) in the tropical regions and **(b)** at 55°N (solid lines) in the temperate regions.

South America, Africa and South and South-East Asia. The extratropics (30°N–90°N and 30°S–90°S) have been divided into four regions; Europe, Northern Asia, North America and Greenland and the extratropical Southern Hemisphere. The trends observed in total annual GPP (Figure 5.13) are also observed at the regional scale with JULES overestimating total annual GPP compared to FLUXNET-MTE and MODIS in the tropics (Figures 5.14c, e and f). JULES overestimates total annual GPP compared to FLUXNET-MTE and MODIS by 9 % and 28 %, respectively, for forests and by 14 % and 36 %, respectively, for grasslands in the American tropics (Figure 5.14f); by 32 % and 45 %, respectively, for forests and by 36 % and 44 % , for grasslands in the African tropics (Figure 5.14e); and by 29 % and 63 %, respectively, for forests and by 27 % and 65 %, respectively, for grasslands in South and South-East Asia (Figure 5.14c). By normalising the FLUXNET-MTE and MODIS GPP by JULES GPP for these three regions (Figures 5.15c, e and f), it is easier to see the differences between the model simulated and observation-based estimates. The dashed line at y=1 for the various regions in Figure 5.15 represents where the model and observation total annual GPP match.

In the extratropics, differences between JULES, FLUXNET-MTE and MODIS GPP are small with total annual GPP ranging from 18–22 Pg C and 48–60 Pg C for forests and grasslands, respectively, in Europe, 47–54 Pg C and 51–65 Pg C for forests and grasslands, respectively, in Northern Asia, 46–51 Pg C and 40–48 Pg C for forests and grasslands, respectively, in North America and Greenland and 7–8 Pg C and 19–20 Pg C for forests and grasslands, respectively, in the Extratropical Southern Hemisphere (Figures 5.14a, b, d and g; Figures 5.15). These results show that JULES overestimates GPP fluxes in the tropics, but is able to simulate fluxes in the extratropics. This was observed with the evaluation of JULES using global and local datasets at multiple flux tower sites in Chapter 4. For the two tropical sites (Santarem Km67 and Santarem Km83), the model was found to overestimate GPP fluxes when using global data (Figure 4.2) with the reason for this being biases in the meteorological data.

In general, JULES was able to simulate GPP in the extratropics, but overestimated GPP in the tropics compared to FLUXNET-MTE and MODIS estimates. The inability of the model to correctly simulate GPP was found in all three tropical regions.

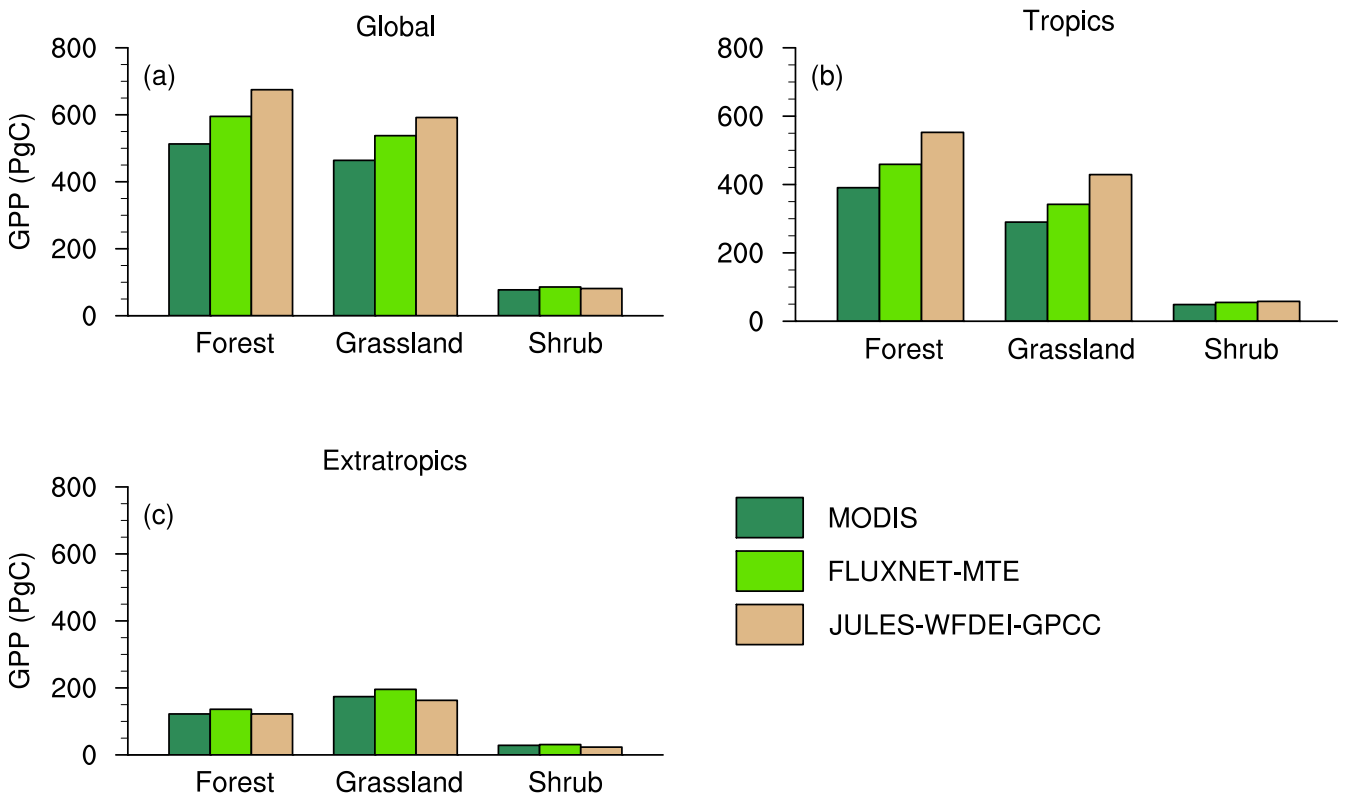

Figure 5.13: Total annual model simulated (JULES-WFDEI-GPCC) and observed (FLUXNET-MTE and MODIS) GPP fluxes for the 2000–2010 period at the global and regional scales (tropics and extratropics) for 3 biome types (Forest, Grassland and Shrub). **(a)** displays the global total annual GPP, **(b)** for the tropics (30°S–30°N) and **(c)** for the extratropics (30°N–90°N and 30°S–90°S) for forests, grasslands and shrubs.

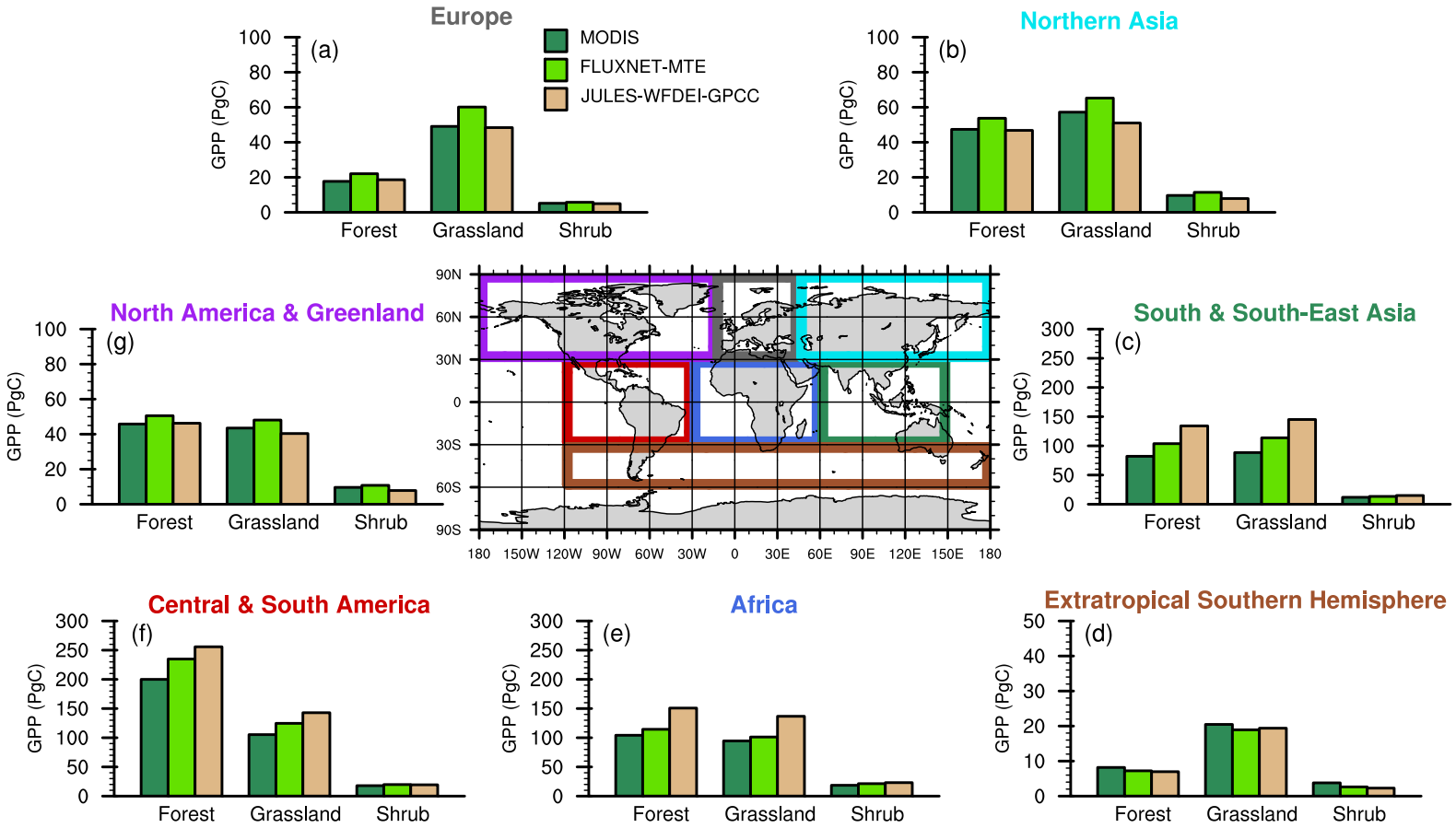

Figure 5.14: Total annual model simulated (JULES-WFDEI-GPCC) and observed (FLUXNET-MTE and MODIS) GPP fluxes for the 2000–2010 period for various regions (Table 5.2) for 3 biome types (Forest, Grassland and Shrub). **(a)** displays integrated GPP for Europe (grey box), **(b)** for Northern Asia (cyan box), **(c)** for South & South-Asia (green box), **(d)** for extratropical Southern Hemisphere (brown box), **(e)** for Africa (blue box), **(f)** for Central & South America (red box) and **(g)** for North America & Greenland (purple box).

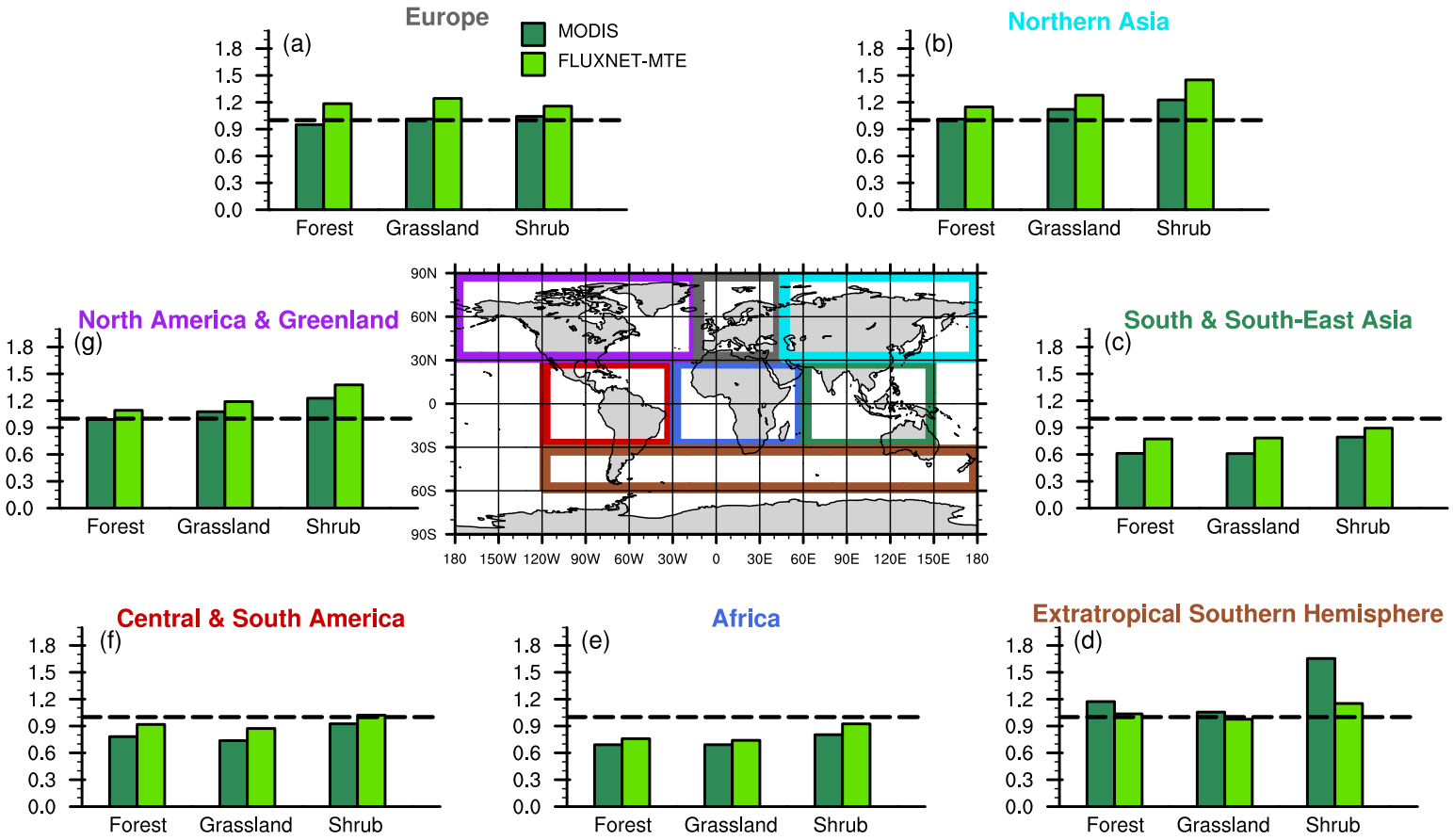

Figure 5.15: Total annual observed (FLUXNET-MTE and MODIS) GPP fluxes for the 2000–2010 period normalised by model simulated (JULES-WFDEI-GPCC) GPP for various regions (Table 5.2) for 3 biome types (Forest, Grassland and Shrub). **(a)** displays integrated GPP for Europe (grey box), **(b)** for Northern Asia (cyan box), **(c)** for South & South-Asia (green box), **(d)** for extratropical Southern Hemisphere (brown box), **(e)** for Africa (blue box), **(f)** for Central & South America (red box) and **(g)** for North America & Greenland (purple box). The dashed line at y=1 represents where the model and observations match.

5.3.4 Sensitivity to spatial resolution

When simulations of GPP were performed at lower spatial resolutions (JULES-WFDEI-GPCC-1degree and JULES-WFDEI-GPCC-2degree; Table 5.1), it was found that the average annual global GPP at $0.5^\circ \times 0.5^\circ$, $1^\circ \times 1^\circ$ and $2^\circ \times 2^\circ$ spatial resolutions was 140 $\mathrm{Pg\,C\,year^{-1}}$, 141 $\mathrm{Pg\,C\,year^{-1}}$ and 142 $\mathrm{Pg\,C\,year^{-1}}$, respectively (Figures 5.5c, 5.16c and 5.17c). The percentage differences between JULES GPP and FLUXNET-MTE and MODIS GPP at the various spatial resolutions are approximately equal with JULES differing from FLUXNET-MTE and MODIS by 25 % and 8 %, respectively, at $0.5^\circ \times 0.5^\circ$ spatial resolution, by 26 % and 8 %, respectively, at $1^\circ \times 1^\circ$ resolution and by 26 % and 9 % , respectively, at $2^\circ \times 2^\circ$ resolution (Figure 5.4).

The annual average global GPP for FLUXNET-MTE and MODIS at the various resolutions are also similar with global GPP being 130 $\mathrm{Pg\,C\,year^{-1}}$ and 112 $\mathrm{Pg\,C\,year^{-1}}$, respectively, at $0.5^\circ \times 0.5^\circ$ resolution, 136 $\mathrm{Pg\,C\,year^{-1}}$ and 113 $\mathrm{Pg\,C\,year^{-1}}$, respectively, at $1^\circ \times 1^\circ$ resolution and 138 $\mathrm{Pg\,C\,year^{-1}}$ and 113 $\mathrm{Pg\,C\,year^{-1}}$, respectively, at $2^\circ \times 2^\circ$ resolution (Figures 5.5a and b, 5.16a and b, and 5.17a and b). The zonal mean of modelled total annual GPP at various spatial resolutions are approximately equal (Figure 5.18) with the greatest differences occurring in the tropics (Figure 5.5d, 5.16d and 5.17d). This insensitivity to spatial resolution is a useful result since it means that model simulations can be performed at $2^\circ \times 2^\circ$ resolution with little difference to model output at $0.5^\circ \times 0.5^\circ$ and due to the lower computational cost, model run times are short (16× faster than the $0.5^\circ \times 0.5^\circ$ resolution simulations).

The insensitivity of the model to spatial resolution is also shown when comparing GPP fluxes for forests, grasslands and shrubs at the global and regional scales (Figure 5.19). At the global scale, differences between the model simulated total annual GPP at $0.5^\circ \times 0.5^\circ$, $1^\circ \times 1^\circ$ and $2^\circ \times 2^\circ$ are small for forests, grasslands and shrub ranging with total annual GPP ranging from 668–675 Pg C, 592–598 Pg C and 81–84 Pg C, respectively (Figure 5.19a). This shows that the insensitivity of the model to spatial resolution occurs at both regional and global scales.

The model performs equally well in the tropics and extratropics at lower spatial resolutions with total annual GPP of 545–553 Pg C, 429–431 Pg C and 58–60 Pg C for forests, grasslands and shrubs, respectively, in the trop-

ics and 122–123 Pg C, 163–167 Pg C and 23–24 Pg C for forests, grasslands and shrubs, respectively, in the extratropics (Figures 5.19b and c). Even at lower spatial resolutions, JULES (JULES-WFDEI-GPCC, JULES-WFDEI-GPCC-1degree and JULES-WFDEI-GPCC-2degree) still overestimates total annual GPP in the tropics (Figure 5.19b; Figures 5.20c, e and f) and in the extratropics, is able to simulate GPP (Figure 5.19b; Figures 5.20a, b, d and g) with the exception of shrubs in northern Asia, the extratropical Southern Hemisphere and North America and Greenland (Figures 5.20b, d and g).

A similar trend is shown in the coefficient of variation (calculated using the annual GPP for each of the seven regions) with JULES (driven with WFDEI-GPCC at $0.5^\circ \times 0.5^\circ$, $1^\circ \times 1^\circ$ and $2^\circ \times 2^\circ$ spatial resolutions) not able to capture the year to year variation in GPP for shrubs in northern Asia, the extratropical Southern Hemisphere and North America and Greenland with an average coefficient of variation of 5 %, 15 % and 7 %, respectively (Figures 5.21b, d and g). The insensitivity of the model to these lower spatial resolutions is also shown in the seasonal cycle of monthly climatologies (Figure 5.22a), the coefficient of variation of the monthly climatologies (Figure 5.22b) and the monthly anomalies (Figure 5.22c).

In general, when simulating GPP at global and regional scales, it was found that there was little impact from varying spatial resolution ($0.5^\circ \times 0.5^\circ$, $1^\circ \times 1^\circ$ and $2^\circ \times 2^\circ$).

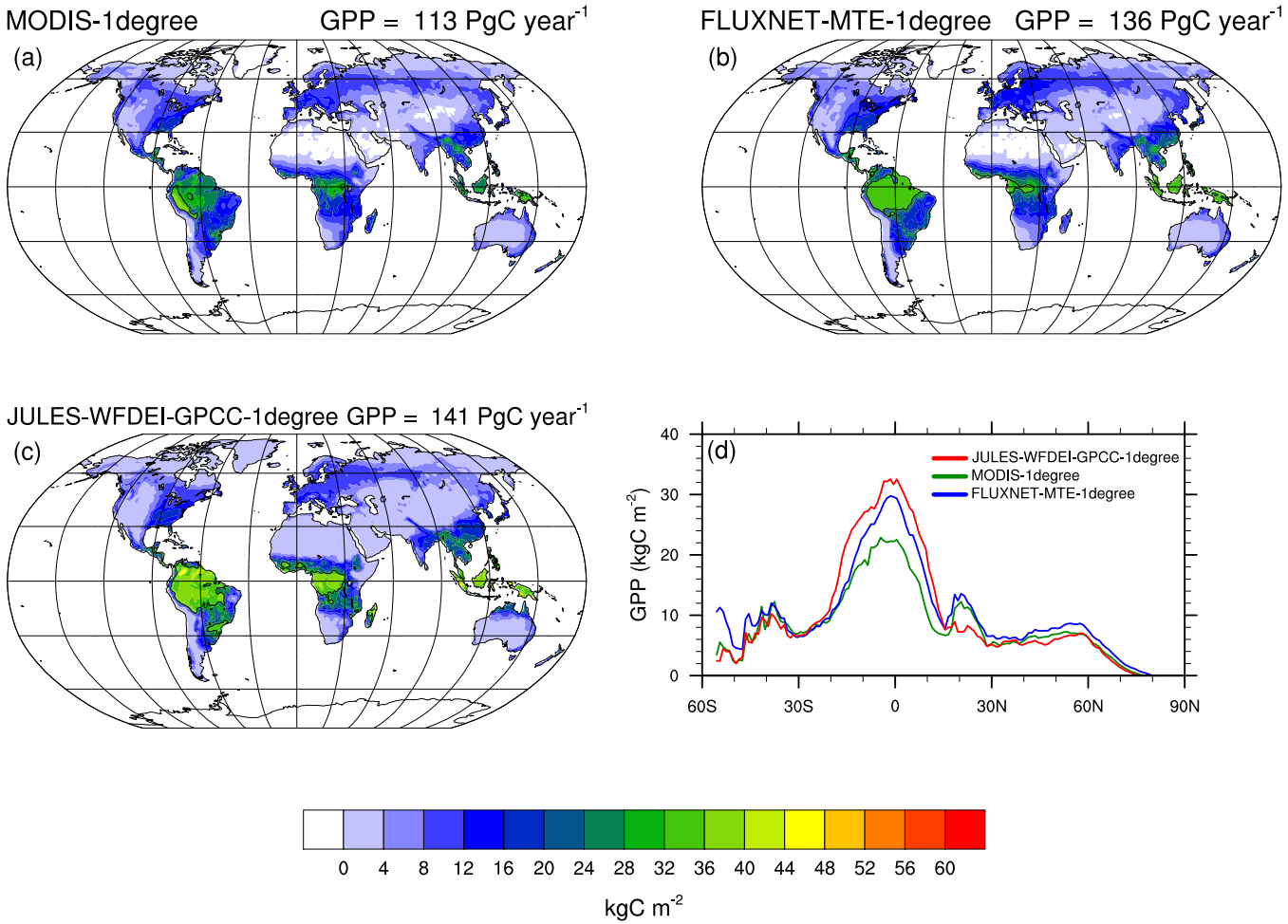

Figure 5.16: Total annual and zonal mean model simulated (JULES-WFDEI-GPCC-1degree) and observed (FLUXNET-MTE-1degree and MODIS-1degree) GPP fluxes for the 2000–2010 period at the global scale ($1^\circ \times 1^\circ$ spatial resolution). **(a)**, **(b)** and **(c)** show the total annual GPP of JULES-WFDEI-GPCC-1degree, FLUXNET-MTE-1degree and MODIS-1degree GPP, respectively. At the top right of each subplot, the average of the annual GPP for 2000–2010 is displayed. **(d)** shows the zonal mean of JULES-WFDEI-GPCC-1degree, FLUXNET-MTE-1degree and MODIS-1degree GPP, respectively.

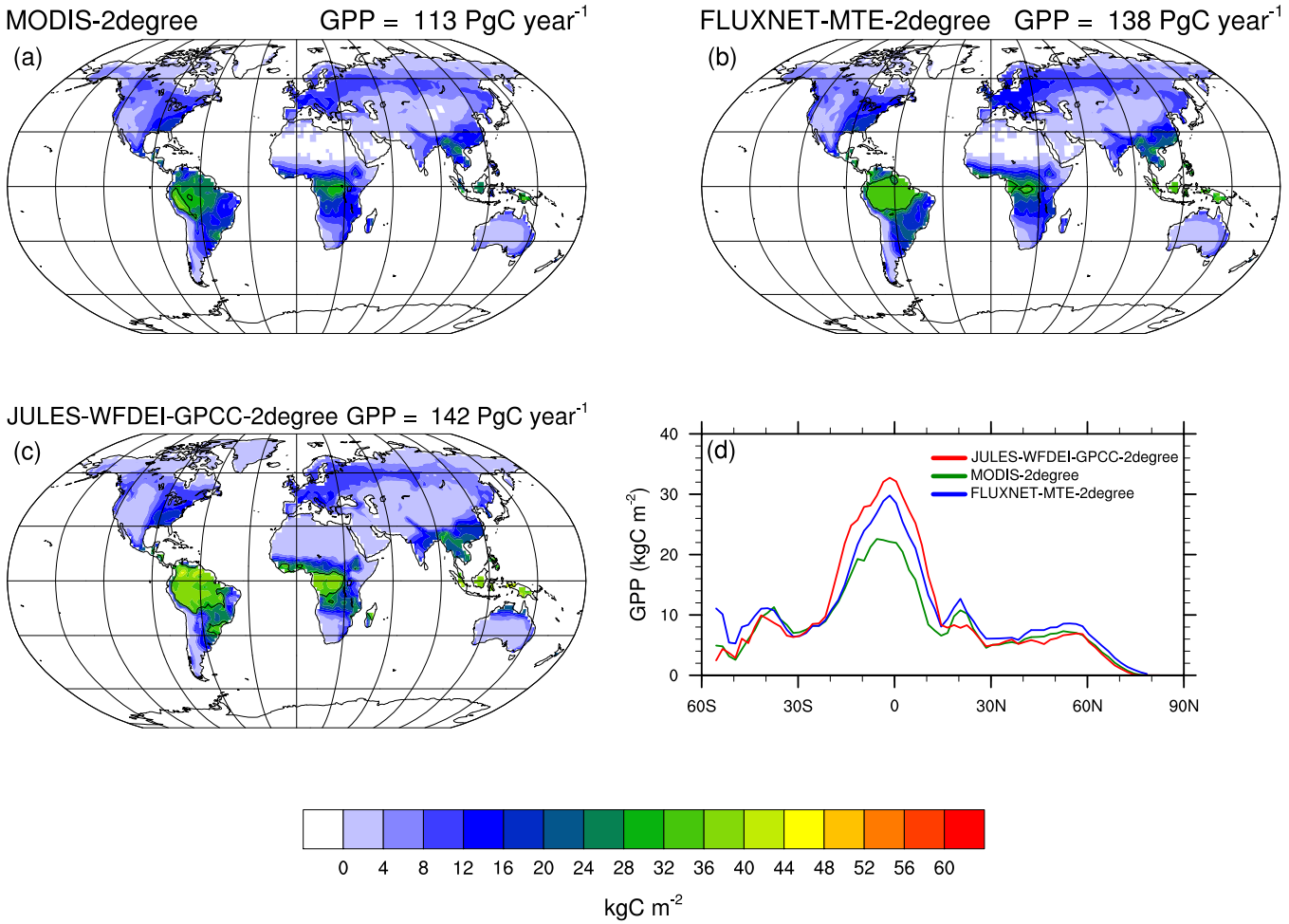

Figure 5.17: Total annual and zonal mean model simulated (JULES-WFDEI-GPCC-2degree) and observed (FLUXNET-MTE-2degree and MODIS-2degree) GPP fluxes for the 2000–2010 period at the global scale ($2^\circ \times 2^\circ$ spatial resolution). **(a)**, **(b)** and **(c)** show the total annual GPP of JULES-WFDEI-GPCC-2degree, FLUXNET-MTE-2degree and MODIS-2degree GPP, respectively. At the top right of each subplot, the average of the annual GPP for 2000–2010 is displayed. **(d)** shows the zonal mean of JULES-WFDEI-GPCC-2degree, FLUXNET-MTE-2degree and MODIS-2degree GPP, respectively.

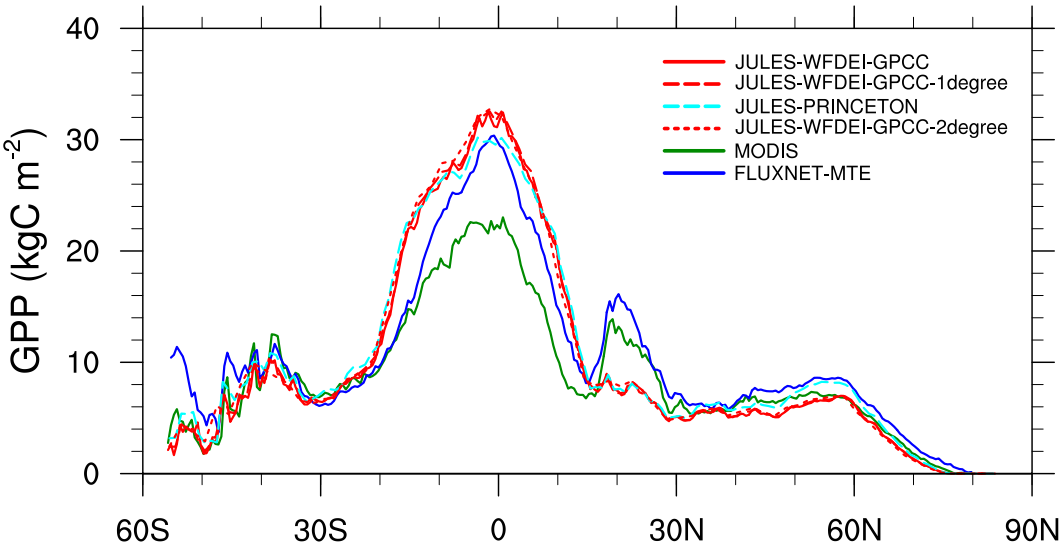

Figure 5.18: Zonal mean of total annual model simulated (JULES-WFDEI-GPCC, JULES-WFDEI-GPCC-1degree, JULES-PRINCETON and JULES-WFDEI-GPCC-2degree) and observed (FLUXNET-MTE and MODIS) GPP fluxes for 2000–2010. JULES-WFDEI-GPCC, FLUXNET-MTE and MODIS are at $0.5^\circ \times 0.5^\circ$ spatial resolution.

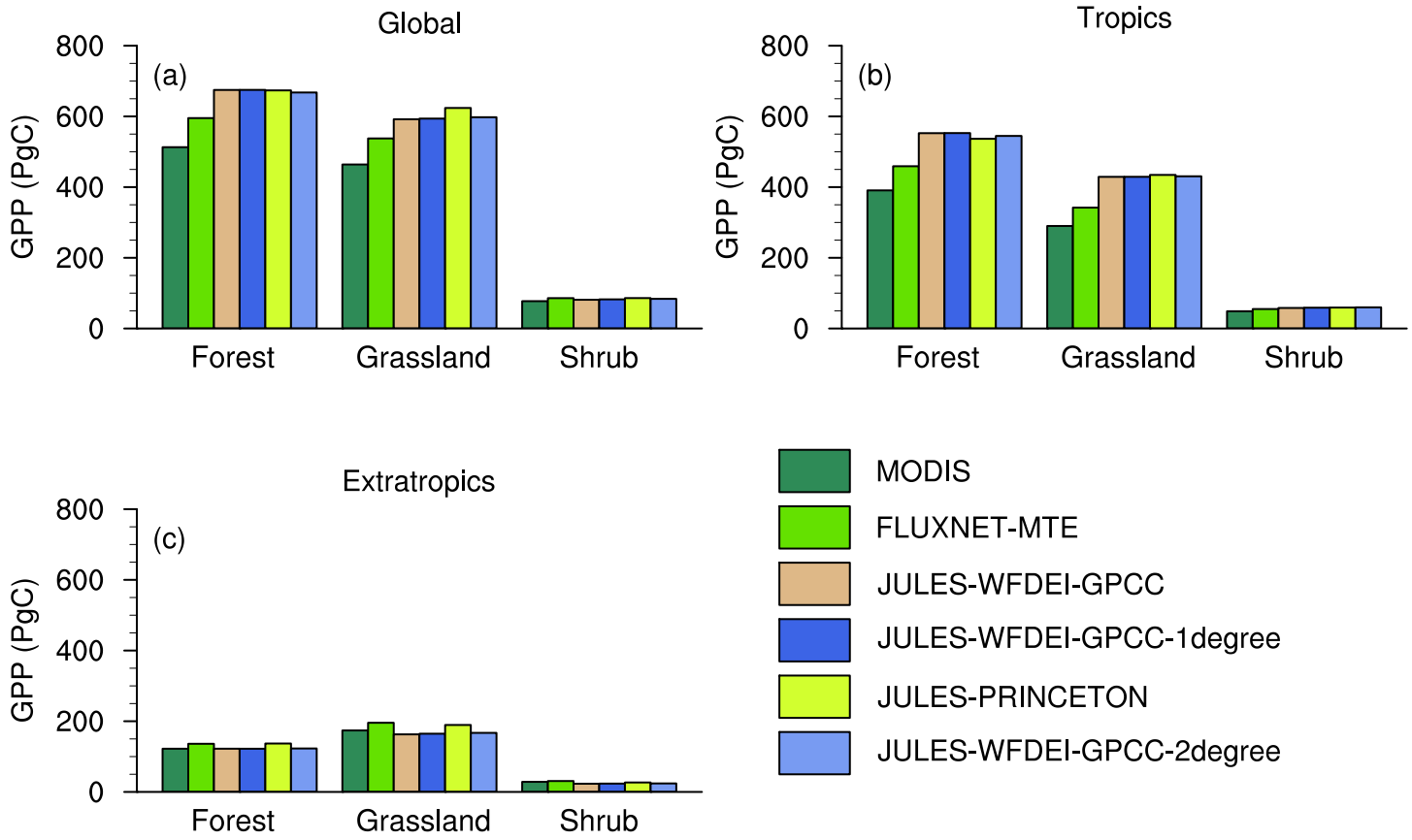

Figure 5.19: Total annual model simulated (JULES-WFDEI-GPCC, JULES-WFDEI-GPCC-1degree, JULES-PRINCETON and JULES-WFDEI-GPCC-2degree) and observed (FLUXNET-MTE and MODIS) GPP fluxes for the 2000–2010 period at the global and regional scales (tropics and extratropics) for 3 biome types (Forest, Grassland and Shrub). **(a)** displays the global total annual GPP, **(b)** for the tropics (30°N–30°S) and **(c)** for the extratropics (90°N–30°N and 30°S–90°S) for forests, grasslands and shrubs.

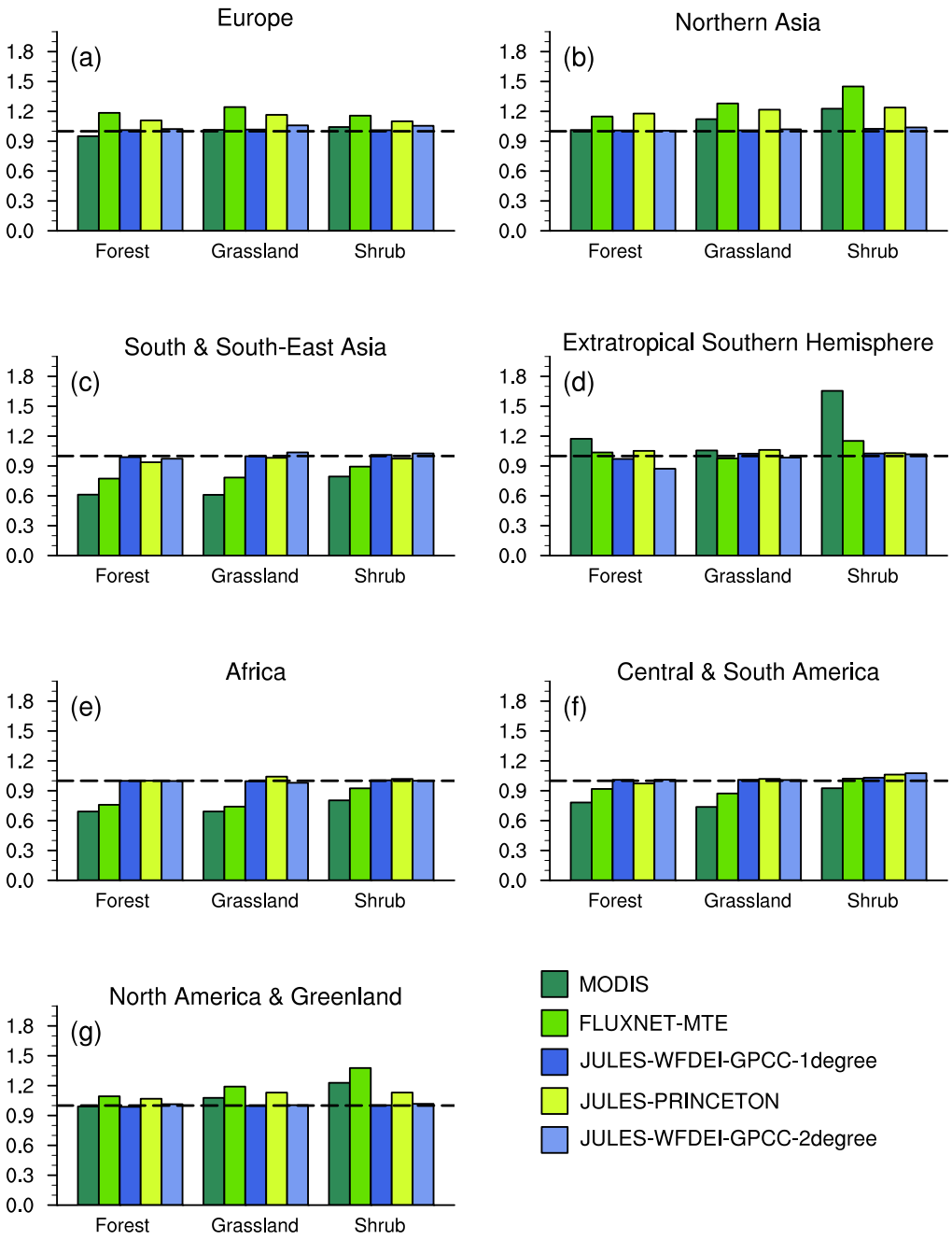

Figure 5.20: Total annual model simulated (JULES-WFDEI-GPCC-1degree, JULES-PRINCETON and JULES-WFDEI-GPCC-2degree) observed (FLUXNET-MTE and MODIS) GPP fluxes for the 2000–2010 period normalised by model simulated (JULES-WFDEI-GPCC) GPP for various regions (Table 5.2) for 3 biome types (Forest, Grassland and Shrub). **(a)** displays normalised GPP for Europe, **(b)** for Northern Asia, **(c)** for South & South-Asia, **(d)** for extratropical Southern Hemisphere, **(e)** for Africa, **(f)** for Central & South America and **(g)** for North America & Greenland. The dotted line at y=1 represents where the model and observations match.

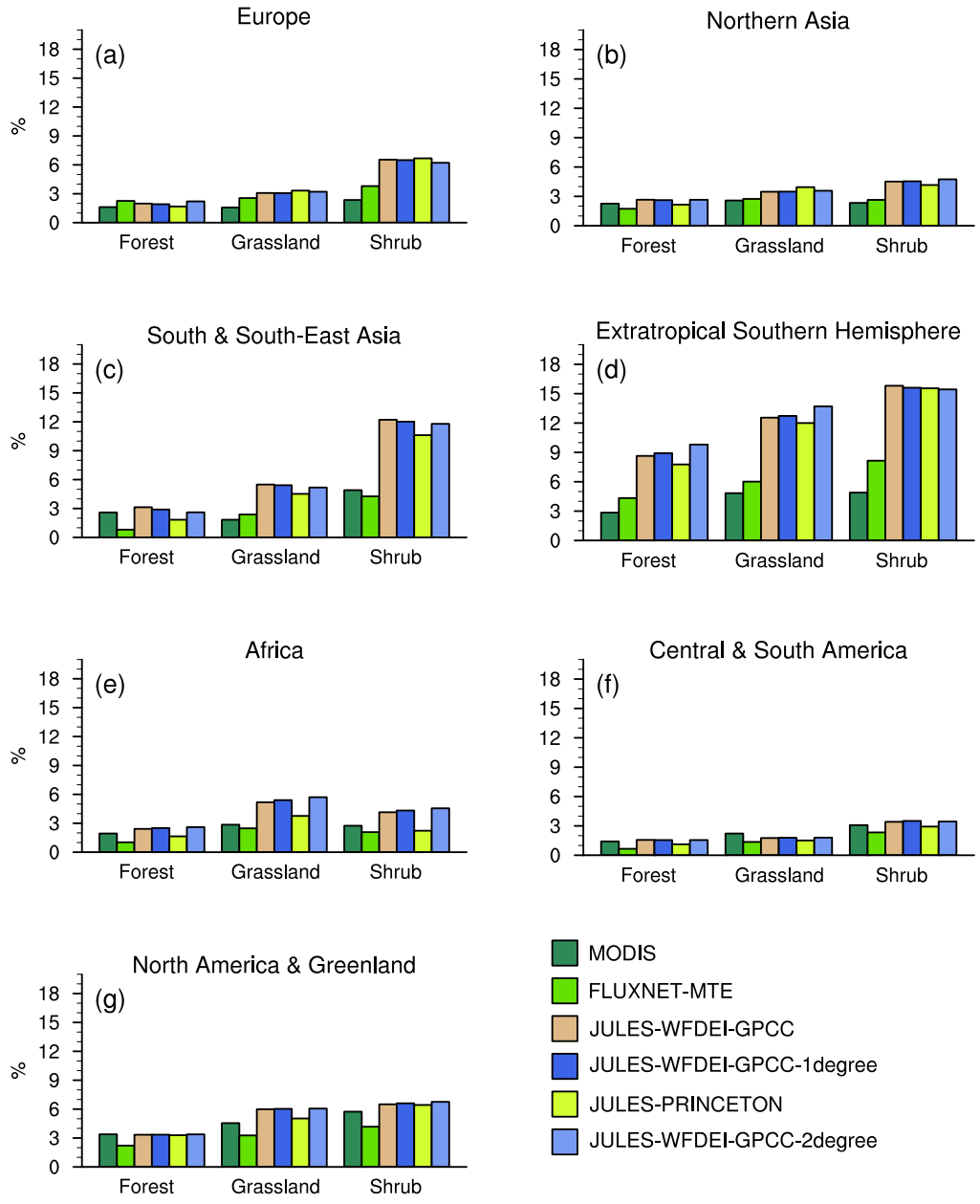

Figure 5.21: Coefficient of variation (CV) computed for annual GPP for model simulated (JULES-WFDEI-GPCC-1degree, JULES-PRINCETON and JULES-WFDEI-GPCC-2degree) and observed (FLUXNET-MTE and MODIS) GPP fluxes for 2000–2010 for various regions (Table 5.2) for 3 biome types (Forest, Grassland and Shrub). **(a)** displays CV for Europe, **(b)** for Northern Asia, **(c)** for South & South-Asia, **(d)** for extratropical Southern Hemisphere, **(e)** for Africa, **(f)** for Central & South America and **(g)** for North America & Greenland.

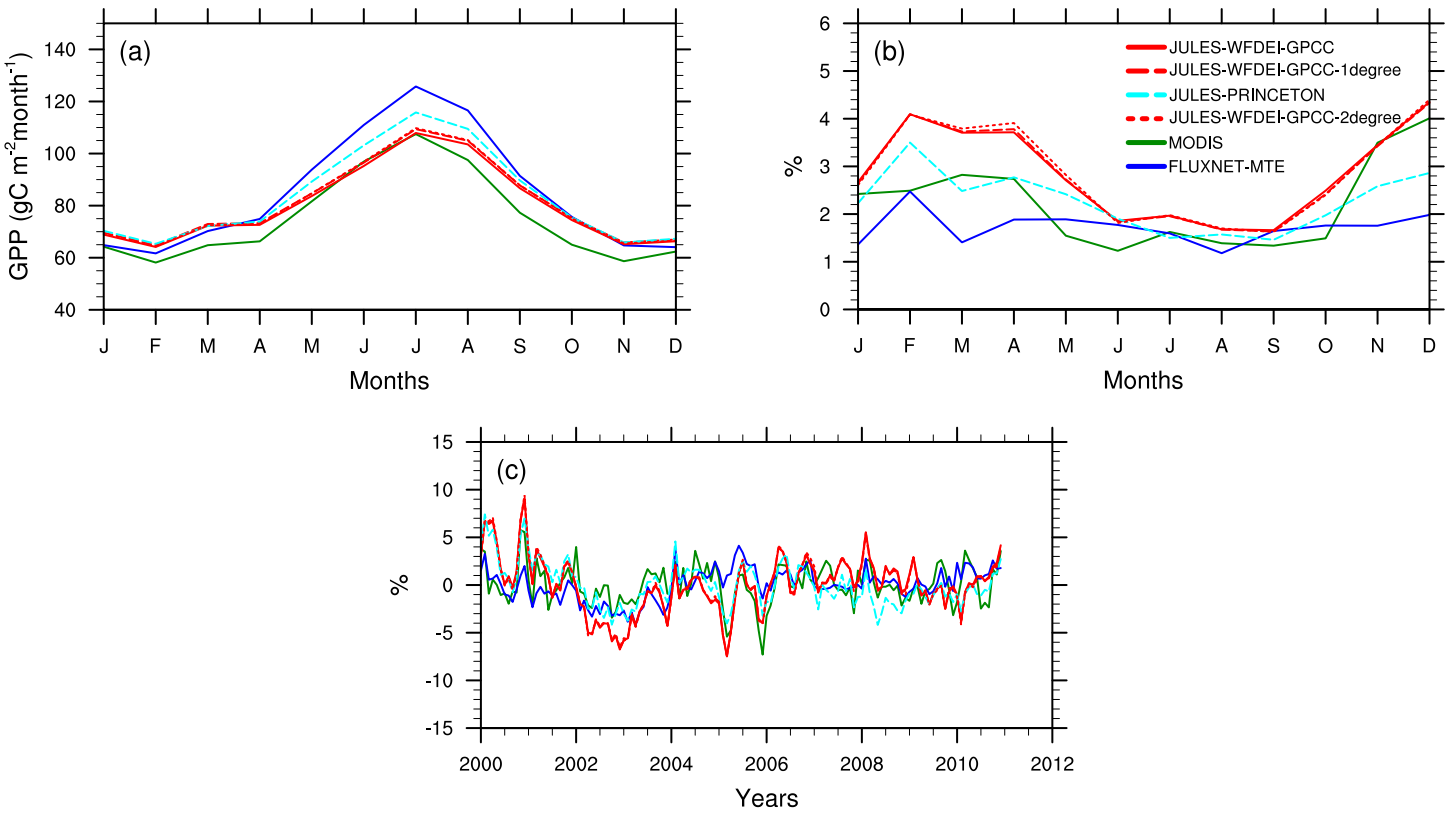

Figure 5.22: Comparison of model simulated (JULES-WFDEI-GPCC, JULES-WFDEI-GPCC-1degree, JULES-PRINCETON and JULES-WFDEI-GPCC-2degree) and observed (FLUXNET-MTE and MODIS) GPP fluxes for 2000–2010 at the global scale. **(a)** displays the global area-weighted average of the monthly climatologies, **(b)** displays the coefficient of variation (CV) expressed as percentages of the monthly climatologies and **(c)** displays the monthly anomalies (global area-weighted mean) expressed as percentages of the monthly climatologies (global area-weighted mean) for each month.

5.3.5 Sensitivity to meteorological dataset

When driven with the PRINCETON dataset (JULES-PRINCETON; Table 5.1), JULES simulates global GPP with an annual average of 145 Pg C year^{-1} (combined GPP across all terrestrial ecosystems) for 2000–2010 (Figure 5.23c). As observed when driving JULES with the WFDEI-GPCC dataset (Figure 5.5), JULES-PRINCETON also simulates higher global GPP than FLUXNET-MTE and MODIS (at 1° × 1° spatial resolution) by 7 % and 28 % on average, respectively. This compares equally well to global GPP simulated by JULES when driven with the WFDEI-GPCC dataset, which had an annual average global GPP of 140 Pg C year^{-1}. GPP simulated by JULES-WFDEI-GPCC was only higher than that of FLUXNET-MTE and MODIS (at 0.5° × 0.5° spatial resolution) by 8 % and 25 % on average, respectively.

The trend in zonal mean of total annual GPP simulated by JULES (driven with PRINCETON) is similar to that when driven with WFDEI-GPCC (at 1° × 1° spatial resolution) with differences being mostly in the tropics (Figures 5.16d, 5.23d and 5.18). Differences between the zonal means of JULES-WFDEI-GPCC-1degree, JULES-PRINCETON, FLUXNET-MTE-1degree and MODIS-1degree are shown in Figure 5.24. The trend in differences between JULES-PRINCETON and JULES-WFDEI-GPCC-1degree and the observation-based estimates (FLUXNET-MTE and MODIS) is similar with model output from both simulations overestimating GPP in the tropics.

When JULES was driven with the PRINCETON dataset, it was found that simulated photosynthesis was mostly Rubisco-limited (Figures 5.25). A similar trend was found when JULES was driven with the WFDEI-GPCC dataset (Figure 5.6). Similar trends in transport limitation were found with the JULES-PRINCETON model simulation, though the number of model gridboxes in which transport limitation dominated was less than that for the JULES-WFDEI-GPCC-1degree model simulation. When comparing the model gridbox fractions for the JULES-WFDEI-GPCC-1degree and JULES-PRINCETON model simulations, it was found that when JULES was driven with the PRINCETON dataset, simulated photosynthesis was more Rubisco-limited than when the model was driven with WFDEI-GPCC (Figure 5.26). Light-limitation was more important in simulating photo-

synthesis when JULES was driven with WFDEI-GPCC than PRINCETON (Figure 5.27). The percentage of model gridboxes which are transport-limited show a pronounced geographical variation with the WFDEI-GPCC driven simulation being more transport-limited in the Southern Hemisphere and the PRINCETON driven simulation being more transport-limited in the Northern Hemisphere (Figure 5.28).

Overall, when JULES was driven with the PRINCETON dataset, estimates of global GPP are similar to those from simulations when driven with WFDEI-GPCC (at $1^\circ \times 1^\circ$ spatial resolution). However, differences in model output between the two occurs mostly in the tropics. It was found that when JULES was driven with the PRINCETON dataset, simulated photosynthesis was Rubisco-limited. This is similar to the WFDEI-GPCC driven model simulation.

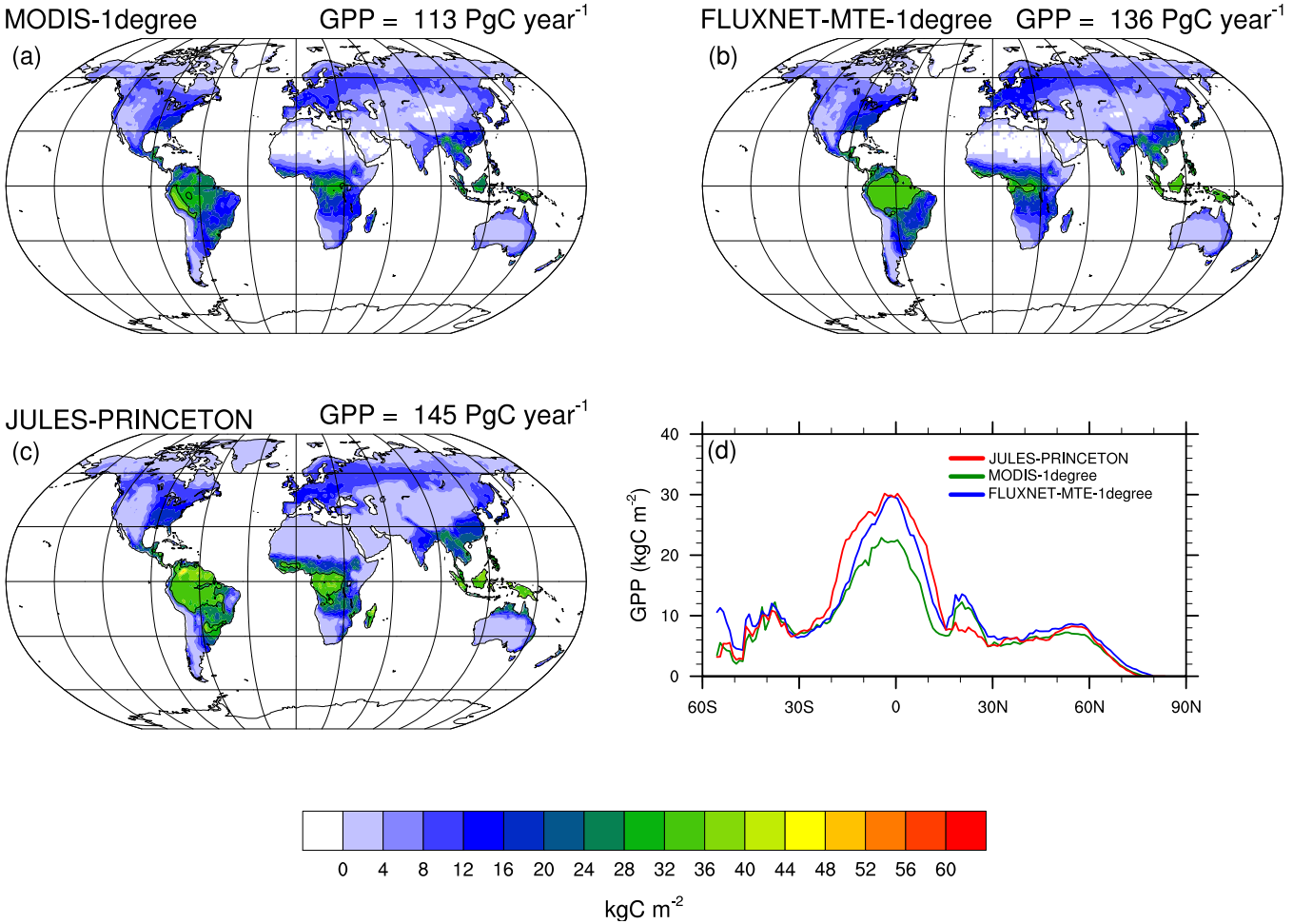

Figure 5.23: Total annual and zonal mean model simulated (JULES-PRINCETON) and observed (FLUXNET-MTE-1degree and MODIS-1degree) GPP fluxes for the 2000–2010 period at the global scale ($1^\circ \times 1^\circ$ spatial resolution). **(a)**, **(b)** and **(c)** show the total annual GPP of JULES-PRINCETON, FLUXNET-MTE-1degree and MODIS-1degree GPP, respectively. At the top right of each subplot, the average of the annual GPP for 2000–2010 is displayed. **(d)** shows the zonal mean of JULES-PRINCETON, FLUXNET-MTE-1degree and MODIS-1degree GPP, respectively.

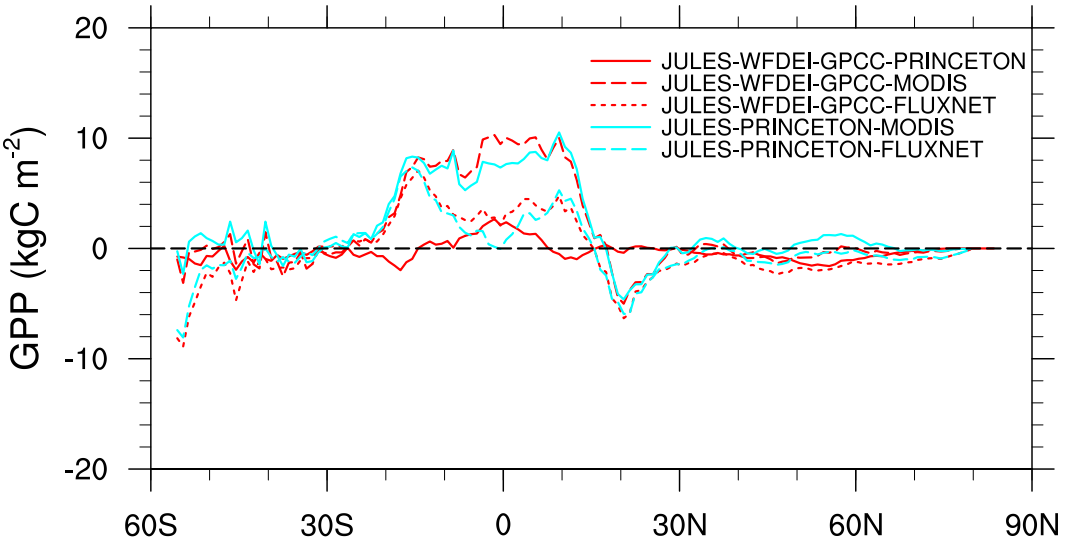

Figure 5.24: Difference in zonal mean of total annual model simulated (JULES-WFDEI-GPCC-1degree, JULES-PRINCETON) and observed (FLUXNET-MTE-1degree and MODIS-1degree) GPP fluxes for 2000–2010. JULES-WFDEI-GPCC-PRINCETON shows the difference in zonal mean between JULES-WFDEI-GPCC-1degree and JULES-PRINCETON, JULES-WFDEI-GPCC-MODIS between JULES-WFDEI-GPCC-1degree and MODIS-1degree, JULES-WFDEI-GPCC-FLUXNET between JULES-WFDEI-GPCC-1degree and FLUXNET-MTE-1degree, JULES-PRINCETON-MODIS between JULES-PRINCETON and MODIS-1degree, and JULES-PRINCETON-FLUXNET between JULES-PRINCETON and FLUXNET-MTE-1degree.

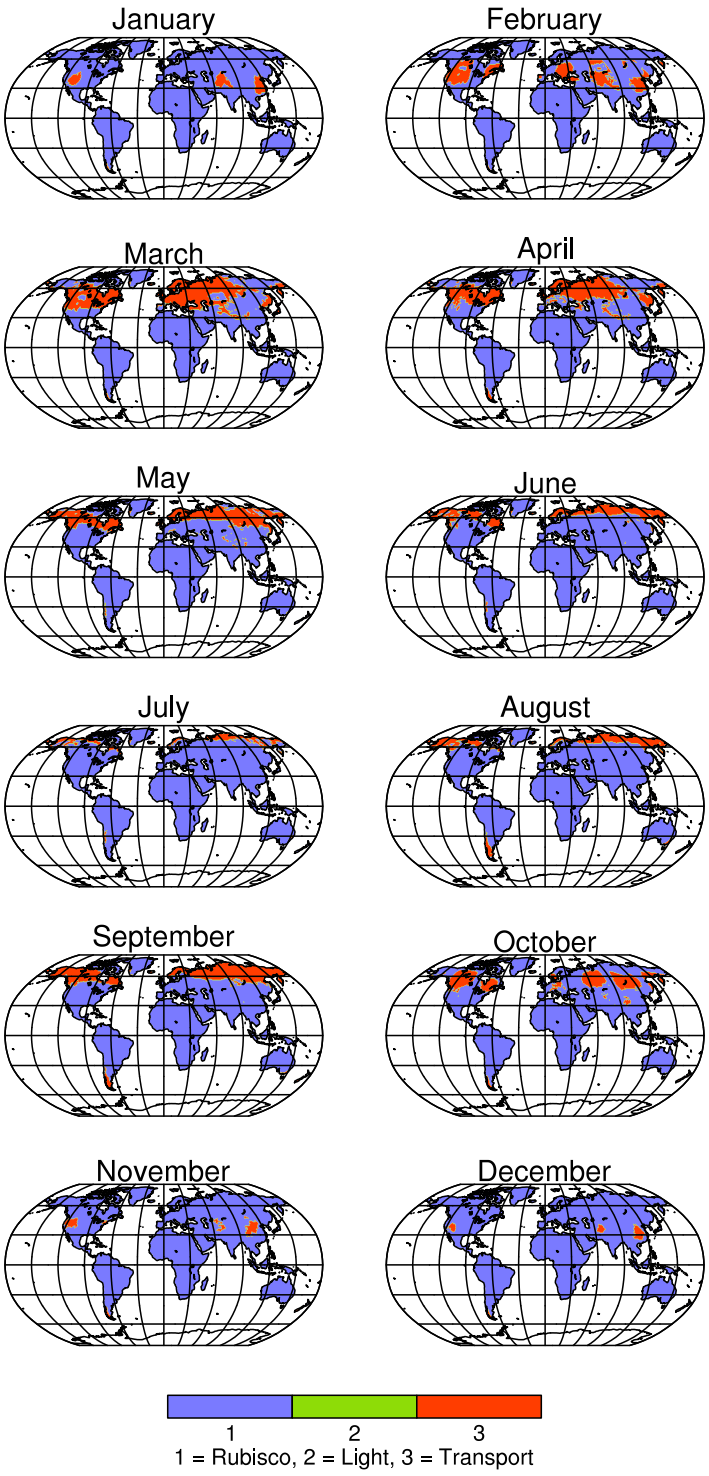

Figure 5.25: Monthly climatologies of potential (nonstressed by water and ozone) leaf photosynthesis minimum limiting rates (1 = Rubisco-limited, 2 = Light-limited and 3 = Transport-limited) which dominate model gridboxes from the JULES-PRINCETON model simulation at global scales (calculated using Method 1 in Appendix F). The Rubisco-limited, Light-limited and Transport-limited photosynthetic rates are determined by Equations 3.1, 3.2 and 3.3, respectively.

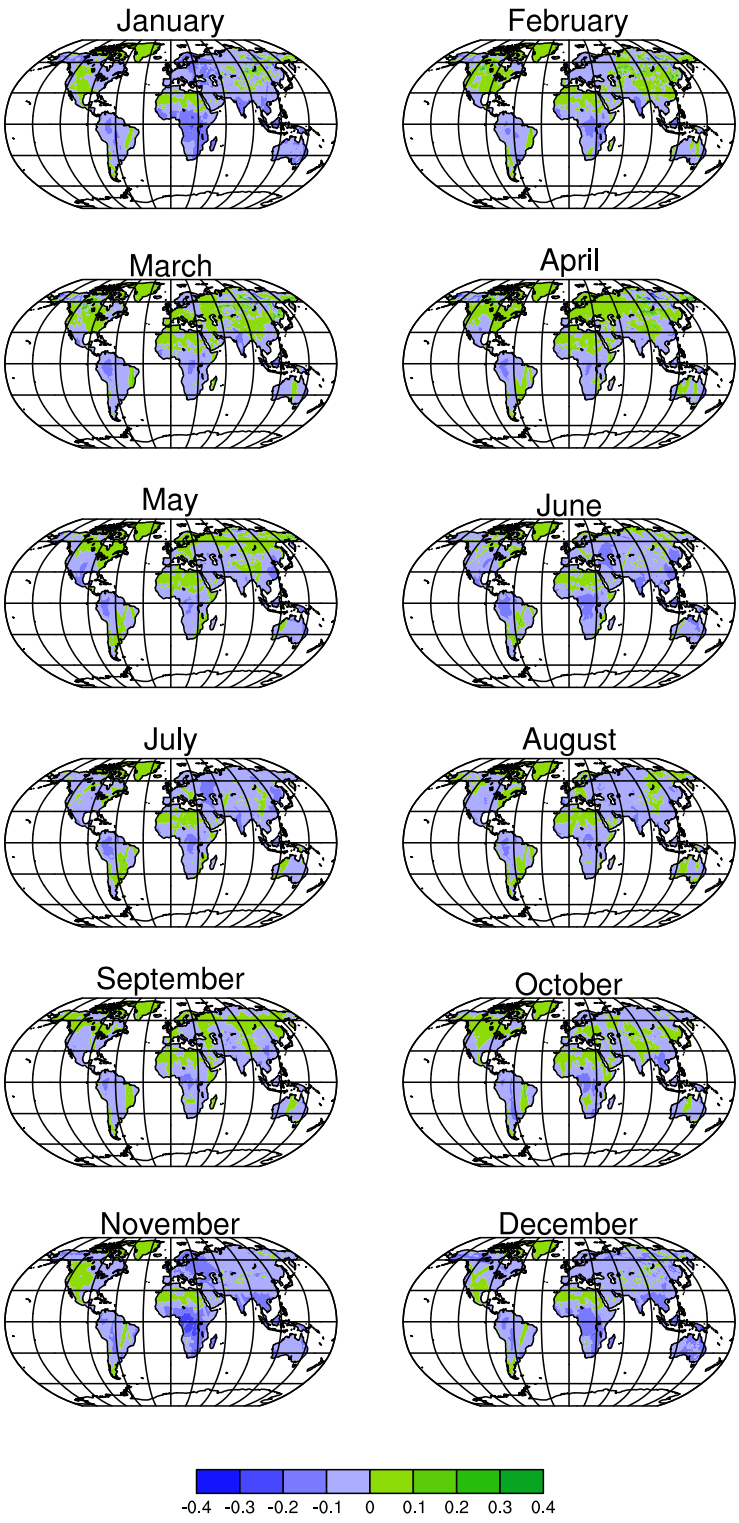

Figure 5.26: Difference in monthly climatologies of Rubisco-limited model gridbox fractions (0–1) between the JULES-WFDEI-GPCC-1degree and JULES-PRINCETON model simulations at global scales (calculated using Method 2 in Appendix F). Green means that fractions of model gridboxes that are Rubisco-limited in the JULES-WFDEI-GPCC-1degree model simulation are greater than those in the JULES-PRINCETON simulation and blue means the opposite.

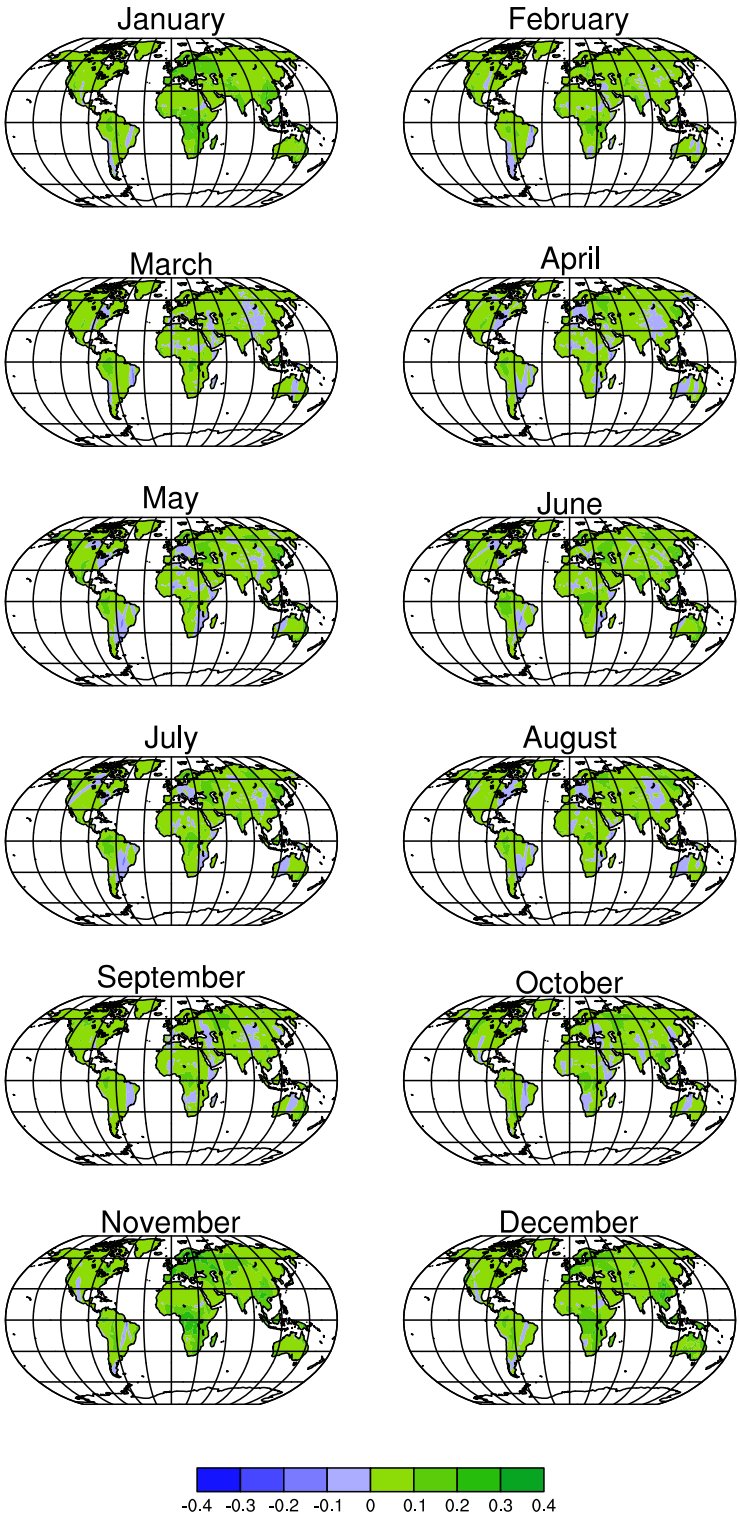

Figure 5.27: Difference in monthly climatologies of Light-limited model gridbox fractions (0–1) between the JULES-WFDEI-GPCC-1degree and JULES-PRINCETON model simulations at global scales (calculated using Method 2 in Appendix F). Green gridboxes mean that the fractions of model gridboxes that are Light-limited in the JULES-WFDEI-GPCC-1degree model simulation are greater than those in the JULES-PRINCETON simulation and blue means the opposite.

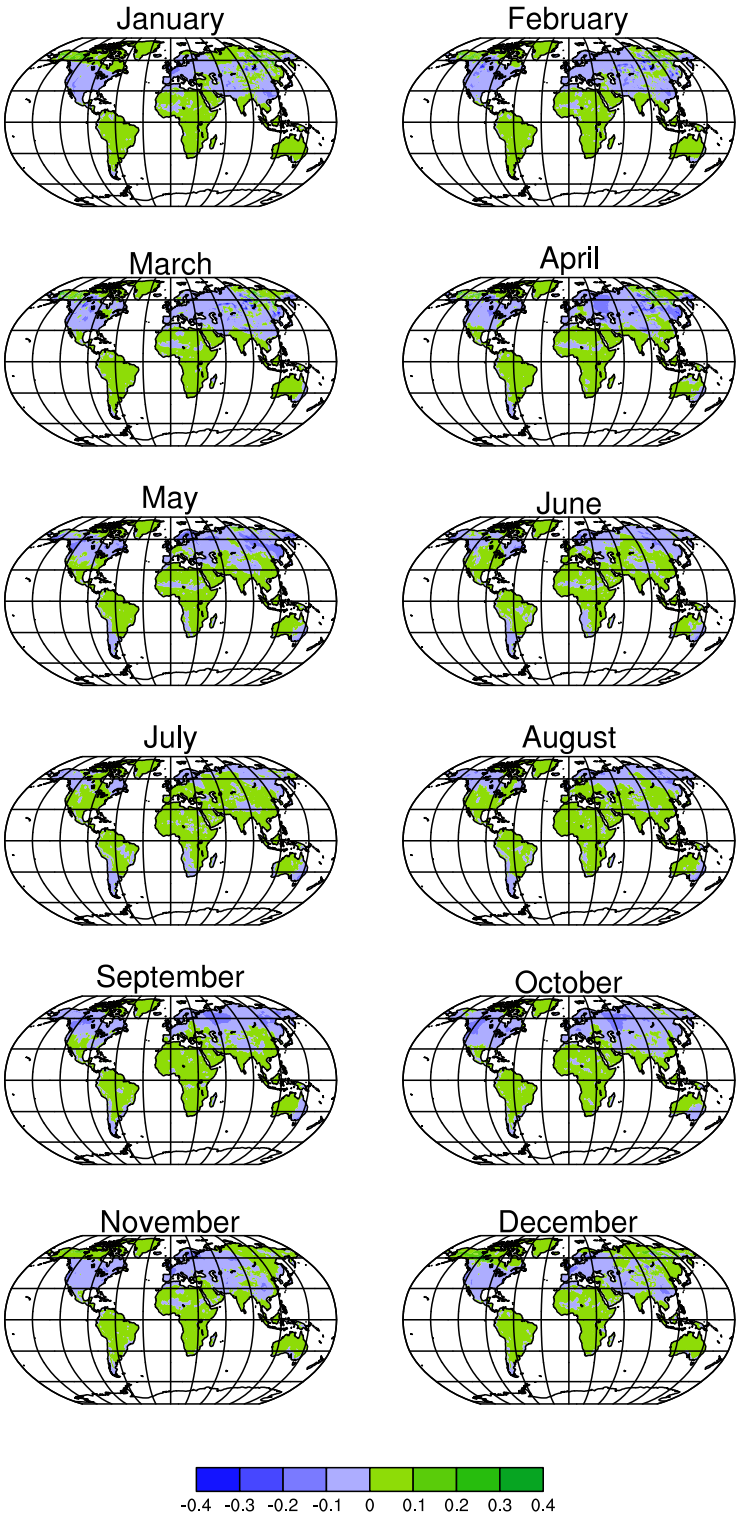

Figure 5.28: Difference in monthly climatologies of Transport-limited model gridbox fractions (0–1) between the JULES-WFDEI-GPCC-1degree and JULES-PRINCETON model simulations at global scales (calculated using Method 2 in Appendix F). Green gridboxes mean that the fractions of model gridboxes that are Transport-limited in the JULES-WFDEI-GPCC-1degree model simulation are greater than those in the JULES-PRINCETON simulation and blue means the opposite.

5.4 Discussion

The ability of JULES to simulate interannual variability (at various spatial scales) and annual average global GPP is discussed here. Simulated GPP is further explored by examining GPP at the regional scale; tropics versus extratropics and dividing the global land area into seven regions (Table 5.2; Figure 5.1). A brief discussion of model sensitivity to spatial resolution and meteorological driving data is provided.

5.4.1 Can JULES capture interannual variability of GPP at the global scale? How do estimates of total annual GPP compare to those from observational datasets?

When JULES was driven with the WFDEI-GPCC dataset (at $0.5^\circ \times 0.5^\circ$ spatial resolution), the model was able to capture interannual variability at the global scale (Figure 5.3c) with the highest modelled variation occuring in the winter and spring months (Figure 5.3b). This was also observed when simulating GPP at lower spatial resolutions ($1^\circ \times 1^\circ$ and $2^\circ \times 2^\circ$; Figures 5.21b and c). At the global scale, JULES estimates the annual average global GPP to be 140 $\mathrm{Pg\,C\,year^{-1}}$ (combined GPP of all terrestrial ecosystems) over 2000–2010, which is greater than FLUXNET-MTE and MODIS GPP by 8 % and 25 % on average, respectively (Figure 5.5). These differences are due to differences in GPP between JULES, FLUXNET-MTE and MODIS for forests and grasslands in the tropics (Figure 5.13).

In the extratropics, JULES was able to simulate GPP compared to FLUXNET-MTE and MODIS due to its phenology model being designed for temperate regions with associated model parameters (Section 4.4.3). When using only local data (soil, vegetation and meteorological data; local-F) for the point scale model simulations (performed in Chapter 4), it was found that when comparing the total annual simulated GPP for the local-F simulations to those using global data (global-WEIG), the same trend was found when comparing the local-F simulations to the global model runs (JULES-WFDEI-GPCC) and the observation-based GPP estimates (Figure 5.29). Differences in model simulations when using local (local-F) or global data

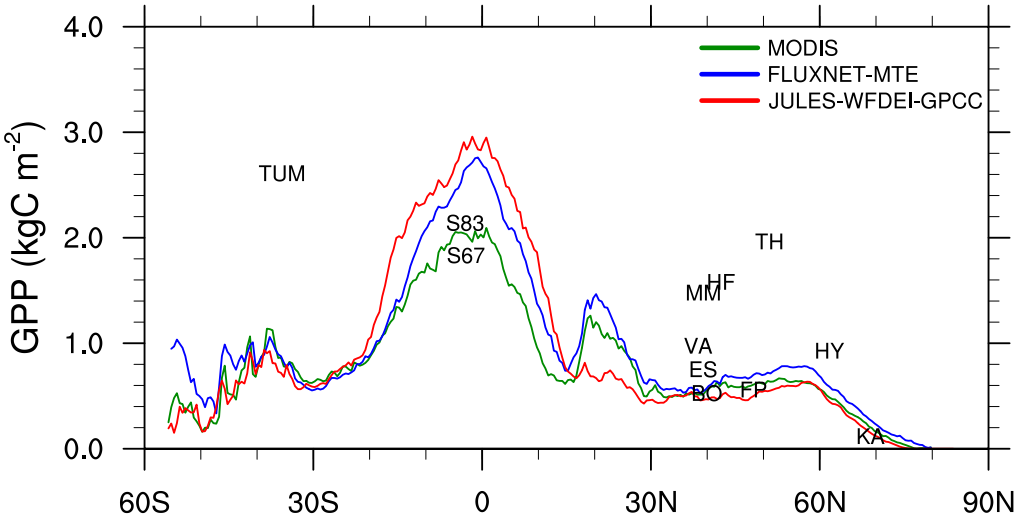

Figure 5.29: Annual zonal mean model simulated (JULES-WFDEI-GPCC) and observed (FLUXNET-MTE and MODIS) GPP fluxes averaged for the 2000–2010 period at the global scale. The total annual model simulated GPP from the point-scale simulations performed in Chapter 4 using only local data (local-F) has been included using the site name for the 12 FLUXNET sites (HF: Harvard Forest, VA: Vaira Ranch, MM: Morgan Monroe, HY: Hyytiala, TH: Tharandt, TUM: Tumbarumba, ES: El Saler, FP: Fort Peck, KA: Kaamanen, S67: Santarem Km67, S83: Santarem Km83, BO: Bondville).

(global-WEIG) at the point scale include higher simulated GPP when using local data compared to global at sites in temperate regions (HF, MM, TH, TUM and FP) and lower simulated GPP when using local data at the tropical sites, S67 and S83, the cropland site, BO and the wetland site, KA (Figure 4.2). This same trend is observed when comparing the total annual GPP for the local-F simulations to those from the global model simulations and the observation-based estimates (Figure 5.29).

At the regional scale, the tropics were divided into three regions (Central and South America, Africa and South and South-East Asia; Figure 5.14) and in all three regions, JULES overestimated GPP compared to FLUXNET-MTE and MODIS. This may be due to biases in the WFDEI-GPCC meteorological data since JULES is very sensitive to the downward shortwave and longwave radiation fluxes and surface air temperature. The difference in the tropics can be seen in the zonal mean of total annual GPP (Figure 5.5d). However, both FLUXNET-MTE and MODIS overestimate GPP at 15°N–30°N. This difference was due to higher GPP in Mexico and Southern China in the observation-based estimates (Figure 5.30). The total annual FLUXNET-MTE and MODIS GPP estimates are higher than that simulated by JULES by 7.5% and 1.7%, respectively, for Mexico. This is also observed in the JULES and MODIS LAI with the zonal mean for MODIS being higher than JULES (Figure 5.10c). One of the major vegetation types in Mexico are drought-deciduous plants (drought-deciduous plants lose their leaves during the dry season or periods of dryness as opposed to temperate deciduous plants which lose their leaves during periods of cold weather) and JULES does not contain this PFT. In the thesis conclusions (Section 7.2), further discussion on adding a drought-deciduous PFT to the model has been included.

In general, it was found that simulated photosynthesis was Rubisco-limited. This occurs under conditions of saturated irradiance and limiting atmospheric CO_2 concentrations.

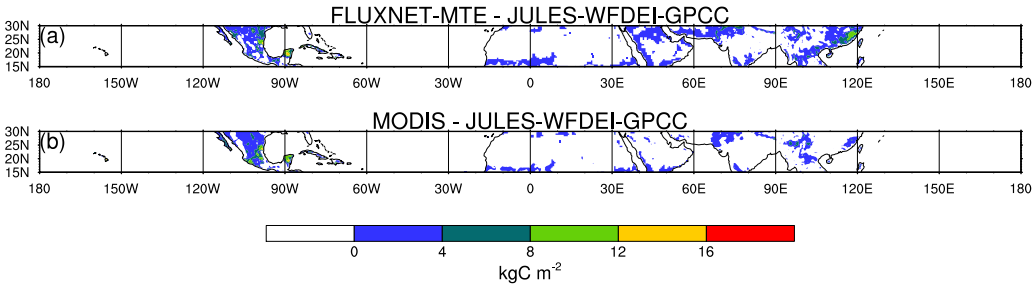

Figure 5.30: Difference in total annual model simulated (JULES-WFDEI-GPCC) and the observation-based estimates (FLUXNET-MTE and MODIS) GPP gluxes for the 2000–2010 period at latitudes 15°N-30°N ($0.5° \times 0.5°$ spatial resolution). **(a)** shows the difference between FLUXNET-MTE and JULES and **(b)** between MODIS and JULES. A positive change in GPP means the observation-based estimate is higher than the model.

5.4.2 How do fluxes of GPP simulated by JULES compare for various biomes at the global and regional scales?

As mentioned in Section 5.4.1, JULES overestimates GPP compared to FLUXNET-MTE and MODIS at the global scale and this was found to be due to greater GPP simulated by forests and grasslands in the tropics (Figures 5.13a and c). The total annual GPP for shrubs at the global scale and in the tropics and extratropics are approximately equal (Figure 5.13a, b and c). JULES simulated annual average GPP to be 61 Pg C year^{-1}, 54 Pg C year^{-1} and 7 Pg C year^{-1} for forests, grasslands and shrubs, respectively. The simulated GPP for forests is similar to that calculated by Beer et al. (2010) (sum of the values for tropical, temperate and boreal forests) with annual average GPP being 59 Pg C year^{-1}. Since Beer et al. (2010) provides annual average GPP values for tropical savannahs and grasslands, temperate grasslands and shrublands and croplands, these are summed in order to obtain an annual average global GPP for grasslands and shrubs 54.6 Pg C year^{-1}, which is lower than the model simulated value of 61 Pg C year^{-1}.

By further dividing the global land area into seven regions (Table 5.2), it was observed that for the three tropical regions (Central and South America, Africa and South and South-East Asia), JULES overestimated total annual GPP for forests, grasslands and shrubs (Figures 5.15c, e, and f). The

four extratropical regions (Europe, Northern Asia, Extratropical Southern Hemisphere and North America and Greenland) simulate similar GPP for JULES, FLUXNET-MTE and MODIS for the three biomes with shrubs in North America and Greenland, Northern Asia and the extratropical Southern Hemisphere being underestimated by JULES (Figures 5.15a, b, d and g).

5.4.3 How sensitive are fluxes of GPP to the spatial resolution of the model?

When JULES was driven with the WFDEI-GPCC dataset at three different spatial resolutions (Table 5.1), it was found that for simulations of GPP, the model was insensitive to spatial resolution with annual average global GPP being 140Pg C year^{-1}, 141 Pg C year^{-1} and 142 Pg C year^{-1} at $0.5^\circ \times 0.5^\circ$, $1^\circ \times 1^\circ$ and $2^\circ \times 2^\circ$ spatial resolutions, respectively (Figures 5.5c, 5.16c and 5.17c). This trend was also observed in the zonal mean of total annual GPP (Figure 5.18). The insensitivity of the model to spatial resolution at the global scale was also observed at the regional scale when comparing simulated GPP fluxes for forests, grasslands and shrubs in the tropics and extratropics (Figure 5.19) and by further dividing the global land area into seven regions (Figure 5.20).

Little research has been performed on the effects of spatial resolution on JULES simulations (as well as other LSMs). Studies using atmospheric chemistry models have shown that the spatial resolution of the input meteorological data can affect model output (Ito et al., 2009; Pugh et al., 2013; Schaap et al., 2015). The results found here agree with those from Compton and Best (2011). Compton and Best (2011) showed that JULES was insensitive to spatial resolution when the WATCH dataset (Section 3.2.2.2) was regridded from half-degree to 1-degree and 2-degree when simulating the terrestrial hydrological cycle. It was found that spatial resolution had little or no effect on simulations of global mean total evaporation and total runoff. However, the study showed that JULES was sensitive to temporal resolution when simulating the same hydrological components.

5.4.4 Is the meteorological dataset used to drive the model important at the global scale?

When JULES was driven with the PRINCETON dataset at $1^\circ \times 1^\circ$ spatial resolution (Table 5.1), it was found that the annual average global GPP was slightly higher by $4\,\mathrm{Pg\,C\,year^{-1}}$ than that simulated by JULES when driven with the WFDEI-GPCC dataset (Figures 5.23c and 5.16c). In general, differences in GPP fluxes for model simulations driven using WFDEI-GPCC and PRINCETON are mainly in the tropics (at 5°N–5°S) with JULES-WFDEI-GPCC-1degree simulating higher GPP than JULES-PRINCETON and in the extratropics at 30°N–60°N, JULES-PRINCETON simulates slightly higher GPP (Figures 5.18 and 5.24). As with the WFDEI-GPCC driven simulation, when JULES was driven with PRINCETON, the monthly simulated photosynthesis was found to be Rubisco-limited.

Other studies have shown that the meteorological dataset used to drive LSMs is a large source of uncertainty in global land surface modelling (Hicke, 2005; Jung et al., 2007; Poulter et al., 2011). Different methods are used to create time series of global gridded climate data in order to drive LSMs and this can introduce uncertainty that can propagate through model simulations (Zhao et al., 2006). Even at the point scale, differences in simulated GPP were observed when driving JULES with the WFDEI-GPCC and PRINCETON datasets (Chapter 4).

Since JULES is sensitive to the downward radiation fluxes used to drive the model (Alton et al., 2007), differences between model simulations driven using WFDEI-GPCC and PRINCETON in the tropics are due to biases in the downward longwave radiation fluxes in WFDEI-GPCC in the Amazonian, African and South-East Asian tropics (Figures G.5b and d) and the higher GPP simulated by JULES (driven with PRINCETON) in the extratropics are a result of positive biases in downward longwave radiation in the PRINCETON dataset in North America and Northern Asia (Figures G.5b) and positive biases in surface air temperature in the PRINCETON dataset in the northern hemisphere (Figure G.6a and c). These small differences between driving JULES with the WFDEI-GPCC and PRINCETON datasets are also observed in estimates of GPP at the global scale, in the tropics and extratropics (Figure 5.19). For the point scale model simulations, soil moisture stress played an important role when simulating GPP (Section 4.4.1).

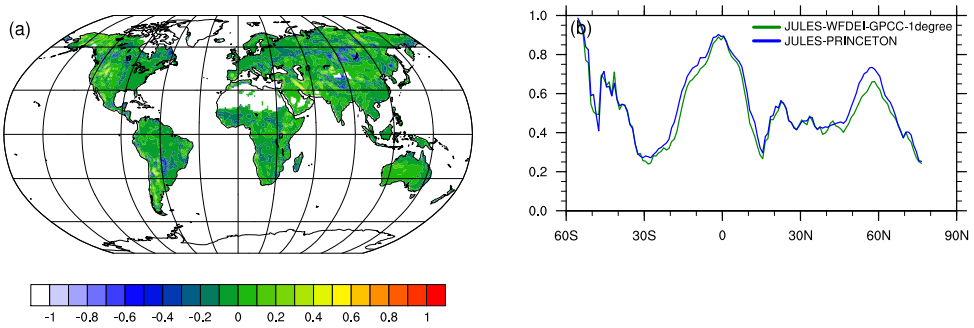

Figure 5.31: Difference in average monthly soil moisture stress (beta factor; values range from 0–1) between JULES driven with the WFDEI-GPCC dataset at 1° × 1° spatial resolution (JULES-WFDEI-GPCC-1degree) and the PRINCETON dataset (JULES-PRINCETON) and the zonal mean of monthly average soil moisture stress for the same model simulations. **(a)** shows the difference in soil moisture stress for the average monthly for the 2000–2010 period and **(b)** shows the zonal mean for the monthly average for the same period.

At global scales, simulated soil moisture stress between the WFDEI-GPCC and PRINCETON driven model simulations were similar in the tropics, but in the northern extratropical regions, the simulation driven using PRINCETON (Figure 5.31b; JULES-PRINCETON) had lower soil moisture stress than the WFDEI-GPCC driven simulation. This trend can be found in simulated GPP, where the PRINCETON driven simulations have higher simulated GPP in the northern extratropical regions (Figure 5.18).

5.5 Conclusions

An evaluation of JULES was performed at the global and regional scales with simulated GPP compared with global gridded ($0.5^\circ \times 0.5^\circ$ spatial and monthly temporal resolution) estimates of GPP derived from upscaled FLUXNET observations (FLUXNET-MTE) and satellite observations from the MODIS sensor. In general, it was found that JULES was able to capture interannual variability at the global scale. JULES overestimated global GPP compared to FLUXNET-MTE and MODIS, but it was found that at the regional scale, these differences were due to differences between model simulated and observation-based estimates in the tropics.

Differences in GPP between model and observation-based estimates at 15°N–30°N are due to higher FLUXNET-MTE and MODIS GPP for Mexico. This is due to a lack of drought-deciduous PFTs in JULES. By dividing the global land area into seven regions, it was found that all three tropical regions (Central and South America, Africa and South and South-East Asia) contribute to model-observation differences at the global scale compared to FLUXNET-MTE and MODIS. The model is able simulate GPP estimates at the four extratropical regions (Europe, Northern Asia, North America and Greenland and the extratropical Southern Hemisphere).

When JULES was driven at the global and regional scale with the WFDEI-GPCC dataset at various spatial resolutions ($0.5^\circ \times 0.5^\circ$, $1^\circ \times 1^\circ$ and $2^\circ \times 2^\circ$), it was found that the model was insensitive to spatial resolution. Similar results were shown by Compton and Best (2011) when simulating components of the terrestrial hydrological cycle. Differences between high ($0.5^\circ \times 0.5^\circ$) and low ($2^\circ \times 2^\circ$) spatial resolution simulations of GPP are very similar. This means that low resolution model simulations at these scales can be performed in place of high resolution for carbon cycle simulations and this results in shorter model run times. The meteorological dataset used to drive LSMs at the global scale is an important source of model uncertainty (Poulter et al., 2011). By using a different meteorological dataset (PRINCETON) to drive the model, it was found that simulated GPP was similar to that when the model was driven with the WFDEI-GPCC dataset (at $1^\circ \times 1^\circ$ spatial resolution) with exceptions to this being in the tropics and the northern extratropics. These differences are due to biases in the downward radiation fluxes and surface air temperature in the meteorolog-

ical data. Differences in precipitation, and hence soil moisture stress, did not play a role in differences between the two model simulations. Simulated photosynthesis in both sets of model simulations (JULES-WFDEI-GPCC-1degree and JULES-PRINCETON) were Rubisco-limited. When JULES was driven with the WFDEI-CRU dataset instead of WFDEI-GPCC, differences in simulated GPP were very small.

5.6 Summary

This study evaluated the ability of JULES to simulate GPP at the global and regional scale with model performance compared against upscaled FLUXNET and satellite data. Firstly, when JULES was driven with the WFDEI-GPCC dataset (at $0.5^\circ \times 0.5^\circ$ spatial resolution), it was found that JULES overestimated the annual average global GPP for 2000–2010 compared to the observation-based estimates, FLUXNET-MTE and MODIS, by 8 % and 25 %, respectively. At the global scale, JULES was able to capture interannual variability with greater variability observed in the winter and spring months. Secondly, by comparing GPP fluxes for various biomes (forests, grasslands and shrubs) at the global and regional scale (tropics and extratropics), it was found that differences between JULES, FLUXNET-MTE and MODIS at the global scale were due to differences in the tropics. The inability of the model to simulate GPP correctly in the tropics is a major source of uncertainty in JULES. Thirdly, when model simulations of GPP were performed at various spatial resolutions ($0.5^\circ \times 0.5^\circ$, $1^\circ \times 1^\circ$ and $2^\circ \times 2^\circ$), JULES was found to be insensitive to spatial resolution. Finally, it was shown that when JULES was driven with the PRINCETON meteorological dataset, estimates of global GPP were similar to those driven with WFDEI-GPCC. When JULES was driven with the WFDEI-GPCC and PRINCETON datasets (both at $1^\circ \times 1^\circ$ spatial resolution), simulated photosynthesis was Rubisco-limited. However, differences between the two were observed with the WFDEI-GPCC driven model simulations estimating higher GPP in the tropics (at 5°N–5°S) and the PRINCETON driven model simulations estimating higher GPP in the extratropics (at 30°N–60°N). At the global scale, the meteorological dataset used to drive JULES was found to be a major source of model uncertainty. Differences between the WFDEI-GPCC and WFDEI-CRU driven model simulations were very small. In the next chapter, the response of JULES to changes in climate is explored at the global and regional scales.

Bibliography

P. Alton, L. Mercado, and P. North. A sensitivity analysis of the land-surface scheme JULES conducted for three forest biomes: Biophysical parameters, model processes, and meteorological driving data. *Global Biogeochemical Cycles*, 20:GB1008, 2007. doi:10.1029/2005GB002653.

C. Beer, M. Reichstein, E. Tomelleri, P. Ciais, M. Jung, N. Carvalhais, C. Rödenbeck, M. A. Arain, D. Baldocchi, G. B. Bonan, A. Bondeau, A. Cescatti, G. Lasslop, A. Lindroth, M. Lomas, S. Luyssaert, H. Margolis, K. W. Oleson, O. Roupsard, E. Veenendaal, N. Viovy, C. Williams, F. I. Woodward, and D. Papale. Terrestrial Gross Carbon Dioxide Uptake: Global Distribution and Covariation with Climate. *Science*, 329: 834–838, 2010. doi:10.1126/science.1184984.

E. Blyth, D. B. Clark, R. Ellis, C. Huntingford, S. Los, M. Pryor, M. Best, and S. Sitch. A comprehensive set of benchmark tests for a land surface model of simultaneous fluxes of water and carbon at both the global and seasonal scale. *Geoscientific Model Development*, 4:255–269, 2011. doi:10.5194/gmd-4-255-2011.

G. B. Bonan, P. J. Lawrence, K. W. Oleson, S. Levis, M. Jung, M. Reichstein, D. M. Lawrence, and S. C. Swenson. Improving canopy processes in the Community Land Model version 4 (CLM4) using global flux fields empirically inferred from FLUXNET data. *Journal of Geophysical Research*, 116:G02014, 2011. doi:10.1029/2010JG001593.

S. Chadburn, E. Burke, R. Essery, J. Boike, M. Langer, M. Heikenfeld, P. Cox, and P. Friedlingstein. An improved representation of physical permafrost dynamics in the JULES land-surface model. *Geoscientific Model Development*, 8:1493–1508, 2015. doi:10.5194/gmd-8-1493-2015.

E. Compton and M. Best. Impact of spatial and temporal resolution on modelled terrestrial hydrological cycle components. Technical Report 44, WATCH Technical Report, 19 pp [Available at http:// www.eu-watch.org.], 2011.

J. A. Hicke. NCEP and GISS solar radiation data sets available for ecosystem modeling: Description, differences, and impacts on net primary production. *Global Biogeochemical Cycles*, 19:GB2006, 2005. doi:10.1029/2004GB002391.

A. Ito, S. Sillman, and J. E. Penner. Global chemical transport model study of ozone response to changes in chemical kinetics and biogenic volatile organic compounds emissions due to increasing temperatures: Sensitivities to isoprene nitrate chemistry and grid resolution. *Journal of Geophysical Research: Atmospheres (1984–2012)*, 114:D09301, 2009. doi:10.1029/2008JD011254.

M. Jung, M. Vetter, M. Herold, G. Churkina, M. Reichstein, S. Zaehle, P. Ciais, N. Viovy, A. Bondeau, Y. Chen, K. Trusilova, F. Feser, and M. Heimann. Uncertainties of modeling gross primary productivity over Europe: A systematic study on the effects of using different drivers and terrestrial biosphere models. *Global Biogeochemical Cycles*, 21:GB4021, 2007. doi:10.1029/2006GB002915.

M. Jung, M. Reichstein, and A. Bondeau. Towards global empirical upscaling of FLUXNET eddy covariance observations: validation of a model tree ensemble approach using a biosphere model. *Biogeosciences*, 6:2001–2013, 2009. doi:10.5194/bg-6-2001-2009.

M. Jung, M. Reichstein, P. Ciais, S. I. Seneviratne, J. Sheffield, M. L. Goulden, G. Bonan, A. Cescatti, J. Chen, R. de Jeu, A. J. Dolman, W. Eugster, D. Gerten, D. Gianelle, N. Gobron, J. Heinke, J. Kimball, B. E. Law, L. Montagnani, Q. Mu, B. Mueller, K. Oleson, D. Papale, A. D. Richardson, O. Roupsard, S. Running, E. Tomelleri, N. Viovy,

U. Weber, C. Williams, E. Wood, S. Zaehle, and K. Zhang. Recent decline in the global land evapotranspiration trend due to limited moisture supply. *Nature*, 467:951–954, 2010. doi:10.1038/nature09396.

G. Lasslop, M. Reichstein, D. Papale, A. D. Richardson, A. Arneth, A. Barr, P. Stoy, and G. Wohlfahrt. Separation of net ecosystem exchange into assimilation and respiration using a light response curve approach: critical issues and global evaluation. *Global Change Biology*, 16:187–208, 2010. doi:10.1111/j.1365-2486.2009.02041.x.

H Lei, M. Huang, L. R. Leung, D. Yang, X. Shi, J. Mao, D. J. Hayes, C. R. Schwalm, Y. Wei, and S. Liu. Sensitivity of global terrestrial gross primary production to hydrologic states simulated by the Community Land Model using two runoff parameterizations. *Journal of Advances in Modeling Earth Systems*, 6:658–679, 2014. doi:10.1002/2013MS000252.

T. R. Marthews, Y. Malhi, C. A. J. Girardin, J. E. Silva Espejo, L. E. O. C. Aragão, D. B. Metcalfe, J. M. Rapp, L. M. Mercado, R. A. Fisher, D. R. Galbraith, J. B. Fisher, N. Salinas-Revilla, A. D. Friend, N. Restrepo-Coupe, and R. J. Williams. Simulating forest productivity along a neotropical elevational transect: temperature variation and carbon use efficiency. *Global Change Biology*, 18:2882–2898, 2012. doi:10.1111/j.1365-2486.2012.02728.x.

B. Poulter, D. C. Frank, E. L. Hodson, and N. E. Zimmermann. Impacts of land cover and climate data selection on understanding terrestrial carbon dynamics and the CO_2 airborne fraction. *Biogeosciences*, 8:2027–2036, 2011. doi:10.5194/bg-8-2027-2011.

T. A. M. Pugh, K. Ashworth, O. Wild, and C. N. Hewitt. Effects of the spatial resolution of climate data on estimates of biogenic isoprene emissions. *Atmospheric Environment*, 70:1–6, 2013. doi:10.1016/j.atmosenv.2013.01.001.

M. Reichstein, E. Falge, D. Baldocchi, D. Papale, M. Aubinet, P. Berbigier, C. Bernhofer, N. Buchmann, T. Gilmanov, A. Granier, T. Grünwald, K. Havránková, D. Ilvesniemi, H abd Janous, A. Knohl, T. Laurila, A. Lohila, D. Loustau, G. Matteucci, T. Meyers, F. Miglietta, J.-M. Ourcival, J. Pumpanen, S. Rambal, E. Rotenberg, M. Sanz, J. Tenhunen,

G. Seufert, F. Vaccari, T. Vesala, D. Yakir, and R. Valentini. On the separation of net ecosystem exchange into assimilation and ecosystem respiration: review and improved algorithm. *Global Change Biology*, 11: 1424–1439, 2005. doi:10.1111/j.1365-2486.2005.001002.x.

L. Rowland, A. Harper, B. O. Christoffersen, D. R. Galbraith, H. M. A. Imbuzeiro, T. L. Powell, C. Doughty, N. M. Levine, Y. Malhi, S. R. Saleska, P. R. Moorcroft, P. Meir, and M. Williams. Modelling climate change responses in tropical forests: similar productivity estimates across five models, but different mechanisms and responses. *Geoscientific Model Development*, 8:1097–1110, 2015. doi:10.5194/gmd-8-1097-2015.

M. Schaap, C. Cuvelier, C. Hendriks, B. Bessagnet, J. M. Baldasano, A. Colette, P. Thunis, D. Karam, H. Fagerli, A. Graff, R. Kranenburg, A. Nyiri, M. T. Pay, L. Rouïl, M. Schulz, D. Simpson, R. Stern, E. Terrenoire, and P. Wind. Performance of European chemistry transport models as function of horizontal resolution. *Atmospheric Environment*, 112:90–105, 2015. doi:10.1016/j.atmosenv.2015.04.003.

D. Slevin, S. F. B. Tett, and M. Williams. Multi-site evaluation of the JULES land surface model using global and local data. *Geoscientific Model Development*, 8:295–316, 2015. doi:10.5194/gmd-8-295-2015.

Chapter 6

Sensitivity of JULES to changes in climate at the global and regional scale

In this chapter, the response of JULES to changes in climate (surface (2m) air temperature, precipitation and atmospheric CO_2 concentrations) when simulating GPP at the global and regional scale for 2000–2010 was investigated. The ability of LSMs to realistically respond to changes in climate is important for predicting climate change at global and regional scales and this was explored with JULES by performing a number of model simulations in which the meteorological data (surface (2m) air temperature, precipitation and atmospheric CO_2 concentrations) were varied with model results compared to the unperturbed simulation (no changes in climate drivers). The effect of changing air temperature on simulated GPP was examined with five model simulations where air temperature was modified by –1 °C, +1 °C, +2 °C, +5 °C and +10 °C, the effect of changes in precipitation was examined with six model simulations where precipitation was modified by +/– 10 %, +/– 20 % and +/– 50 %, and changes in the annual average atmospheric CO_2 concentration was examined with four model simulations with fixed CO_2 concentrations of 400 ppm, 450 ppm, 550 ppm and 750 ppm. The response of the model to changes in climate was examined at the global scale, followed by exploring its response at the regional and biome scale. This simple sensitivity study of JULES helps to explain and reinforce re-

sults from studies by Galbraith et al. (2010) and Rowland et al. (2015) at regional and point scales, respectively.

6.1 Introduction

Continuing increases in atmospheric CO_2 concentrations in the 21st century will lead to increases in air temperature and changes in precipitation with globally averaged changes in temperature and precipitation over land exceeding those over oceans (Held and Soden, 2006; Collins et al., 2013; Liu and Allan, 2013; Wu et al., 2013). LSMs provide a means of predicting the response of the land surface (and terrestrial carbon cycle) to climate change (Adams and Piovesan, 2002; Friedlingstein et al., 2006, 2014). The response of LSMs to changes in climate can vary between models and such uncertainties can propagate throughout models. The correct simulation of GPP is important since errors in its calculation can affect other flux calculations such as biomass and NEE (Chapter 1). In JULES, NEE is calculated as total ecosystem respiration minus GPP. Previous studies have investigated the sensitivity of JULES to the meteorological data at the point scale (Alton et al., 2007; Rowland et al., 2015) and regional scale (Galbraith et al., 2010). Alton et al. (2007) performed a sensitivity/uncertainty analysis of JULES at three forest sites (sparse, boreal needleleaf; moderately dense, temperate broadleaf; and dense tropical broadleaf) which focused on the biophysical parameters, model processes and meteorological data which have the most effect on modelled GPP (Section 2.7). Alton et al. (2007) showed that the most influential meteorological variables used to force the model were the downward shortwave and longwave radiation fluxes. Galbraith et al. (2010) found that JULES' ability to simulate biomass in the Amazon region was more sensitive to increased temperature than reduced precipitation. Rowland et al. (2015) evaluated the capability of five vegetation models (including JULES) to simulate leaf-scale and canopy-scale productivity to changes in temperature and precipitation at an Amazonian site and found that for simulations of GPP, the models did not agree on whether GPP was more sensitive to changes in temperature or precipitation in the tropics, but found that GPP is higher at cooler temperatures in the tropics across all models.

In this chapter, a simple sensitivity study of JULES was performed in

which the response of the model to changes in climate when simulating GPP was examined at the global and regional scale. Only changes to one climate variable were made at a time due to complex interactions associated with multiple changes in climatic factors resulting in complex non-linear ecosystem responses (Rowland et al., 2015). Model response to change in multiple climatic factors can also be difficult to explain (Luo et al., 2008). In particular, the following research questions are addressed:

- How sensitive is JULES to changes in temperature, precipitation and atmospheric CO_2 concentrations at the global scale?
- Which regions contribute most to the model's sensitivity at the global scale?
- Does the sensitivity of the model's biome types to changing climate explain the results at the global and regional scales?

6.2 Methods

In this section, a description of the simulations performed in order to explore model sensitivity to changes in climate at the global scale (including model setup) is provided along with how model performance was quantified.

6.2.1 Experimental design

For the global scale model simulations performed in this chapter, JULES version 3.4.1 was used (Section 3.1.2). As with the model simulations in Chapter 5, this version was used due to the ability to run JULES at multiple points in parallel in order to reduce model run times, which is important when performing many model simulations at global scales. Model simulations were carried out at 2-degree ($2^\circ \times 2^\circ$) spatial resolution since it was found that there was no difference in annual average global GPP for half-degree and 2-degree model simulations (Section 5.3.4) and the 2-degree model simulations were 16 $\times$ faster than those at half-degree. Offline simulations of GPP using JULES driven with the WFDEI-GPCC dataset (Section 3.2.2.2) were performed at the global and regional scale for 2000–2010 at $2^\circ \times 2^\circ$ spatial resolution. Model spin-up was performed using the WFDEI-GPCC dataset from 1979–1999 (described in more detail in Section 5.2.2)

and following this spin-up period, model simulations with varying climate (air temperature, precipitation, atmospheric CO_2 concentrations) for 1999–2010 were performed.

There was no difference in model results if changes to air temperature, precipitation and CO_2 concentrations were included in the spin-up period or if the climate data was varied only for 1999–2010 with the model simulation being started from 1999 using data (stored in the dump file) from the control simulation (no changes in climate). This was due to small differences in modelled soil moisture (bringing soil moisture to equilibrium during model spin-up is important for simulating GPP) with changes in surface air temperature (Figure G.9) and precipitation (Figure G.10) during the spin-up process on 1 January 1999 (this was the date in which the dump file from the control simulation was used to initialise the shorter simulations) between simulations with changes in climate implemented during the entire spin-up period and those with no changes in climate included in the spin-up period. There were no differences in modelled soil moisture for simulations with changes in atmospheric CO_2 concentrations included during the spin-up period and those without changes included during spin-up (figure not shown). The second method was used for simulations in this chapter due to reduced model run times. However, only model output for 2000–2010 was analysed as the MODIS instrument only started recording data in February 2000. One of the reasons for performing the multi-site evaluation of JULES for 2000–2010 (Chapter 4) was due to the availability of satellite LAI data.

Varying the surface air temperature will affect specific humidity. When calculating the new specific humidity, the relative humidity implied by the original data (no changes in air temperature) was held constant when recalculating the new specific humidity to avoid supersaturation due to changes in air temperature (Cosgrove et al., 2003). A more detailed description of how specific humidity was recalculated is given in Appendix E. Increasing air temperatures (with the corresponding adjustment of specific humidity) means that the water holding capacity of the atmosphere increases due to primarily a consequence of the Clausius-Clapeyron relationship in the lower troposphere (Collins et al., 2013). In this study, it is assumed that with increases in air temperature, the atmosphere is more humid.

To examine how changes in surface air temperature (T_{air}) affect global and regional GPP, five model simulations, with varying T_{air}, were performed

with 3-hourly 2000–2010 ambient T_{air} modified by –1 °C, +1 °C, +2 °C, +5 °C and +10 °C. For each of the updated air temperature datasets, specific humidity was re-calculated. To examine how changes in precipitation affect GPP, six model simulations, with varying precipitation rates were performed by adjusting precipitation by +/– 10 %, +/– 20 % and +/– 50 %. In the WFDEI-GPCC dataset, precipitation consists of two fields: rainfall and snowfall rate ($kg\,m^{-2}\,s^{-1}$), which are both increased or decreased uniformly as required. The effect of atmospheric CO_2 concentration on simulated GPP was investigated with four model simulations in which JULES, in addition to being driven with the WFDEI-GPCC dataset, is driven with annual average atmospheric CO_2 concentrations set to 400 ppm, 450 ppm, 550 ppm and 750 ppm. For the control simulation, no changes were made to the driving data and historical observed CO_2 concentrations were used to force the model.

As with the model simulations performed in Chapter 5, the phenology model was switched on for all model simulations and vegetation competition and TRIFFID were switched off. All model simulations were performed at $2^\circ \times 2^\circ$ spatial resolution.

6.2.2 Data

The datasets used for the model simulations performed in this chapter are the same as those used for the global scale simulations performed in the previous chapter (JULES-WFDEI-GPCC-2degree; Table 5.1).

6.2.3 Model Analyses

In order to explore the effects of varying (perturbing) climate drivers (i.e. surface (2m) air temperature, precipitation and annual average atmospheric CO_2 concentrations) at the global scale, the annual average global and regional GPP (integrated across all ecosystems) calculated for the control simulation (JULES-WFDEI-GPCC-2degree; Table 5.1) were subtracted from the perturbed model simulations (ΔGPP; Equation 6.1). The same method was used to quantify differences in LAI using the area-weighted average of the monthly climatology global LAI (ΔLAI; Equation 6.2).

$$\Delta\text{GPP} = \sum \text{GPP}_{\text{C}+\delta\text{C}} - \sum \text{GPP}_{\text{CONTROL}} \tag{6.1}$$

$$\Delta\text{LAI} = \sum \text{LAI}_{\text{C}+\delta\text{C}} - \sum \text{LAI}_{\text{CONTROL}} \tag{6.2}$$

C is the unperturbed climate driver (air temperature, precipitation or annual average atmospheric CO_2 concentrations) and δC is the change in the driver (Section 6.2.1). Seasonal differences in global and regional GPP and LAI were also computed between the perturbed and control model simulations.

6.3 Results

Results from model simulations investigating the response of JULES to changes in key climate drivers, such as surface air temperature, precipitation and atmospheric CO_2 concentrations, when simulating GPP are presented here. The sensitivity of the model to changes in climate at the global scale was followed by a regional analysis of the results. The sensitivity of forest, grassland and shrub GPP to changes in climate was also examined.

6.3.1 Simulation of GPP changes at the global scale

At the global scale, JULES was found to be sensitive to all three climate drivers (surface air temperature, precipitation and atmospheric CO_2 concentrations) when simulating GPP (Figure 6.1). Of the three climate drivers, the model was found to be most sensitive to changes in atmospheric CO_2 concentrations (annual average) with average changes in total annual GPP (ΔGPP) of $24\,\text{Pg}\,\text{C}\,\text{year}^{-1}$ (Figure 6.1c). It was observed that the model is more sensitive to simulated reductions in precipitation (drought) than increases when simulating GPP with average increases and decreases in ΔGPP of $17\,\text{Pg}\,\text{C}\,\text{year}^{-1}$ and $34\,\text{Pg}\,\text{C}\,\text{year}^{-1}$, respectively (Figure 6.1b).

Compared to precipitation and atmospheric CO_2 concentrations, JULES was less sensitive with varying air temperature with average changes in

ΔGPP of $2\,\mathrm{Pg\,C\,year^{-1}}$ for temperature changes of +1 to +10 °C (Figure 6.1a). For small increases and decreases in air temperature (+/– 1 °C, +2 °C), there are only small changes in annual average global GPP with changes in GPP ranging from –2 to $+3\,\mathrm{Pg\,C\,year^{-1}}$ for these three temperature changes, which is a 1.4 to 2 % change in GPP from the control simulation. At the temperature extreme of +10 °C, the change in GPP is $-0.4\,\mathrm{Pg\,C\,year^{-1}}$, which is only 0.3 % of the annual average global GPP for the control.

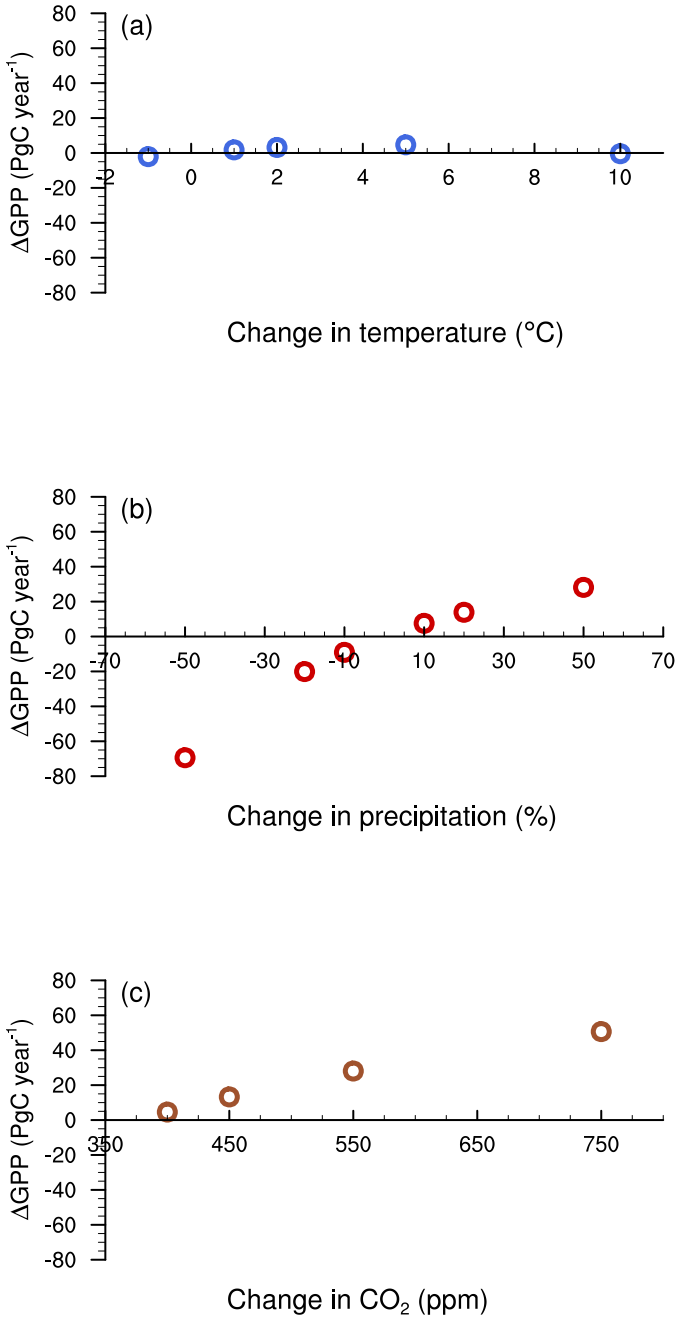

Figure 6.1: Difference in annual average global GPP between model simulations driven with perturbed and unperturbed meteorological data (control simulation). **(a)** shows the difference in GPP between model simulations with perturbed surface air temperature (unperturbed air temperature (T_{air}) −1 °C, +1 °C, +2 °C, +5 °C and +10 °C) and the control simulation (T_{air}+0 °C); **(b)** between model simulations with perturbed precipitation (unperturbed precipitation +/− 10 %, +/− 20 % and +/− 50 %,) and the control (no changes to precipitation); and **(c)** between model simulations with perturbed atmospheric CO_2 concentrations (driven with annual atmospheric CO_2 concentrations at 400 ppm, 450 ppm, 550 ppm and 750 ppm) and the control (historical observed CO_2 concentrations).

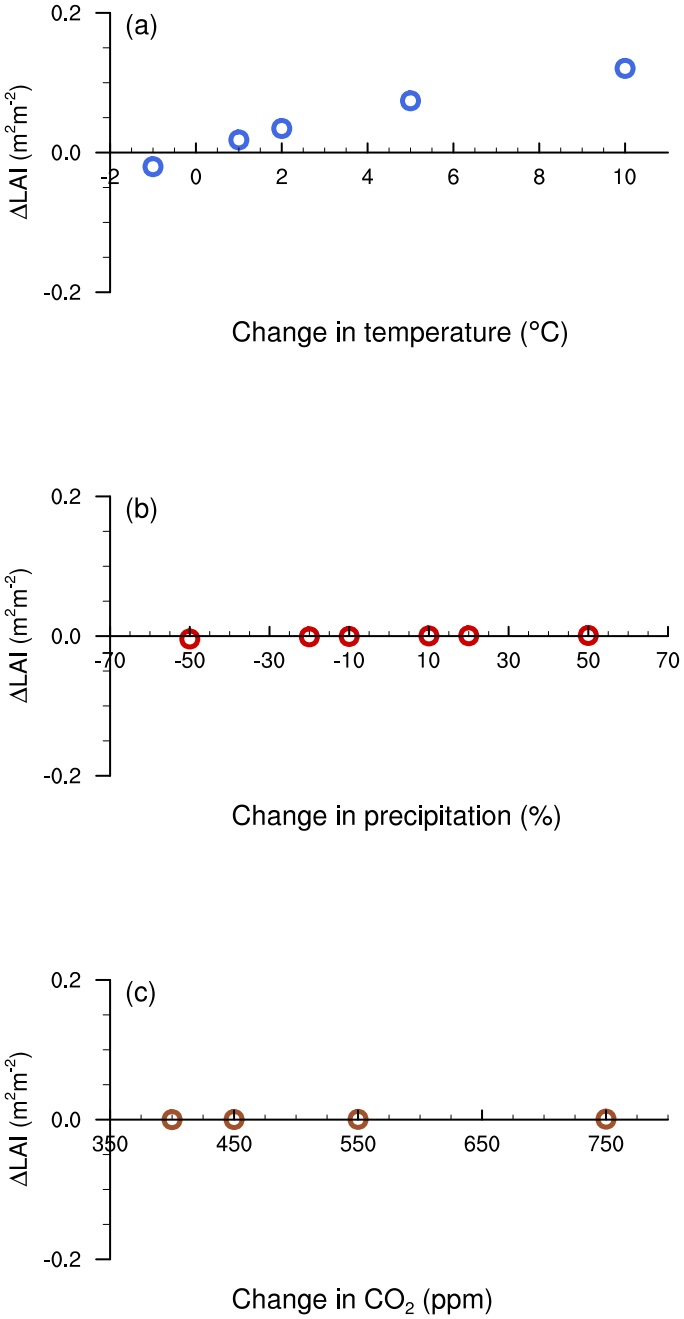

Figure 6.2: Difference in monthly (area-weighted) average global LAI between model simulations driven with perturbed and unperturbed meteorological data (control simulation).**(a)** shows the difference in LAI between model simulations with perturbed surface air temperature and the control simulation , **(b)** between model simulations with perturbed precipitation and control and **(c)** between model simulations with perturbed atmospheric CO_2 concentrations and control. Further detail on the perturbed model simulations can be found in the caption of Figure 6.1.

The response of the model to changes in air temperature were found to be approximately linear for temperature changes below +5°C (Figure 6.1a). With a uniform increase and decrease in air temperature of 1 °C, changes in GPP were found to change by 1.3 % and 1.5 %, respectively, of the annual average global GPP with further increases in air temperature of +2 °C and +5 °C resulting in changes to annual average global GPP by 2.2 % and 3.3 % (Figure 6.1a). The non-linearity of the temperature response of the model occurs not only for global GPP, but it can be observed in the tropics (Figure 6.3a). For precipitation, the response of the model is non-linear with changes in precipitation of +10 % and –10 % resulting in changes in global GPP by 5.3 % and 6.4 %, respectively, and changes of +20 % and –20 % resulting in changes in global GPP by 9.8 % and 14.2 %, respectively (Figure 6.3b). Changes in simulated GPP with increasing atmospheric CO_2 is observed to be non-linear (Figure 6.3c). For the three climate variables, JULES GPP was found to be non-linear mostly in the tropics with air temperature showing the highest non-linearity.

The trends in GPP are different from those in LAI for the three climate drivers. Different trends are observed in the sensitivity of the model to LAI with changes in air temperature having the most effect (Figure 6.2a). Across all positive air temperature changes, it was found that ΔLAI (average change in monthly area-weighted average LAI from the control) was $0.1\,m^2m^{-2}$. JULES LAI was found to be insensitive (negligible differences) to changes in precipitation and atmospheric CO_2 concentrations (Figures 6.2b and c, respectively). However, these results are not surprising since the JULES' phenology module updates LAI once per day using a temperature constraint (i.e. the annual maximum LAI is multipled by a scaling factor).

Overall, simulated GPP is sensitive to changes in all three climate drivers with simulated LAI only sensitive to changes in surface air temperature. The response of model GPP to changes in all three climate factors is non-linear, with the highest non-linearity occurring in the tropics.

6.3.2 Simulation of GPP changes at the regional scale

The response of JULES to changes in the three climate drivers at the global scale is influenced by its sensitivity to changes in the drivers at the regional

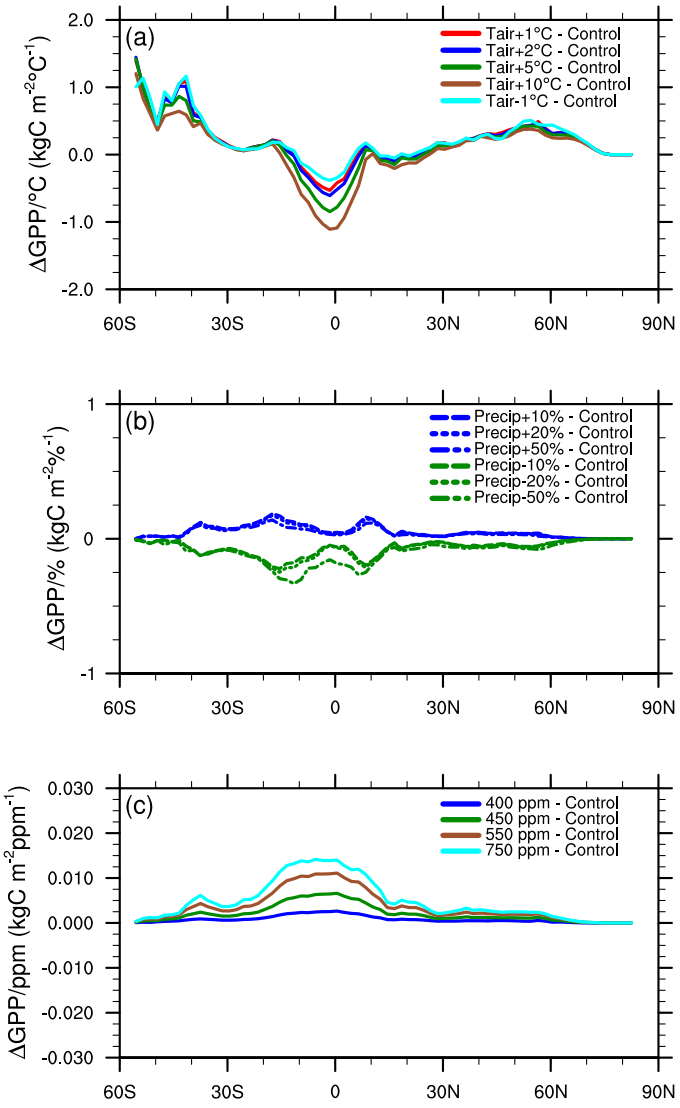

Figure 6.3: Difference in rate of change of zonal mean of total annual GPP for changes in each of the three climate drivers (surface air temperature, precipitation and atmospheric CO_2 concentrations). **(a)** shows the rate of change of GPP per °C (surface air temperature), **(b)** the rate of change of GPP per % (precipitation) and **(c)** the rate of changes of GPP per ppm (atmospheric CO_2 concentrations).

scale. The trend in simulated GPP in the tropics and extratropics or the various subregions (Figure 5.1) may either be the same (with all regions simulating increasing or decreasing GPP with changes in climate) or the opposite (with some regions simulating increasing GPP and others simulating decreasing GPP with changes in climate). Simulation of GPP with changes in climate at the regional scale means that these trends can be discerned.

JULES GPP is more sensitive to changes in precipitation and atmospheric CO_2 concentrations than surface air temperature at the global scale. The greater sensitivity of JULES in simulated GPP to changes in precipitation and atmospheric CO_2 concentrations at the global scale can be observed at the regional scale with the tropics and extratropics both sensitive to changes (Figures 6.4b and c; Figures 6.10). This is observed more strongly in the seasonal differences in GPP with JULES more sensitive to changes in precipitation in summer than winter with no sensitivity in the American, African and South and South-East Asian tropics (Figures 6.10c and d).

As with changes in precipitation at the global scale, the model is more sensitive to a reduction in precipitation than an increase (Figures 6.4b). The model's sensitivity to air temperature is mostly a result of its sensitivity in the tropics (10 °S–10 °N) and extratropics (Figures 6.4a). With increasing air temperature changes (+5 °C and +10 °C), simulated GPP is higher in the extratropics and lower in the tropics.

With changes in air temperature, the trends in simulated LAI are different from those observed for GPP at the regional scale. JULES is only sensitive to changing air temperature with changes in the extratropics ranging from 0.2 to 2.2 m^2m^{-2} with no changes in the tropics (Figure 6.5a; Figure 6.11). While modelled GPP was more sensitive to changes in precipitation and CO_2 concentration than air temperature, LAI was mostly sensitive to temperature in summer in the Northern Hemisphere and the extratropical Southern Hemisphere (Figures 6.11a and b). As observed at the global scale, JULES is insensitive to changes in simulated LAI with varying precipitation and atmospheric CO_2 concentrations (Figure 6.5b and c).

The sensitivity of GPP fluxes to changes at the regional scale was further examined for seven regions (described in Chapter 5 when evaluating simulated GPP fluxes at the regional scale; see Table 5.2). With changing air temperature, it was found that with increasing temperatures the model

was not very sensitive to changes globally (Figure 6.1a). At the regional scale, the trend is different for the various regions (Figure 6.6).This was also shown for precipitation and atmospheric CO_2 concentrations.

It can be seen that in the extratropical regions (Europe, Northern Asia, Extratropical Southern Hemisphere and North America and Greenland), the changes in GPP are positive with positive increases in air temperature from +1 to +10 °C resulting in ΔGPP ranging from +0.4 to +4.4 Pg C year^{-1} (+16.1 to +139.1 Kg C m^{-2} year^{-1}) for Europe (Figure 6.6a), +0.7 to +6.2 Pg C year^{-1} (+26.9 to +226.7 Kg C m^{-2} year^{-1}) for Northern Asia (Figure 6.6b), +0.2 to +1.4 Pg C year^{-1} (+5.1 to +38.5 Kg C m^{-2} year^{-1}) for the extratropical Southern Hemisphere (Figure 6.6d) and +0.5 to +4.0 Pg C year^{-1} (+18.6 to +137.6 Kg C m^{-2} year^{-1}) for North America and Greenland (Figure 6.6g).

The opposite trend was observed for the three tropical regions (Central and South America, Africa and South and South-East Asia) which had decreasing GPP with increases in air temperature. This resulted in ΔGPP ranging from –0.2 to –8.8 Pg C year^{-1} (–4.7 to –178.8 Kg C m^{-2} year^{-1}) for Central and South America (Figure 6.6f), +0.4 to –1.3 Pg C year^{-1} (+8.8 to –23.8 Kg C m^{-2} year^{-1}) for Africa (Figure 6.6e) and -0.2 to –6.8 Pg C year^{-1} (–4.8 to –138.6 Kg C m^{-2} year^{-1}) for South and South-East Asia (Figure 6.6c). The sensitivity of the model to changes in precipitation for the seven regions are similar to those at the global scale (Figure 6.7). Unlike the sensitivity of JULES to changes in air temperature, the trend in simulated GPP to changes in precipitation follow a similar trend with a reduction of GPP with decreases in precipitation and an increase of GPP with increases in precipitation. As with the global trends, the model is more sensitive to reductions in precipitation than increases with this trend occurring in all seven regions (Figure 6.7).

However in the tropical regions, JULES is more sensitive to reductions in precipitation than increases with changes in ΔGPP ranging from –2.3 to –19.5 Pg C year^{-1} (–48.3 to –410.8 Kg C m^{-2} year^{-1}) for reduced precipitation and +1.8 to +6.2 Pg C year^{-1} (+38.8 to +132.0 Kg C m^{-2} year^{-1}) for increased precipitation in Central and South America (Figure 6.7f), –3.0 to –20.5 Pg C year^{-1} (–63.0 to –423.0 Kg C m^{-2} year^{-1}) for reduced precipitation and +2.6 to +9.5 Pg C year^{-1} (+53.0 to +198.4 Kg C m^{-2} year^{-1}) for increased precipitation in Africa (Figure 6.7e), and –1 to –10 Pg C year^{-1}

(–21.2 to –213.3 $\mathrm{Kg\,C\,m^{-2}\,year^{-1}}$) for reduced precipitation and +0.8 to +3.3 $\mathrm{Pg\,C\,year^{-1}}$ (+17.6 to +71.9 $\mathrm{Kg\,C\,m^{-2}\,year^{-1}}$) for increased precipitation in South and South-East Asia (Figure 6.7f). The same trends occurs in the extratropical regions with smaller values of ΔGPP for both reductions and increases in precipitation.

Forcing the model with increased annual average atmospheric CO_2 concentrations (400 ppm, 450 ppm, 550 ppm and 750 ppm) results in increased ΔGPP for all four concentrations (Figure 6.8). Again as with the precipitation experiments, the increase in productivity of JULES observed at the global scale is the same at the regional scale with the main differences being the magnitude of the effect. JULES is more sensitive to changes in atmospheric CO_2 concentrations in the tropics (Figures 6.8c, e and f) than the extratropics (Figures 6.8a, b, d and g). On average, ΔGPP ranges from +1 to +2.7 $\mathrm{Pg\,C\,year^{-1}}$ (+7.6 to 81.1 $\mathrm{Kg\,C\,m^{-2}\,year^{-1}}$) in the four extratropical regions and +1.2 to +13.0 $\mathrm{Pg\,C\,year^{-1}}$ (+24.3 to +271.9 $\mathrm{Kg\,C\,m^{-2}\,year^{-1}}$) in the three tropical regions.

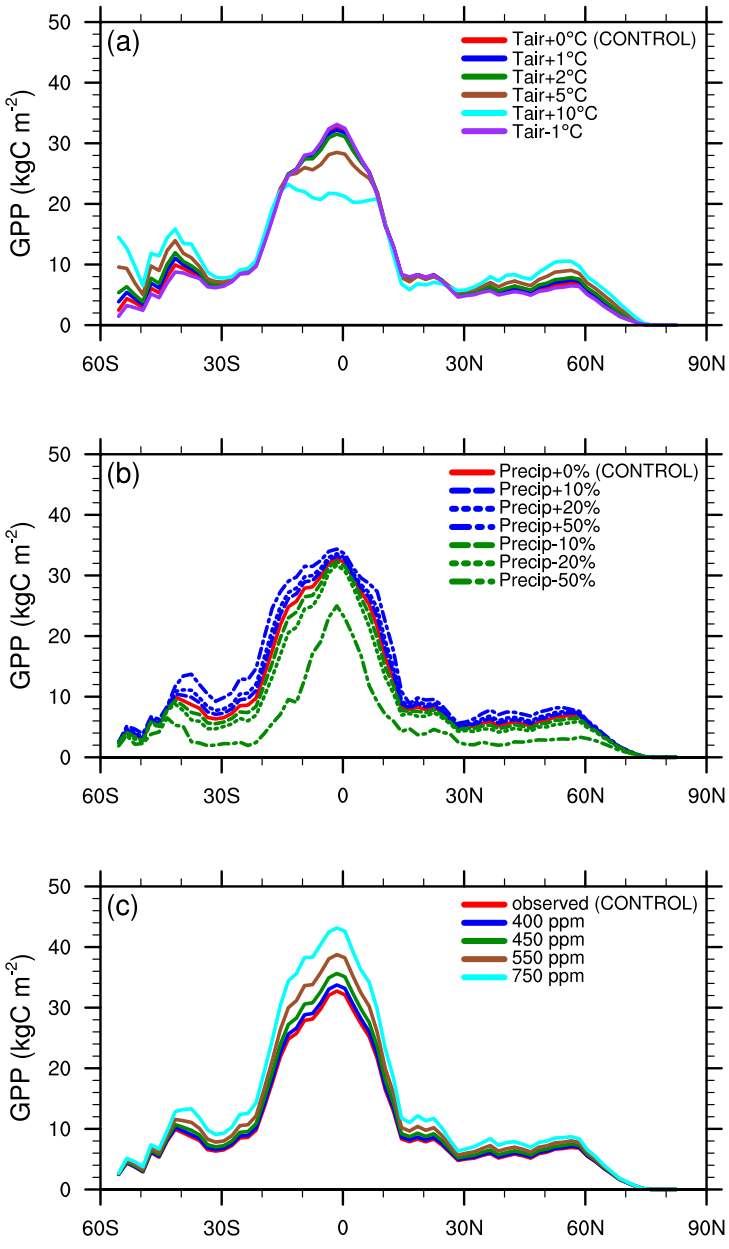

Figure 6.4: Zonal mean of total annual GPP for model simulations with either adjusted **(a)** surface air temperature (T_{air}), **(b)** precipitation (Precip) or **(c)** annual average atmospheric CO_2 concentrations.

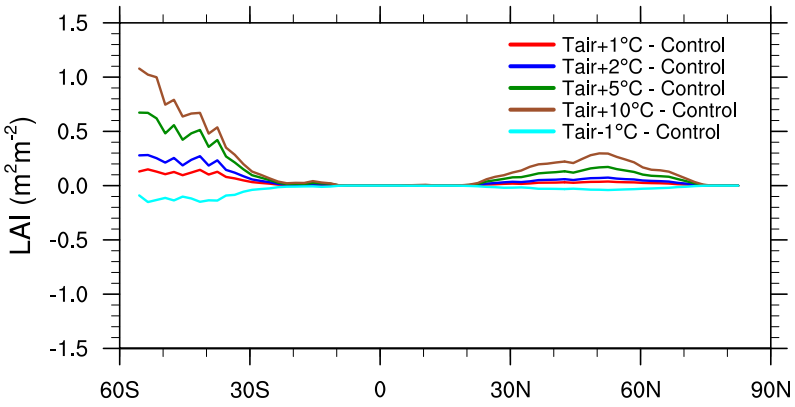

Figure 6.5: Differences in monthly zonal mean LAI between the control simulation (no changes in surface air temperature) and those with adjusted air temperature.

The regional trends in simulated LAI were very similar to those observed at the global scale. Model simulated LAI was found to be sensitive to changes in air temperature at the regional scale (Figure 6.9), but insensitive to changes in precipitation (see Figure G.7 in Appendix G) and CO_2 concentrations (see Figure G.8 in Appendix G). As previously mentioned in Section 6.3.2, modelled LAI was sensitive to changes in temperature in the extratropics, but not in the tropics. Modelled changes in LAI were observed in all four extratropical regions (Figure 6.9a, b, d and g) with little or no changes to LAI in the American, African and South and South-East Asian tropics (Figure 6.9c, e and f). Of the four extratropical regions, model sensitivity was largest in the extratropical Southern Hemisphere with changes in ΔLAI ranging from 0.08 to 0.4 m^2m^{-2} for positive temperature increases (+1 °C to +10 °C).

In general, it was found that the response of JULES to changes in climate is determined by its response at the regional scale. The low sensitivity of the model to changes in temperature at the global scale is a result of opposing changes in the tropics (decline in GPP with increasing temperature) and extratropics (increase in GPP with increasing temperature). Modelled GPP was sensitive to changes in precipitation and atmospheric CO_2 concentrations, but the magnitude of the change from the control simulation depended on the region. Changes in simulated LAI due to changes in temperature at the global scale were driven by changes in LAI in the extratropics.

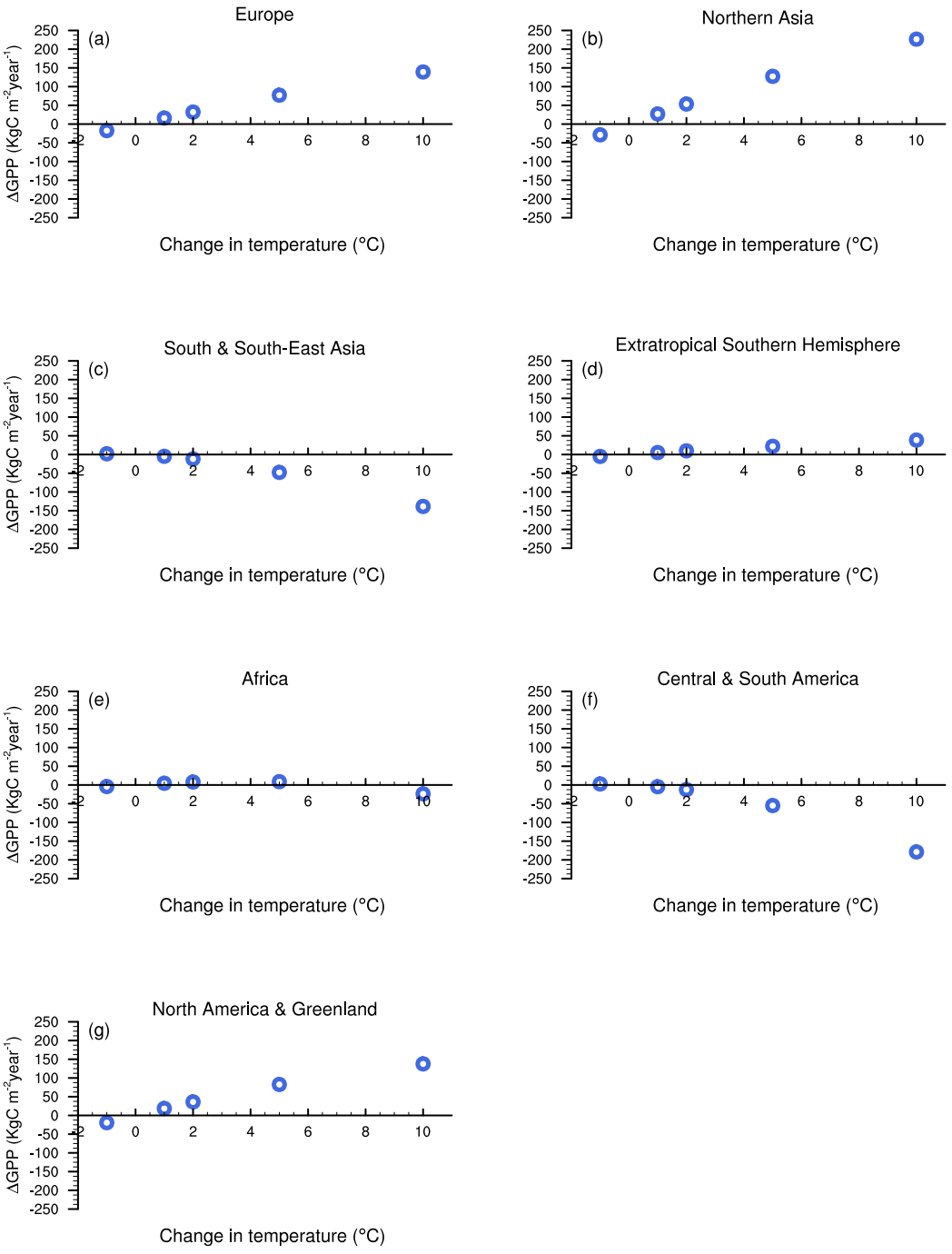

Figure 6.6: Difference in annual average regional GPP between model simulations driven with perturbed and unperturbed meteorological data (control simulation) for the seven regions listed in Table 5.2. The various perturbed model simulations contain only changes to the surface air temperature (unperturbed air temperature (T_{air}) −1 °C, +1 °C, +2 °C, +5 °C and +10 °C) and the control simulation contains no changes to the surface air temperature (T_{air}+0 °C).

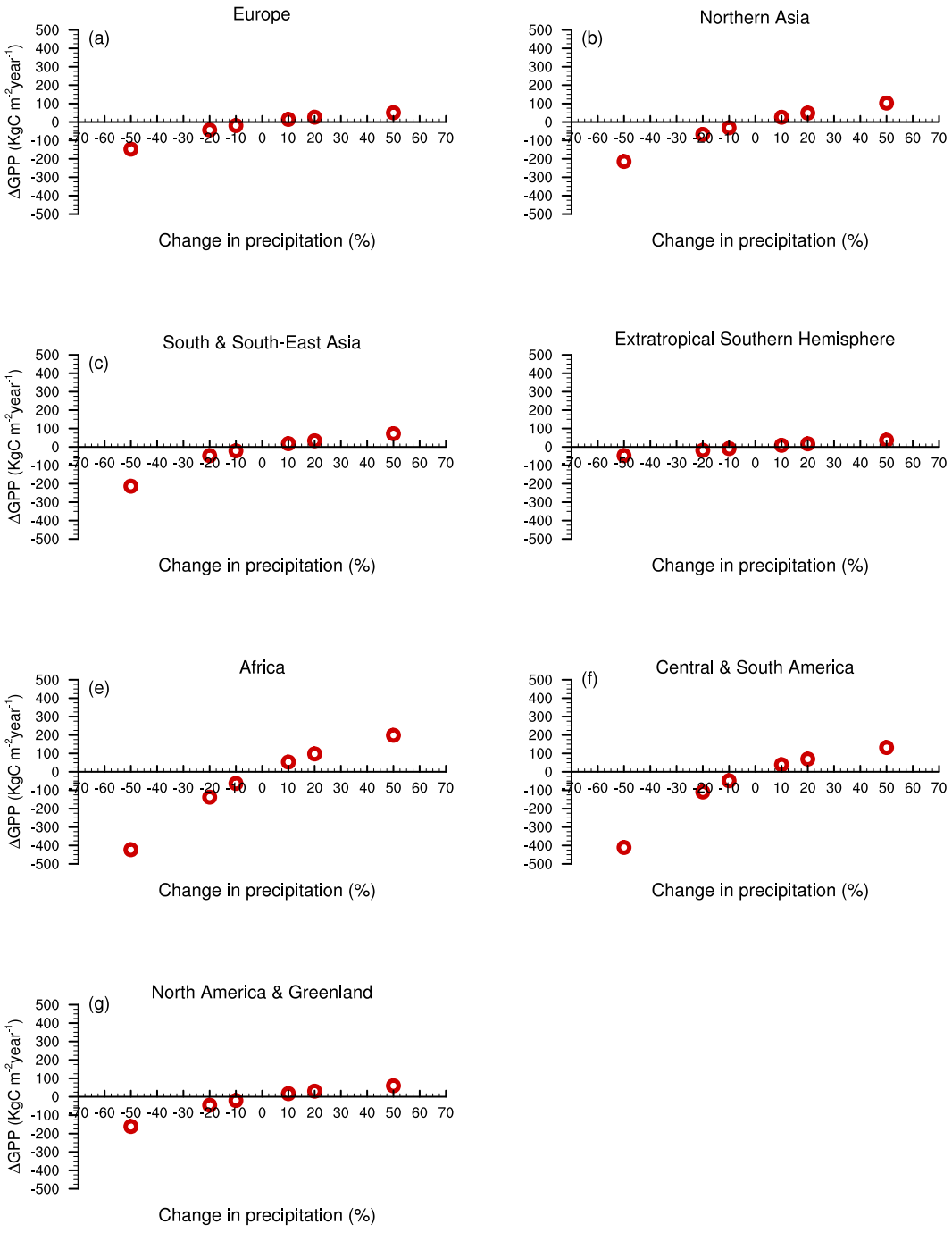

Figure 6.7: Difference in annual average regional GPP between model simulations driven with perturbed and unperturbed meteorological data (control simulation) for the seven regions listed in Table 5.2. The various perturbed model simulations contain only changes to precipitation (unperturbed precipitation +/− 10 %, +/− 20 % and +/− 50 %,) and the control simulation contains no changes to precipitation.

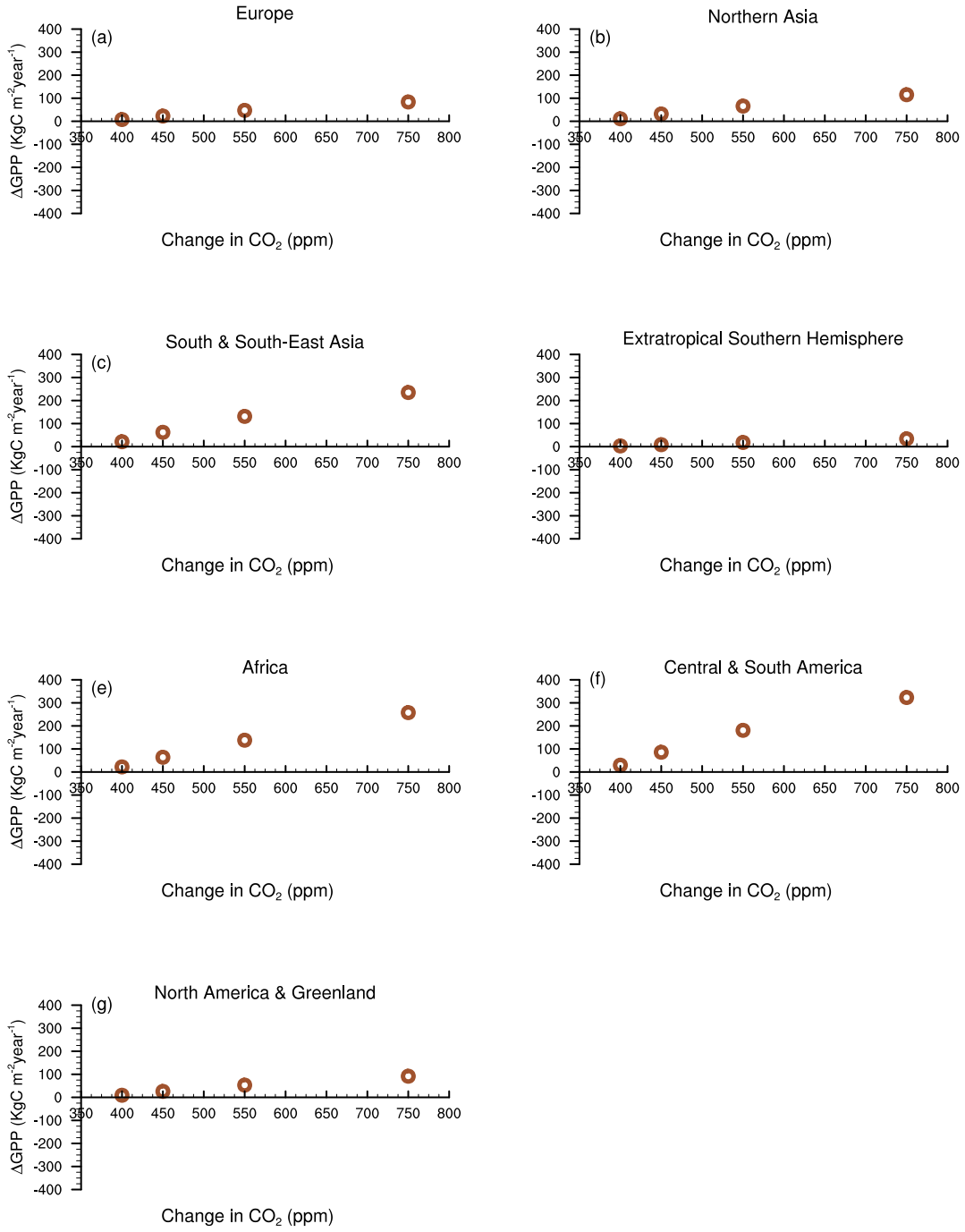

Figure 6.8: Difference in annual average regional GPP between model simulations driven with perturbed and unperturbed meteorological data (control simulation) for the seven regions listed in Table 5.2. The various perturbed model simulations contain only changes to the annual average atmospheric CO_2 concentrations (400 ppm, 450 ppm, 550 ppm and 750 ppm) and the control simulation contains no changes to the historical record.

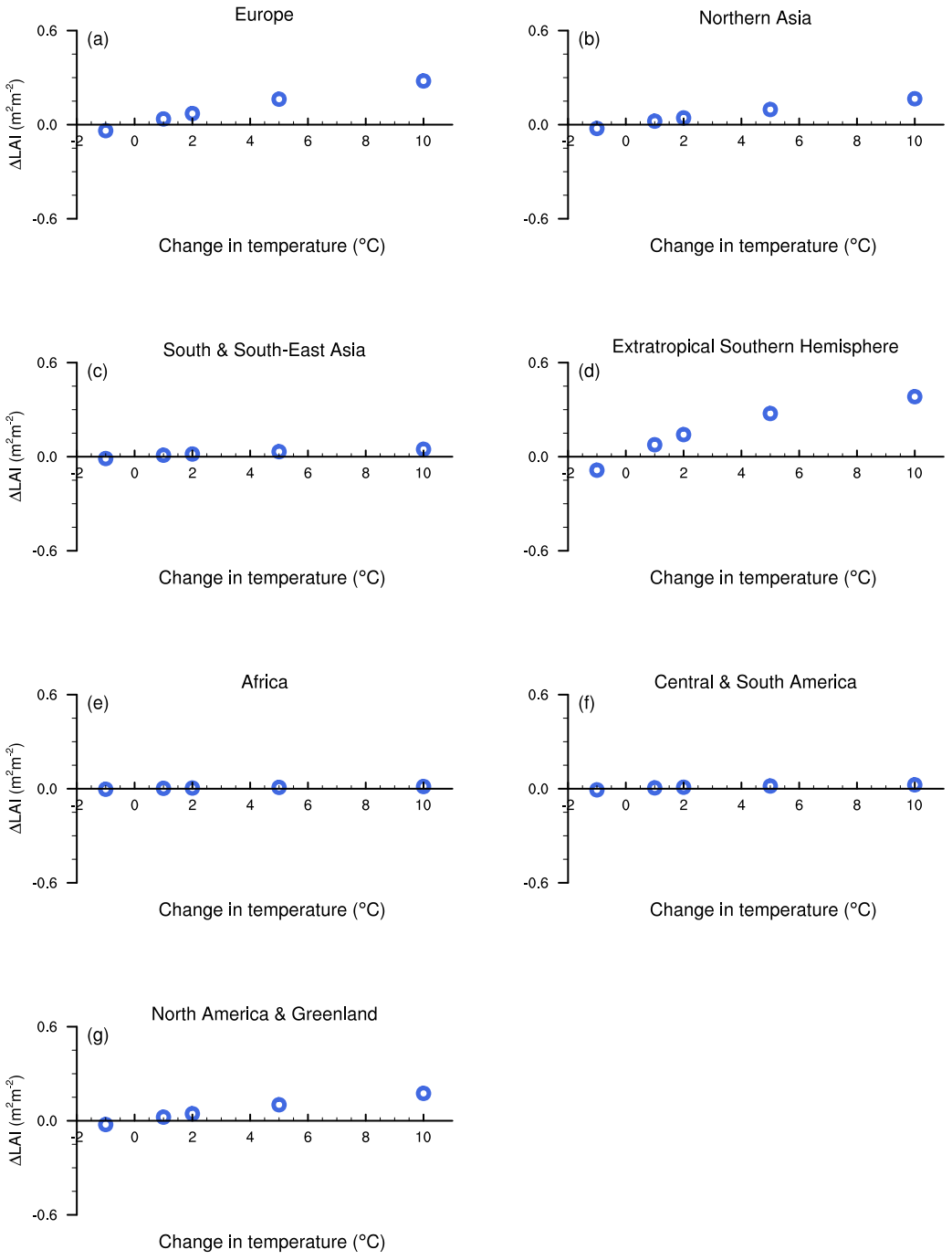

Figure 6.9: Difference in monthly climatology regional LAI between model simulations driven with perturbed and unperturbed meteorological data (control simulation) for the seven regions listed in Table 5.2. The various perturbed model simulations contain only changes to the surface air temperature (unperturbed air temperature (T_{air}) –1 °C, +1 °C, +2 °C, +5 °C and +10 °C) and the control simulation contains no changes to the surface air temperature (T_{air}+0 °C).

6.3.3 Simulation of GPP changes at the biome scale

Forests contribute most to the annual average global GPP for 2000–2010 (61 Pg C year^{-1} on average), followed by grasslands (54 Pg C year^{-1} on average) and then shrubs (8 Pg C year^{-1} on average). Forest, grassland and shrub GPP was found to be sensitive to changes in all three climate drivers (Figures 6.12). Even though forest and grassland GPP make a greater contribution to global GPP than shrubs, shrubs are still sensitive to changes in climate (Figures 6.12g-i). Simulated LAI was sensitive to changes only in surface air temperature with the tropical regions being the most sensitive (Figures 6.13a and d).

The sensitivity of forest GPP to changes in air temperature was very small with increases in air temperature of +1 °C and +2 °C resulting in increases in simulated GPP of less than 1 % (Figure 6.12a). With high air temperature increases of +5 °C and +10 °C (T_{air}+5 °C and T_{air}+10 °C), JULES was less productive with simulated GPP found to decrease by 2 % and 13 %, respectively. Forest GPP was more sensitive to changes in precipitation with increases in annual average global GPP of 3 % to 12 % for increases in precipitation and decreases of 4 % to 42 % for reductions in precipitation (Figure 6.12b).

Grassland GPP was found to be more sensitive to changes in precipitation than air temperature with increases in precipitation resulting in increased GPP of 4 %–14 % and reductions resulting in decreased GPP by 8 %–54 % (Figures 6.12d and e). With increases in atmospheric CO_2, both forest and grassland GPP increase by 3 %–34 % and 3 %–37 %, respectively (Figure 6.12c and f).

Though the contribution of shrub GPP to the global carbon cycle is small compared to forests and grasslands, shrubs are still sensitive to changes in all three climate drivers (Figures 6.12g–i). Simulated GPP by shrubs was more sensitive to reductions in precipitation (–9 % – -58 %) than increases (+8 % – +32 %). With increases in air temperature, smaller increases in GPP were observed (+3 % – +16 %) than with increases in atmospheric CO_2 concentrations (+3 % – +40 %).

At the global scale, the model was very sensitive to changes in precipitation with an increase in productivity with increases in precipitation and a decrease in productivity with a reduction in precipitation (Figure 6.1b)

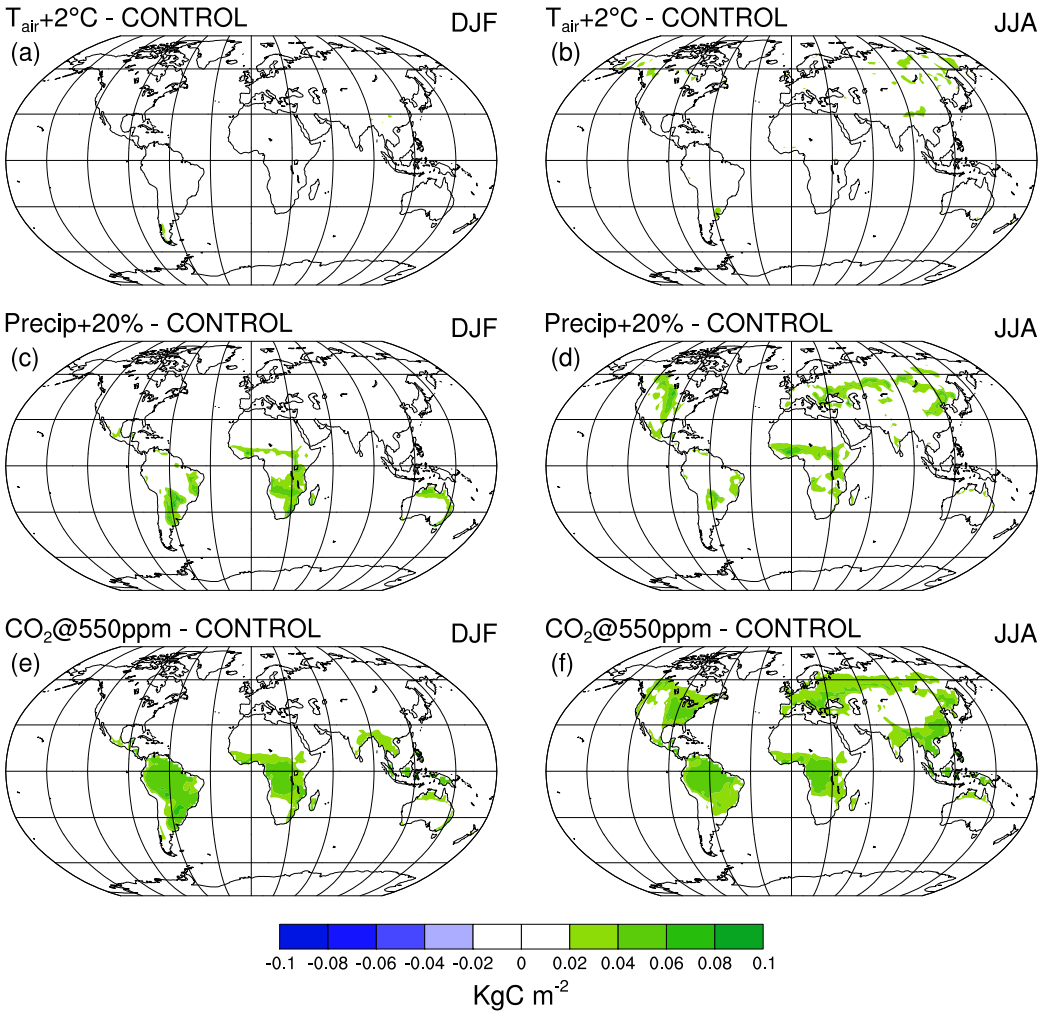

Figure 6.10: Seasonal differences in global GPP ($\mathrm{Kg\,C\,m^{-2}}$) between model simulations with either adjusted surface air temperature ($\mathrm{T_{air}}$), precipitation (Precip) or annual average atmospheric CO_2 concentrations and the control simulation (no changes to either temperature, precipitation or CO_2 concentrations). **(a)** and **(b)** shows the difference in GPP between model simulations with air temperature modified by $+2\,^{\circ}\mathrm{C}$ and the control simulation for DJF and JJA, respectively, **(c)** and **(d)** the difference between model simulations with precipitation modified by adding 20 % and the control, and **(e)** and **(f)** the difference between model simulations forced with constant atmospheric CO_2 concentration of 550 ppm and the control. Blue indicates reduced GPP with increase in climate driver, green indicates increase and white indicates little or no change.

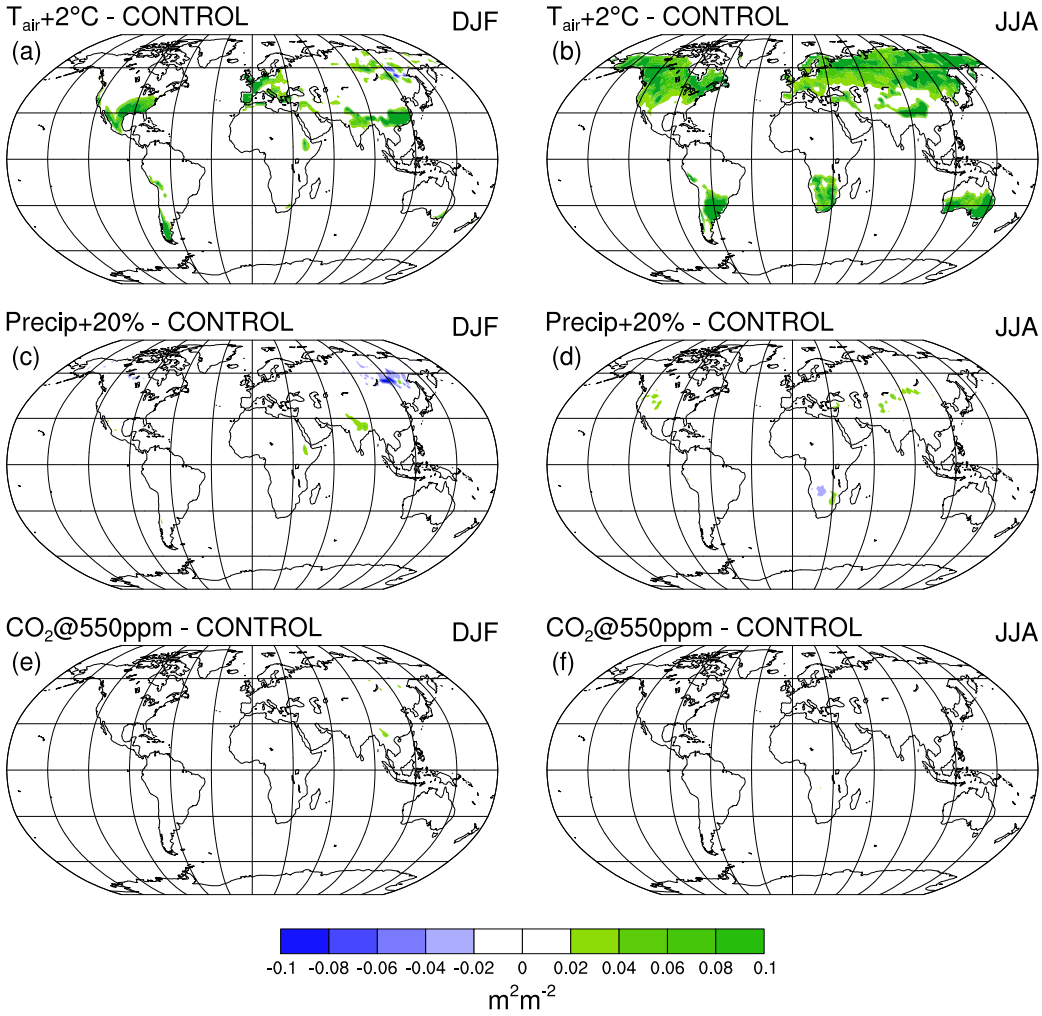

Figure 6.11: Seasonal differences in monthly climatology global LAI (m^2m^{-2}) between model simulations with either adjusted surface air temperature (T_{air}), precipitation (Precip) or annual average atmospheric CO_2 concentrations and the control simulation (no changes to either temperature, precipitation or CO_2 concentrations). Temperature, precipitation and atmospheric CO_2 concentrations were varied as in Figure 6.10. Blue indicates reduced LAI with increase in climate driver, green indicates increase and white indicates little or no change.

and this pattern was observed at the biome scale for both forests and grasslands in the tropics and extratropics (Figures 6.12b and e) with simulated LAI insensitive to changes in precipitation (Figures 6.13b and e). Shrubs were found to be sensitive to increases and reductions in all three climate drivers, but their contribution to global GPP is smaller than that of forests and grasslands. Only forest and grassland LAI were sensitive to changes in air temperature with no changes in modelled LAI with varying precipitation and atmospheric CO_2.

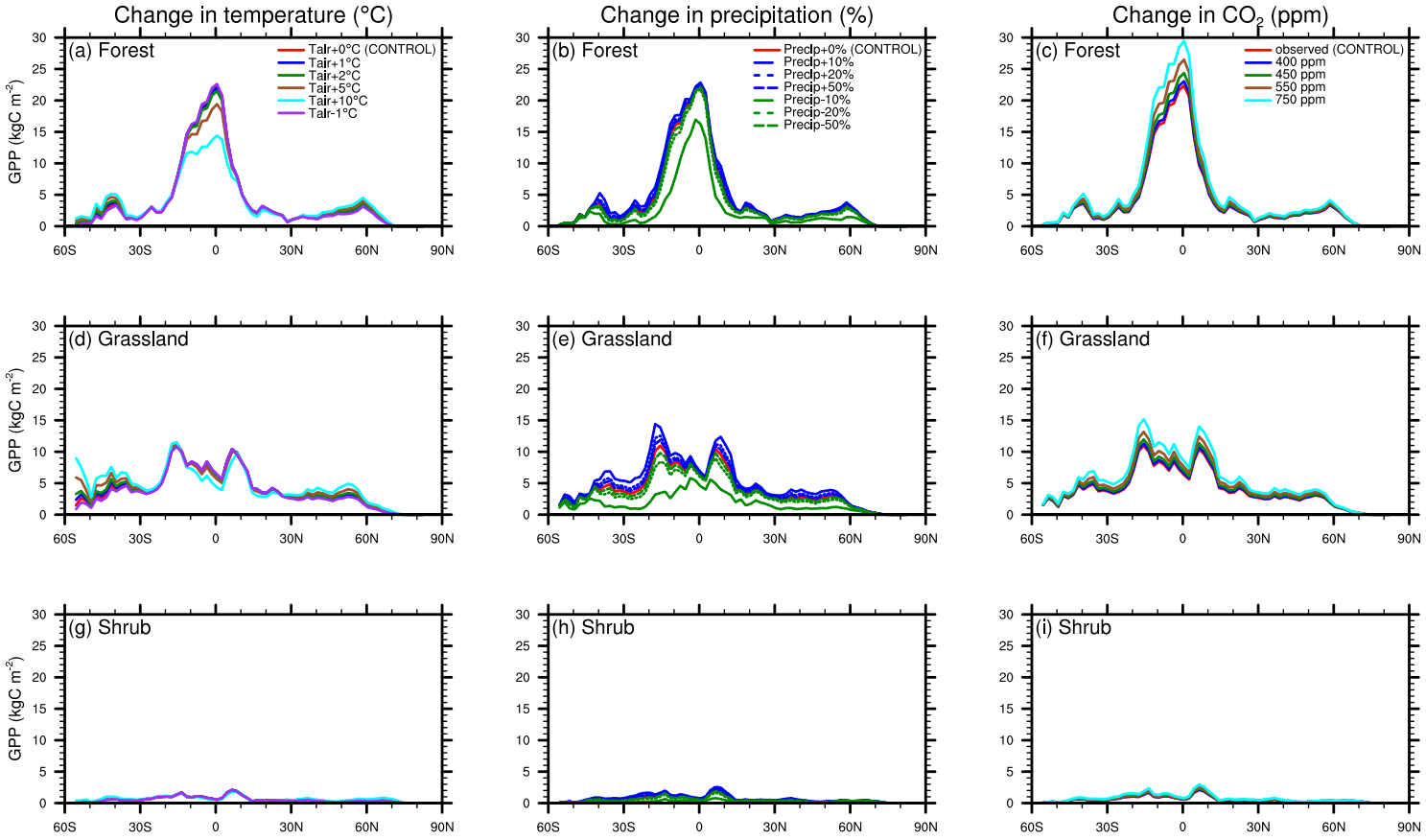

Figure 6.12: Zonal mean of total annual GPP for model simulations with either varying surface air temperature (T_{air}), precipitation (Precip) or annual average atmospheric CO_2 concentrations for 3 biome types (Forest, Grassland and Shrub). **(a)**–**(c)** displays the zonal mean GPP for forests with varying air temperature, precipitation and CO_2 concentrations, respectively, **(d)**–**(f)** for grasslands and **(g)**–**(i)** for shrubs.

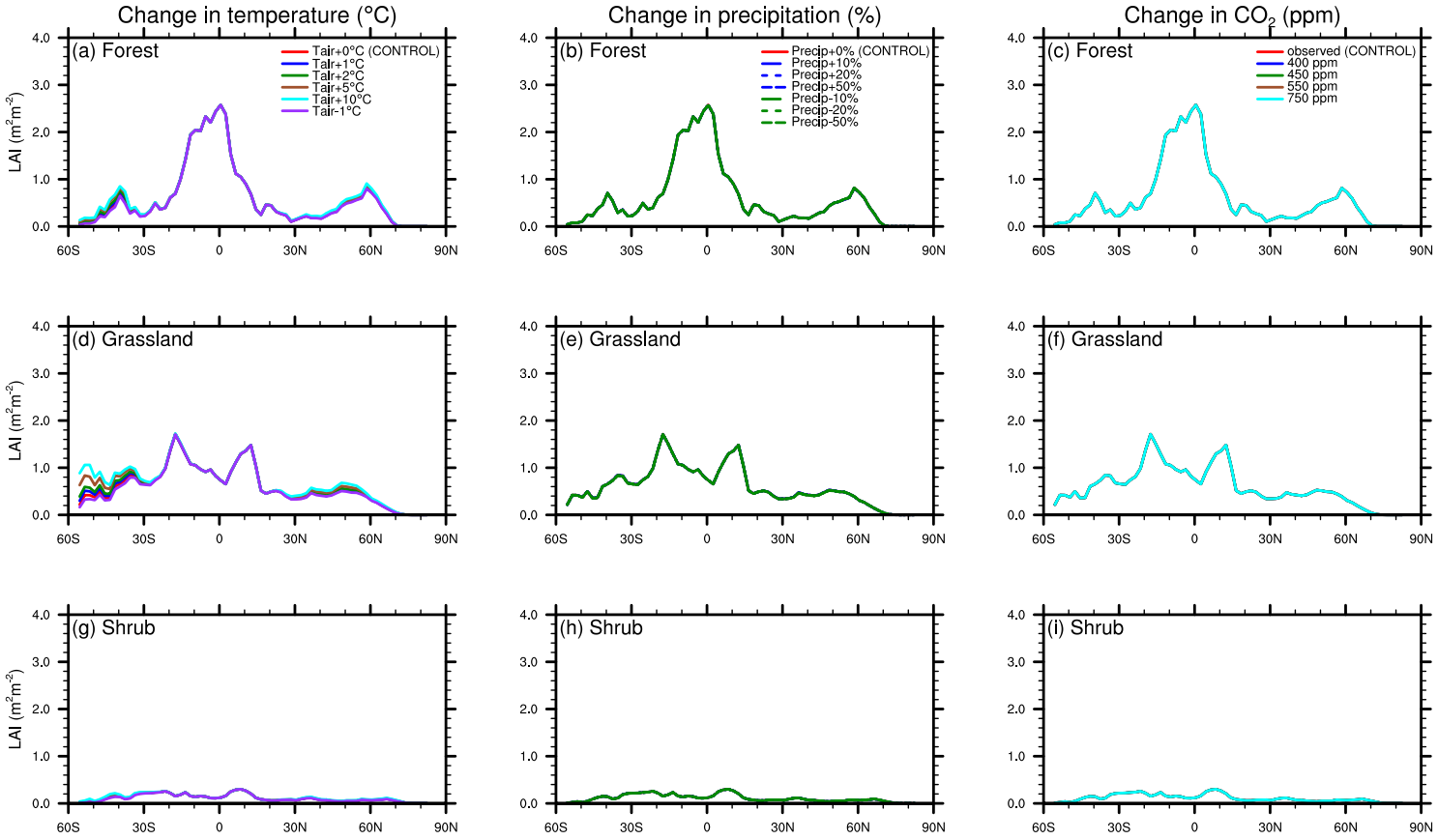

Figure 6.13: Zonal mean of monthly climatology LAI for model simulations with either varying surface air temperature (T_{air}), precipitation (Precip) or annual average atmospheric CO_2 concentrations for 3 biome types (Forest, Grassland and Shrub). **(a)**–**(c)** displays the zonal mean LAI for forests with varying air temperature, precipitation and CO_2 concentrations, respectively, **(d)**–**(f)** for grasslands and **(g)**–**(i)** for shrubs.

6.4 Discussion

The response of the model to changes in climate at the global and regional scale is discussed here as well as the response of forest, grassland and shrub GPP to changes in the climate drivers.

6.4.1 How sensitive is JULES to changes in surface air temperature, precipitation and atmospheric CO_2 concentrations at global and regional scales?

At the global scale, JULES GPP was sensitive to changes in all three climate drivers (surface air temperature, precipitation and atmospheric CO_2 concentrations). The greatest differences resulted from changes in precipitation and annual average atmospheric CO_2 concentrations (Figure 6.1). The greater sensitivity of the model to reductions in precipitation than increases are due to reductions in soil moisture availability, which is accounted for in JULES by multiplying the potential (nonstressed) leaf photosynthesis by a soil water factor (Cox et al., 1998). The increase in simulated GPP due to increasing atmospheric CO_2 concentrations means that JULES has the ability to simulate the CO_2 fertilisation effect (Section 2.3.2).

The low sensitivity of the model to changes in air temperature at the global scale is mostly due to opposing changes in simulated GPP in the tropics (little or negative changes in GPP from the control with increasing temperature) and the extratropics (positive changes in GPP with increasing temperature) (Figure 6.6). As described in Section 6.2.1, changing surface air temperature affects specific humidity which must then be recalculated (Appendix E). JULES was found to be very sensitive to changes in surface air temperature with no corresponding changes in specific humidity (Figure 6.14). Increasing surface air temperature without the corresponding change in humidity implies a warmer and drier atmosphere and results in reduced productivity of the model at global scales (Figure 6.14). In the extratropics, simulated GPP was found to be insensitive to increases in air temperature and in the tropics, GPP was found to decrease with increases in air temperature.

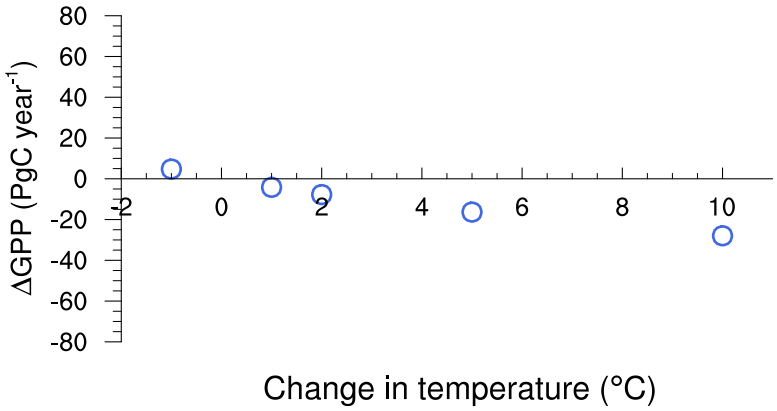

Figure 6.14: Difference in annual average global GPP between model simulations driven with perturbed and unperturbed surface air temperature (control simulation). For these model simulations, specific humidity was not adjusted.

Surface air temperature can affect four major aspects of plant growth; photosynthesis, respiration, soil nutrients and development (Lewis et al., 2005). The initial response of plants to rises in air temperature will be positive with increases in GPP, but then will slow or decline after reaching the optimum range which varies from plant to plant in the real world and for the various PFTs in the model. At high air temperatures, photosynthesis is limited due to changes in leaf biochemistry which is a result of permanent changes and possible damage to proteins Rowland et al. (2015). The decrease in annual average GPP in the three tropical regions (Central and South America, Africa and South and South-East Asia) with rising air temperatures is due to the upper temperature limit for photosynthesis being surpassed. The upper temperature limit for photosynthesis in broadleaf trees and C4 grasses in JULES (in the tropics, these are the dominant land cover types used by the model) is 36.0 °C and 45.0 °C, respectively (Clark et al., 2011). Using field measurements from a tropical forest site in Brazil, Doughty and Goulden (2008) showed that reductions in forest productivity occurred at air temperatures above 28 °C, which corresponds to decreases in photosynthesis at leaf temperatures above 30–33 °C (Rowland et al., 2015). Doughty and Goulden (2008) suggested that tropical forests may already be at a high temperature threshold, above which primary productivity will decline.

Since predicting LAI is important for predicting carbon, water and energy fluxes between the land and atmosphere, it is essential that model LAI can respond realistically to changes in climate. In addition to being a measure of vegetation amount, it directly influences plant transpiration and interception evaporation (Törnros and Menzel, 2014). JULES LAI was observed to be only sensitive to air temperature, but not precipitation or atmospheric CO_2 concentrations (Figures 6.2 and 6.5). The sensitivity of model simulated GPP to changes in air temperature is expected since JULES phenology is updated usually once per day by multiplying the annual maximum LAI with a temperature dependent scaling factor known as the phenological status and the updated LAI is then used to calculate GPP (Clark et al., 2011). In JULES, canopy scale fluxes are calculated from leaf-level photosynthesis as the sum of leaf-level fluxes in each layer, scaled by LAI (Clark et al., 2011). If leaf-level fluxes are scaled using inaccurate LAI, then canopy scale fluxes cannot be predicted accurately (Lloyd et al., 2010; Bonan et al., 2012). Therefore, the model's ability to simulate LAI correctly with changing precipitation and atmospheric CO_2 is essential for realistic predictions of GPP.

With changes in precipitation, JULES GPP was found to be more sensitive to reductions in precipitation than increases at the global scale with the same trend observed in the tropics and extratropics (Figure 6.1; Figure 6.7). The magnitude of the effect varied between regions (Figure 6.7). Galbraith et al. (2010) showed that JULES was more sensitive to increased temperature than reduced precipitation when simulating vegetation carbon (net primary productivity) in Amazonian forests. The insensitivity of JULES LAI to changes in precipitation may help to explain the results from Galbraith et al. (2010). Net primary productivity (NPP) in JULES is calculated using the difference between GPP and plant respiration. TRIFFID allocates a fraction of this NPP for increasing the fractional coverage of the vegetated area with the remainder used for increasing the vegetation carbon content (Cox, 2001). The partitioning coefficient in the equations used to divide NPP into that used for growth and fractional coverage is assumed to be piecewise linear in LAI with all of the NPP used for growth for small LAI values and all of it used for fractional coverage for large LAI values (Cox, 2001).

Changes in vegetation carbon (leaf, root, and total stem carbon) are

related allometrically to changes in the balanced LAI (seasonal maximum which is mulitplied by a phenological status to calculate the actual LAI). Since the phenological status is sensitive to changes in air temperature, but not precipitation and atmospheric CO_2 concentrations, then changes in precipitation and atmospheric CO_2 will have no effect on simulated NPP. This helps to explain why Galbraith et al. (2010) observed the insensitivity of JULES vegetation carbon to changes in precipitation in the Amazon.

6.4.2 Which biomes contribute most to the model's sensitivity at the global and regional scale?

GPP simulated by each of the three biomes was found to be sensitive to changes in all three climate drivers. Since forests and grasslands were the largest contributors to global GPP, they were found to contribute the most to changes in climate (Figures 6.12a-c and d-f). At the global scale, it was observed that changes in simulated GPP due to changes in air temperature were small because of opposing changes in the tropics and extratropics (decreases in GPP with increasing air temperature in the tropics and increases in GPP with increasing air temperature in the extratropics). This is due to the response of tropical forests to changes in air temperature when simulating GPP (Figure 6.12a). In the tropics, simulated forest GPP decreased with increasing air temperature (Figures 6.6c, e and f) and as discussed in Section 6.4.1, this is most likely caused by the tropical regions currently at a temperature threshold, above which primary productivity will decline.

JULES LAI was sensitive to changes in air temperature for forests and grasslands (Figures 6.13a and d). With increases in air temperature, simulated LAI was found to increase only in the extratropics with most changes in forest and grassland LAI occurring in the extratropical Southern Hemisphere (Figure 6.13). In the tropics, the insensitivity of the model may be due to photosynthesis being driven by precipitation (and hence soil water availability) rather than air temperature. Whereas in the extratropics, it is the other way around with temperature being more important than precipitation. Shrub LAI was observed to be insensitive to changes in air temperature.

6.5 Conclusions

A simple sensitivity analysis of JULES was performed in which the response of the model to changes in three climate drivers (surface (2m) air temperature, precipitation and atmospheric CO_2 concentrations) was explored at the global and regional scale. At the global scale, it was found that model GPP was sensitive to changes in air temperature, precipitation and atmospheric CO_2 with increases or decreases observed with the corresponding changes in the meteorological variables. JULES was found to be more sensitive to changes in precipitation and atmospheric CO_2 concentrations than air temperature. However, simulated LAI was only sensitive to changes in surface air temperature, but not to changes in precipitation or atmospheric CO_2 concentrations.

This pattern of the sensitivity of global GPP fluxes to changes in climate is also observed at the regional scale, but the magnitude of the effect was dependent on the region, with the exception of changes in simulated GPP with changes in air temperature. The response of JULES to changes in the three climate drivers was found to be non-linear with the model response to air temperature having the highest non-linearity. Model GPP was mostly non-linear in the tropics. With increasing surface air temperature, JULES was not very sensitive and I would expect the model to be very sensitive to changes in air temperature since its phenology module is sensitive to changes in air temperature, but not precipitation or atmospheric CO_2. The small changes in annual average global GPP with changes in temperature were due to opposing changes in GPP in the tropical and extratropical regions. The decreases in GPP with increasing air temperature may be due to tropical ecosystems already functioning at their temperature limits with further temperature rises resulting in declines in GPP. Changes in simulated LAI with changing temperature was found only in the extratropics and not in the tropics. This suggests that leaf phenology in the tropics is not controlled by air temperature alone, but may be due to soil moisture availability being the major environmental variable controlling leaf phenology and climatic variables (such as specific humidity) which contribute to evaporative demand.

Changes in simulated GPP due to changes in climate for the various biomes were observed for forests, grasslands and shrubs. With changes in

climate, shrub GPP contributed less to changes in global GPP than forests or grasslands. As with changes in simulated LAI at the global and regional scale, forests, grasslands and shrubs were found to be insensitive to changes in precipitation and atmospheric CO_2 with JULES LAI being sensitive to air temperature only in the extratropics for forests and grasslands.

6.6 Summary

In this study, the response of JULES to changes in climate (surface (2m) air temperature, precipitation and atmospheric CO_2 concentrations) was explored at the global, regional and biome scale. JULES GPP was found to be sensitive to changes in all three climate variables with modelled LAI only sensitive to changes in surface air temperature. At the regional scale, for model simulations with varying air temperature, GPP increased with increasing temperature in the extratropics, but decreased with increasing temperature in the tropics. The trend with changing precipitation at the regional scale was the same as that at the global scale with GPP increasing with increasing precipitation and decreasing with decreasing precipitation except for the magnitude of the effect observed. This was observed with increases in annual average atmospheric CO_2 concentrations. The sensitivity of the model was further examined at the biome scale with GPP simulated by forests, grasslands and shrubs sensitive to changes in all three climate forcings. In the next chapter, the dissertation conclusions and areas for future research are discussed.

Bibliography

J. M. Adams and G. Piovesan. Uncertainties in the role of land vegetation in the carbon cycle. *Chemosphere*, 49:805–819, 2002. doi:10.1016/S0045-6535(02)00382-X.

P. Alton, L. Mercado, and P. North. A sensitivity analysis of the land-surface scheme JULES conducted for three forest biomes: Biophysical parameters, model processes, and meteorological driving data. *Global Biogeochemical Cycles*, 20:GB1008, 2007. doi:10.1029/2005GB002653.

G. B. Bonan, K. W. Oleson, R. A. Fisher, G. Lasslop, and M. Reichstein. Reconciling leaf physiological traits and canopy flux data: Use of the TRY and FLUXNET databases in the Community Land Model version 4. *Journal of Geophysical Research*, 117:G02026, 2012. doi:10.1029/2011JG001913.

M. Collins, R. Knutti, J. Arblaster, J.-L. Dufresne, T. Fichefet, P. Friedlingstein, X. Gao, W. J. Gutowski, T. Johns, G. Krinner, M. Shongwe, C. Tebaldi, A. J. Weaver, and M. Wehner. Long-term Climate Change: Projections, Commitments and Irreversibility. In *Climate Change 2013: The Physical Science Basis. Contribution of Working Group I to the Fifth Assessment Report of the Intergovernmental Panel on Climate Change [T. F. Stocker, D. Qin, G.-K. Plattner, M. Tignor, S. K. Allen, J. Boschung, A. Nauels, Y. Xia, V. Bex and P. M. Midgley (eds)]*, pages 1029–1136. Cambridge University Press, Cambridge, United Kingdom and New York, NY, USA, 2013.

B. A. Cosgrove, D. Lohmann, K. E. Mitchell, P. R. Houser, E. F. Wood, J. C. Schaake, A. Robock, C. Marshall, J. Sheffield, Q. Duan, L. Luo, R. W. Higgins, R. T. Pinker, J. D. Tarpley, and J. Meng. Real-time and retrospective forcing in the North American Land Data Assimilation System (NLDAS) project. *Journal of Geophysical Research*, 108(D22), 2003. doi:10.1029/2002JD003118.

P. M. Cox. Description of the TRIFFID dynamic global vegetation model. *Hadley Centre Technical Note*, 24:1–16, 2001.

C. E. Doughty and M. L. Goulden. Are tropical forests near a high temperature threshold? *Journal of Geophysical Research*, 113:G00B07, 2008. doi:10.1029/2007JG000632.

P. Friedlingstein, P. Cox, R. Betts, L. Bopp, W. Von Bloh, V. Brovkin, P. Cadule, S. Doney, M. Eby, I. Fung, et al. Climate-Carbon Cycle Feedback Analysis: Results from the C4MIP Model Intercomparison. *Journal of Climate*, 19:3337–3353, 2006. doi:10.1175/JCLI3800.1.

P. Friedlingstein, M. Meinshausen, V. K. Arora, C. D. Jones, A. Anav, S. K. Liddicoat, and R. Knutti. Uncertainties in CMIP5 climate projections due to carbon cycle feedbacks. *Journal of Climate*, 27:511–526, 2014. doi:10.1175/JCLI-D-12-00579.1.

D. Galbraith, P. E. Levy, S. Sitch, C. Huntingford, P. Cox, M. Williams, and P. Meir. Multiple mechanisms of Amazonian forest biomass losses in three dynamic global vegetation models under climate change. *New Phytologist*, 187:647–665, 2010. doi:10.1111/j.1469-8137.2010.03350.x.

I. M. Held and B. J. Soden. Robust Responses of the Hydrological Cycle to Global Warming. *Journal of Climate*, 19:5686–5699, 2006. doi:10.1175/JCLI3990.1.

S. L. Lewis, O. L. Phillips, and Y. Malhi. *Tropical Forests and Global Atmospheric Change*, chapter Predicting the impacts of global environmental changes on tropical forests, pages 41–56. Oxford University Press, Oxford, UK, 2005.

C. Liu and R. P. Allan. Observed and simulated precipitation responses in wet and dry regions 1850–2100 . *Environmental Research Letters*, 8: 034002, 2013. doi:10.1088/1748-9326/8/3/034002.

J. Lloyd, S. Patiño, R. Q. Paiva, G. B. Nardoto, C. A. Quesada, A. J. B. Santos, T. R. Baker, W. A. Brand, I. Hilke, H. Gielmann, M. Raessler, F. J. Luizão, L. A. Martinelli, and L. M. Mercado. Optimisation of photosynthetic carbon gain and within-canopy gradients of associated foliar traits for amazon forest trees. *Biogeosciences*, 7:1833–1859, 2010. doi:10.5194/bg-7-1833-2010.

Y. Luo, D. Gerten, G. Le Maire, W. J. Parton, E. Weng, X. Zhou, C. Keough, C. Beier, P. Ciais, W. Cramer, J. S. Dukes, B. Emmett, P. J. Hanson, A. Knapp, S. Linder, D. Nepstad, and L. Rustad. Modeled interactive effects of precipitation, temperature, and CO_2 on ecosystem carbon and water dynamics in different climatic zones. *Global Change Biology*, 14:1986–1999, 2008. doi:10.1111/j.1365-2486.2008.01629.x.

L. Rowland, A. Harper, B. O. Christoffersen, D. R. Galbraith, H. M. A. Imbuzeiro, T. L. Powell, C. Doughty, N. M. Levine, Y. Malhi, S. R. Saleska, P. R. Moorcroft, P. Meir, and M. Williams. Modelling climate change responses in tropical forests: similar productivity estimates across five models, but different mechanisms and responses. *Geoscientific Model Development*, 8:1097–1110, 2015. doi:10.5194/gmd-8-1097-2015.

T. Törnros and L. Menzel. Leaf area index as a function of precipitation within a hydrological model. *Hydrology Research*, 45:660–672, 2014. doi:10.2166/nh.2013.143.

P. Wu, N. Christidis, and P. Stott. Anthropogenic impact on Earth's hydrological cycle. *Nature Climate Change*, 3:807–810, 2013. doi:10.1038/nclimate1932.

Chapter 7

Conclusions and future work

In the introduction, I stated that the overall objectives of this dissertation were to investigate sources of uncertainty in the JULES LSM when simulating fluxes of GPP at various scales (point, regional and global). In this final chapter, I will conclude with a review of my progress in this area. I will highlight the original questions asked and summarise the major and minor sources of uncertainty. Finally, ways for which the work presented here could be extended in the future are discussed.

7.1 Conclusions

The aim of this thesis was to investigate sources of uncertainty in the JULES LSM. Chapter 2 described the importance of the land surface in the climate system; from acting as the lower boundary for the atmosphere, with which it exchanges surface fluxes such as carbon, water, energy and various trace gases; being the location of the terrestrial carbon cycle, with changes to it acting as a source or sink affecting its ability to influence atmospheric CO_2 concentrations; and having the ability to influence weather and climate at regional and global scales and on various timescales from intraseasonal to interannual and from decadal to century periods, caused by land use change (Dirmeyer et al., 2013). Models and observations have both shown the reduced ability of land surface to absorb increased anthropogenic CO_2 emissions (Friedlingstein et al., 2006; Canadell et al., 2007; Friedlingstein et al., 2014) with Friedlingstein et al. (2006) and Friedlingstein et al. (2014)

suggesting that the terrestrial carbon cycle is a major source of model uncertainty.

Land surface models (LSM) simulate land-atmosphere interactions at various spatial scales (point, regional and global) and represent processes such as the surface energy balance, water and carbon cycles and the climatic effect of snow. Since LSMs are designed using information from a variety of sources (research literature, idealised laboratory experiments and limited field campaigns), this can lead to sources of uncertainty such as the mathematical description of ecosystem processes and the associated biophysical parameters, initial conditions and the meteorological driving data (Liu and Gupta, 2007). As LSMs become more complicated, there is a need to evaluate their ability to simulate various land-atmosphere fluxes at a range of scales. LSMs are evaluated *offline* (i.e. outside of their host GCM), since it is easier to explore the sensitivity of the model to changes in model parameters, meteorological driving data or land cover datasets without the uncertainties associated with land-atmosphere feedbacks and GCM climate biases and due to low computational cost, and this can help to reduce model uncertainty.

There are a variety of ways to evaluate LSMs and these include directly comparing output from model simulations to observations, parameter perturbation experiments, multi-model intercomparison projects and benchmarking projects. Previous analyses of JULES have yielded some interesting results; Galbraith et al. (2010) showed greater sensitivity of the model to increased temperature than decreased precipitation when simulating biomass in the Amazonian forest; Blyth et al. (2011) showed that at a number of flux tower sites, JULES underestimated GPP in the tropics, but was able to simulate it in the extratropics; and Chadburn et al. (2015) improved the representation of permafrost in the model and evaluated it at an Arctic site.

7.1.1 Global versus local data

The ability of JULES to simulate GPP at 12 FLUXNET sites when using local, global and satellite data was investigated. In addition to this, the model's phenology module was tested by comparing model simulations forced with daily MODIS LAI to those using the default phenology module.

The following research questions were asked:

- How well does JULES perform when using the best available local meteorological *and* parameter datasets? Can the model simulate interannual variability?
- How well does JULES perform when using global data?
- Of the global meteorological datasets used in this study which one compares best to FLUXNET data?
- Are improvements in simulated GPP observed when forcing JULES with daily satellite phenology compared to using the default phenology module?

It was found that the quality of the input data (global and local) is a major source of uncertainty in JULES. When using local data (model parameter and meteorological data), JULES was found to be biased with total annual GPP underestimated by 16 % across all sites and with global data, model performance decreased further with total annual GPP underestimated by 30 % when compared to observations (Figure 4.2). The use of local parameter and meteorological data resulted in JULES being able to simulate GPP at the temperate sites with a negative bias observed at the tropical and cropland sites. This trend was also observed with the multi-year model simulations performed at a limited number of sites (Figure 4.4).

The results from this multi-site evaluation compare well with the evaluation of JULES by Blyth et al. (2011) where only global data was used. Differences between this study and that of Blyth et al. (2011) include model versions and the meteorological datasets used. In both studies, when using global data, GPP was underestimated at temperate and tropical forests and grasslands. However, the improvement in model performance with the use of local data is due to using values for the vegetation properties which are more accurate than the global. Model simulations where the model parameters differed (Figure 4.3e) and those in which the meteorological datasets differed (Figure 4.3d) showed that model parameters are a minor source of uncertainty compared to the meteorological dataset. Of the two global meteorological datasets used, WFDEI compared better to FLUXNET than PRINCETON (Figure 4.5).

It was found that forcing JULES with daily satellite LAI resulted in only small improvements in simulated GPP compared to when using the default phenology model (Figure 4.7). Model performance improved at sites with low annual LAI, such as at the grassland (Vaira Ranch, Fort Peck, Kaamanen) and cropland (Bondland) sites and at the tropical sites (Santarem Km67 and Santarem Km83). There was large day-to-day variation in MODIS LAI at the boreal sites (Tharandt and Hyytiala) which led to underestimated GPP. As a result of this, JULES' phenology module performed just as well as driving the model using satellite data. However, in order for JULES to simulate global GPP, the phenology module must be able to simulate LAI correctly both in the extratropics and tropics.

7.1.2 Global and regional evaluation

The ability of JULES to simulate GPP at global and regional scales for the 2000–2010 was explored in Chapter 5 with the following research questions asked:

- Can JULES capture interannual variability of GPP at the global scale? How do estimates of global GPP compare to those from observational datasets?
- How do fluxes of GPP simulated by JULES compare for various biomes at the global and regional scales?
- How sensitive are fluxes of GPP to the spatial resolution of the model?
- Is the meteorological dataset used to drive the model important at the global scale?

Firstly, the model's ability to reproduce interannual variability of GPP and total annual GPP (integrated across all ecosystems) was examined at the global scale. It was observed that JULES could capture interannual variability of GPP compared to FLUXNET-MTE and MODIS with the highest variation occuring in the winter and spring months (Figure 5.3). The model simulated higher average annual global GPP (integrated across all ecosystem types) than FLUXNET-MTE and MODIS by 8 % and 25 % on average, respectively, with higher GPP simulated by forests and grasslands in the tropics (10°S-10°N and 15°N-30°N) being the main reason for the

global differences (Figure 5.13). Therefore, in JULES simulating GPP in the tropics is a major source of uncertainty.

The effect of spatial resolution on simulations of GPP has been studied with further simulations performed at $1^\circ \times 1^\circ$ and $2^\circ \times 2^\circ$ spatial resolution compared to those at $0.5^\circ \times 0.5^\circ$ resolution (Table 5.1). It was observed that there was little difference in simulations of GPP at the three spatial resolutions (Figure 5.18). This insensitivity to spatial resolution was observed at the regional scale (tropics versus extratropics) and also when the global land area was divided into seven regions (Figure 5.20). The insensitivity to spatial resolution is a minor source of uncertainty in JULES. This turns out to be a useful result since it means that the response of the model to changes in climate at the global scale can be explored more effectively with low spatial resolution ($2^\circ \times 2^\circ$) model simulations.

Since predictions of GPP are largely determined by the meteorological driving data, the uncertainty associated with the meteorological data can be examined by using alternate meteorological datasets to WFDEI-GPCC, such as WFDEI-CRU and PRINCETON. It was found that differences between model simulations driven with WFDEI-GPCC and WFDEI-CRU, which differ only in the precipitation product (Section 3.2.2.2), were very small with differences in simulated annual average global GPP (combined GPP of all terrestrial ecosystems) of $2\,\mathrm{Pg\,C\,year^{-1}}$ at $0.5^\circ \times 0.5^\circ$ spatial resolution (Figures 5.5c and G.3c). The precipitation product when simulating GPP is a minor source of uncertainty. This meant that simulations driven with WFDEI-GPCC could be used for the simulations in Chapter 5. WFDEI-GPCC was used for simulations in Chapter 5 due to wider station coverage of the GPCC dataset, when adjusting monthly precipitation totals in the ERA-Interim reanalysis precipitation data, especially in the high latitudes and for the end of the 20^{th} century.

Driving JULES with the PRINCETON dataset resulted in a slightly higher annual average global GPP of $145\,\mathrm{Pg\,C\,year^{-1}}$ for 2000–2010, which is $5\,\mathrm{Pg\,C\,year^{-1}}$ greater than that simulated by JULES driven with WFDEI-GPCC at 2-degree resolution. At the regional scale, it was found that driving the model with the WFDEI-GPCC dataset resulted in higher simulated GPP in the tropics than when using PRINCETON compared to the observation-based estimates (FLUXNET-MTE and MODIS) with slightly higher simulated GPP by the PRINCETON driven simulation in the ex-

tratropics (Figure 5.18). The meteorological data used to drive JULES at the global scale is considered a major source of model uncertainty. Both sets of model simulations (JULES-WFDEI-GPCC-1degree and JULES-PRINCETON) were found to be Rubisco-limited when simulating photosynthesis.

7.1.3 Sensitivity analysis

In Chapter 6, a simple sensitivity study in which the response of JULES to changes in climate (surface (2m) air temperature, precipitation and atmospheric CO_2 concentrations) was explored when simulating GPP for 2000–2010 at the global and regional scale. The research questions asked were:

- How sensitive is JULES to changes in temperature, precipitation and atmospheric CO_2 concentrations at the global scale?
- Which regions contribute most to the model's sensitivity at the global scale?
- Does the sensitivity of the model's biome types to changing climate explain the results at the global and regional scales?

It was found that JULES GPP was sensitive to changes in all three climate factors with simulated GPP most sensitive to changes in precipitation and atmospheric CO_2 concentrations at the global scale (Figure 6.1). The response of JULES GPP to changes in the three climate drivers was non-linear with model response to surface air temperature having the highest non-linearity. Non-linearity occurred mostly in the tropics. JULES LAI was found to be sensitive only to changes in air temperature with the most sensitive regions being the extratropics (Figure 6.2; Figure 6.5).

JULES LAI was found to be insensitive to changes in precipitation and atmospheric CO_2. In the model, the relationship between model GPP and LAI is not tightly coupled as evidenced by the magnitude of the changes in the two with changes in the climate factors. At the regional scale, with increasing air temperature simulated GPP was found to decrease with increasing temperature in the tropics, but increase with increasing temperature in the extratropics. Doughty and Goulden (2008) suggested that tropical forests could be at their temperature threshold, above which primary

productivity would decline. The insensitivity of JULES LAI to changes in precipitation and atmospheric CO_2 is a major source of model uncertainty as is the link between JULES GPP and LAI.

In Chapter 4, I showed that with the use of more accurate information regarding FLUXNET sites, improved predictions of GPP are possible. In the tropical regions, negative biases still exist and this is due to errors in modelling tropical processes. When simulating GPP in the tropics, differences between model and observation-based estimates were observed in Chapter 5. Other sources of uncertainty that were explored include spatial resolution (no impact on simulations of GPP) and the effect of various meteorological driving datasets on GPP simulations (differences mostly in the tropics). Improved model performance when simulating the terrestrial carbon cycle could be attained with the introduction of more PFT classes (version 4.2 of JULES now contains nine PFTs), and their associated model parameters and a phenology model which can simulate LAI in both temperate and tropical regions. The response of JULES to changes in climate at the global and regional scales was examined with a simple sensitivity study in Chapter 6. As expected, model GPP was sensitive to the three climate drivers examined with model LAI only sensitive to changes in surface air temperature (LAI should be affected by changes in precipitation and atmospheric CO_2 concentrations). Improvements in GPP simulations can be achieved with a stronger coupling between model GPP and LAI.

7.2 Future work

There exist many other areas of research when quantifying the uncertainty associated with modelling the terrestrial carbon cycle in the JULES LSM. These areas suggest a variety of research directions in which a more comprehensive reduction of uncertainty in the model can be achieved.

In Chapter 4, the difference between using datasets at the local and global scale when simulating GPP was examined with the major result being that when using local (i.e. site-specific) information, improved predictions of GPP were observed at the majority of sites. When using global data, model performance was further reduced. Using local data as input to the model means that model performance can be quantified when using the best

available information. I concluded that the quality of the input data affected simulated GPP. When the effect of model parameters and meteorological data on simulated GPP was quantified, it was found that the meteorological data had a greater impact on model GPP than parameters. However, it is known that within global gridded meteorological data (such as WFDEI and PRINCETON) derived from reanalyses data, there may be biases in the data which can affect LSM outputs. It is still worthwhile to find model parameters which enable better simulation of GPP fluxes. This could be done using the Adjoint version of JULES (ADJULES). Using ADJULES, simulations can be performed in order to find optimised values of a select number of model parameters for each of the 12 flux tower sites chosen in Chapter 4. This means that model performance using optimised parameters can be compared with using global data. However, using data relevant to a particular flux tower site is a more common practice. Following on from this, instead of using global meteorological data derived from reanalysis datasets, an alternative would be to use meteorological data obtained from the HadGEM model, though this would introduce errors into simulations of GPP since there exist biases in the climate generated by GCMs.

At the global scale, there exist a number of possible future researches in model uncertainty. Firstly, one important source of uncertainty that was briefly mentioned in Chapter 4 when suggesting that differences in simulations of GPP when using local and global data at the various FLUXNET sites may be due to the land cover fractions specified for the sites. In Chapter 5, the land cover classification scheme used was the Global Land Cover Characterization database and the model results may differ if a different land cover classification scheme was used. Most land cover and land cover change maps are derived from satellite data and land cover forcing is a major source of model uncertainty in global land surface modelling (McGuire et al., 2001; Quaife et al., 2008; Poulter et al., 2011). Uncertainties in land cover forcing have been examined at the continental (Jung et al., 2007) and global scales (Poulter et al., 2011) with various LSMs, but no study has been performed with JULES.

Land cover and human-induced land cover change can affect the biophysics, biogeochemistry, and biogeography of the land surface and also has an affect on the atmosphere (Pielke et al., 2011; Giri et al., 2013). Land cover (and land use change) can affect fluxes of water, energy and carbon

as well as other trace gases (biogenic aerosols) with changes in atmospheric turbulence (Dirmeyer et al., 2010; Pielke et al., 2011; Mahmood et al., 2014). Global land cover products include GLC2000 derived from SPOT VEGETATION (Bartholomé and Belward, 2005), the MODIS Collection 5 global land cover (Friedl et al., 2010) and the GLOBCOVER product derived using data from MERIS (Arino et al., 2008). Using these land cover datasets, the uncertainties associated with different land cover forcings when using JULES to simulate global GPP could be quantified. In this study, the version of JULES used was 3.4.1 (Section 3.1.2). In this version, each model grid box is composed of nine different surface types and five of these are PFTs (Section 3.1.1.1). Since model version 4.2, each JULES gridbox can contain nine PFTS (tropical broadleaf evergreen, temperate broadleaf evergreen, broadleaf deciduous, needleleaf evergreen, needleleaf deciduous, C3, C4, evergreen shrub, deciduous shrub). In addition to these new PFTs, updated parameter values have been included. Global scale model simulations using version 4.2 could be compared to those from version 3.4.1.

The addition of extra PFTs, such as crop and drought-deciduous PFTs, would help to improve simulations of GPP at both point and global scales. In the versions of JULES (3.0 and 3.4.1) used in this thesis, an explicit parameterisation of crops is not included. The C3 or C4 grass PFTs are used in place of agricultural lands. The implementation of a drought-deciduous forest PFT in JULES would help to improve model simulations of GPP at latitudes 15°N-30°N (mostly in Mexico) (Section 5.4.1). JULES version 4.0 includes the JULES-crop crop model, which allows for a generic parameterisation of annual crops and includes parameterisations for four globally important crops: wheat, soybean, maize and rice (Osborne et al., 2015). Croplands occupy 12% of the Earth's ice-free land surface and are the dominant vegetation type in several regions of the world, such as midwestern USA, the Ganges basin in India and the Yellow River region of China (Osborne et al., 2015).

In order to implement crops in JULES, new crop plant functional types were added to the model with associated equations and parameters for crop growth and development. With the standard version of JULES (no crop PFT included), the accumulated carbon fluxes calculated by the physiology component of JULES are passed, usually every 10 days, to the dynamic vegetation model (TRIFFID), which allocates NPP into the growth of ex-

isting vegetation (leaf, woody biomass and root) and the expansion of the vegetated area. The additional model equations in JULES-crop must also allocate NPP into several crop organs (leaf, stem, root and harvested organ) and the size of the crop (Osborne et al., 2015). These equations specify the start and duration of the crop growing season and the rate of crop growth for the different crops (Osborne et al., 2015). The start (sowing) and end date (harvesting) of the crop growing season can be prescribed or calculated dynamically using environmental criteria and basically determine the start and end of the simulation.

For point scale model simulations at FLUXNET crop sites, the sowing and harvest dates are usually determined locally. For regional and global scale model simulations, a gridded crop calender data set, such as that from the Center for Sustainability and the Global Environment (SAGE) at the University of Wisconsin-Madison, that specifies the average sowing and harvesting dates for 19 crops can be used (Sacks et al., 2010, https://nelson.wisc.edu/sage/data-and-models/crop-calendar-dataset/index.php). In order to perform regional and global scale model simulations with the 5 PFTs and 4 crop PFTs together, the sowing and harvesting dates dataset must be provided as an ancillary file to the model as well as the relevant land fractions for all 9 PFTs.

In order to implement a drought-deciduous PFT, such as drought-deciduous broadleaf forests which can be found in the seasonally dry tropical forests of Mexico, Central America and northwestern South America (this would solve the problem of the differences between the observation-based and model estimates of GPP at latitudes 15°N-30°N; Section 5.4.1), changes to the JULES phenology model are required. In JULES, phenology is updated once per day by multiplying the annual maximum LAI by a scaling factor, which is calculated using temperature-dependent leaf turnover rates. Leaf turnover rates are a function of temperature and increase when temperature drops below T_{off} (threshold temperature used in leaf phenology). While this is suitable for deciduous broadleaf forests in temperate regions, such as Northern Europe, it will lead to inaccurate modelled LAI for drought-deciduous forests. Instead of modifying modelled LAI using a temperature-derived scaling factor, the scaling factor could be calculated by using periods of dryness as the controlling factor. Two other parameters which are important for leaf photosynthesis are T_{low} and T_{upp} (used when

calculating V_{cmax}). These PFT specific parameters decide the lower and upper temperatures for photosynthesis. The values of T_{low} and T_{upp} could be modified for drought-deciduous plants.

In Chapter 6, a simple sensitivity study was performed in which the response of JULES to changes in climate (surface air temperature, precipitation and atmospheric CO_2 concentrations) at the global scale was performed. This meant that the sensitivity of model GPP to changes in climate could be explored more effectively without the complex interactions associated with multiple changes in climatic factors which could result in complex non-linear responses of ecosystems. Model response to changes in both temperature and precipitation can be difficult to interpret due to effects which can reinforce each other (Luo et al., 2008). A major source of uncertainty that was found in the model was the insensitivity of JULES LAI to increases or decreases in precipitation and atmospheric CO_2 concentrations. Further work on a more direct link between model GPP and LAI would improve predictions of GPP.

An extension to this study would be to perform the sensitivity analysis using extra models such as CLM and CABLE (Table 2.1). This would mean that JULES' response to changes in climate could be compared to that of various LSMs. An interesting area for future research would be to investigate the response of the model to changes in future climate. This could be done by using model output from the Met Office Hadley Centre Global Environment Model version 2 (HadGEM2) for the 21st Century for four climate scenarios (RCP2.6, RCP4.5, RCP6 and RCP8.5) to drive JULES and compare future simulated GPP with model and observation-based estimates from 2000–2010.

7.3 Summary

In summary, I have explored and identified multiple sources of uncertainty in the JULES LSM. An important source of uncertainty explored was how the quality of the input data (local, global and satellite) affected GPP fluxes across a range of biomes and climatic conditions. I showed that the use of data relevant to a particular flux tower site (local) improved GPP estimates with global data introducing biases into model simulations. At the point

scale, it was found that the model parameters were a minor source of uncertainty compared to the meteorological data used to drive JULES. It was shown that JULES could simulate interannual variability at global scales with the model simulating higher global GPP than observation-based estimates. However, at the regional scale, JULES was able to predict GPP estimates in the extratropics, but not the tropics. This inability of JULES to simulate GPP in the tropics is a major source of model uncertainty.

It was found that the model was insensitive to spatial resolution with little differences between the various resolutions tested and when examining the uncertainty associated with the meteorological driving data, differences in model simulations were observed mostly in the tropics. As well as being a major source of uncertainty at the local scale, the meteorological data used to force JULES at the global scale can introduce biases into model output. The response of JULES GPP (and LAI) to changes in climate at the global scale was performed with a simple sensitivity study. This produced some interesting results with how model response varied with changes in surface air temperature, precipitation and atmospheric CO_2 concentrations. Model GPP was observed to be sensitive to changes in all three climate drivers with model LAI only sensitive to changes in air temperature. A stronger coupling between GPP and LAI could reduce GPP uncertainty and improve model estimates. Many other areas of research exist in order to explore and reduce uncertainty in the JULES LSM.

Bibliography

O. Arino, P. Bicheron, F. Achard, J. Latham, R. Witt, and J. L. Weber. GLOBCOVER - The most detailed portrait of Earth. *ESA Bulletin-European Space Agency*, pages 24–31, 2008.

E. Bartholomé and A. S. Belward. GLC2000: a new approach to global land cover mapping from Earth observation data. *International Journal of Remote Sensing*, 26:1959–1977, 2005. doi:10.1080/01431160412331291297.

S. Chadburn, E. Burke, R. Essery, J. Boike, M. Langer, M. Heikenfeld, P. Cox, and P. Friedlingstein. An improved representation of physical permafrost dynamics in the JULES land-surface model. *Geoscientific Model Development*, 8:1493–1508, 2015. doi:10.5194/gmd-8-1493-2015.

P. A. Dirmeyer, N. Niyogi, D.and de Noblet-Ducoudré, R. E. Dickinson, and P. K. Snyder. Impacts of land use change on climate. *International Journal of Climatology*, 30:1905–1907, 2010. doi:10.1002/joc.2157.

P. A. Dirmeyer, Y. Jin, B. Singh, and X. Yan. Trends in Land–Atmosphere Interactions from CMIP5 Simulations. *Journal of Hydrometeorology*, 14: 829–849, 2013. doi:10.1175/JHM-D-12-0107.1.

M. A. Friedl, D. Sulla-Menashe, B. Tan, A. Schneider, N. Ramankutty, A. Sibley, and X. Huang. MODIS Collection 5 global land cover: Algorithm refinements and characterization of new datasets. *Remote Sensing of Environment*, 114:168–182, 2010. doi:10.1016/j.rse.2009.08.016.

C. Giri, B. Pengra, J. Long, and T. R. Loveland. Next generation of global land cover characterization, mapping, and monitoring. *International Journal of Applied Earth Observation and Geoinformation*, 25:30–37, 2013. doi:10.1016/j.jag.2013.03.005.

Y. Luo, D. Gerten, G. Le Maire, W. J. Parton, E. Weng, X. Zhou, C. Keough, C. Beier, P. Ciais, W. Cramer, J. S. Dukes, B. Emmett, P. J. Hanson, A. Knapp, S. Linder, D. Nepstad, and L. Rustad. Modeled interactive effects of precipitation, temperature, and CO_2 on ecosystem carbon and water dynamics in different climatic zones. *Global Change Biology*, 14:1986–1999, 2008. doi:10.1111/j.1365-2486.2008.01629.x.

R. Mahmood, R. A. Pielke, K. G. Hubbard, D. Niyogi, P. A. Dirmeyer, C. McAlpine, A. M. Carleton, R. Hale, S. Gameda, A. Beltrán-Przekurat, B. Baker, R. McNider, D. R. Legates, M. Shepherd, J. Du, P. D. Blanken, O. W. Frauenfeld, U.S. Nair, and S. Fall. Land cover changes and their biogeophysical effects on climate. *International Journal of Climatology*, 34:929–953, 2014. doi:10.1002/joc.3736.

A. D. McGuire, S. Sitch, J. S. Clein, R. Dargaville, G. Esser, J. Foley, M. Heimann, F. Joos, J. Kaplan, D. W. Kicklighter, R. A. Meier, J. M. Melillo, B. Moore III, I. C. Prentice, N. Ramankutty, T. Reichenau, A. Schloss, H. Tian, L. J. Williams, and U. Wittenberg. Carbon balance of the terrestrial biosphere in the Twentieth Century: Analyses of CO_2, climate and land use effects with four process-based ecosystem models. *Global Biogeochemical Cycles*, 15:183–206, 2001. doi:10.1029/2000GB001298.

T. Osborne, J. Gornall, J. Hooker, K. Williams, A. Wiltshire, R. Betts, and T. Wheeler. JULES-crop: a parametrisation of crops in the Joint UK Land Environment Simulator. *Geoscientific Model Development*, 8: 1139–1155, 2015. doi:10.5194/gmd-8-1139-2015.

R. A. Pielke, A. Pitman, D. Niyogi, R. Mahmood, C. McAlpine, F. Hossain, K. K. Goldewijk, U. Nair, R. Betts, S. Fall, M. Reichstein, P. Kabat, and N. de Noblet. Land use/land cover changes and climate: modeling analysis and observational evidence. *Wiley Interdisciplinary Reviews: Climate Change*, 2:828–850, 2011. doi:10.1002/wcc.144.

B. Poulter, D. C. Frank, E. L. Hodson, and N. E. Zimmermann. Impacts of land cover and climate data selection on understanding terrestrial carbon dynamics and the CO_2 airborne fraction. *Biogeosciences*, 8:2027–2036, 2011. doi:10.5194/bg-8-2027-2011.

T. Quaife, S. Quegan, M. Disney, P. Lewis, M. Lomas, and F. I. Woodward. Impact of land cover uncertainties on estimates of biospheric carbon fluxes. *Global Biogeochemical Cycles*, 22:GB4016, 2008. doi:10.1029/2007GB003097.

W. J. Sacks, D. Deryng, J. A. Foley, and N. Ramankutty. Crop planting dates: an analysis of global patterns. *Global Ecology and Biogeography*, 19:607–620, 2010. doi:10.1111/j.1466-8238.2010.00551.x.

Appendix A

Deriving global model parameters used by the global operational version of JULES

In the Global Land Cover Characterization database version 2.0 (GLCC2.0), land cover is classified into 17 categories using the International Geosphere–Biosphere Programme (IGBP) scheme. Each flux tower has a land cover category assigned to it in the GLCC2.0 database (IGBP code in Table 4.4). These IGBP codes are then used to derive the annual maximum LAI (Table A.1) and canopy height factor (Table A.2) for each PFT. The canopy height (metres) is calculated from the canopy height factor (metres) and annual maximum LAI by using Eq. A.1.

$$\text{Canopy height} = \text{Canopy height factor} \times \text{LAI}^{\frac{2}{3}} \tag{A.1}$$

		Leaf Area Index of JULES PFTs				
IGBP code	IGBP class	BL	NL	C3g	C4g	sh
1	EN forest		6.0	2.0		
2	EB forest	9.0		2.0	4.0	
3	DN forest		4.0	2.0		
4	DB forest	5.0		2.0	4.0	3.0
5	Mixed forest	5.0	6.0	2.0		
6	Closed shrub			2.0		3.0
7	Open shrub	5.0		2.0	4.0	2.0
8	Woody savannah	9.0		4.0		2.0
9	Savannah	9.0			4.0	
10	Grassland			3.0	4.0	3.0
11	Permanent wetland	9.0		3.0		3.0
12	Cropland	5.0		5.0	4.0	3.0
13	Urban					
14	Crop/natural mosaic	5.0	6.0	4.0	4.0	3.0
15	Snow and ice					
16	Barren					
17	Water bodies					

Table A.1: Annual Maximum Leaf Area Index (LAI) of JULES vegetation land cover types (PFTs) (BL: broadleaf tree, NL: needleleaf tree, C3g: C3 grass, C4g: C4 grass, sh: shrubs) for each of the 17 IGBP categories. Note that for the Snow and ice, Barren and Water bodies categories, there are no LAI values available.

	BL	NL	C3g	C4g	sh
Canopy Height Factor	6.5	6.5	0.5	0.5	1.0

Table A.2: Canopy height factor (metres) of JULES vegetation land cover types (PFTs) (BL: broadleaf tree, NL: needleleaf tree, C3g: C3 grass, C4g: C4 grass, sh: shrubs).

Appendix B

Global and local soil parameters

B.1 Soil texture fractions

The global and local soil texture fractions (% of sand, silt and clay) for the 12 FLUXNET sites used in Chapter 4 are shown in Table B.1. The global soil data was extracted from the Harmonized World Soil Database version 1.2 (Section 3.2.1.2) and the local data was obtained from site Primary Investigators and research literature. These soil texture fractions are used to compute the soil thermal and hydraulic conductivity parameters listed in Table B.2.

B.2 Soil thermal and hydraulic parameters

The soil thermal and hydraulic parameters required by JULES are derived from fractions of sand, silt and clay for each soil type using Cosby et al. (1984) and are defined in Table B.2. F_s, F_{st} and F_c are the soil texture fractions for sand, silt and clay, respectively. The thermal conductivities, λ, for sand, silt and clay are defined to be $\lambda_{sand} = \lambda_{silt} = 1.57025\ \mathrm{W\,m^{-1}\,K^{-1}}$ and $\lambda_{clay} = 1.16025\ \mathrm{W\,m^{-1}\,K^{-1}}$, respectively and for air, it is $\lambda_{air} = 0.025\ \mathrm{W\,m^{-1}\,K^{-1}}$. The heat capacities, c, for sand, silt and clay are defined to be $c_s = c_{st} = 2.133{\times}10^6\ \mathrm{J\,m^{-3}\,K^{-1}}$ and $c_c = 2.373{\times}10^6\ \mathrm{J\,m^{-3}\,K^{-1}}$, respectively.

	Soil Texture	HF	VA	MM	HY	TH	TUM	ES	FP	KA	S67	S83	BO
Global	Sand fraction (0-30cm)	0.85	0.47	0.47	0.87	0.42	0.62	0.34	0.36	0.87	0.75	0.75	0.35
	Silt fraction (0-30cm)	0.10	0.29	0.32	0.09	0.38	0.12	0.48	0.41	0.09	0.05	0.05	0.41
	Clay fraction (0-30cm)	0.05	0.24	0.21	0.04	0.20	0.26	0.18	0.23	0.04	0.20	0.20	0.24
	Sand fraction (30-100cm)	0.86	0.39	0.40	0.88	0.45	0.53	0.36	0.29	0.88	0.08	0.08	0.30
	Silt fraction (30-100cm)	0.10	0.27	0.29	0.08	0.35	0.13	0.46	0.42	0.08	0.13	0.13	0.36
	Clay fraction (30-100cm)	0.04	0.34	0.31	0.04	0.20	0.34	0.18	0.29	0.04	0.79	0.79	0.34
Local	Sand fraction	0.66[a]	0.30[b]	0.34[c]	0.36[d]	0.17[e]	0.33[f]	0.80[g]	0.60[h]	0.33[i]	0.03[j]	0.50[k]	0.08[f]
	Silt fraction	0.29	0.57	0.03	0.28	0.71	0.34	0.10	0.20	0.33	0.08	0.07	0.65
	Clay fraction	0.06	0.13	0.63	0.07	0.12	0.33	0.10	0.20	0.33	0.89	0.43	0.27

[a] Harvard Forest Data Archive/Exchange (http://atmos.seas.harvard.edu/lab/data/nigec-data.html)
[b] Ameriflux Biological Data (ftp://cdiac.ornl.gov/pub/ameriflux/data/Level1/Sites_ByName/Vaira_Ranch/biological_data/)
[c] Ameriflux Biological Data (ftp://cdiac.ornl.gov/pub/ameriflux/data/Level1/Sites_ByName/Morgan_Monroe_State_Forest/biological_data/)
[d] Personal communication from Pasi Kolari, Department of Forest Sciences, University of Helsinki. The observed soil texture consisted of data at 3 depths: 5-10 cm, 10-31 cm and 31- cm. The average of the three layers was used for the site soil texture.
[e] Personal communication from Thomas Grünwald, Institut für Hydrologie und Meteorologie, TU Dresden. The observed soil texture consisted of data at 7 depths: 0-3 cm, 3-6 cm, 6-12 cm, 12-36 cm, 36-66 cm, 66-96 cm and 96-121 cm. The average of these seven layers was used for the site soil texture. The observed soil depth is 115 cm.
[f] Kato et al. (2007)
[g] Stöckli et al. (2008)
[h] Gilmanov et al. (2005)
[i] Laurila et al. (2001)
[j] Malhi et al. (2009)
[k] Goulden et al. (2004)

Table B.1: Global and local soil texture fractions (% of sand, silt and clay) for the 12 FLUXNET sites (HF: Harvard Forest, VA: Vaira Ranch, MM: Morgan Monroe, HY: Hyytiala, TH: Tharandt, TUM: Tumbarumba, ES: El Saler, FP: Fort Peck, KA: Kaamanen, S67: Santarem Km67, S83: Santarem Km83, BO: Bondville). The global data was extracted from the HWSD dataset (Section 3.2.1.2) and is for two soil depths (0-30 and 30-100cm).

Parameter name	Parameter symbol	Description	Formula	Units
b	b	Exponent in soil hydraulic characteristics	$3.10 + (15.70 \times F_c) - (0.3 \times F_s)$	dimensionless
sathh	Ψ_s	Absolute value of the soil matric suction at saturation	$0.01 \times 10^{2.17-1.58\times F_s-0.63\times F_c}$	m
satcon	K_s	Soil hydraulic conductivity at saturation	$10^{-2.75-0.64\times F_c+1.26\times F_s}$	$\mathrm{kg\,m^{-2}\,s^{-1}}$
sm_sat	θ_s	Volumetric soil moisture content at saturation	$0.505 - 0.037 \times F_c - 0.142 \times F_s$	$\mathrm{m^3}$ water per $\mathrm{m^3}$ soil
sm_crit	θ_c	Critical volumetric soil moisture content	$\theta_s \times (\frac{\Psi_s}{3.364})^{\frac{1}{b}}$	$\mathrm{m^3}$ water per $\mathrm{m^3}$ soil
sm_wilt	θ_w	Volumetric soil moisture content at the wilting point	$\theta_s \times (\frac{\Psi_s}{152.9})^{\frac{1}{b}}$	$\mathrm{m^3}$ water per $\mathrm{m^3}$ soil
hcap	c	Dry soil heat capacity	$(1-\theta_s) \times (F_c \times c_c + F_s \times c_s + F_{st} \times c_{st})$	$\mathrm{J\,m^{-3}\,K^{-1}}$
hcon	λ	Dry soil thermal conductivity	${\lambda_{air}}^{\theta_s} \times {\lambda_{clay}}^{(1-\theta_s)\times F_c} \times {\lambda_{sand}}^{(1-\theta_s)\times F_s} \times {\lambda_{silt}}^{(1-\theta_s)\times F_s t}$	$\mathrm{W\,m^{-1}\,K^{-1}}$

Table B.2: Soil parameter data required by the JULES model.

Appendix C

MODIS LAI Land Product Subsets

The MODIS LAI data (Figure C.1) used to drive JULES at the point scale in Chapter 4 was obtained from the MODIS Land Product Subsets (Section 3.2.2.4).

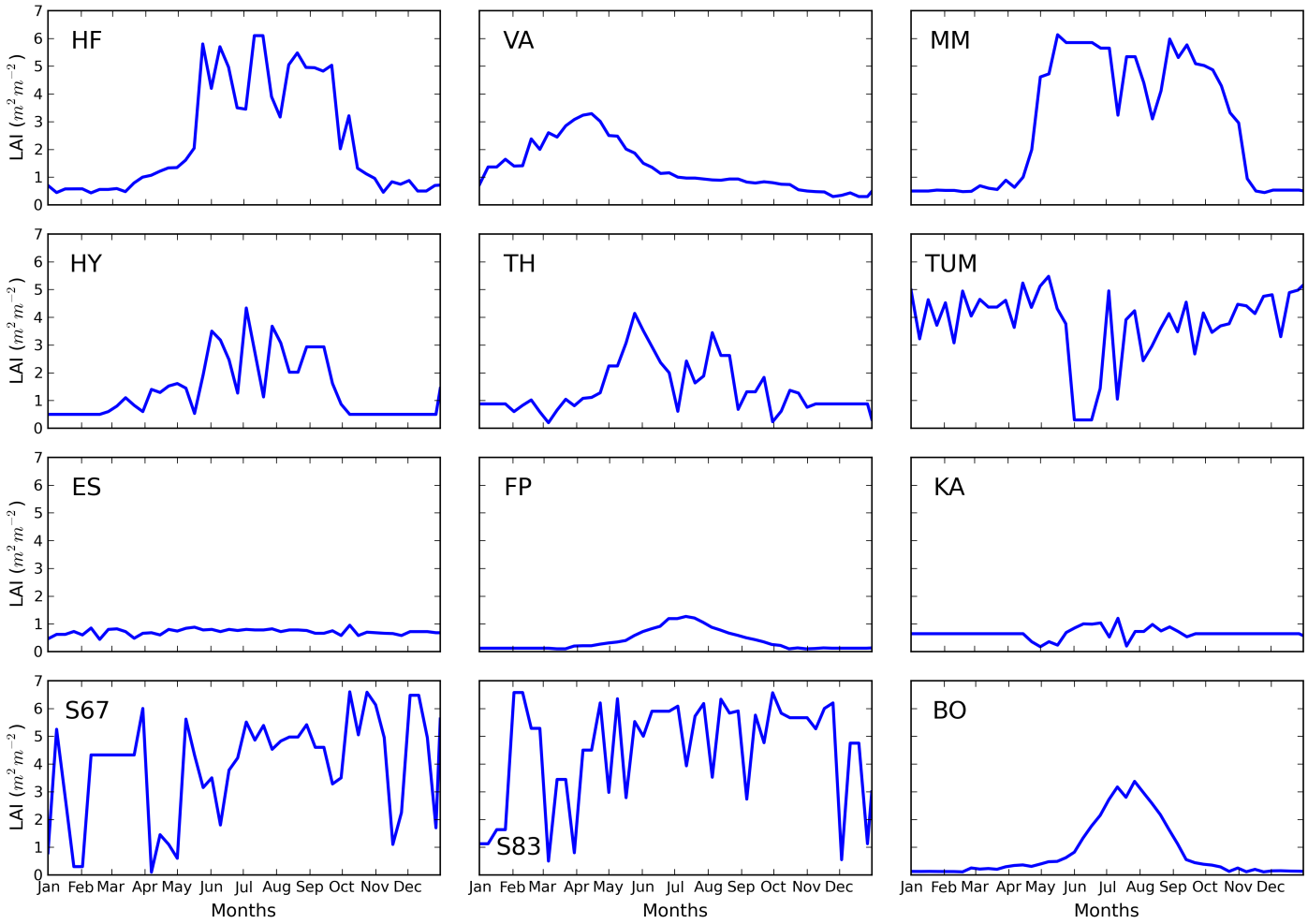

Figure C.1: Seasonal cycle of MODIS LAI obtained from the MODIS Land Product Subsets (Section 3.2.2.4) which is used to drive JULES at the 12 FLUXNET sites in Chapter 4 (HF: Harvard Forest, VA: Vaira Ranch, MM: Morgan Monroe, HY: Hyytiala, TH: Tharandt, TUM: Tumbarumba, ES: El Saler, FP: Fort Peck, KA: Kaamanen, S67: Santarem Km67, S83:Santarem Km83, BO: Bondville).

Appendix D

Converting JULES ancillaries and meteorological data from $0.5^\circ \times 0.5^\circ$ to $1^\circ \times 1^\circ$ spatial resolution

In order to perform model simulations using the WFDEI dataset at $1^\circ \times 1^\circ$ resolution, the ancillary data (soil and vegetation) and the meteorological data (WFDEI) was regridded from $0.5^\circ \times 0.5^\circ$ to $1^\circ \times 1^\circ$ spatial resolution. Regridding is the process of interpolating data from one grid resolution to another. The method used is outlined as follows.

D.1 Ancillary data

The file containing the land mask data was the first to be regridded from $0.5^\circ \times 0.5^\circ$ to $1^\circ \times 1^\circ$ spatial resolution (Figures D.2a and b, respectively). This land mask dataset contains a 720×360 grid of 1s and 0s with 1 representing land and 0 representing ocean (Figure D.1a). The first order conservative remapping function (remapcon) of the Climate Data Operators (CDO) software package (https://code.zmaw.de/projects/cdo) was used for the interpolation process. Once the land mask had been conservatively regridded, the resulting grid consisted of a grid of 1s, 0s and numbers between 0 and 1 (Figure D.1b). Since the land mask can only contain 1s and 0s, the

old land mask values (referred to as *land_mask_old*) were processed using Equation D.1 (the new land mask values are referred to as *land_mask_new*).

$$land\_mask\_new = \begin{cases} 0, & \text{if } 0 < land\_mask\_old < 0.5, \\ 1, & \text{if } 0.5 \leq land\_mask\_old \leq 1. \end{cases} \tag{D.1}$$

This resulted in a new land mask with 5% of the total number of grid boxes (both land and ocean) being modified. The number of land points in the new land mask grid is 16766. This is approximately 4 times smaller than the number of land points in the $0.5^\circ \times 0.5^\circ$ spatial resolution grid (67209 land points). The other ancillary data such as pft fractions and soil parameter data must now use this land mask and this was done by multiplying the ancillary data by the new land mask.

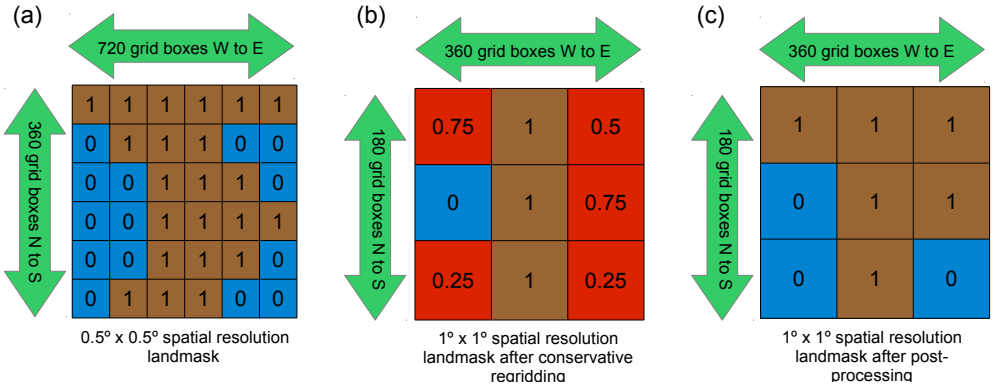

Figure D.1: Steps showing the regridding process of the land mask grid from $0.5^\circ \times 0.5^\circ$ (720×360 grid boxes) to $1^\circ \times 1^\circ$ (360×180 grid boxes) spatial resolution; **(a)** shows the original $0.5^\circ \times 0.5^\circ$ (720×360 grid boxes) resolution land mask with 1s representing land (brown grid boxes) and 0s representing ocean (blue grid boxes), **(b)** shows the land mask after conservative regridding with numbers between 0 and 1 representing areas consisting of land and ocean before the regridding process (red grid boxes) and **(c)** shows the land mask after post-processing of the conservatively regridded data using Equation D.1.

The dataset containing the PFT fractions for each grid box was also modified. In JULES, each grid box can be either a land ice or soil point. If it is a land ice point, then its land ice grid box fraction is set to 1 (JULES does not allow grid boxes to have partial fractional ice cover) and the other 8 land cover type fractions are set to 0. If it is a soil point, then its land ice

grid box fraction is set to 0 and the other 8 land cover type fractions are set to a number between 0 and 1. After the conservative regridding, some of the land ice grid box fractions were numbers between 0 and 1. The land ice grid box fractions (referred to as *land_ice_old*) and the other 8 land cover type fractions (referred to as *land_types_old*) were processed using Equations D.2 and D.3, respectively (*land_ice_new* and *land_types_new* are the updated land ice grid box and other 8 land cover type fractions, respectively).

$$land\_ice\_new = \begin{cases} 1, & \text{if } 0.5 \leq land\_ice\_old \leq 1, \\ 0, & \text{if } 0 \leq land\_ice\_old < 0.5. \end{cases} \tag{D.2}$$

$$land\_types\_new = \begin{cases} 0, & \text{if } 0.5 \leq land\_ice\_old \leq 1, \\ land\,ice\,fraction\,is\,added\,to & \\ land\,cover\,type\,with\,maximum & \\ coverage, & \text{if } 0 \leq land\_ice\_old < 0.5. \end{cases} \tag{D.3}$$

In order to distinguish between land ice and soil points, JULES uses the sm_sat variable (Table B.2) which is the volumetric soil moisture content at saturation. If sm_sat > 0, this indicates a soil point and if sm_sat $= 0$, it is a land ice point. The soil parameter data containing the sm_sat variable was modified so that the land ice and soil points were mutually exclusive.

D.2 Meteorological data

The meteorological data was also regridded from $0.5^\circ \times 0.5^\circ$ to $1^\circ \times 1^\circ$ spatial resolution using the conservative method. In addition to this, the meteorological data must use the same land mask grid as the ancillary data. This was done by multiplying the meteorological data at each time step by the land mask grid. Since the model requires meteorological data for each grid box, the meteorological data was checked at each land point to make sure it contained valid meteorological data and not _FillValue values. The same method was used to regrid the ancillary and meteorological data from

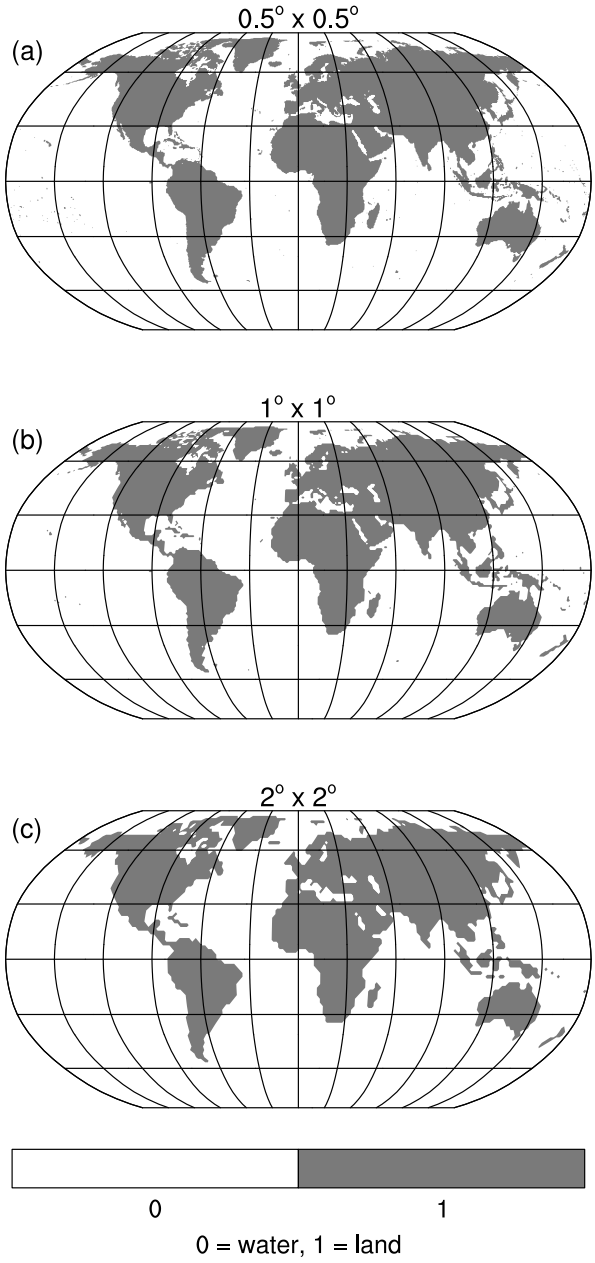

Figure D.2: Land mask grids used by model simulations at **(a)** $0.5^\circ \times 0.5^\circ$, **(b)** $1^\circ \times 1^\circ$ and **(c)** $2^\circ \times 2^\circ$ spatial resolutions.

$0.5^\circ \times 0.5^\circ$ (720×360 grid boxes) to $2^\circ \times 2^\circ$ (180×90 grid boxes) spatial resolution. The $2^\circ \times 2^\circ$ land mask grid has 4187 land points (Figures D.2c) and is approximately 16 times smaller than the number of land points in the $0.5^\circ \times 0.5^\circ$ grid.

Appendix E

Adjusting specific humidity due to changes in surface (2m) air temperature

In Chapter 6, adjusting the surface (2m) air temperature (in this case, by +1°C, +2°C, +5°C, +10°C and –1°C) affects specific humidity and this variable must be recalculated using the method from Weedon et al. (2010), which created a new global sub-daily meteorological forcing dataset (Section 3.2.2.2) derived from the ERA-40 reanalysis product. When calculating the new specific humidity (q_{new}), the relative humidity (RH) implied by the original data was kept fixed when recalculating specific humidity (q) to avoid supersaturation due to adjustments to surface air temperature (Cosgrove et al., 2003). Firstly, the saturated vapour pressure (e_{sat}) for the unadjusted temperature was calculated using equation 4a of Buck (1981):

$$e_{sat} = a\, exp\left[\frac{(b - \frac{T}{d})\, T}{T + c}\right] \tag{E.1}$$

where the constants a, b, c and d were obtained from Table 2 of Buck (1981) and are calculated as a function of temperature (T; °C), optimised for several temperature intervals (Table E.1). Saturated vapour pressure (Equation E.1) must be multipled by a correction factor, f (Equation E.2; referred to as an enhancement factor in Buck (1981)), which depends on

temperature and surface pressure (P; mb) and is calculated using equation 6 of Buck (1981):

$$f = 1 + A + P(B + C(T + D + EP)^2) \tag{E.2}$$

where the constants A, B, C, D and E were obtained from Table 3 of Buck (1981) and calculated as a function of temperature and pressure (Table E.2).

Temperature interval (°C)	a	b	c	d
$0 < T \leq 100$	6.1121	18.564	255.57	254.4
$-80 \leq T \leq 0$	6.1115	23.036	279.82	333.7

Table E.1: Constants for calculating the vapour pressure (mb) of pure water as a function of temperature (T; °C) optimised for temperatures above or below freezing.

Temperature interval (°C)	A	B	C	D	E
$0 < T \leq 100$	7.2×10^{-4}	3.2×10^{-6}	5.9×10^{-10}	0	0
$-80 \leq T \leq 0$	2.2×10^{-4}	3.83×10^{-6}	6.4×10^{-10}	0	0

Table E.2: Constants for calculating the correction factor as a function of temperature (°C) and pressure (mb) for temperatures above or below freezing.

The correction factor was applied to the saturated vapour pressure using

$$e_{sat} = e_{sat} \times f \tag{E.3}$$

The saturated specific humidity (q_{sat}) was then calculated as

$$q_{sat} = \frac{0.62198 \times e_{sat}}{P - (0.37802 \times e_{sat})} \tag{E.4}$$

and relative humidity as

$$\mathrm{RH} = \frac{q \times 100.0}{q_{sat}} \tag{E.5}$$

The above process is repeated using the new surface air temperature and pressure to obtain the new saturated vapour pressure ($\mathrm{e}_{sat,new}$; Equation E.1) and saturated specific humidity ($\mathrm{q}_{sat,new}$; Equation E.4). Since relative humidity is being held constant over the course of the adjustment, the new specific humidity is calculated as

$$q_{new} = \frac{\mathrm{RH} \times q_{sat,new}}{100.0} \tag{E.6}$$

Appendix F

Calculating which potential limiting rate for leaf-level photosynthesis dominates each model grid box at global scales

In JULES, the potential (without water and ozone stress) leaf-level photosynthesis is calculated as the minimum of three potentially-limiting rates: (1) Rubisco-limited (W_c), (2) Light-limited (W_l) and (3) Transport-limited (W_e). Section 3.1.1.3 contains a detailed description of the equations involved. For all model simulations in this thesis, the multi-layer approach for light interception and photosynthesis was used (option 4 in Table 3.1). The number of canopy layers was 10. This minimum limiting rate is calculated for each canopy layer of each PFT. In JULES, information on which minimum limiting rate is used to calculate leaf photosynthesis is not a model output, so the JULES code (and its io) was modified in order to calculate (and output) this limiting rate information. To calculate which minimum limiting rate dominates each model gridbox, an array was created for each corresponding canopy layer. Each array holds the number of the minimum limiting rate (1 = W_c (Rubisco-limited), 2 = W_l (Light-limited) and 3 = W_e (Transport-limited)) which has been used to calculate the potential leaf-level photosynthesis for each land grid point for each PFT (Figure F.1). The minimum limiting rate which occurs most often over the 10 canopy layers

is taken to be that PFT's minimum limiting rate.

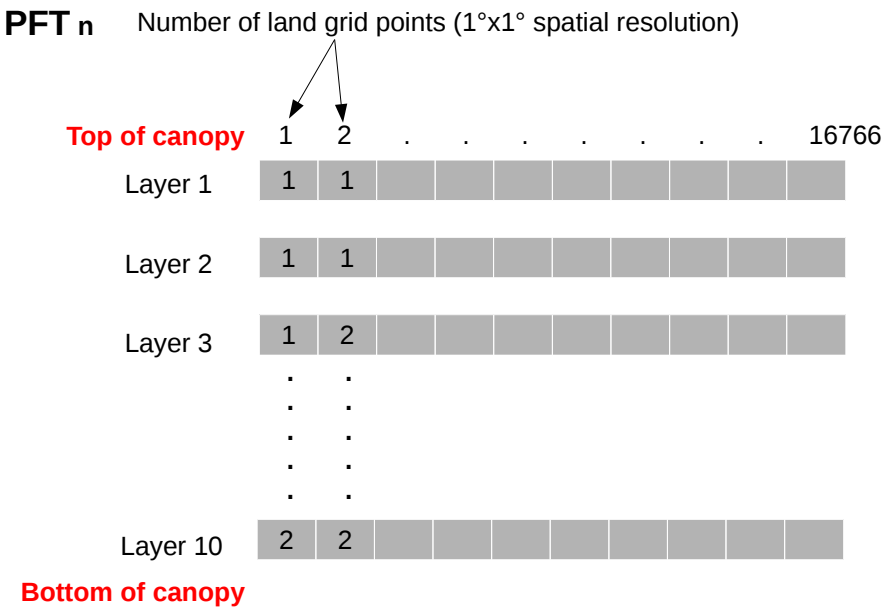

Figure F.1: Scheme showing the calculation of minimum limiting rate numbers for each canopy layer. In the grey boxes, the numbers represent the minimum limiting rate which is used to calculate the potential leaf-level photosynthesis (1 = W_c (Rubisco-limited), 2 = W_l (Light-limited) and 3 = W_e (Transport-limited)). The limiting rate which is used the most over the 10 canopy layers is taken to be that PFTs dominant minimum limiting rate number.

Once the dominant minimum limiting rate number has been calculated for each PFT, two methods were used to create global maps showing which limiting rate dominates each model grid box.

Method 1 The minimum limiting rate number, either 1 (W_c), 2 (W_l) or 3 (W_e), of the PFT with the highest grid box fraction is the limiting rate number for that model grid box. This creates a global map of dominant limiting rate numbers.

Method 2 The grid box fractions associated with each PFT minimum limiting rate number are summed to provide 3 global maps of the percentage of each model grid box is dominated by each minimum limiting rate number.

The calculation of minimum limiting rate numbers occurs at every time

step. To scale this up to monthly time steps, the model output was processed so that for each model grid box, the minimum limiting rate number which dominates across all hourly timesteps within a month, becomes that month's limiting rate. This limiting rate information was obtained from model simulations driven with the WFDEI-GPCC and PRINCETON datasets (both at $1^\circ \times 1^\circ$ spatial resolution).

Appendix G

Additional Figures

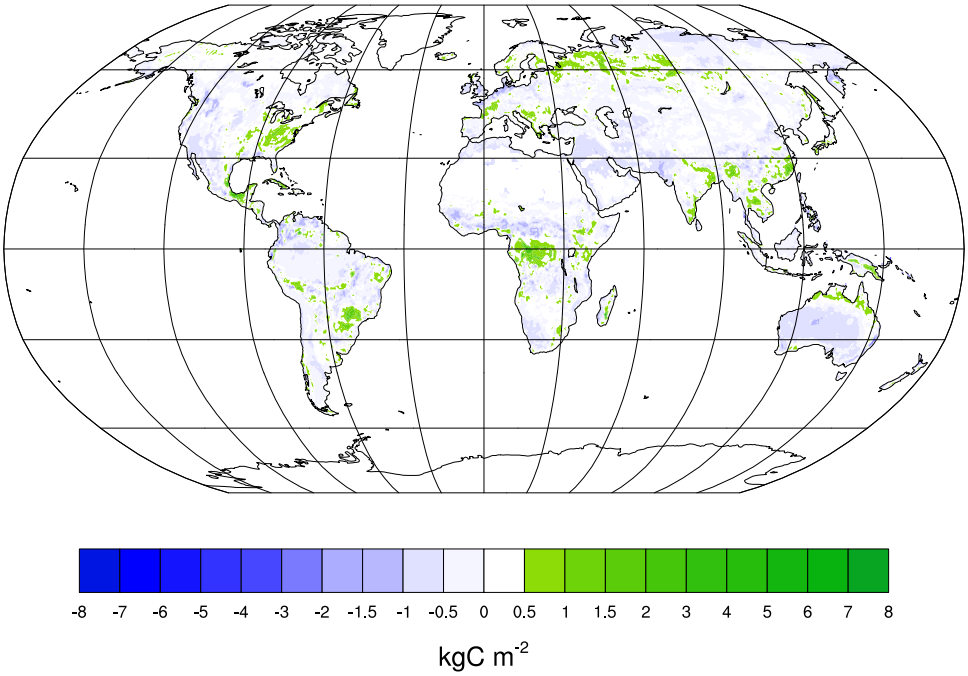

Figure G.1: Difference in total annual GPP for 2000–2010 between the two upscaled FLUXNET datasets that differ by the way in which net ecosystem exchange of CO_2 (NEE) is separated into GPP and terrestrial ecosystem respiration (Section 3.2.3.2). The difference has been calculated by subtracting upscaled observations of GPP based on the work of Lasslop et al. (2010) from that of Reichstein et al. (2005).

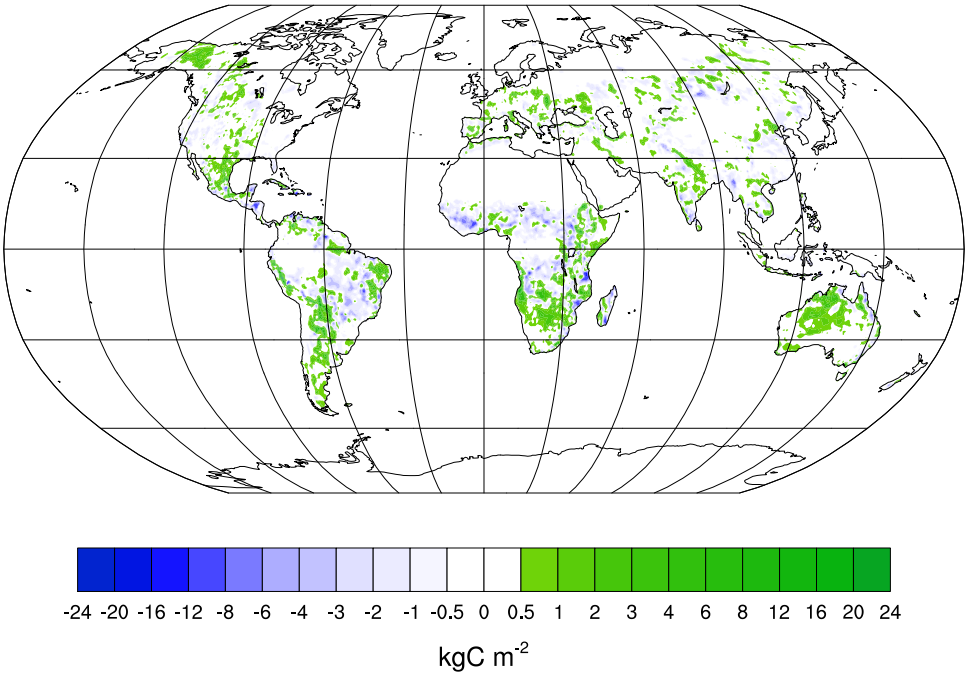

Figure G.2: Difference in simulated total annual GPP for 2000–2010 between JULES-WFDEI-GPCC and JULES-WFDEI-CRU (Table 5.1). The difference was calculated by subtracting JULES-WFDEI-CRU from JULES-WFDEI-GPCC.

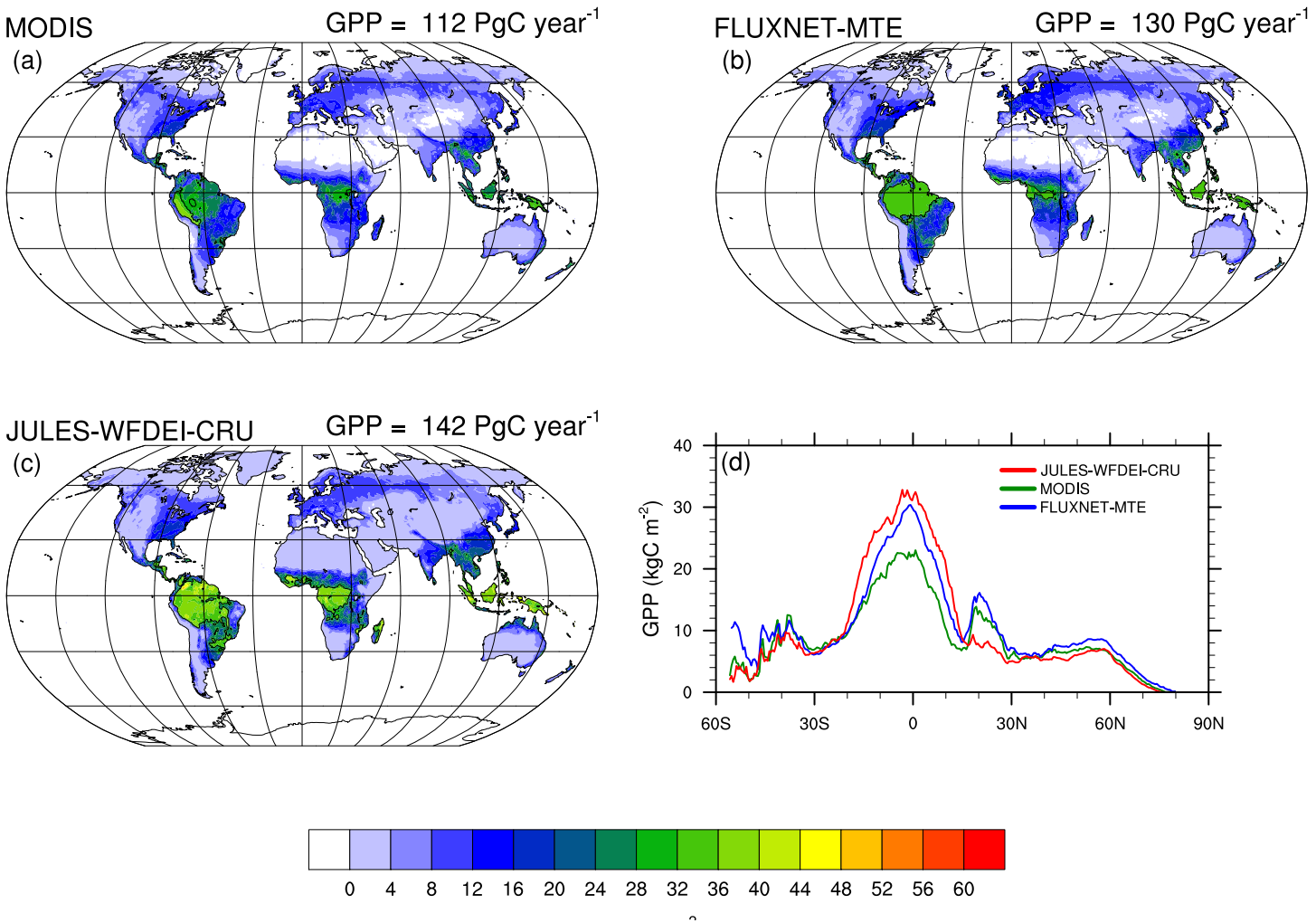

Figure G.3: Total annual and zonal mean model simulated (JULES-WFDEI-CRU) and observed (FLUXNET-MTE and MODIS) GPP fluxes for the 2000–2010 period at the global scale ($0.5^\circ \times 0.5^\circ$ spatial resolution). **(a)**, **(b)** and **(c)** show the total annual GPP of JULES-WFDEI-CRU, FLUXNET-MTE and MODIS GPP, respectively. At the top right of each subplot, the average annual global GPP for 2000–2010 is displayed. **(d)** shows the zonal mean of the total annual JULES-WFDEI-CRU, FLUXNET-MTE and MODIS GPP, respectively.

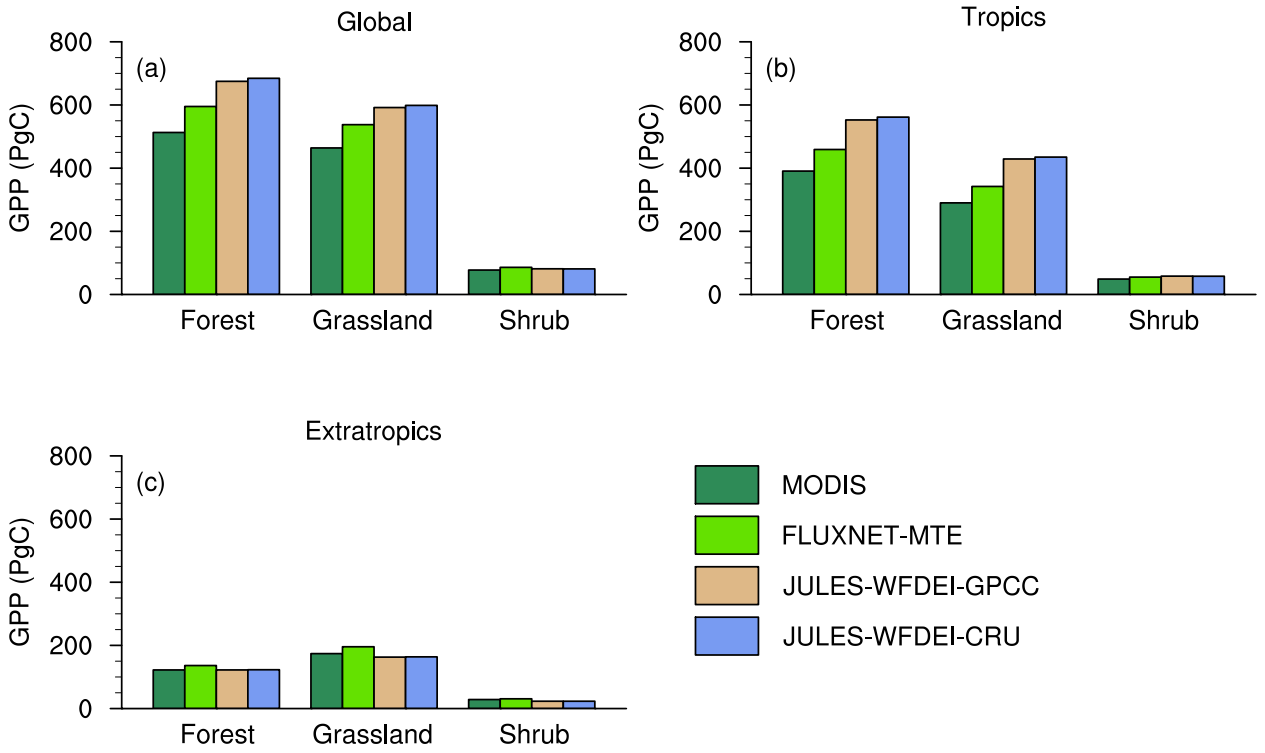

Figure G.4: Total annual model simulated (JULES-WFDEI-GPCC and JULES-WFDEI-CRU) and observed (FLUXNET-MTE and MODIS) GPP fluxes for the 2000–2010 period at the global and regional scales (tropics and extratropics) for 3 biome types (Forest, Grassland and Shrub). **(a)** displays the global total annual GPP, **(b)** for the tropics (30°S–30°N) and **(c)** for the extratropics (30°N–90°N and 30°S–90°S) for forests, grasslands and shrubs.

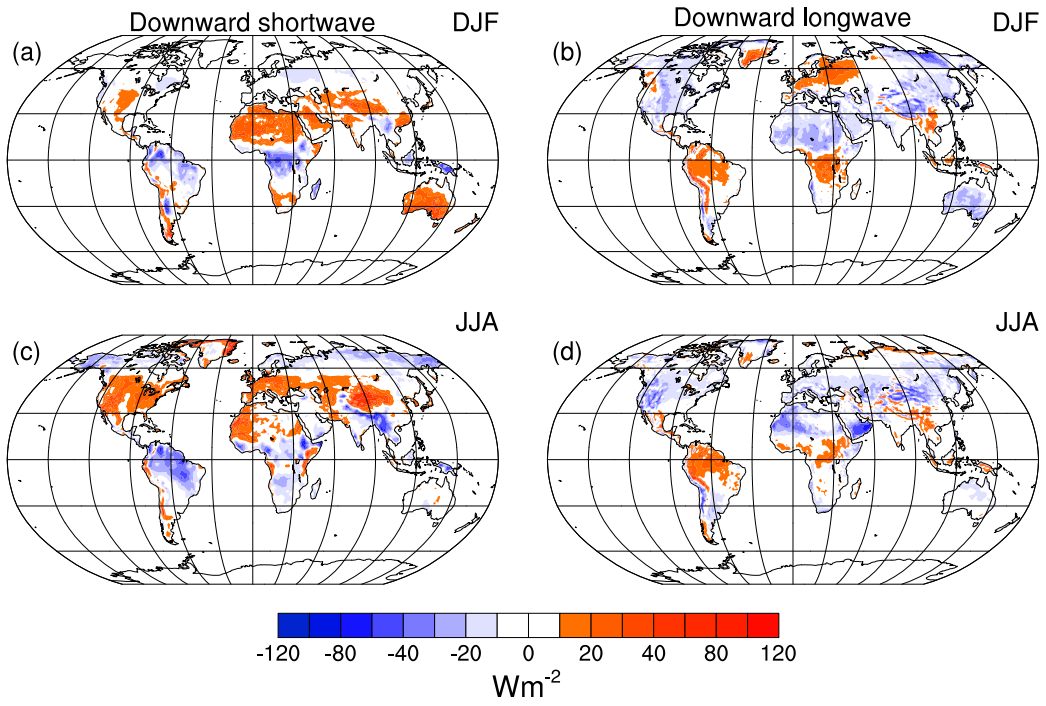

Figure G.5: Difference in seasonal climatology between the WFDEI-GPCC and PRINCETON datasets for downward shortwave radiation for **(a)** DJF and **(c)** JJA and for downward longwave radiation for **(b)** DJF and **(d)** JJA. Blue grid boxes mean positive biases in PRINCETON and orange grid boxes mean positive biases in WFDEI-GPCC.

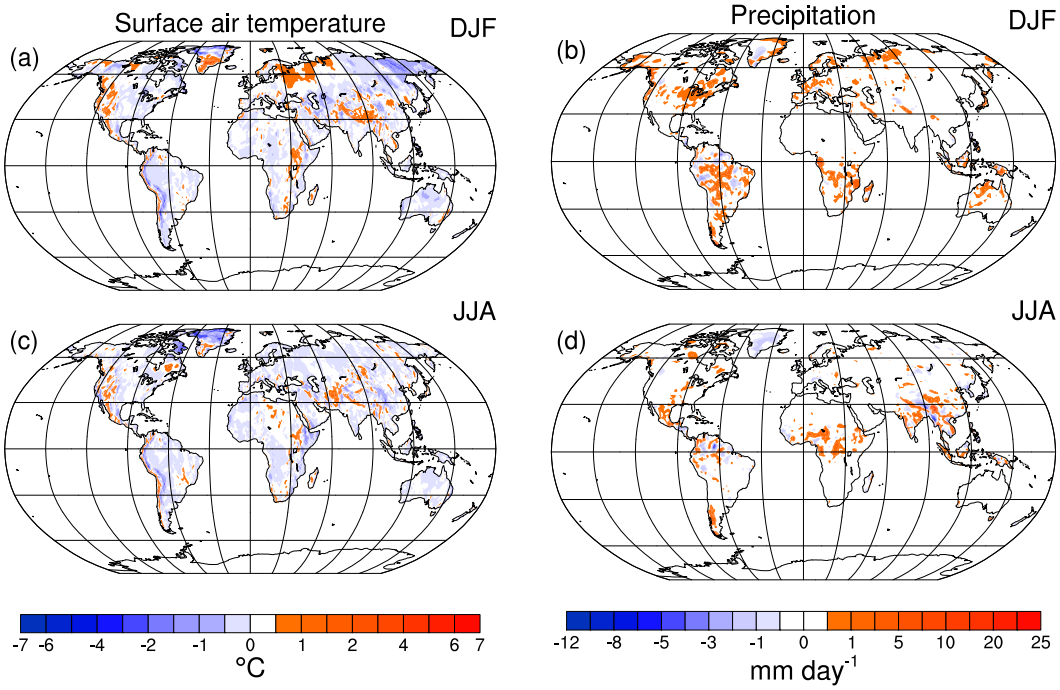

Figure G.6: Difference in seasonal climatology between the WFDEI-GPCC and PRINCETON datasets for surface air temperature for **(a)** DJF and **(c)** JJA and for precipitation for **(b)** DJF and **(d)** JJA. Blue grid boxes mean positive biases in PRINCETON and orange grid boxes mean positive biases in WFDEI-GPCC.

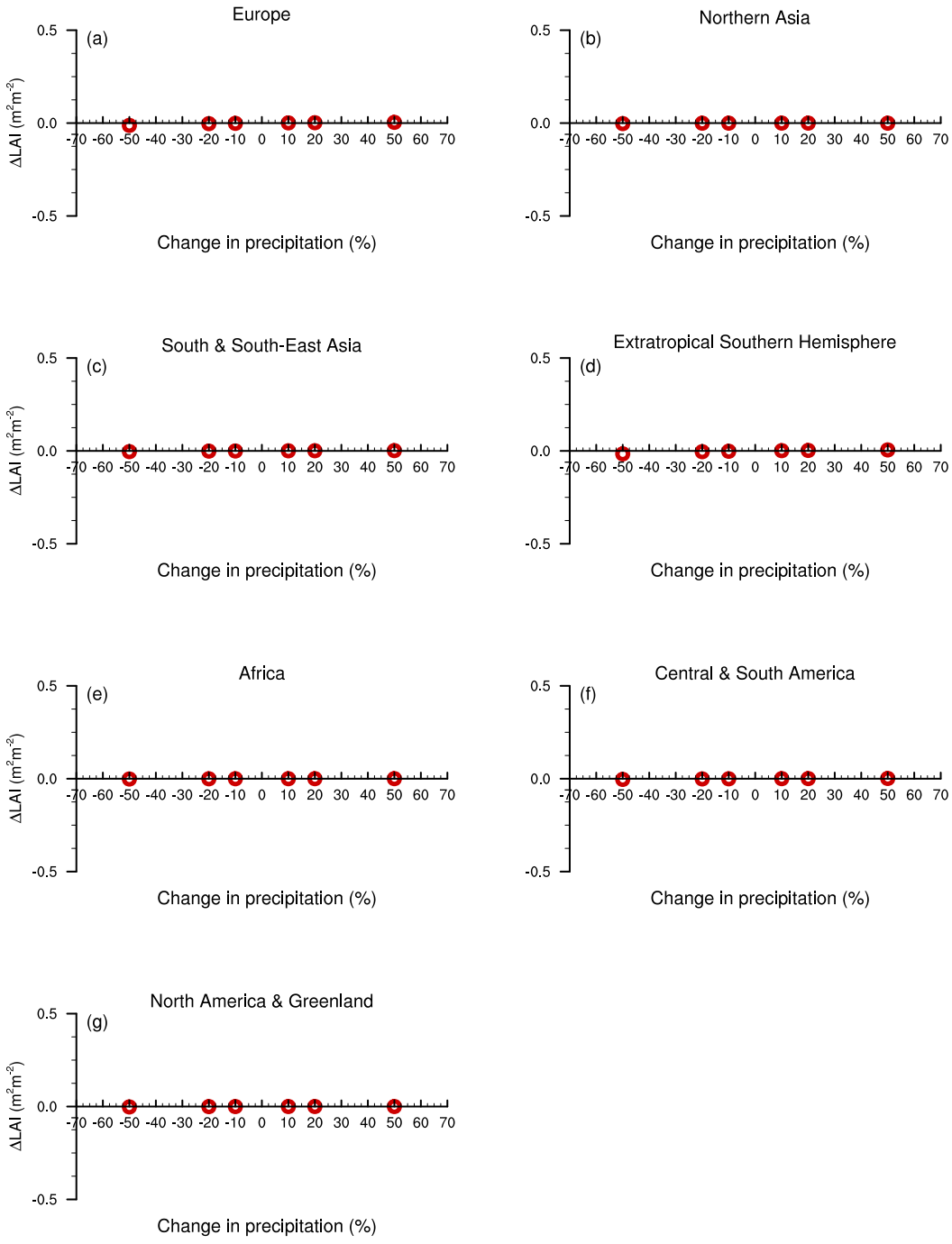

Figure G.7: Difference in monthly climatology regional LAI between model simulations driven with perturbed and unperturbed meteorological data (CONTROL simulation) for the seven regions listed in Table 5.2. The various perturbed model simulations contain only changes to precipitation (unperturbed precipitation +/– 10 %, +/–20 % and +/–50 %,) and the CONTROL simulation contains no changes to precipitation.

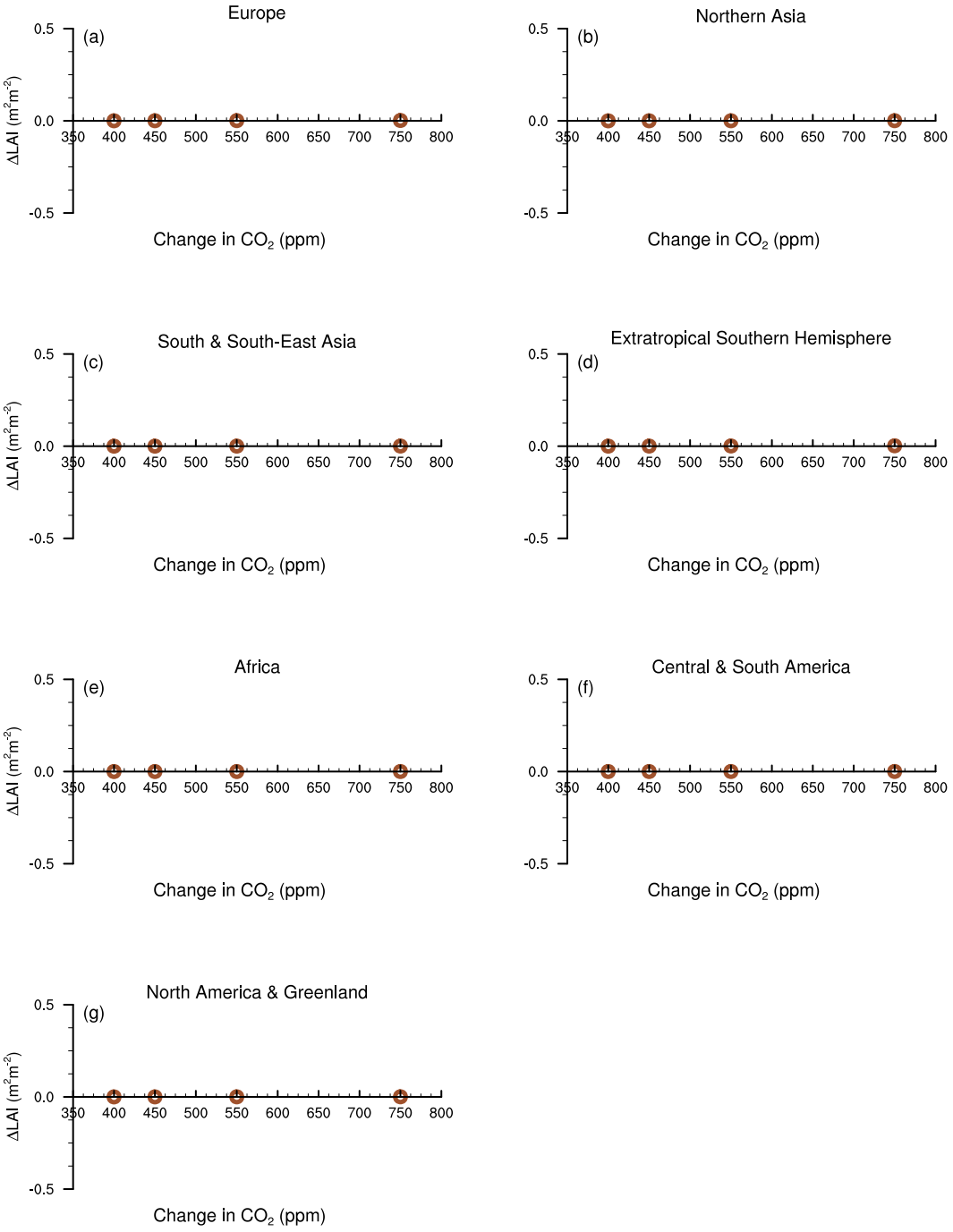

Figure G.8: Difference in monthly mean regional LAI between model simulations driven with constant atmospheric CO_2 concentrations (400 ppm, 450 ppm, 550 ppm and 750 ppm) and with observed (historical) CO_2 (CONTROL simulation) for the seven regions listed in Table 5.2.

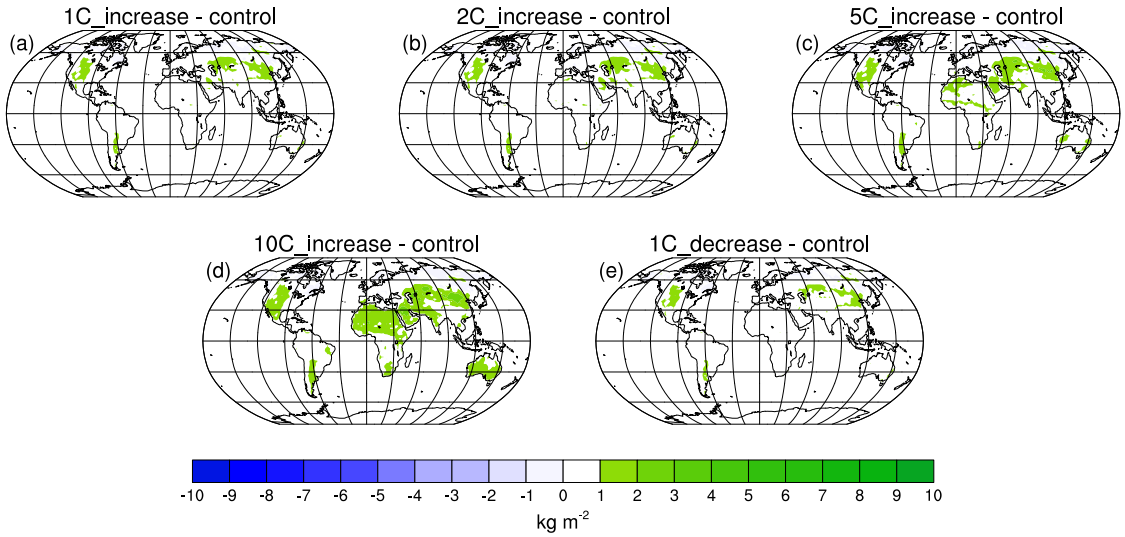

Figure G.9: Differences in soil moisture on 1 January 1999 (this was the date in which the dump file from the control simulation was used to initialise the shorter simulations) between model simulations in which changes to surface air temperature were included in the spin-up period and those in which no changes were included.

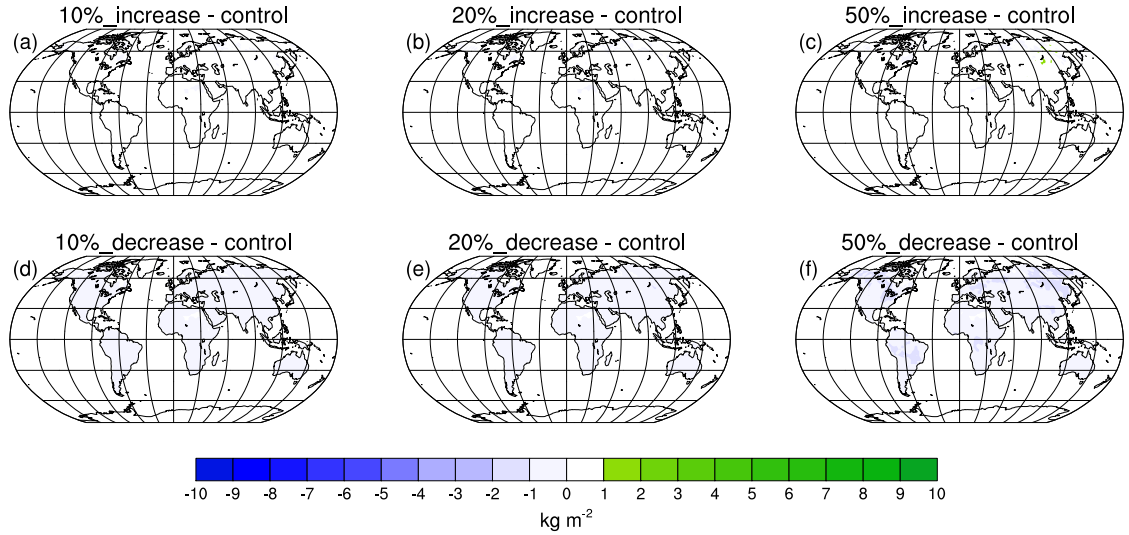

Figure G.10: Differences in soil moisture on 1 January 1999 (this was the date in which the dump file from the control simulation was used to initialise the shorter simulations) between model simulations in which changes to precipitation were included in the spin-up period and those in which no changes were included.

Bibliography

A. L. Buck. New Equations for Computing Vapor Pressure and Enhancement Factor. *Journal of Applied Meteorology*, 20:1527–1532, 1981. doi:10.1175/1520-0450(1981)020<1527:NEFCVP>2.0.CO;2.

B. J. Cosby, G. M. Hornberger, R. B. Clapp, and T. R. Ginn. A Statistical Exploration of the Relationships of Soil Moisture Characteristics to the Physical Properties of Soils. *Water Resources Research*, 20:682–690, 1984. doi:10.1029/WR020i006p00682.

B. A. Cosgrove, D. Lohmann, K. E. Mitchell, P. R. Houser, E. F. Wood, J. C. Schaake, A. Robock, C. Marshall, J. Sheffield, Q. Duan, L. Luo, R. W. Higgins, R. T. Pinker, J. D. Tarpley, and J. Meng. Real-time and retrospective forcing in the North American Land Data Assimilation System (NLDAS) project. *Journal of Geophysical Research*, 108(D22), 2003. doi:10.1029/2002JD003118.

T. G. Gilmanov, L. L. Tieszen, B. K. Wylie, L. B. Flanagan, A. B. Frank, M. R. Haferkamp, T. P. Meyers, and J. A. Morgan. Integration of CO_2 flux and remotely-sensed data for primary production and ecosystem respiration analyses in the Northern Great Plains: Potential for quantitative spatial extrapolation. *Global Ecology and Biogeography*, 14:271–292, 2005. doi:10.1111/j.1466-822X.2005.00151.x.

M. L. Goulden, S. D. Miller, H. R. Da Rocha, M. C. Menton, H. C. de Freitas, A. M. e Silva Figueira, and C. A. D. de Sousa. Diel and seasonal

patterns of tropical forest CO_2 exchange. *Ecological Applications*, 14: 42–54, 2004. doi:10.1890/02-6008.

H. Kato, M. Rodell, F. Beyrich, H. A. Cleugh, E. Van Gorsel, H. Z. Liu, and T. P. Meyers. Sensitivity of Land Surface Simulations to Model Physics, Land Characteristics, and Forcings, at Four CEOP Sites. *Journal of the Meteorological Society of Japan*, 85:187–204, 2007. doi:10.2151/jmsj.85A.187.

G. Lasslop, M. Reichstein, D. Papale, A. D. Richardson, A. Arneth, A. Barr, P. Stoy, and G. Wohlfahrt. Separation of net ecosystem exchange into assimilation and respiration using a light response curve approach: critical issues and global evaluation. *Global Change Biology*, 16:187–208, 2010. doi:10.1111/j.1365-2486.2009.02041.x.

T. Laurila, H. Soegaard, C. R. Lloyd, M. Aurela, J.-P. Tuovinen, and C. Nordstroem. Seasonal variations of net CO_2 exchange in European Arctic ecosystems. *Theoretical and Applied Climatology*, 70:183–201, 2001. doi:10.1007/s007040170014.

Y. Malhi, L. E. O. C. Aragao, D. B. Metcalfe, R. Paiva, C. A. Quesada, S. Almeida, L. Anderson, P. Brando, J. Q. Chambers, A.C.L. da Costa, L. R. Hutyra, P. Oliveira, S. Patiño, E. H. Pyle, A. L. Robertson, and L. M. Teixeira. Comprehensive assessment of carbon productivity, allocation and storage in three Amazonian forests. *Global Change Biology*, 15:1255–1274, 2009. doi:10.1111/j.1365-2486.2008.01780.x.

M. Reichstein, E. Falge, D. Baldocchi, D. Papale, M. Aubinet, P. Berbigier, C. Bernhofer, N. Buchmann, T. Gilmanov, A. Granier, T. Grünwald, K. Havránková, D. Ilvesniemi, H abd Janous, A. Knohl, T. Laurila, A. Lohila, D. Loustau, G. Matteucci, T. Meyers, F. Miglietta, J.-M. Ourcival, J. Pumpanen, S. Rambal, E. Rotenberg, M. Sanz, J. Tenhunen, G. Seufert, F. Vaccari, T. Vesala, D. Yakir, and R. Valentini. On the separation of net ecosystem exchange into assimilation and ecosystem respiration: review and improved algorithm. *Global Change Biology*, 11: 1424–1439, 2005. doi:10.1111/j.1365-2486.2005.001002.x.

R. Stöckli, D. M. Lawrence, G. Y. Niu, K. W. Oleson, P. E. Thornton, Z. L. Yang, G. B. Bonan, A. S. Denning, and S. W. Running. Use of FLUXNET

in the Community Land Model development. *Journal of Geophysical Research*, 113:G01025, 2008. doi:10.1029/2007JG000562.

G. P. Weedon, S. Gomes, P. Viterbo, H. Österle, J. C. Adam, N. Bellouin, O. Boucher, and M. Best. The WATCH Forcing data 1958–2001: A meteorological forcing dataset for land surface- and hydrological-models. Technical Report Technical Report No. 22, February 2010.